Investigation of the influence of material and manufacturing parameters on the flux distribution and noise of transformer cores

Hamid Shahrouzi

A thesis submitted to Cardiff University in candidature for the degree of Doctor of Philosophy

Wolfson Centre for Magnetics
Cardiff School of Engineering, Cardiff University
Wales, United Kingdom

April 2018

Acknowledgements

Firstly, I would like to express my deepest thanks to my supervisor Dr. Philip Anderson for all the supports and encouragements that he gave me. I would also like to sincerely thank to my co-supervisor, Dr. Jeremy Hall for his technical comments during this work.

I would like to express my special thanks to Professor Anthony Moses, for his encouragements and valuable guidance. Without his guidance and constant feedbacks this PhD would not be achievable. His challenging questions and constructive critics helped me to improve the technical aspects of my PhD. I'm very thankful to Dr. John Homewood, Dr. Mathew Pearson and Dr. John McCrory for their invaluable helps for setting up the noise and vibration instrumentations.

This research was fully funded by Shanghai Baosteel Group Corporation. I gratefully acknowledge the generous funding which made my PhD work possible.

I owe a debt of gratitude to all my colleagues at Wolfson Centre for Magnetics for their support; especially, Dr. Christopher Harrison for his helps to develop and diagnose the magnetic measurement systems, Dr. Hugh Stanbury for discussions on measurement uncertainty. I would like to thank Dr. Hamed Hamzeh Bahmani, Dr. Tomasz Kutrowski, Dr. Vishu Goel, and Dr. Nicolas Lewis for the intimate friendship. I would also like to thanks other members of school of engineering of Cardiff University, for their comments and supports during my research, specifically, Dr. David Clark, Dr. Turgut Meydan and Dr. Paul William in energy department, Mrs Aderyn Reid and Ms Jeanette Whyte in Research Office and Mr Ian Andrew King and his colleagues in mechanical workshop.

I would like to especially thank my Mum and Dad who their blessing and support has been always so inspiring to me. I owe their great gratitude as without their constant love, encouragement and strong support, none of my achievements would have been possible.

The Last but not the least, I'm greatly indebted to my beloved friend and wife, Sahar, who deserves a considerable recognition for her continuing love, friendship and support. Mainly, without her love, motivation, patience and support none of the achievements in this work would have been possible.

Summary

Flux distribution in transformer core has a significant effect on vibration-born-noise of the ferromagnetic core. The grade of electrical steel and the geometry of the core joints as well as the manufacturing and utilisation parameters affect the flux distribution in the core, mainly in the joints. Understanding the effect of materials and the manufacturing parameters on flux density distribution would enable transformer design engineers to improve the core performance.

In this study, localised search coils were used to measure the flux density distribution in a linear joint assembled from different grades of electrical steel and the results were verified using COMSOL Multiphysics software with a 2D model. The flux density distribution was also measured in a mitred corner joint and the effect of the variability of the airgaps was investigated. A 3D laser scanning vibrometer was deployed to measure the vibration of the mitred joint and the results were compared with the flux density distribution. The front surface of a three phase three limb production transformer core was scanned using the 3D laser scanner and the emitted noise was measured in the same induction level to find a correlation between the noise and vibration.

The flux in the limb is non-uniform due to the longitudinal airgaps in the joints and the length of this non-uniformity greatly depends on the airgap length and the permeability of electrical steel. The peak value of the interlaminar flux density was found to be higher in NO steel than GO and the flux density in the rolling direction in the NO assembly was more uniform than GO. The flux in the outer layers of the stacked transformer core was found to be higher than in the central layers and increasing the height of stack made the flux more uniform. The calculated Maxwell forces and mechanical deformation in the joint had a good correlation with flux distribution and the scanned vibration data. A reasonable correlation was found between the surface vibration acceleration and the emitted noise of the production transformer core with frequency domain analyses.

Table of Contents

List of Figures

List of Tables

List of Symbols

A	Cross sectional area
$\vec{A}$	Magnetic vector potential
$\vec{B}$	Magnetic flux density
B_{800}	Magnetic flux density at magnetic field 800 A/m, 50 Hz
B_c	Critical induction
B_{gap}	Airgap flux density
$B_{gap\ bridge}$	Gap bridge flux density
B_{normal}	Interlaminar flux density
B_{pk}	Peak magnetic flux density
B_{rem}	Remnant magnetisation
B_{sat}	Magnetic saturation flux density
c	Sound speed
c_i	Sensitivity coefficient
D	Displacement current
e_{rms}	RMS voltage
e	Induced electromagnetic force
e_{av}	Average voltage
$\vec{E}$	Electric field
E_A	Magneto-crystalline Anisotropy Energy
E_k	Instantaneous kinetic energy
E_λ	Magneto-elastic energy
f	Frequency
f	Force per unit volume
h	thickness
H	Magnetic field
H_c	Magnetic coercive field
H_d	Demagnetising field
i	Current
J	Current density

J_e	Current density with external source
J_i	Induced current density
K_{95}	Coverage factor with a level of confidence of 95%
K_i	Anisotropy constant
L	Length
l_m	Effective magnetic path length
LpA	A-weighted sound pressure level
Lp_i	Sound pressure level
m_a	Active mass
M_s	Saturation magnetisation
M	Magnetisation
n	number of measurement
N_S	Number of step laps
N	Number of turns
N_d	Demagnetising factor
N_{mic}	Number microphones
P	sound pressure level
P_0	Reference sound pressure
P_{an}	Anomalous power loss
P_{ed}	Eddy current power loss
P_{hy}	Hysteresis power loss
P_m	Total magnetic power loss
q	Electrical charge
R	Reluctance
RD	Rolling direction
S	estimated standard deviation
S_d	Standard deviation
t	Time
T	Temperature
T_c	Curie temperature
$T_{i,j}$	Stress tensor component
u_c	Combined standard uncertainty
U_i	Expanded uncertainty
v	Volume
W	deflection of a plate

X	vibration displacement
X_{pk}	Peak vibration displacement
Y	young's modulus
α_i	Direction cosines
ϵ_0	Vacuum permittivity
λ_s	Saturation magnetisation
ρ	Density
ρ_f	free charge density
φ	Magnetic flux
φ_{pk}	Peak magnetic flux density
ω	Angular frequency
б	Electric conductivity
v	Poisson ratio
$\overleftrightarrow{T}$	Stress tensor
μ	Permeability
μ_0	Permeability of free space
μ_r	Relative permeability

List of Abbreviations

2D	2 dimensional
3D	3 dimensional
AC	Alternative current
BF	Building factor
BUDR	Ball unit domain refine
CGO	Conventional grain oriented
DC	Direct current
emf	Electro motive force
FEM	Finite element method
GIC	Geographically induced current
GO	Grain oriented electrical steel
HGO	Highly grain oriented electrical steel
MSL	Multi step lap
NDR	Non-domain refined
NO	Non-oriented electrical steel
ND	Normal to the plane direction
RD	Rolling direction
SPL	Sound pressure level
SSL	Single step lap
SST	Single sheet tester
TD	Transverse direction

1. Introduction

1.1 Background

Transformers are one of the crucial components of electrical networks and their efficiency has been improved significantly in the last decades. Demand of electricity is increasing and this will lead to the install of more power stations and transformers in urban areas. Since transformers are increasingly installed in urban areas, their emitted noise becomes more important since the regular exposure to consistent environmental noise can cause health issues like annoyance and sleep disturbance. Unlike the efficiency, the emitted noise of majority of the transformers is still higher than the desired values. In many countries, maximum allowed noise levels are determined in standards by local governments and are getting stricter and stricter every year. For instance the maximum allowed average sound level emitted from a 50 KVA transformer reduced from 51 dB in 2006 to 48 dB in 2013 according to the US national electrical manufacturer association standards[1]. Although some adjustments can be made at significant cost to reduce the noise, a large reduction in the noise has not been achieved. Mainly, transformers have three sources of noise: the core, the winding and the cooling parts. The winding noise depends on the load which for most transformers under normal continuous load is not significant. The cooling parts noise is linked to the noise coming from the fans. The core noise is emitted all the time and is independent of winding current. Because of the very limited knowledge of the mechanism of core noise generation, decreasing the level of this noise is still challenging. Forasmuch as the core is a fundamental noise source, the aim of this investigation is about the contribution of flux distribution to generation of core noise.

1.2 Objectives

It is generally accepted that the magnetostriction of electrical steel, interlaminar Maxwell forces and the resonance frequencies of the core all contribute to

transformer noise. In some of the latest research which has been conducted in Cardiff University [2], it is proved that the magnetostriction is more significant when a core operates at the low flux density. Magnetic forces have more significant effect on transformer core vibration when the operating flux density is high due to the increased airgap flux density in the joint. In real world applications the core usually works at high flux density, thus the Maxwell forces have higher contribution to the emitted noise.

The core configuration and build has a very large impact on the flux distribution in the core. Therefore it is very important to well understand the mechanism of the flux distribution at the vicinity of the mitred joint. A few investigations have been conducted in this field so far, which were mostly simulations with many assumptions to reduce the complexity of the models and limited technical information about the material properties. The best approach is to investigate the problem both analytically and experimentally and the following research objectives were developed to meet this aim:

1- To quantify the flux distribution at the vicinity of the transformer core corner joints experimentally and analytically with different grades of electrical steels.

2- To investigate the effect of longitudinal airgap length on the flux distribution in mitred joint.

3- To quantify the effect of transformer core stack height on flux distribution.

4- To investigate the relationship between the surface vibration and the emitted noise.

In order to achieve these aims, a standard Epstein frame was used to simulate the transformer core joint in a linear fashion. Two different grades of electrical steel were used to study the effect of materials grade on flux distribution. A translation table was developed in order to study the effect of airgap length on flux distribution. The flux distribution was measured in different airgap lengths at the vicinity of the mitred joint of a transformer core assembled from nine layers of CGO electrical steel. Simultaneously, a scanning 3D laser vibrometer was used for measuring the surface vibration of the core at different airgap lengths in order to find a correlation between the flux distribution and vibration. The same assembly was used to study the effect of stack height on flux density distribution.

The linear 2D models of the core joints with the same grades of electrical steels were developed in order to assess the experimental findings.

2 Basics of Magnetism and transformer cores

This chapter reviews some general terms of magnetism and then specifically focuses on the microstructure of electrical steel because two different grades of electrical steels have been used in this research. Then the structure of power transformer cores and their joints will be discussed. Then forces which present in the jointed regions will be introduced.

2.1 Basic terms in magnetism

A magnetic field is produced whenever there is electrical charge in motion. This can be due to electrical current flowing in a conductor. The magnetic field in the space around an electric current is proportional to the electric current which serves as its source and is measured in amperes per meter. For steady currents Ampere's law is defined as the following:

$$Ni = \int_{Closed\ Path} \vec{H}.\overrightarrow{dl} \qquad \textbf{(2-1)}$$

where N is the number of current-carrying conductors, each carrying the current i amps. This is the source of the magnetic field H, and l is a line vector. The integral is calculated over a closed path.

When a magnetic field H has been generated in a medium by a current according to Ampere's Law, the response of the medium is its magnetic induction, B in Tesla. The relation between the magnetic induction and the magnetic field is a property called the permeability which is the degree of magnetisation of a material in response to an applied magnetic field. The H and B relation to permeability is as follows:

$$\vec{\boldsymbol{B}} = \mu\vec{\boldsymbol{H}} \qquad \textbf{(2-2)}$$

Where the permeability, μ, is a scalar if the medium is isotropic. Relative permeability, denoted by the symbol μ_r, is the ratio of the permeability of the specific medium to the permeability of free space μ_0:

$$\mu = \mu_r \mu_0 \qquad \textbf{(2-3)}$$

Where $\mu_0 = 4\pi \times 10^{-7} \ Hm^{-1}$.

Regions in a ferromagnetic material are formed by the long-range ordering of atomic dipoles, even with no external magnetic field which exhibit a weak magnetisation (M). Each atomic dipole can be considered as a permanent magnet with constant magnetisation. These dipoles contribute to the overall magnetic induction in the material therefore equation (2-2) can be re-written as follows:

$$\vec{\boldsymbol{B}} = \mu(\vec{\boldsymbol{H}} + \vec{\boldsymbol{M}}) \qquad \textbf{(2-4)}$$

For ferromagnetic materials μ_r is non-constant and non-linear as shown in Fig 2-1 along with the initial magnetisation B-H curve. The relationship between B and H under alternative magnetising conditions is more complicated (see Fig 2-2). The B-H curve is a closed loop with the path over time moving in an anticlockwise direction over each cycle. The remnant magnetisation, B_{rem} is marked on the graph and is the magnetisation remaining after the external magnetic field is removed. The magnetic coercivity, H_c, is a measure of the ability of a ferromagnetic material to withstand an external magnetic field without becoming demagnetised (H=0, B=0 state). The saturation induction, B_s, theoretically, is the state that the material reaches when the increase in applied field does not increase the induction level in the material. Mathematically, this happens when $\frac{\Delta M}{\Delta H} = 0$ or the permeability of the ferromagnetic material becomes equal to free space. Technically yielding this condition is very difficult for electrical steel because large ampere-turns; e.g. $N.i > 10^5$, needs a large value of N or i which with respect to the limitations on ordinary standard apparatus and instruments it is impossible to be produced.

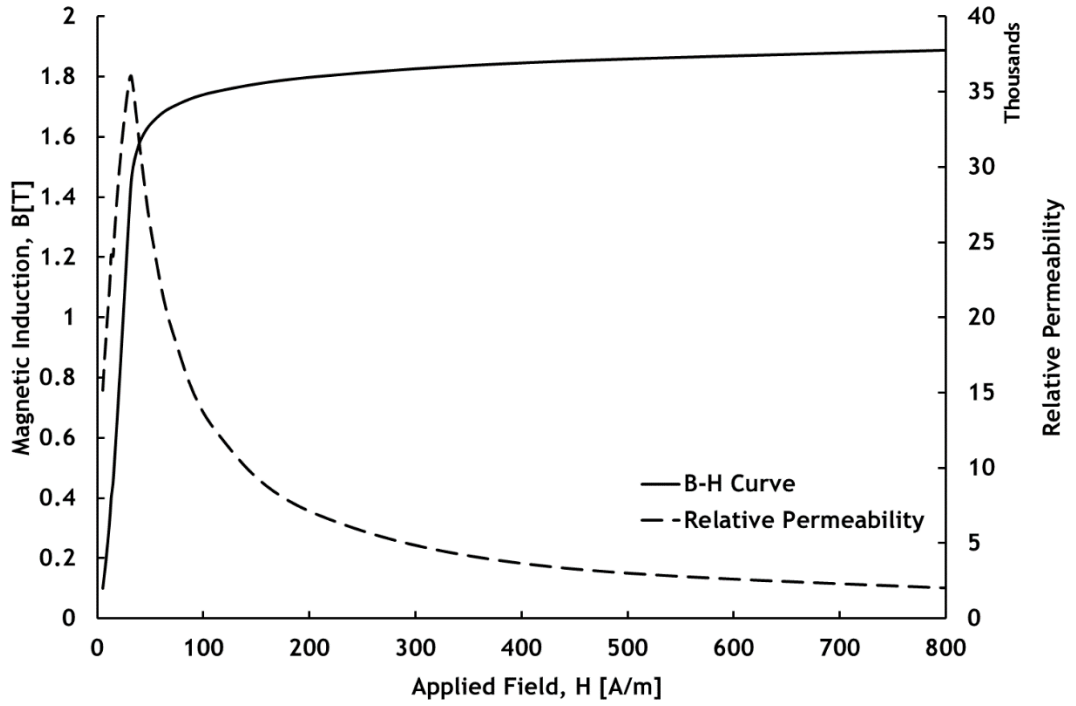

Fig 2-1 A Sample relative permeability and the initial magnetisation B-H curve of grain oriented electrical steel of grade M130-30 at 50 Hz

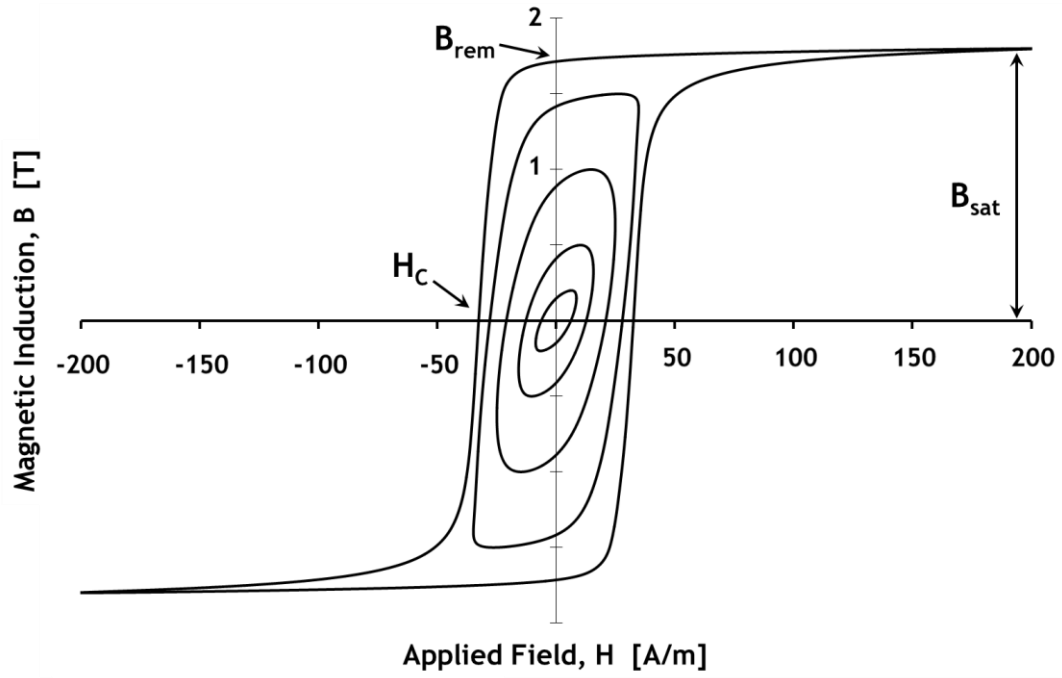

Fig 2-2 Sample B-H loops of electrical steel of grade M080-23 in 0.2, 0.5, 1.0, 1.5 and 1.8 Tesla

2.2 Lattice planes and Miller indices

The orientation of a surface or a crystal plane may be defined by considering how the plane intersects the main crystallographic axes of the solid. Miller indices, h,

k and l written in round brackets are a method of describing the orientation of a specific plane within a lattice in relation to the Cartesian axes[3]. When referring to a set of planes related to each other by symmetry braces are used: {h,k,l}. If (h,k,l) are the Miller indices of a plane, then the plane cuts the axes into 1/h, 1/k and 1/l. In some instances the Miller indices are best multiplied or divided by a common number in order to simplify them by removing a common factor[4]. This operation of multiplication simply generates a parallel plane which is at a different distance from the origin of the particular unit cell. Some examples of Millerr indices for different planes are illustrated in Fig 2-3.

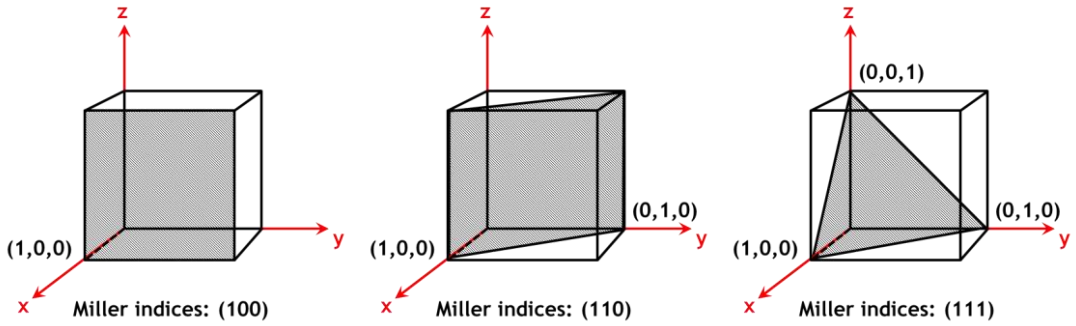

Fig 2-3 Millerr indices for different planes

2.3 Ferromagnetism in Silicon steel

Metals are normally crystalline solid bodies consisting of a large number of grains tightly united by grain boundaries. In these structures the atoms are arranged in a space lattice. The iron cubic-space-centred lattice is illustrated in Fig 2-4 [5].

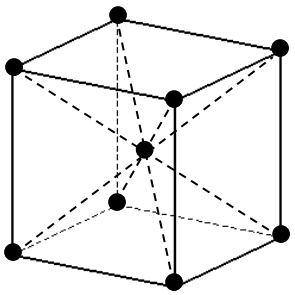

Fig 2-4 Space lattice of iron

Materials with crystalline structure have preferred magnetisation directions where the magnetic characteristic rises steeply up to the approach of saturation [5]. Electrical steel also has a crystalline structure. In non-oriented electrical steel these cubes are oriented haphazardly to minimise the overall magneto-crystalline anisotropy energy but in grain oriented electrical steel with Goss texture the

crystal cubes are oriented in the direction of rolling. A single cubic crystal lattice of electrical steel with Miller indices is shown in Fig 2-5. In Goss texture the (011) plane is in the rolling direction and the cube edge direction in ((001)) is the easiest direction for magnetisation. The diagonal direction ((111)) is the hardest direction of magnetisation. In grain oriented electrical steel a majority of the grains are aligned in a cube on edge orientation close to the rolling direction (RD). The average misorientation (θ) in grain oriented electrical steels varies from 7° in CGO conventional grain oriented electrical steel (with average grain size of 5 mm) to average 3° in highly grain oriented (HGO) electrical steel. The area in which the individual magnetic moments of the atoms are aligned with one another and pointing in the same direction is called a magnetic domain.

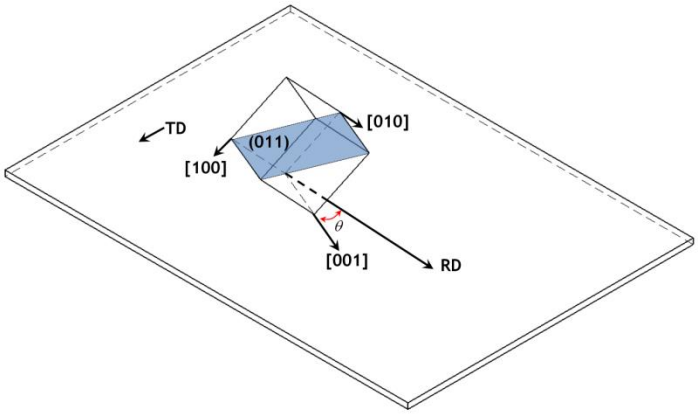

Fig 2-5 (011)((100)) or Goss texture of GO electrical steel in demagnetised state. In magnetized state, as the magnetic field increases $\theta \rightarrow 0$

2.3.1 Magneto-crystalline Anisotropy Energy

If the measured magnetic properties are different when it is measured in different directions, then the term "magnetic anisotropy" is assigned to that property. The anisotropy of the material can be intrinsic or can be induced to the material by special selection of processing methods.

Magneto-crystalline anisotropy is the tendency of the magnetisation to align itself along the favoured easy direction. In a crystal of cubic structure, it is supposed that any physical property of the crystal has cubic symmetry. Therefore the properties in the direction of any cube edge would be the same as that in the direction of any other cube edges. In electrical steel, which has a cubic structure, an anisotropy energy per unit volume, E, can be written as a series

expression of the direction cosines, α_i, of the saturation magnetisation relative to the crystal axes:

$$E_A = K_0 + K_1(\alpha_1{}^2\alpha_2{}^2 + \alpha_2{}^2\alpha_3{}^2 + \alpha_3{}^2\alpha_1{}^2) + K_2(\alpha_1{}^2\alpha_2{}^2\alpha_3{}^2) + \quad \textbf{(2-5)}$$

where the component of energy K_0 is independent of direction and so the directional properties of the domain aHDrMSe dependent on anisotropy constant K_1 and K_2, which in different materials may have positive or negative values. Good agreement with experimental results have been obtained without the higher powers of α_i [6].

2.3.2 Magnetostatic energy and domain subdivision

The work per unit volume required to assemble a population of magnetic "free poles" into a particular configuration is called the magnetostatic energy [7] . If a crystal of iron is considered to be in the form of one square shaped domain which is saturated in its easy direction, then the ends of the domain would act as free magnetic poles. The saturation vector M_s would align with one of the cube edge directions since this would minimise the magnetic anisotropy energy. The demagnetising field H_D inside the domain would be:

$$\overrightarrow{H_D} = N_D\overrightarrow{M_S} \quad \textbf{(2-6)}$$

Where N_D is demagnetising factor which depends on the shape of the presumed domain and is equal to $1/3\mu_0$ for a cube [8]. The demagnetising field energy can be calculated as follows:

$$E_m = \frac{1}{2}N_D M_s{}^2 = \frac{M_s{}^2}{6\mu_0} \quad \textbf{(2-7)}$$

From the minimum energy perspective, a single domain is not favourable. The magnetic energy can be reduced by splitting the large domain into smaller domains. The energy would reduce by dividing the domain into some sub domains with antiparallel settlement of the M_s vectors. The most stable condition considering the minimisation of the system total energy is illustrated in Fig 2-6-d. The small triangular domains with the boundaries at 45° to the direction of M_s are called closure domains. The relative position of M_s to the boundaries defines the type of the boundaries. Where there is a change of direction in M_s equal to 90°,

the associated boundaries are called 90° boundaries and those between two antiparallel boundaries are known as 180° boundaries. Dividing the domains into very smaller sub-domains will reduce the magnetostatic energy further. However, dividing the domains introduces more boundaries which are in fact domain walls. The domain walls also have thickness and associated energy with them. The distance between these domain walls are determined by minimisation of sum of the energy of them and the magneto-elastic energy [6].

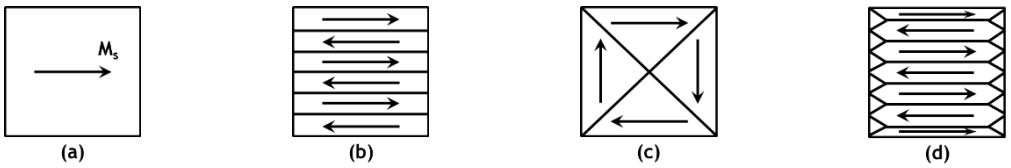

Fig 2-6 Changing domain patterns in the iron to reduce the magnetostatic energy(a) single domain model with maximum energy (b) antiparallel settlement of the M_s vectors with non-maximum energy (c) Ms vectors with non-minimum settlement (d) Ms vectors with minimum settlement

2.3.3 Domain boundary energy

A set of aligned magnetic moments are called a magnetic domain. There is a transitional region between two opposite aligned domains which is called the domain wall (180° domain wall). In the wall, the orientation of the dipoles changes in a screw like fashion from the direction of one domain to the direction of another as shown in Fig 2-7. The domain wall energy is the sum of the anisotropy and the exchange energy. The energy per magnetic moment is known as the exchange energy which causes alignment of magnetic moments within a domain. The exchange energy of the wall decreases and the anisotropy energy increases as the wall thickness increases. The thickness of the wall is determined when the sum of these two energies are minimised.

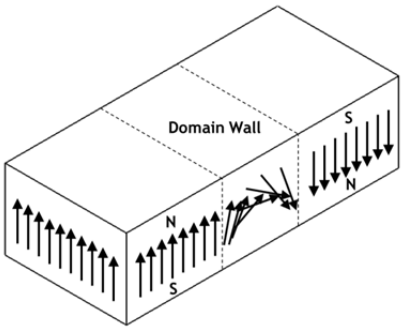

Fig 2-7 180° domain wall in a magnetic material

2.3.4 Magneto-elastic energy and spontaneous magnetostriction

All magnetic crystals have some magneto-elastic interactions which means that the magnetic field affects the elastic properties and the elastic properties affect the magnetic properties [9]. The atomic moment interactions giving rise to ferromagnetism and magnetic anisotropy produces forces between the atoms which tend to strain the lattice in an anisotropic manner. The magnetic energy associated with these lattice strains is called the magneto-elastic energy E_λ [10]. The magneto-elastic energy decreases linearly with increasing lattice strain in cubic crystals.

Magnetostriction is a property of ferromagnetic materials that causes them to change their shape or dimensions during the process of magnetisation. There are two types of magnetostriction in ferromagnetic materials: volume magnetostriction and Joule magnetostriction. Volume magnetostriction is the expansion or contraction of the material in all directions which requires a high external field. Joule magnetostriction is the change in the linear dimensions of a ferromagnetic material. Joule magnetostriction has two parts: spontaneous magnetostriction and the field induced magnetostriction. As a material is cooled below its Curie temperature the material experiences a strain which is called the Spontaneous magnetostriction and the strain associated with it (e/3) is a material dependant constant [11] (see Fig 2-8). "e" is the maximum change in length from paramagnetic state to ferromagnetic state magnetised to saturation. The Curie temperature is the temperature at which the thermal agitation of the atoms in a ferromagnetic material overcomes the exchange interaction and the ferromagnetic properties disappear.

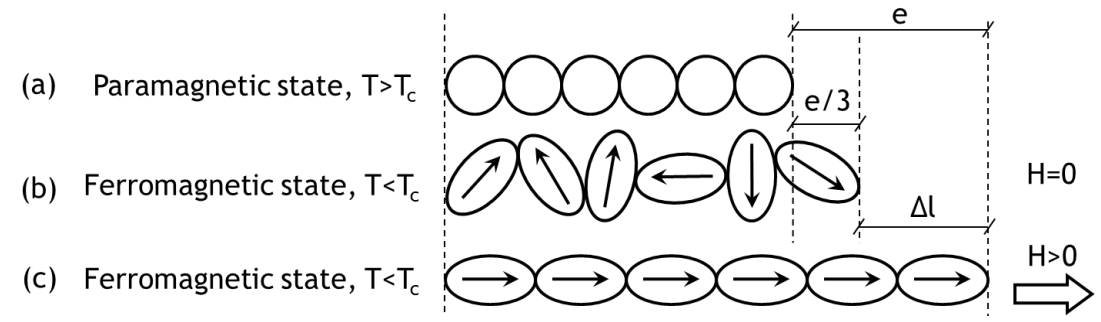

Fig 2-8 Schematic of magnetostrictive effect (a) Above the Curie temperature and without magnetostriction (b) Spontaneous magnetostriction in ambient temperature without any external field (c) Field induced magnetostriction (magnetised to saturation) in ambient temperature at the external H field [12]

By applying energy equal to the magneto-elastic energy (E_λ), the spontaneous magnetostriction will be equal to saturation magnetostriction λ_s. For an isotropic material this energy is equal to:

$$E_\lambda = -\frac{3}{2}\lambda_s \sigma \sin^2\theta \qquad \textbf{(2-8)}$$

Where, θ is the angle between the direction of magnetisation and direction of the stress σ.

2.4 Grain oriented electrical steels

Grain oriented electrical steels are widely used in transformer manufacturing industries because of the superior properties in the rolling direction. The method of producing the grain oriented steel was developed by Goss in the United States [13]. He introduced a certain combination of chemistry, rolling and heat treatment, which would increase the material permeability.

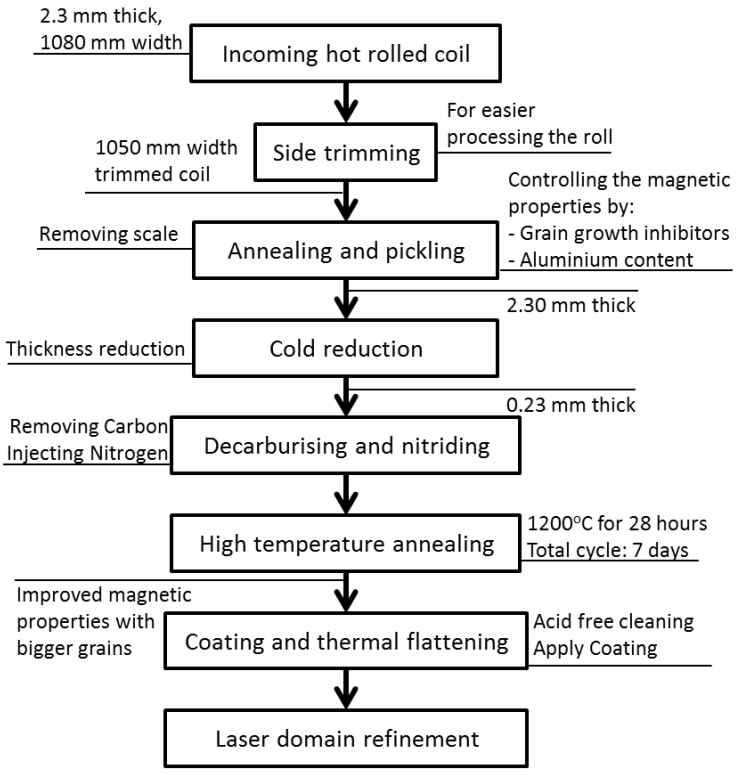

Fig 2-9 Process flowchart to obtain grain oriented electrical steel

When the iron crystallises it forms into grains a size of a few microns in NO materials and a few centimetres in GO materials. Increasing the grain size will

cause a decrease in the number of the domain walls in electrical steel as shown in Fig 2-10. Increasing the grain size is favourable up to a point when the grains approach fingernail size. Beyond this point, the number of the domain walls would not decrease but domains will grow. Wider spacing means that the walls have to move so much more rapidly to change the crystal magnetisation that additional energy loss occurs which will be discussed in the next section. To overcome this effect artificial boundaries are applied mechanically to the metal sheets. These lines do not fully penetrate the sheet, but are sufficient to change the domain wall patterns. Most commercially domain refined materials are produced by laser scribing.

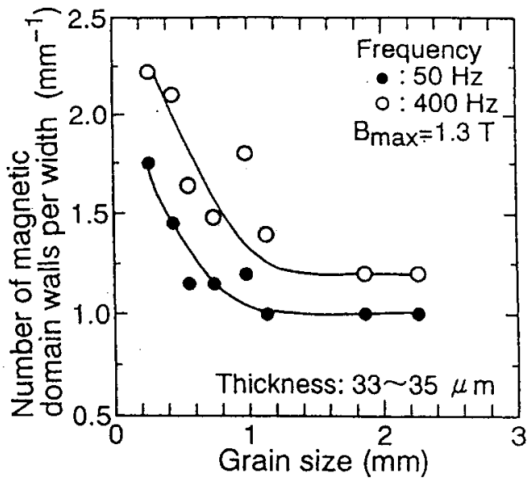

Fig 2-10 Grain size dependence of the number of magnetic domain walls in a 33 to 35 μm thick grain oriented electrical steel which was cold rolled and annealed from 0.27 mm conventional grain oriented electrical steel. The grain sizes where controlled by changing the cold rolling speed and the annealing conditions [14]

Rolling and stamping of electrical steel introduces high stress in the material which is especially critical in the case of small components. The stress which is introduced by cutting or stamping has adverse effects on magnetic properties of the electrical steel. Annealing treatments are conducted to relieve internal stresses and to modify the grain structure. These operations are carried out by heating to the required temperature and soaking at this temperature for sufficient time to allow the required changes to take place, usually followed by slow cooling at the predetermined rate.

2.5 Power loss

As mentioned in section 2.1, the B-H loop gives the relationship between the magnetic flux density B and the magnetic field intensity H for a closed cycle of magnetisation. The area of the B-H loop is proportional to the energy loss per unit volume per cycle. Therefore, the magnetic power which is consumed to magnetise the electrical steel to B Tesla is given by:

$$P_m = \int_0^B HdB \qquad \textbf{(2-9)}$$

Total power loss in electrical steel is decomposed into three components: hysteresis loss (P_{hy}), eddy current loss (P_{ed}) and anomalous loss (P_{an}) [15]. The hysteresis loss relates to domain wall pinning and it represents the energy expended during one cycle of the hysteresis loop to align those domains which were pinned. The hysteresis loss is not only dependent of magnetising frequency but the size, shape and distribution of impurities affect the hysteresis loss. The eddy current loss is related to the loss caused by eddy currents which are induced by the change in magnetic flux density B. The eddy current loss depends on magnetising frequency and lamination thickness and resistivity. The anomalous loss was proposed because the sum of hysteresis and eddy current loss does not match with the total loss. The anomalous losses are not understood very well yet but it is discovered that by a structure of many parallel domain walls - which decreases the movement of the walls during magnetisation – they are reduced [15]. This explains the effectiveness of laser scribing in reducing loss.

2.6 Power transformer cores

A power transformer is a static device consisting of one to three coupled windings wrapped around a ferromagnetic core for inducing mutual coupling between circuits. Transformers are exclusively used in electric power systems to transfer power by electromagnetic induction between circuits at the same frequency, usually with changed values of voltage and current [16]. The power transferred between the circuits is unchanged, except for the typical small loss that happens in the windings and cores.

2.6.1 History

Transformer operation is based on the principal of induction discovered by Faraday in 1831 [17]. He found that when a changing magnetic flux links a circuit a voltage, or an electromotive force (emf), is induced in the circuit. The induced voltage is proportional to the number of turns linked by the changing flux. A very primitive transformer was comprised of a straight core which had to close its magnetic circuit through the air. A Hungarian engineer, Karoly Zipernowsky, invented the first practical transformer in 1885 [16] in which the core was built up of an iron wire. By the 19th century it was realised that the chief aim of the transformer manufacturer was:

- To build the magnetic circuit completely of iron.
- To shorten the magnetic circuit and increase the cross sectional area of the core (considering the weight) as much as possible.
- To use iron with higher permeability.

After more than 100 years modern transformers, which range in size from small units to units as large as a house, differ considerably from those early prototypes, although the operating principal is still the same.

2.6.2 Transformer Theory

An ideal single transformer core is shown in Fig 2-11. In an ideal core, the winding and the core losses are considered to be negligible. Thus the permeability of the core and the conductivity of the windings material is presumed to be infinity. The linking flux between two windings is confined in the core and no leakage flux is considered. According to Faraday's law the induced electromotive force e in each winding with N turns is equal to the negative of the time rate of change of the magnetic flux ϕ enclosed by the circuit:

$$e = -N\frac{d\phi}{dt} \qquad \textbf{(2-10)}$$

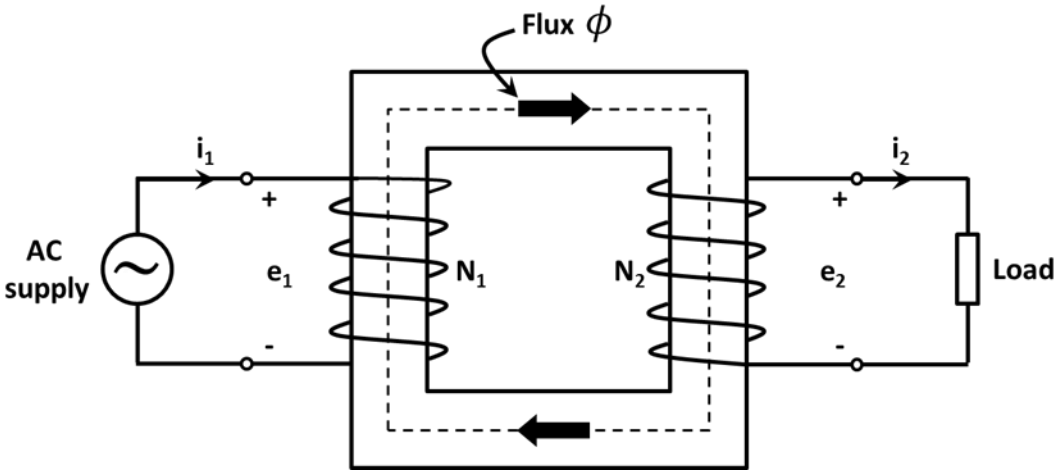

Fig 2-11 Ideal single phase transformer core

Therefore considering the fact that the rate of change of the magnetic flux density for both the primary and secondary windings is equal, the primary and secondary voltages are directly proportional to the number of winding turns:

$$\frac{e_1}{e_2} = \frac{N_1}{N_2} \tag{2-11}$$

where e_1 and e_2 are the e.m.f in the primary and secondary windings respectively. If the voltage waveform applied to the primary hence the flux in the core is sinusoidal, then the flux as a function of time can be written as:

$$\phi(t) = \phi_{pk} \sin \omega t \tag{2-12}$$

where ϕ_{pk} is the peak value of the flux and ω is $2\pi f$ with f being the frequency. Substituting (2-12) into Faraday's law for the secondary voltage:

$$e_2(t) = N_2 \frac{d\phi(t)}{dt} = \omega N_2 \phi_{pk} \cos \omega t \tag{2-13}$$

The *rms* value of the induced voltage over a time period T therefore is equal to:

$$e_{rms} = \sqrt{\frac{1}{T}\int_0^T e_2{}^2(t)dt} = 4.44\, f N_2 B_{pk} A \tag{2-14}$$

and the average secondary voltage is given by:

$$e_{av} = \frac{2}{T}\int_0^{T/2} e_2(t)dt = 4\, f N_2 B_{pk} A \tag{2-15}$$

The amount of applied voltage can be calculated using equations (2-14) or (2-15) to have a desired peak flux density ϕ_{pk} in the core under sinusoidal excitation.

2.6.3 Transformer Core forms

Transformers are classified according to their electrical characteristics such as power and voltage ratings. From the core structure point of view, there are two main core types: core form and shell form which are shown in Fig 2-12. In distribution transformers the shell form design is favoured because it is more compact than the core form design and it has great mechanical strength and KVA to weight ratio. Also natural cooling is sufficient for this core type. The shell form design is much more difficult to assemble than the core form design therefore there are very few manufacturers that still make shell form transformers [16]. The core form design is adaptable to a wide range of design parameters and economical to manufacture therefore for moderate to large power transformers the core form design is popular [18]. This type of core is usually used for large low voltage transformers and because of the cylindrical-shaped windings the short circuit forces can be managed better. Natural cooling is not sufficient for this type. Both forms are constructed from thin layers of laminations. In this research we will just concentrate on core form transformers.

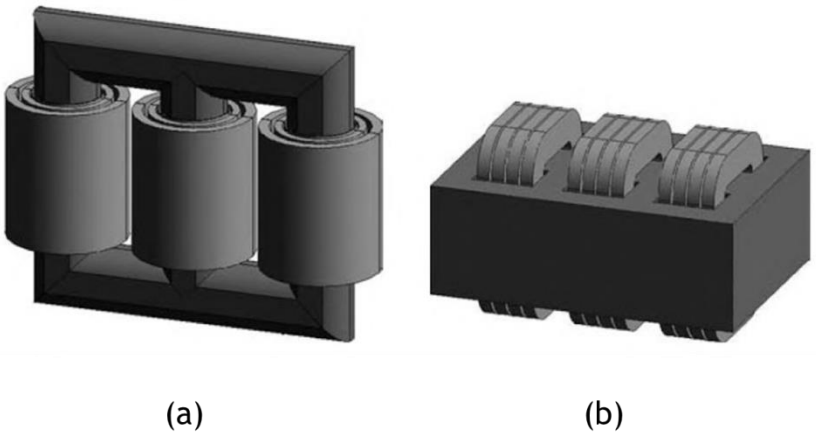

Fig 2-12 A (a) core form and (b) shell form three phase transformer core [17]

2.6.4 Transformer core corner joints

The performance of transformer core depends on the joint types. Very primitive transformer cores were assembled using “L-L” shape laminations as shown in

Fig 2-13-a. These laminations were stacked alternately to each other to produce an overlapping joint. To avoid wasting the material and ease of preparation the butt joint configuration was introduced as shown in Fig 2-13-b.

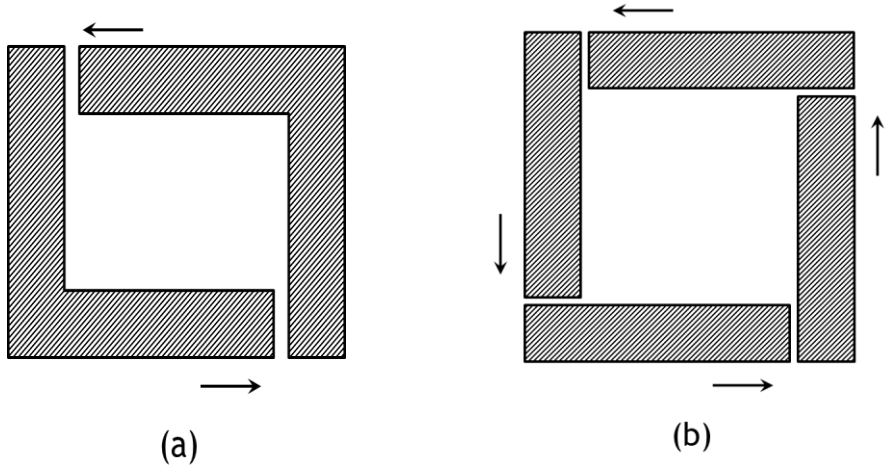

Fig 2-13 Transformer core assemblies with butt and lap joints assembled with(a) L-shape laminations (b) I shape laminations. Arrows are next to butts of each joint.

These joints were sufficient till the advent of grain oriented electrical steel in which the flux has the preferred rolling direction. In order to limit the extent to which the flux path cuts across the grain direction, the joint between limbs and yokes are cut at 45^{o}. This jointing is known as a mitred joint as shown in Fig 2-14. The laminations at these mitred corners are overlapped to let the flux transfer to the adjacent layer rather than crossing the airgap. The 45^{o} mitred joints always have small protruding right-angle triangle at each corner, as shown in Fig 2-15. Some flux distortion up to 7th harmonic have been reported in these regions [19]. In single step lap (SSL) the stack of the laminations has just one step of overlap and in multi-step lap (MSL) joint (See Fig 2-15) the stack has more than one step lap. Depending on the size and rating of the core each step can be composed of one, two or more layers. The joint type is an important factor which affects the building factor of a transformer. The building factor is the ratio of built transformer core loss (per W/kg) to the material nominal core loss and is a function of several parameters such as the material grade, geometry of the joint, number of layers per step and clamping pressure of the core.

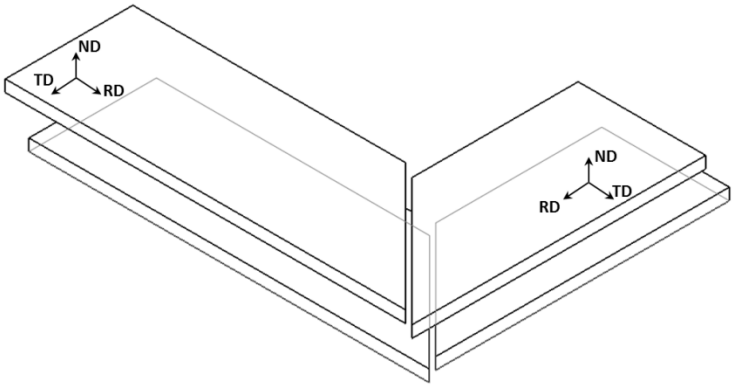

Fig 2-14 A 45º mitred joint assembled with grain oriented electrical steel. RD: Rolling Direction, TD: transverse Direction and ND: Normal to the plane Direction

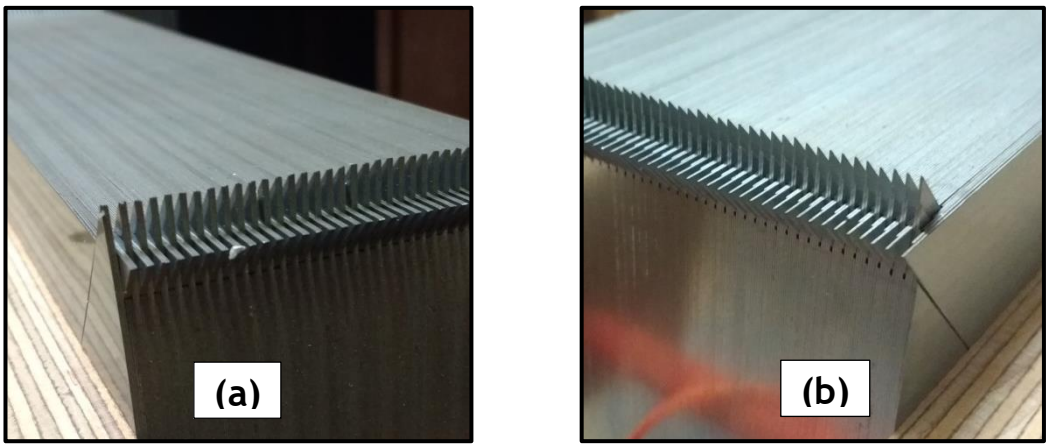

Fig 2-15 Two model transfer cores with Mitred corner joints (a) Single step lap with 5 laminations per step (b) Five step lap with single lamination per step

2.7 Maxwell equations and Maxwell force

The equations governing electromagnetic phenomena are Maxwell's equations, which for sources in a vacuum are (All symbols are introduced in the *symbols list*):

$$\nabla \cdot E = \frac{\rho}{\varepsilon_0} \qquad \text{(Gauss Law)} \qquad \textbf{(2-16)}$$

$$\nabla \cdot B = 0 \qquad \textbf{(2-17)}$$

$$\nabla \times E = -\frac{\partial B}{\partial t} \qquad \text{(Faraday's Law)} \qquad \textbf{(2-18)}$$

$$\nabla \times B = \mu_0 j + \mu_0 \varepsilon_0 \frac{\partial E}{\partial t} \qquad \text{(Ampere's Law with Maxwell's correction)} \qquad \textbf{(2-19)}$$

Together with the force law,

$$F = q(E + v \times B) \quad \textbf{(2-20)}$$

They summarize the entire theoretical content of classical electrodynamics.

Total electromagnetic force on charges in volume v is calculated as follows:

$$F = \int_v (E + v \times B)\rho d\tau \quad \textbf{(2-21)}$$

The force per unit volume is evidently

$$f = \rho E + J \times B \quad \textbf{(2-22)}$$

By eliminating ρ and J using Maxwell's equations, substituting Faraday's law in the resulting expression and doing some simplifications, the total force on the charges in v is calculated as follows:

$$F = \oint_S \overleftrightarrow{T} \cdot da - \varepsilon_0 \mu_0 \frac{d}{dt} \int_v S \cdot d\tau \quad \textbf{(2-23)}$$

Where $\overleftrightarrow{T}$ is the force per unit area (or stress) acting on the surface and S is the Poynting vector (**S**=**E**×**H** where **E** is the electric field and **H** is the magnetic field). In the static case the second term drops out and the electromagnetic force on the charge configuration can be expressed entirely in terms of the stress tensor at the boundary. The stress tensor, $\overleftrightarrow{T}$ has nine components. $T_{i,j}$ is the force (per unit area) in the i^{th} direction acting on element of surface oriented in the j^{th} direction which is described as follows:

$$T_{ij} = \epsilon_0 E_i E_j + \frac{1}{\mu_0} B_i B_j \quad \textbf{(2-24)}$$

T_{xx}, T_{yy} and T_{zz} represent pressure and T_{xy} and etc. are shears. [20].

3 Parameters affecting flux distribution, noise and vibration of a transformer core

3.1 Effect of edge burrs

A Burr is defined as a raised edge created during the manufacturing or processing of a workpiece and is generally small in volume [21]. In electrical steels, these unwanted pieces are usually introduced at the edge of the material after it is cut into smaller pieces. Burrs of electrical steel in laminated cores are important because they decrease the efficiency by creating a short circuit path causing an increase in the loss in power transformers. In severe cases, this can even create some localised heat which will melt the steel at those regions and create more electrical connections. Many studies have been done on burrs and their effects on flux distribution and the core loss in transformers some of which are introduced in this section.

In preparing electrical steels to be used in electrical machines, usually three types of procedures produce burrs: shearing operations [22], punching [13] or laser cutting [23] of which the latter is not used for any bulk commercial applications. According to the British Standard BS EN 10251:1997 burr height is the difference in the material thickness at the cut edge and at 10 mm away from that edge. In electrical steels, the burrs sizes are usually less than 10 μm in height and depend on the type and quality of the cutting tool and the hardness of the material being cut. The coating can influence the burrs height which Organic coatings minimises the burrs in compare to the inorganic coatings [13]. For example Lindenmo [24] has compared the punching characteristics of different types of coatings which is shown in Fig 3-1. Suralac 1000 is an organic coating and Suralac 7000 is an inorganic coating.

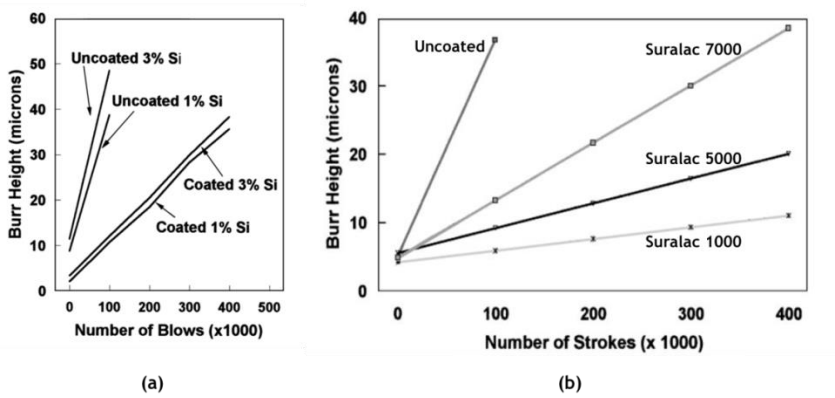

Fig 3-1 (a) Effect of coating on punching performance (b) A comparison between Punching characteristics of organic (Suralac 1000), semi organic (Suralac 5000) and inorganic (Suralac 7000) coatings [24]

In 1989 Moses [25] Studied the effect of artificial edge burrs on the properties of a model transformer core. In this study a single phase experimental transformer core was used with artificial burrs applied by drilling 0.3 mm holes close to the edge of the laminations and inserting a steel pin to short out the required number of laminations in the stack. The schematic plan view of the used single phase core showing the position of the artificial burrs is shown in Fig 3-2. It is reported that the total core loss rose by 100% and the localised loss rose to over 50 Wkg^{-1} when the laminations were completely shorted by connecting the laminations by the steel pin completely. This case is not realistic because it is unlikely to have a short circuit between all of the laminations and at only one point like this experiment. It is reported that the partial burrs caused losses in the regions where applied. As more laminations were shorted with artificial burrs, the power loss increased as shown in Fig 3-2. The authors proposed the computed eddy current path close to the edge burr at one side of the core which is shown in Fig 3-3. As shown, at 25 mm away from the edge burrs the maximum value of the eddy current density occurs. The effect of eddy current on flux distribution in the core has not been discussed in the paper. In order to have current flow there should be a returning path. The returning path length has a direct impact on the amount of power loss. The paper however omitted to consider categorising these returning paths. Therefore a systematic conclusion cannot be drawn from the burr positions and the power loss or their effect on flux distribution. The joints are critical regions in a transformer core which are more vulnerable to burrs but no results have been reported about point 4 and 8 which are close to the joints.

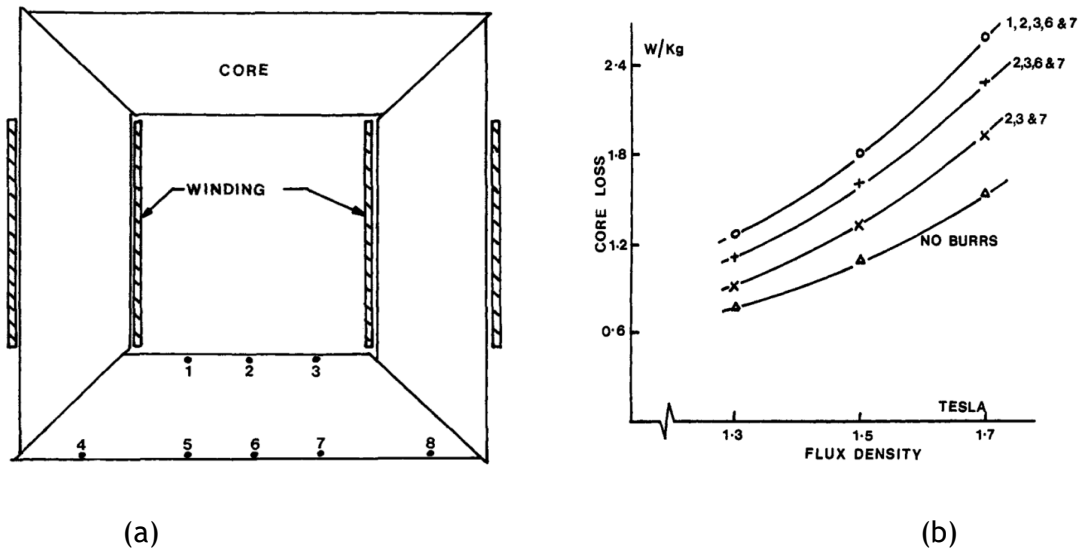

(a) (b)

Fig 3-2 (a) Schematic plan view of the single phase core showing 8 point of artificial burrs (b)Total core loss variation with flux density for different burr conditions

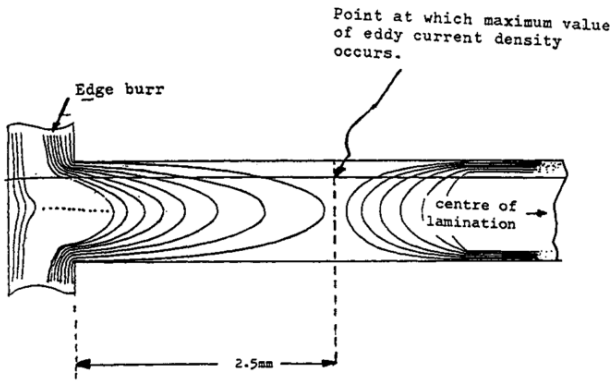

Fig 3-3 Cross sections through the laminations in the stack showing edge burrs (left hand side) and its effect on the eddy current paths near the edge (adjacent laminations) above and below the laminations above and below the lamination shown connected by edge burr are not shown) [25]

In 2010, Mazurek [26] studied the effect of artificial burrs on the total power loss of a three phase transformer core. It was asserted that the loss increases linearly with increased length of burrs. He also confirmed that the flux density inside the core near to the burrs will reduce due to the opposing magnetising field which is produced by the circulating eddy current in the paths created by burrs. As the length of the burred region increases, the specific power loss increases. The rate of increment is bigger in higher induction levels as seen in Fig 3-4.

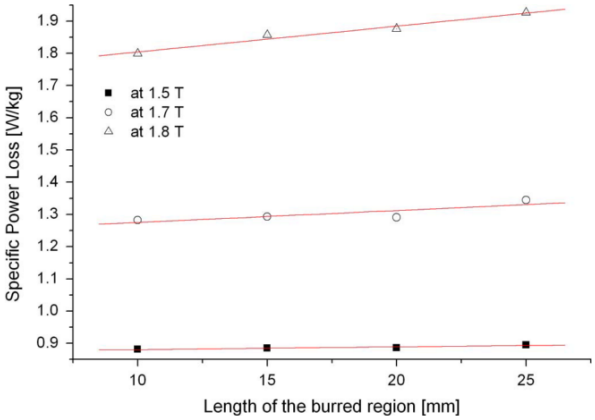

Fig 3-4 variation of specific loss with length of burrs for maximum 33 laminations burred at 1.5, 1.7 and 1.8 T [26]

Mazurek reported the effect of burrs on local power loss in the same three phase transformer core composed of 5 packets [27] in 2012. Using a conductive clamp, 66 layers of the central packet were shorted for applying artificial burrs. A needle probe technique was used to measure the flux distribution in the burred laminations. The flux density dropped significantly when the magnetic flux density dropped in comparison to the overall induction (see Fig 3-5). This is due to the large eddy currents which close their path through the burrs. Magnetic flux density of the burred region between 1.0 T to 1.5 T drops to less than 50% of the overall core flux density which was argued is because of the lower relative permeability of the burred region in comparison to the central part of the core. It was not clarified why this permeability drop did not happen between 1.0 T to 1.5 T.

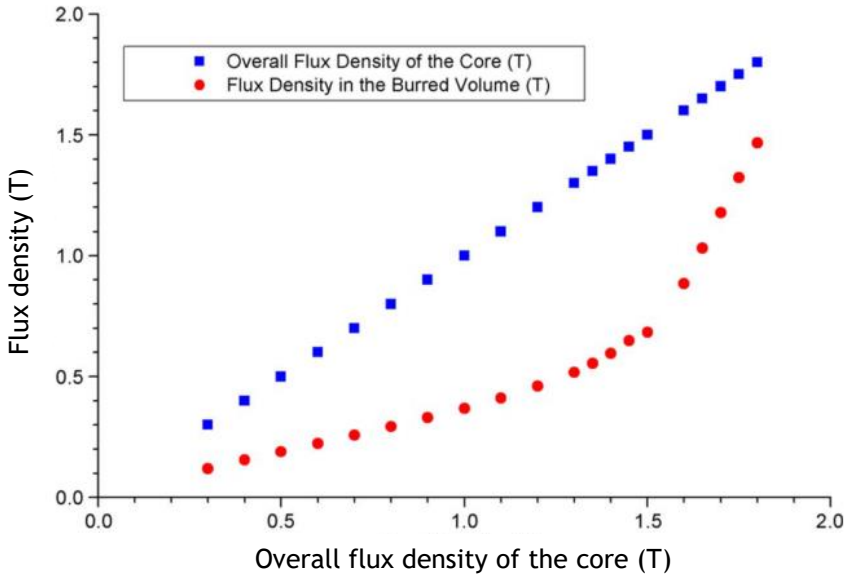

Fig 3-5 Variation of flux density within the burred region versus overall core flux density [27]

In 2014, Hamzehbahmani [28, 29] introduced a comprehensive study on eddy current loss estimation of edge burr-affected magnetic laminations based on equivalent electrical network. The author states that "the burrs and consequently the interlaminar faults change the configuration of the magnetic cores to be similar to a solid core which leads to interlaminar fault currents and larger eddy current loops." (see Fig 3-6)

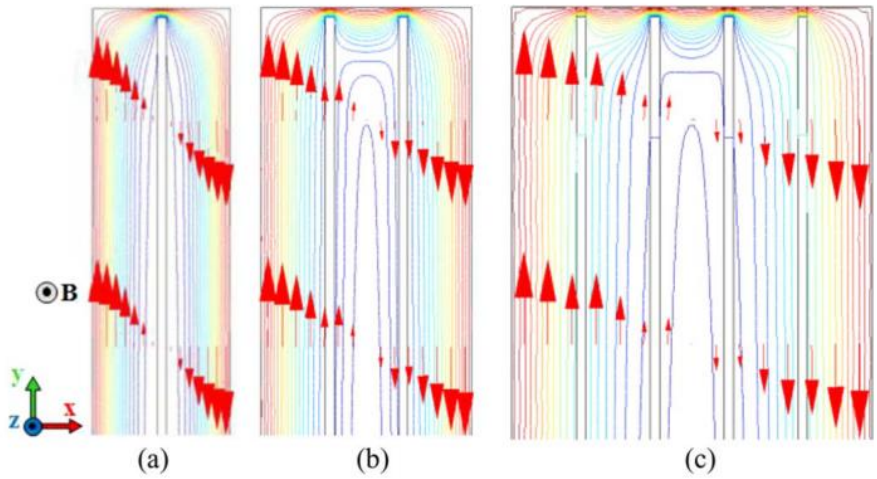

Fig 3-6 2D finite element model of eddy current distribution in burr-affected magnetic laminations at a magnetising frequency of 50 Hz, (a) two, (b) three, and (c) five laminations [28]

It was proved that the eddy current density, hence the local power loss at the shorted ends are higher. Because of the changed configuration of the burred

laminations, the skin effect in these laminations becomes significant and hence flux distribution changes can be even greater than expected.

In general, burrs have adverse effects on the magnetic characteristics of the whole core and especially at the edges which will cause excess loss in the core. Burrs can change the magnetic flux distribution in the core; therefore they can affect the noise and vibration. The amount of burr's contribution to noise generation is very small in compared to other sources, therefore no report on the effect of burrs on noise and vibration has been found.

3.2 Effect of grade of steel

Usually, manufacturers look for a compromise between minimum power loss and noise requirements and the price of the material. However, specific requirements of each transformer determine the combination of characteristics that should be considered in selection of the most appropriate grade of core material. In general lower price materials are compromised to quality. For instance, lowest price material cannot be selected if low core loss is required. If a low core temperature or high efficiency is required, the higher cost low-loss material is suitable to be selected. Where transformer cores should be kept relatively light or the core dimensions must be small, inevitably the materials with high operating flux density are required which is likely to be more costly than the previously mentioned materials. The power loss per unit of electrical steels change when they are used in transformer cores, but mainly the overall power loss of the cores has a direct relationship with the nominal power loss value of electrical steel.

The effect of core material grades (M4 conventional, MOH high permeability and ZDKH domain refined electrical steels) on transformer core audible noise were investigated experimentally on single phase model cores in [30]. The cores assembled in two different designs including single step and multistep lap. It is reported that the models with MOH and ZDKH materials had roughly the same noise levels. The model cores which were built up of M4 grade material had higher noise levels than those with MOH and ZDKH. The loss of each model core was also reported as shown in Table 3-1 which clearly shows that the power loss of ZDKH is the least and M4 is the highest as expected. According to the catalogue, the power loss of M4 at 1.7 T is 1.2 W/kg while for ZDKH is typically less than 1.0 W/kg.

Table 3-1 Measured core losses in W/kg in Single Sheet Tester (SST), Single Step Lap Configuration (SSL) and Multi-Step Lap configuration (MSL) assembled from different grades of electrical steel

	M4	MOH	ZDKH	Core induction
SST	0.829	0.693	0.664	1.5
	1.246	0.954	0.895	1.7
SSL	0874	0.747	0.707	1.5
	1.295	0.998	0.950	1.7
MSL	0.826	0.704	0.668	1.5
	1.251	0.983	0.912	1.7

In [31] the impact of different laser domain refined steel on a three phase transformer noise was investigated. Laser domain refinement helps to reduce the anomalous loss component by decreasing the 180^{o} domain wall spacing but creates additional closure domains which can increase the magnetostriction and hence the transformer core noise. So both goals of reducing the power loss and magnetostriction are contradictory. The laser parameters like spot size and power density, line spacing and the speed of scanning changed to produce different types of domain refined materials. A few of these materials were selected based on magnetostriction measurements and the estimated emitted noise level of the core. Some cores with the same dimensions but different materials were built and the emitted noise level was measured. The authors reported that the magnetostriction data utilised for estimating transformer noise was giving only a rough estimation. They commented that the final judgment is only possible by characterising the real core. It was also claimed that optimising the domain refinement process led to improvement in the loss and slight improvement in noise level (reduced from 67 dB to 64 dB at 1.9 T) compared to non-domain refined situation especially at inductions above 1.50 T.

In [32] the emitted noise from transformer cores assembled from 27M0H and 27M3 grades were compared in different core configurations. The sound measurements were conducted in a small sound booth (no dimensions provided except a picture with a three phase core in it) instead of an anechoic chamber. The problem with these types of rigs is the sound reflection due its small dimensions. The background A-weighted sound pressure level was reported to be 30 dB. The sound level was measured just with one microphone in different locations and then

combined to calculate the overall emitted noise. The results for 27M3 and 27MOH which are presented in this paper do not show a unique trend. The core assembled from 27MOH with a single layer per step emitted 4dB lower noise than 27M3 at 1.7 T while the same material assembled in two layers per step configuration emitted 2.5 dB more noise. Regarding these results, the author concluded that the effect of material type is less dominant than the core quality and design. In addition to these, it is believed that the experimental procedures gave a high uncertainty for the results.

In [33] the influence of material permeability on noise level of the model transformer cores were investigated. Four grades of electrical steel comprising 23RGH090N, 23RGH090, 30RGH105N and 30RGH110 were used in this research. Model three-phase three-limb transformer cores were constructed from each grade and the noise was measured. It was reported that the noise level showed an inverse correlation with the material B_{800} value (flux density when magnetized at 800 A/m). The authors showed that the noise level decreases by slightly less than 2 dB for each difference of 0.01 T in B_{800}. The authors have found that the higher B_8 material shows lower noise level than the lower B_{800} one, regardless of thickness. It was also shown that the magnetostriction harmonic component was smaller in materials with higher B_{800} values. It was shown that the dependence of the A-weighted magnetostrictive vibration acceleration level calculated from magnetostriction harmonic components of a 0.23 mm thick material linearly reduces as the B_{800} value of the material increases.

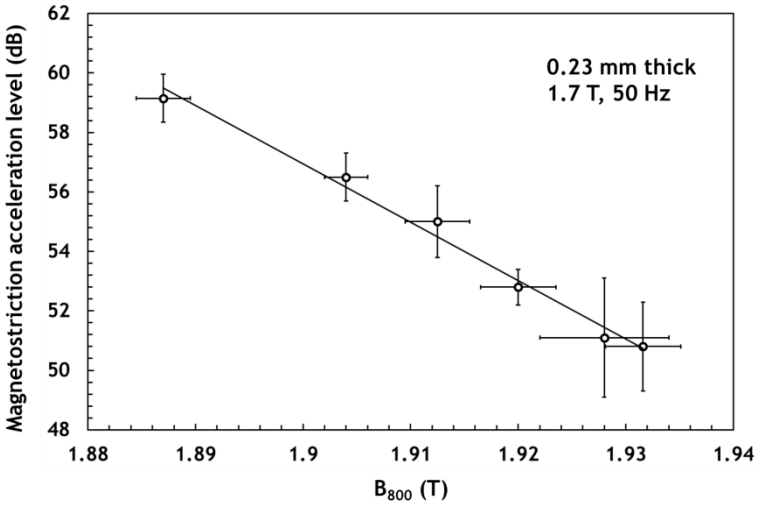

Fig 3-7 Dependence of magnetostriction oscillation acceleration level on B_8 values of 0.23 mm thick material. This figure is adopted from [33]

According to [34] Hi-B grade and scribed core materials gave 2 to 3 dB reduction as compared to non Hi-B grades while according to [35] this reduction can be up to 7 dB.

According to the literature, the grade of electrical steel has a direct effect on the performance of the transformer in terms of noise and power loss. A core built from material with high saturation magnetostriction and permeability emits less noise. Also the lamination's thickness and nominal power loss have a direct influence on the transformer core efficiency. The effect of four main manufacturing factors on the produced electrical steel is presented in Table 3-2. The Coating and its effect on electrical steel performance is not mentioned here.

Table 3-2 The effect of increasing the chemical and physical manufacturing factors on the properties of laminations of electrical steels. Blank cells represent indirect or poor relationship between the governing factors and the magnetic, electrical or mechanical properties

If ↑:		Impurities	grain size	Thickness	Si Content
M_s		↓ [36]	↑		↓ [37]
λ				↑ [38]	↓ [37]
μ		↓ [36]	↑ [39]		↑↓ [37]
Loss	P_{hy}	↑ [36]	↓ [40]	↓ [41]	↓ [36]
	P_{ed}		↑ [42]	↑ [36]	↓
	P_{ex}		↓↑ [43]		↓
Yield stress				↑	↑↓ [37]
Conductivity		↓			↓↑ [37]
Density					↓ [37]

If the core build quality and the design are at their perfect condition, the significance of material grade becomes more important. However, a sample of the influence of the stacking quality on the emitted noise of two identical transformers built form the same material will be presented in subsection 3.8.

3.3 Effect of mixed materials

The idea of using different grades of electrical steel in constructing a transformer core has always been considered as a way to minimise the manufacturing cost. Few investigations have been conducted on the effect of material mix in stacked transformer cores which will be discussed below.

In 1988, Moses and Hamdaneh [44] made one of the first attempts to investigate the effect of mixing materials on losses and cost of operation of three phase transformer cores. Three types of materials comprising of CGO, HiB and laser scribed high permeability ZDKH materials were used in this investigation. Six model cores were assembled using these materials as the following: core A: all CGO, core B: all HiB, core C: all ZDKH, core D: centre limb CGO, rest HiB, core E: centre limb CGO, rest ZDKH, core F: limbs CGO yokes HiB. Moses reported that the mixed cores all had building factors lower than the high-permeability cores B and C as shown in Table 3-3. It is claimed that the flux is more uniform in core A, so the loss is less but this was not proved. No obvious trend is observed in the presented results. It is known that the mechanical stress and the airgaps at the corner joints cause the BF to increase [45]. The influence of the airgaps in different assemblies can be monitored by the consumed reactive power of each core which was not mentioned. The lamination's cutting accuracy and the airgap variability in different cores were not discussed in [44]. All the nominal loss of the materials had been obtained using a single strip tester. As will be discussed in the next chapter it is better to measure the magnetic properties of high permeability grain oriented electrical steels with single sheet tester. So there might be some errors associated in the reported data. Furthermore, the uncertainty budget for the magnetising and the measurement system has not been reported.

Table 3-3 Building factors and per unit losses of six cores at 1.5 T and 1.7 T, 50 Hz. Core A: all CGO, core B: all HiB, core C: all ZDKH, core D: centre limb CGO, rest HiB, core E: centre limb CGO, rest ZDKH, core F: Limbs CGO, yoke HiB [44]

	1.5 T		1.7 T	
Core	Loss (W/kg)	B.F.	Loss (W/kg)	B.F.
A	0.98	1.16	1.36	1.12
B	0.95	1.26	1.24	1.23
C	0.88	1.23	1.16	1.22
D	0.93	1.20	1.24	1.18
E	0.89	1.20	1.19	1.18
F	0.95	1.17	1.31	1.15

Moses, conducted the economic assessment of the mixing materials in transformer cores by comparing the cost of ownership of the various transformers, which includes the cost of material and capitalised loss cost and assuming all the

other costs were constant. It was assumed that the iron cost of HiB and the ZDKH are 10% and 25% higher than the CGO respectively. His investigations showed that mixing different grades of electrical steel potentially had some economic advantages. This advantage greatly depended on the capitalised loss and material cost and the operating point of the transformer core. As a general rule with the above mentioned hypothesises, he proposed that at low capitalisation values, using high permeability materials in conjunction with CGO were most economical but as the capitalization value increases, the mixing was not economical anymore.

In 2003, Snell [46] investigated the influence of core material and mix on the building factor and loss of a 100 kVA three phase transformer core. Researchers used two different grades of materials in stacking the cores including non-domain refined (NDR) and ball unit domain refined (BUDR) electrical steels. The cores were constructed from one grade of a material to a certain height, the core being completed using the other grade of material. Several experiments conducted with different amount of mixture of the materials and the results showed that the core loss at 1.70 T reduces as the amount of BUDR material in percentage is increased in the core. Also two batches of NDR material with different permeabilities were mixed with different ratios and observed that the loss will increase as the amount of low permeability material increases in the mixed core. The grade of NDR materials were not specified.

The author argued that the ball unit domain refined material and non-domain refined material can be successfully mixed in the same core, without degrading performance but they will exhibit losses in relation to the proportion of the losses of complete cores made from the batches used in the mixed. The effect of mixing the materials on the emitted noise and apparent power loss was not reported.

In [47] the effect of mixing CGO in predominantly three phase three limb HGO core was studied on the core performance. The author also calculated the specific core power loss for each combination. The method of mixing the materials in the three phase core was not mentioned. As shown in Fig 3-8, the specific power loss of the core depended on the proportion of the mixed materials. This relationship was found to be nonlinear and it was argued that this nonlinearity is because of the additional losses in the cores due to the harmonics generated because of the holes in the core. Regarding the power loss results, no advantage was found to mixed materials in the core. The core's noise and vibration in each condition was not reported.

In general, limited research has been conducted on material mix in transformer cores. It was not made clear why those specific materials were used in the mix and why they had been mixed in that specific order. If these points become clear, further optimization of the core's cost would be possible. Some tips on intelligent and purposive material mix will be made based on the results in next chapters which will show that these investigations can be supported by some scientific reasoning of mix and order.

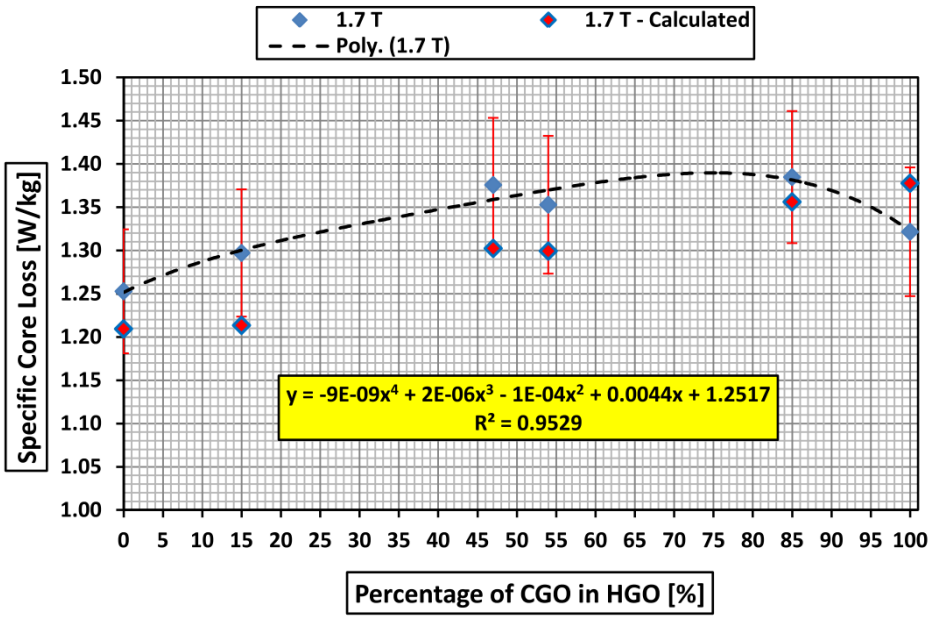

Fig 3-8 variation of specific power loss with CGO content in a three phase three limb core at 1.7 T, 50 Hz [47]

3.4 Effect of DC bias

Geographically induced currents (GIC) are those currents in pipelines or electrical transmission grids which are induced due to electric charge variations of ionosphere and magnetosphere of the earth caused by space weather events. DC currents run in the transformers due to GIC phenomena or power electronic devices in the network which can drive the transformer core into half cycle saturation (see Fig 3-9). Even very small DC bias has detrimental effects on transformer performance which will increase no-load loss, such as higher harmonic stray flux. Also it has some side effects like increasing the noise level, and demanding more reactive power. Several studies have been done recently

about the effect of DC bias on magnetic properties of electrical steels and power transformer core performance [48-60].

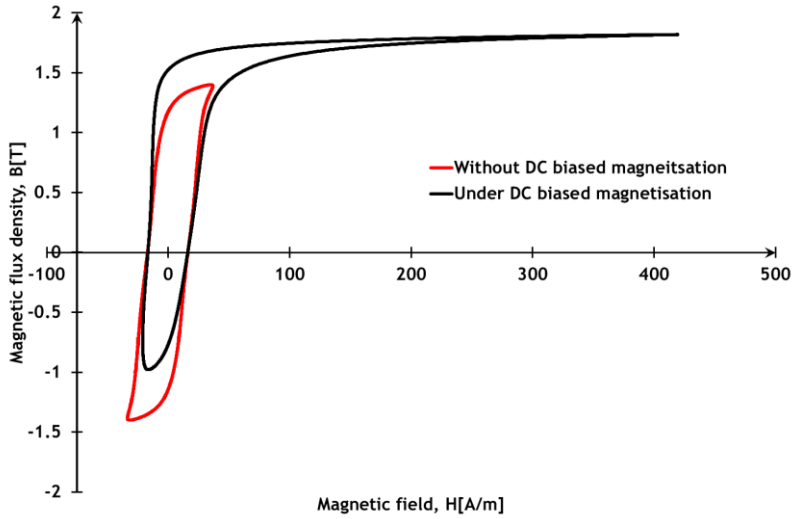

Fig 3-9 The effect of DC bias on B-H curve of conventional electrical steel

In [51] the authors have studied the effect of geo-magnetically induced current on the magnetic performance of transformer cores and concentrated on the effect of GIC on local distribution of planar eddy currents on different cores. In [57] the effects of DC bias on a single phase (T1) and a three phase (T2) transformer cores were studied which their specifications are shown in Table 3-4.

Table 3-4 Specifications of the tested transformers in [57]

	Unit	T1 (single phase)	T2 (Three phase)
Rated power	MVA	134.4	100
Frequency	Hz	60	50
Rated flux density (RFD)	T	1.717	1.561
Required excitation to reach the RFD	A/m	44.7	27.5

Both the transformers were tested in a back to back connection with a second transformer in which direct current was inserted at the neutral point. The amount of direct current which was inserted was not reported. It is reported that with the direct current the no-load sound pressure level (SPL) increases sharply (see Fig 3-10) and the frequency spectrum shifts towards higher harmonics (Fig 3-11). It is depicted that at 1.4 T the noise increase was larger in single phase cores. As

the overall induction increases the excess noise due to the direct current reduces. The authors showed that a very small direct current can lead to an enormous change of the noise level. It is remarked that a direct current of approximately one third of the AC excitation current increases the sound pressure level by 16.9 dB(A) [57].

In the presence of direct current the no load loss of the single phase cores increased, as shown in Fig 3-12. The rate of increase was bigger when the core was working at the lower flux densities. At lower inductions (e.g. 1.4 T) some of the domain walls disappeared gradually and therefore the remaining domain walls could move with higher average velocity. This was linked with increased anomalous loss. The majority of the domain walls disappear at higher magnetic induction (e.g. 1.7 T). At this stage the domains and dipoles just rotated to align with the external field and no domain wall movement was involved, so less anomalous loss was linked.

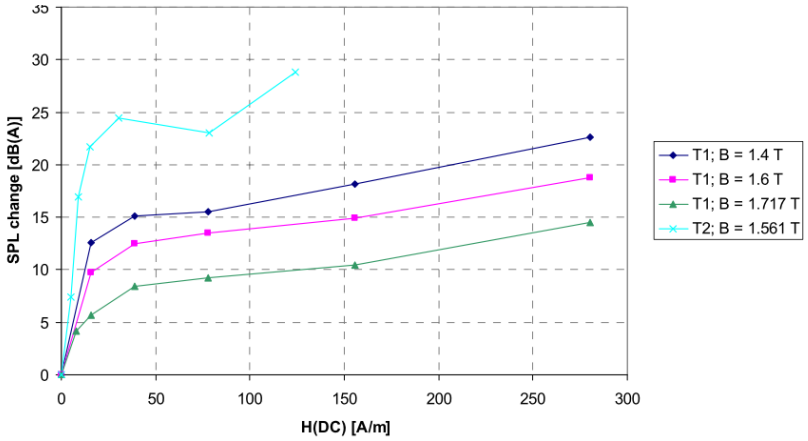

Fig 3-10 Change of sound pressure level with DC magnetic field, for both transformers. The single phase transformer (T1) has been measured at three different levels of induction [57]

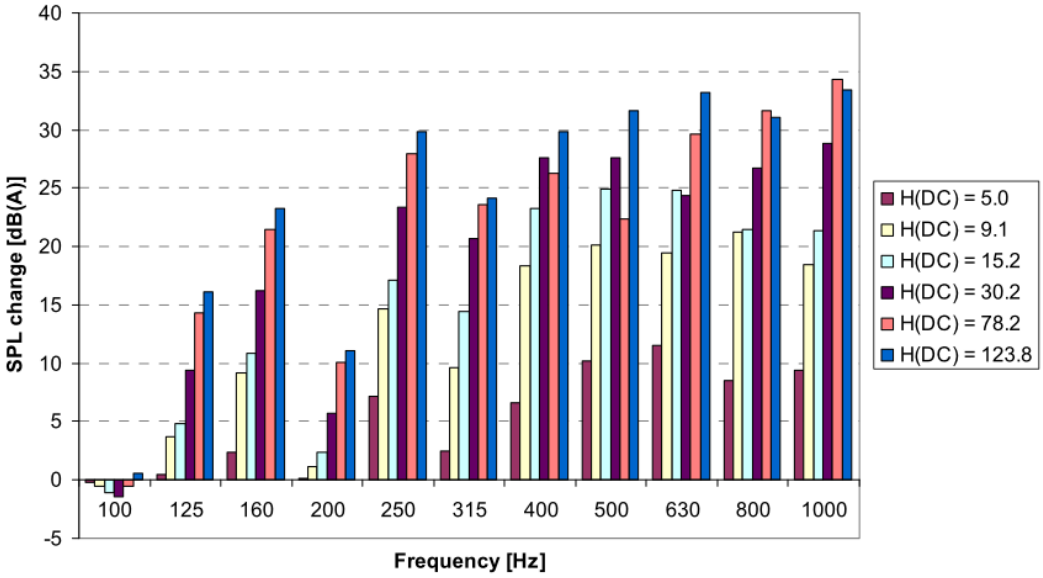

Fig 3-11 Change of sound pressure level in dependence of DC magnetisation: third octave bands of no-load noise of T2 [57]. H(DC) in A/m.

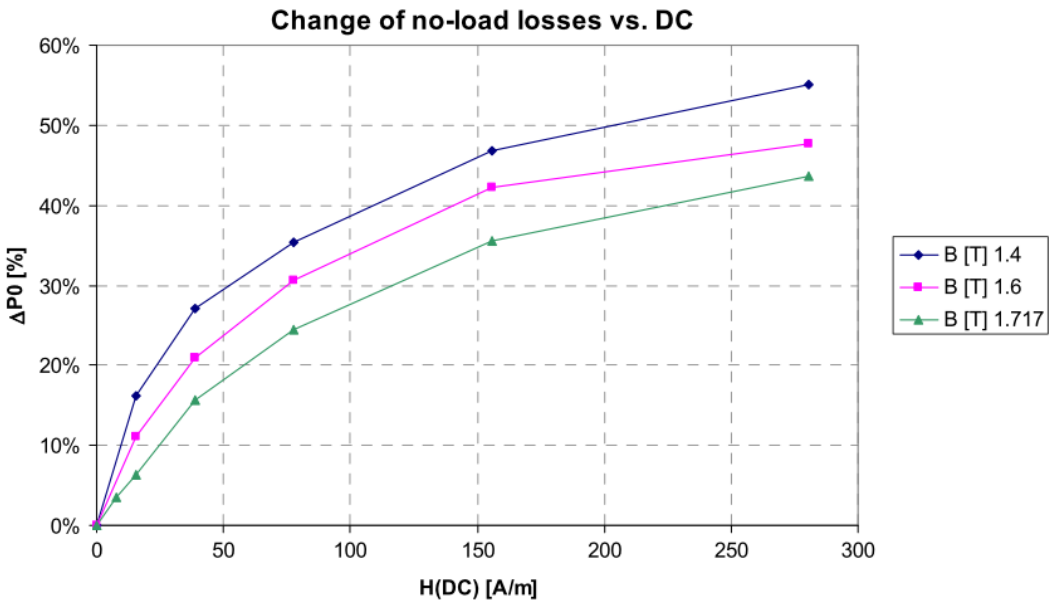

Fig 3-12 Relative change of no-load loss in dependence on direct magnetisation, for the single phase transformer in three different levels of induction [57]

Magnetic properties including the iron loss and the acoustic noise of grain oriented electrical steel in a model transformer under DC magnetic field was investigated in [60]. Loss with DC offset was found to be higher in HGO than CGO under DC magnetic field higher than 30 A/m due to the pinning effect of the domain walls and Barkhausen jumps as illustrated in Fig 3-13. Up to a certain level of H field

the domain walls move and if the H field is removed they return to their previous position as if they are pinned to that point. This process is reversible in the materials as shown in the state 1 of the figure. If the H field passes that certain level the domain walls will jump from their current position to the next pinning point in a way that the most favourably oriented domains grow. These movements are irreversible. The rest of the magnetising process shown in Fig 3-13 are reversible. In HGO material under normal conditions, the top and bottom part of B-H loop are at state 3 (but antiparallel). Introducing the DC bias pushes the top part of the B-H loop into state 4 and pulls the bottom part to state 2. Therefore the domain walls in each cycle move between two extremes. In contrary, in CGO, the bottom of the B-H loop pulled to state 1. So domain walls just move to the extreme in one direction and therefore the iron loss is smaller in CGO. In one complete magnetising cycle, the domain walls in HGO move more in comparison to CGO.

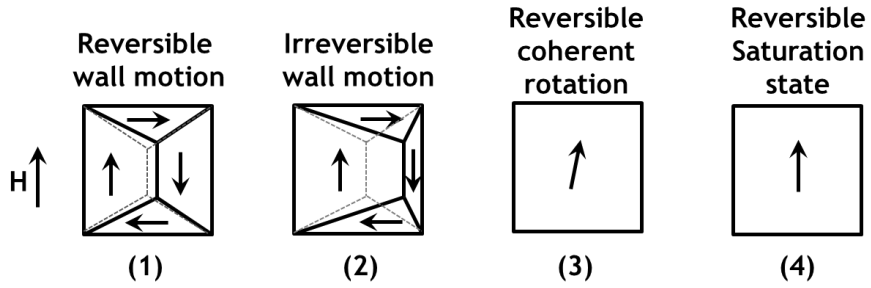

Fig 3-13 Schematic diagram of initial magnetisation of a cubic ferromagnetic material. The dotted lines in state 1 and 2 show the domain walls in their previous states. In the state 1 the domain wall can return back to its previous state if the H field removed. In the state 2, if the field is removed the domain walls will not return back to their previous states. This is called the pinning wall effect. The domain wall jump from previous state to current state called the Barkhausen jump which is irreversible. In state 3 all the domains have been removed except the one which favourably oriented in the H field direction. When all the domains and dipoles are completely aligned with the external H field, the material saturates as shown in state 4

The spectrum of the emitted noise at 0 A/m and 200 A/m which were reported for both materials are presented in Fig 3-14. The noise level of the core which was built up of CGO material for DC magnetic fields more than 50 A/m was reported higher than HGO. At less than 50 A/m the noise level of both cores were reported to be in the same level. At 200 A/m it was observed that in addition to the noise of even-order harmonics, the noise of odd-order harmonics increased.

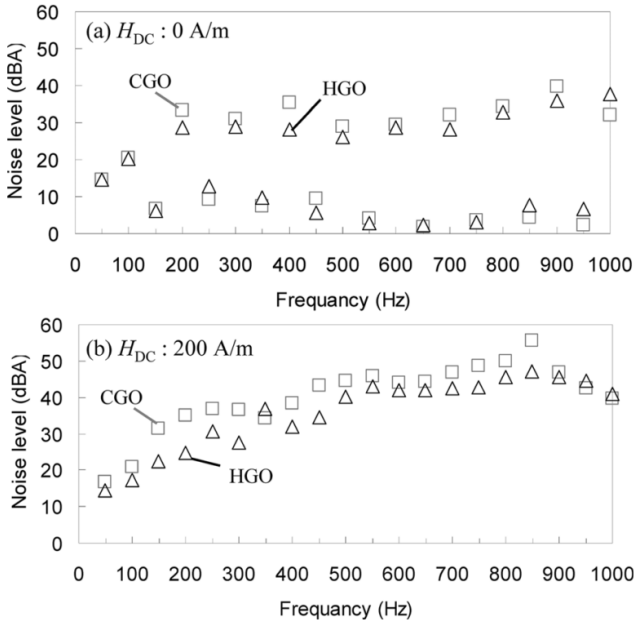

Fig 3-14 Comparison of noise spectrum between HGO and CGO (a) H_{DC}=0 A/m and (b) H_{DC}=200 A/m [60]

In general, DC bias drives the transformer core into saturation in alternative half cycles. In the saturation state, the core will draw too much current from the primary which will burn the primary winding or trip the protection circuit in the worst case. Even a small continuous dc bias will not only produce excess noise but also will heat the transformer and reduce its life time.

3.5 Effect of number of laminations per step

In [61] it is shown that increasing the number of laminations per step both in SSL and MSL configurations will lead to increasing noise. It is thought that increasing the number of layers in the assembly will lead to an increase in the non-uniformity of the flux in the vicinity of the joint and consequently increase the noise. Also it was shown that the higher number of laminations per step resulted in higher harmonic components over 400 Hz. This was related to the change in the flux distribution and hence the harmonics of magnetostriction in the core. Valkovic [62] presented the effect of transformer core design on noise level. Single step lap and multistep lap (4 steps) of some cores variants were assembled with one, two and three laminations per step. The results which are presented in Fig 3-15 showed that by changing the number of laminations per stacking layer from 1 to 3 small changes were observed in emitted noise in SSL configuration. However, two laminations per stacking layer showed approximately 2 dB lower

noise than the others in multistep lap configuration. In spite of this trend, the author commented that within the limits of experimental accuracy these differences were not significant and therefore the number of laminations does not affect the emitted noise.

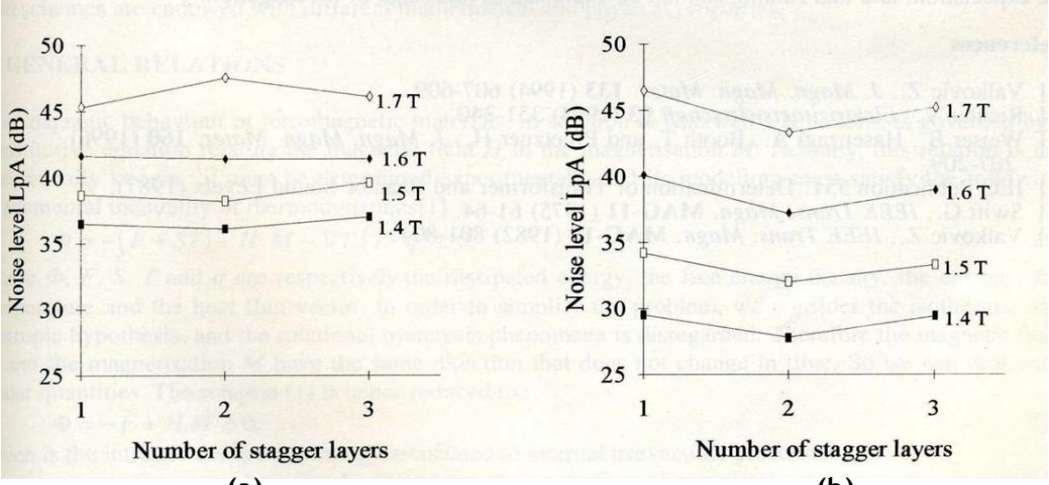

Fig 3-15 Variation of the noise level with number of the stagger layer for (a) single step lap (b) multistep lap (4 steps) model [62]

Snell [32] also investigated the effect of number of laminations per stacking layer. Cores were assembled from M0H and M3 0.27 thick laminations with one and two laminations per step configuration (4 cores). For the range of 1.5 T to 1.8 T the emitted noise of the configuration which had two layers per step was also reported higher. In [63] it was confirmed that the building factor of the core will also increase at least 2% if the core is assembled with two laminations per step rather than one lamination per step in any joint configuration (SSL or MSL).

In [64] the flux distribution in a linear 5 step lap joint with 9mm overlap length and 3 mm gap length were studied. The interlaminar normal to the plane flux distribution between two steps are illustrated in Fig 3-16 while the assembly was stacked with one and two layers per step in each test. As it is seen, the maximum normal to the plane flux density in the assembly with two layers per step was more than 200 mT while for the single layer per step was less than that. The Maxwell force between the laminations was proportional to the B^2 which means than the laminations in the assembly with 2 layers per step vibrated more and hence produced more noise.

Almost all researchers have confirmed that building the transformer cores with fewer layers per steps improves their magnetic characteristics but increases

building complexity. It is reported that the power loss of a four layers per step assembly is 4% higher than two layers per step. There is a 2% to 3% power loss reduction when the assembly has one layer per step instead of two [34]. According to the above mentioned experimental results it is confirmed that less noise emitted when the steps are composed of less layers but the results presented in [62] seem contradictory which shows that the 2 layer per step configuration is better than single layer per step. This might be explained by considering that the magnetic characteristics of a core are dependent on several parameters including the core size, joint configuration and parameters and the building quality. Also the accuracy of the measurements is important which the author of [62] has mentioned.

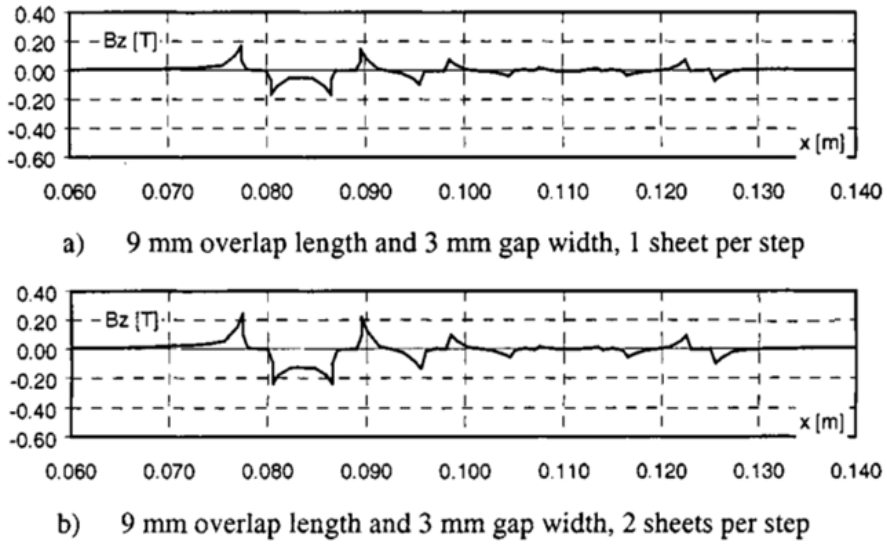

Fig 3-16 Flux change between steps with different overlap lengths and different numbers of laminations per step in a step-lap joint along line 8 of Fig. 8: (a) 9 mm overlap length and 3 mm gap width, 1 sheet per step, (b) 9 mm overlap length and 3 mm gap width, 2 sheets per step [64]

3.6 Effect of joint configuration

The power loss and the emitted noise of transformer cores changes with the joint type. Nowadays, there are two major and popular configurations for joints; single step lap (SSL) and multistep lap (MSL) 45^{o} mitred joint.

In [65] it is argued that the MSL shows better performance in terms of emitted noise in compare to SSL. The author proposed that by increasing the number of steps in each book, the magnetic characteristics of the core will improve and the

core would be less sensitive to imperfections caused by manufacturing or by design.

Ilo discussed the behaviour of the multi-step lap transformer core in [66]. He investigated the flux distribution as a function of joint design and tried to find the relevance of flux distribution to the noise and power loss. The results for a three phase transformer core showed that the MSL core shows lower values for core loss and the exciting current compared to the SSL one. The difference in power loss and excitation current were reported as large as 8% at 1.50 T and 50% at 1.7 T respectively. The researcher defined the term critical induction to mark the operating magnetic flux density which causes the bridging laminations above and below the airgaps to reach saturation as:

$$B_c = \frac{N_s}{N_s+1} B_s \qquad (3\text{-}1)$$

Where the N_s is the number of steps per book and B_s is the saturation induction. The author demonstrated that the advantage of MSL is driven by the critical induction. As the number of the laps increases, the critical induction level increases as shown in Fig 3-17. In induction levels beyond the critical induction the MSL configuration has no benefit.

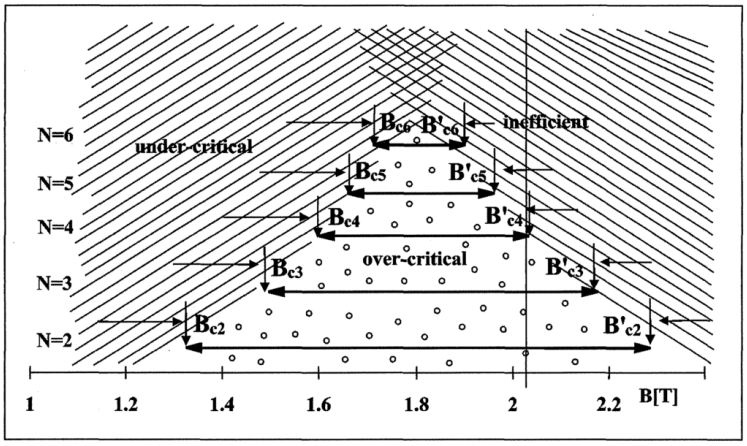

Fig 3-17 Induction window (B_c'-B_c) depending on overlap steps N_s [66]

Valkovic [67] studied the effect of overlap length on transformer core emitted noise. A single phase SSL model core was assembled from GO electrical steel of grade M4. The overlap length was changed from 2.8 to 19.8 mm and the core was magnetised at different induction levels. The author reported that the emitted noise level increased as the overlap length increased in the core. The measured noise levels were more sensible to variation in overlap length at lower (1.4 T)

than at higher (1.6 and 1.75) core inductions. The total increases in noise levels were about 7 and 3-3.5 dB for inductions 1.4 and 1.6/1.75 T, respectively. The author did not provide any reason for this but this clearly shows that besides the joint configuration, the flux density distribution in the core and the grade of the steel play a key role in transformer core performance. In chapter 7.4 the effect of changing the overlap length on flux distribution will be discussed in detail.

Ilo studied the influence of geometric parameters of the core joint like overlap and airgap length on the magnetic properties of model transformer cores [68] . A stack of 20 Epstein size 0.23 mm thick laminations of grade ZDKH-LS were used to build SSL and MSL (for N_s=2) joint configurations in a linear fashion. This assembly was magnetized with two sets of coils at either side of the linear joint. It was reported that the step numbers and the airgap length had the strongest effect on noise and power loss but it is not quantified in the paper. Also it is shown that by doubling the overlap length, the emitted noise level reduced by 50%. It is argued that by increasing the overlap length the interlaminar flux density and hence the interlaminar magnetostatic force reduced.

The influence of step lap design on transformer core noise has been studied in [2] using three phase transformer cores with SSL and MSL (5 step per book) configurations which were built from conventional grain oriented electrical steel. The variation of sound power level (SPL) versus flux density at a clamping torque of 4 N.m was shown as Fig 3-18 and was argued that the MSL configuration emits less noise than SSL. As it is clearly seen, the SPL of the SSL configuration shows a defect in the core which will be discussed in subsection 3.8 (page 44).

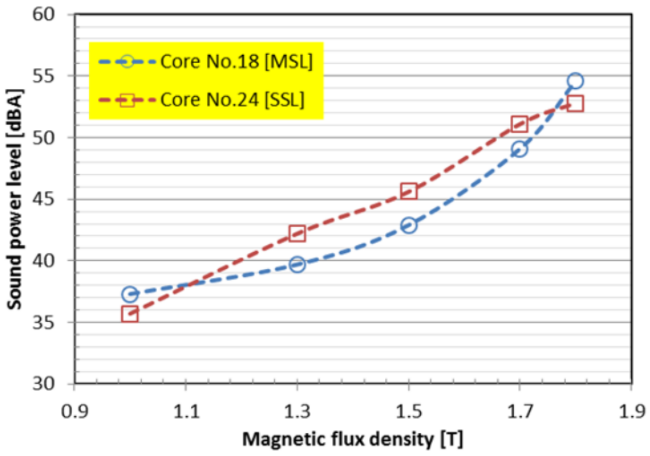

Fig 3-18 comparision of sound power level between multistep lap and single step lap transformer core with clamping torque 4 N.m at 1.0 T to 1.8 T, 50 Hz [2]

The results about the relevance of emitted noise and the overlap length from [67] and [68] appear contradictory. The test which was conducted in [68] was done in a linear joint whereas, in a real core, increasing the overlap length increases the triangular area of the joint and consequently the flux disturbance in the joint will probably generate more noise. The results presented in [68] confirm the findings of [65] and [66] about the superiority of MSL over SSL which convey that the flux in MSL distributes more uniform than SSL by deloading the airgaps by bridges in a more efficient way which cause distinctly lower stray fields in the overlap region. Also they are not as sensitive to the airgaps as SSL cores and show lower global z-flux component.

3.7 Effect of clamping pressure

Transformer cores are generally clamped in the process of manufacturing to prevent the laminations from moving during handling and to produce a stable final structure. The clamping affects both the power loss and the emitted noise of transformer cores [63, 69-74]. It is generally accepted that the application of the clamping pressure can initially reduce the power loss of the core, but too much pressure can increase it [32]. The same is true for the emitted noise.

In [33] three phase model transformer cores were assembled from RGH and new RGH grain oriented electrical steel (B_8=1.9 T and 1.93 T respectively). In cores with RGH material, It was reported that the noise level in SSL configuration decreases with increasing clamping pressure before reaching a minimum; independent of the flux density, at a stress of about 0.05 MPa and then increases with further increases. In the MSL core the minimum value of noise level was reported at the presence of 0.1 MPa at 1.50 T and 0.025 MPa at 1.80 T which shows that by increasing the flux density in the core the required clamping pressure to yield the minimum emitted noise decreases. Investigation on clamped and unclamped states for different materials and joint types showed that when a clamping force was not applied to the core the difference between materials and between core stacking methods tended to increase as the induction level increased, but in the presence of 0.2 MPa clamping pressure, the difference between the materials showed little change, while the difference between the stacking methods tended to decrease as the induction level increased [33] (see Fig 3-19). This means that in the clamped condition and at higher inductions, material grade plays a more important role rather than joint configuration. In the

above mentioned report, it is shown that under the clamped condition the emitted noise of the SSL core built of high permeability material is lower than the MSL core which is built of a material with lower permeability. This superiority was only at 1.80 T and above in the clamped condition. It is reported that the rate of increase of the noise level is more moderate with MSL joints than with SSL. The change in emitted noise with clamping pressure is considered to be a transition process in which the dominant source of noise shifts from electromagnetic vibration to magnetostrictive vibration as the applied pressure increases. This might be the reason of different required clamping pressure to have minimum emitted noise in different inductions.

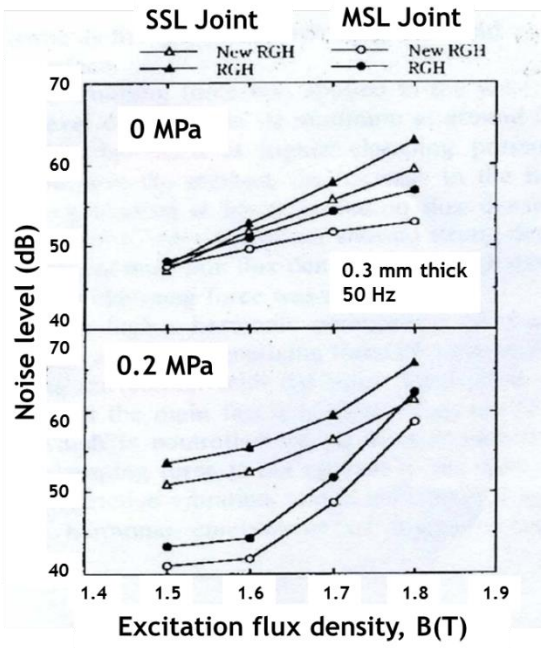

Fig 3-19 Dependence of noise level on excitation flux density with and without clamping pressure applied [33]

In [74] a single phase model transformer core with butt and lap joint configuration was assembled with sheets of GO Powercore H 0.3 mm thick laminations to quantify the impact of the clamping pressure on the losses. The author changed the clamping pressure from 0 Pa to 1 KPa and it was confirmed that the core loss and the corner joint displacement at the middle of the joint reduce continuously by increasing the clamping pressure. At the interior of the corner, the minimum displacement happens when the clamping pressure is 0.8 KPa. By means of FEM modelling and studying the flux distribution with different interlaminar airgaps, the author argued that a lack of clamping or a non-uniform one has a direct adverse influence on the core loss.

In [2] the influence of clamping torque on a three phase transformer core built from conventional grain oriented material with MSL configuration under magnetic flux densities from 1.0 T to 1.7 T with a clamping torque from 2 N.m to 6 N.m has been studied. The equivalent average stress of these torques were calculated 0.16 to 0.49 MPa respectively. It is reported that at 1.0 T, the A-weighted sound pressure level was not significantly affected by clamping torque which conveys that at 1.0 T and lower the interlaminar forces are not significant. At 1.5 T the highest sound pressure level is found at a clamping torque of 6 Nm whereas at 1.7 T, the lowest noise occurs at 4 Nm. It is reported that the random variation of sound pressure on the effect of clamping torque is due to the core surface not being clamped especially at the inner and outer corners. Some studies on the relevance of vibration and clamping torque was also conducted in this research and it was concluded that an optimal pressure is needed to minimise the core vibration at each induction level.

The amount of clamping pressure is still a controversial topic which is hard to determine for different cores. It is clear that the grade of the material and the core geometry have a direct effect on the optimum clamping pressure.

3.8 Effect of core and laminations quality

The core stacking quality and the lamination flatness and thickness are known to be one of the influential factors of noise generation in transformer cores. Limited studies have been conducted in this field. Mizokami [75] showed that if an irregular overlap as shown in Fig 3-20 happens by accident during core stacking the emitted noise will increase. It is reported that the emitted noise pattern will be shifted up, and above 1.0 T there would be an abnormal bulge at certain induction levels (See Fig 3-21 b)

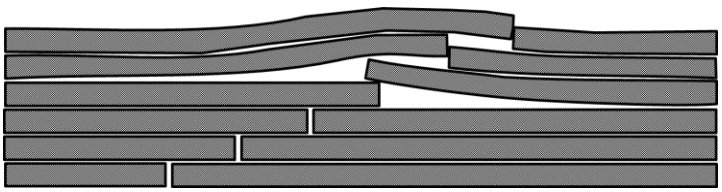

Fig 3-20 Cross section of an abnormal core joint

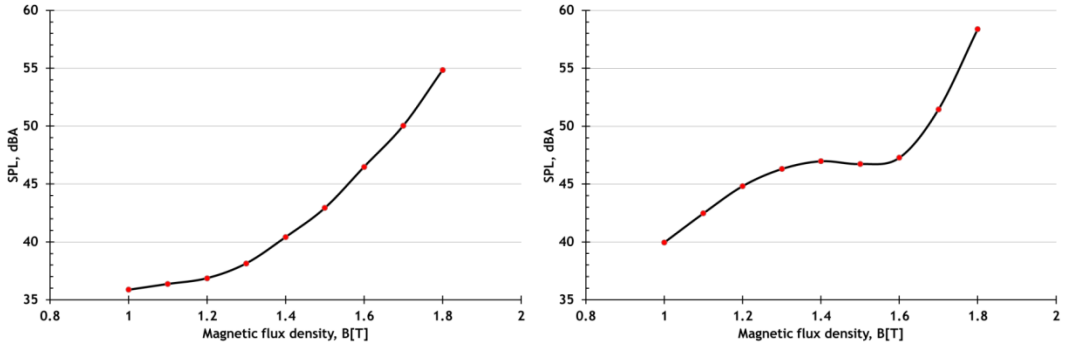

Fig 3-21 Sample emitted noise of model transformer cores (a) In normal condition (b) In abnormal joint condition as shown in Fig 3-20

In theory because of symmetry it is expected that all the electromagnetic forces in the core should cancel each other out. In [76] the relevance of magnetostatic forces for transformer core vibrations has been investigated and it was argued that the deficiencies of the electrical steel laminations introduced unwanted asymmetrical interlaminar airgaps as shown in Fig 3-22 which consequently introduce asymmetrical magnetostatic forces hence vibration and noise.

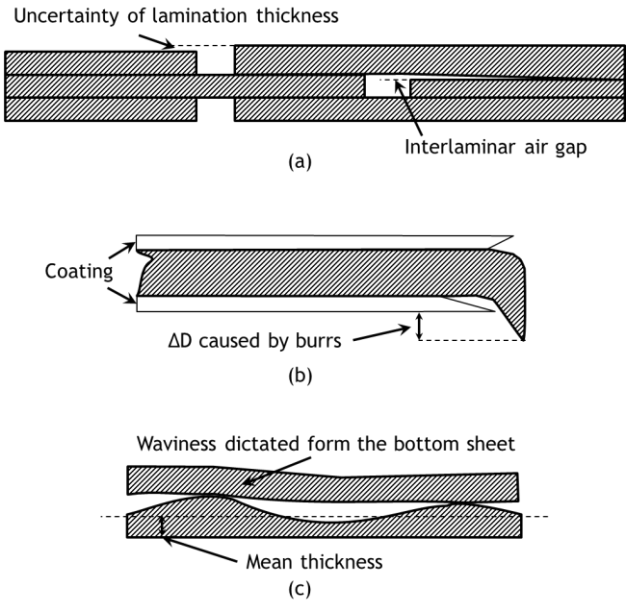

Fig 3-22 Schematic diagram of possible reasons of introducing interlaminar airgaps caused by statistical scatter of laminations thickness, burrs or waviness

In [2] the influence of core building on transformer core noise was studied using six pairs of three phase identical cores built with different materials and step lap configuration with clamping torque 4 Nm at magnetic flux density from 1.5 T to

1.8 T. The results are presented in Fig 3-23. The variation of A-weighted sound power level between each build is up to 2dB, 4 dB and 6 dB at 1.5 T, 1.7 T and 1.8 T since it is already known that this variation between each material should not exceed 2 dB for all levels of flux density. So it was concluded that this excess noise was due to the quality of the core assembly.

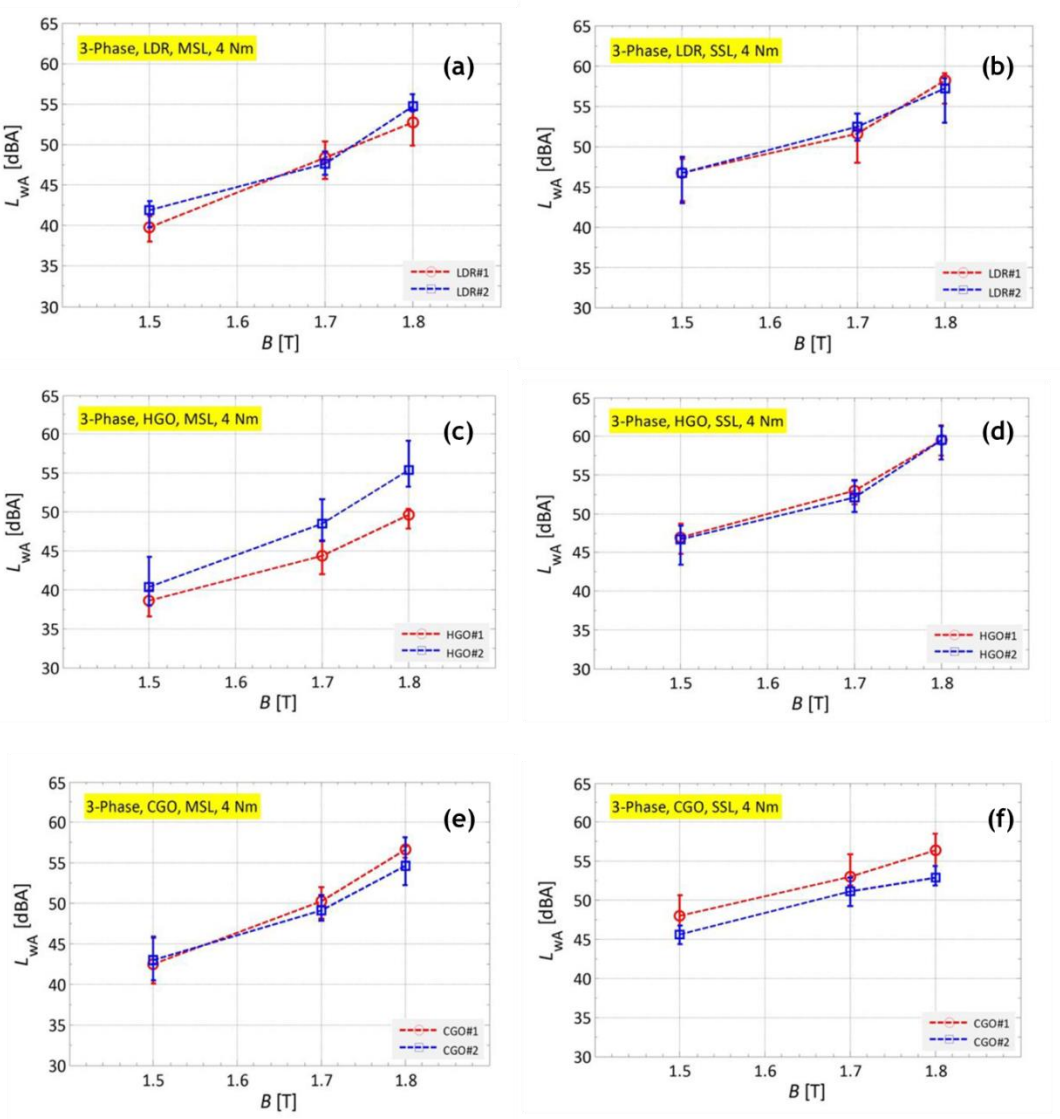

Fig 3-23 Comparison of A-weighted sound power level of two three phase (a) MSL DLR (b) SSL LDR (c) MSL HGO (d) SSL HGO (e) MSL CGO (f) SSL CGO transformer cores with clamping torque 4 Nm at 1.5 T to 1.8 T, 50 Hz [2]

3.9 Effect of packet shift

The ratio of area to the circumference of the circle is the biggest among all other shapes, which is why to have bigger cross sectional area with less amount of material the ideal shape of transformer core is circular. Because of the economic

and technical considerations the manufacturers build the core as shown in Fig 3-24 which; in this example, consists of eight groups of laminations called packets. A real transformer core consisting of 10 packets is shown in Fig 3-25 and the terminology of package shift is illustrated in the figure. The package shift will lead to a large amount of interlaminar flux through two packages as shown in Fig 3-26. This interlaminar flux will produce some interlaminar forces which will produce excess noise.

In [68], as discussed previously, a linear joint was set up to study the transformer core joints. It is reported that the shift of a group of laminations in the linear joint has significant effect on power loss, noise and excitation current as shown in Fig 3-27. As shown, the power loss has an increasing trend as the package shift increases. The excitation current also has a uniform trend with an Increasing package shift which leads to less excitation current. The presented emitted noise has some irregularities which make it difficult to find a consistent trend but the overall impression is that, by increasing the package shift the emitted noise from the joint increased.

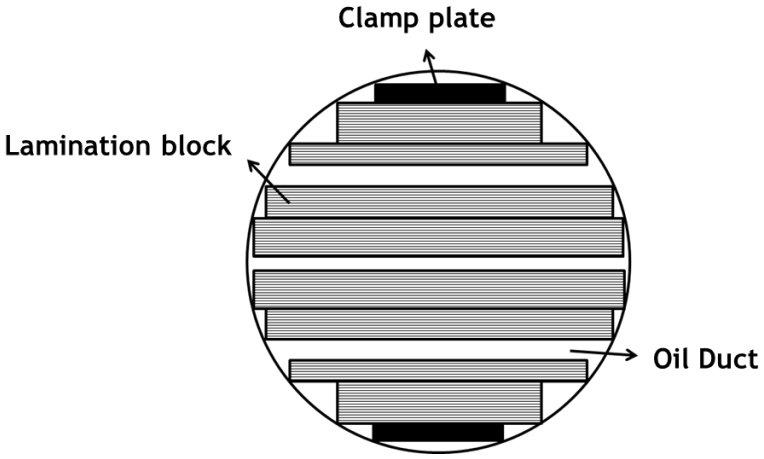

Fig 3-24 Typical transformer core cross section which consist of several eight packets

Fig 3-25 Five packet three phase transformer core corner joints (a) the airgap and the overlap region at two packages are pointed. (b) The perpendicular view of the same joint in which the shift of the joints in two peripheral packages is highlighted

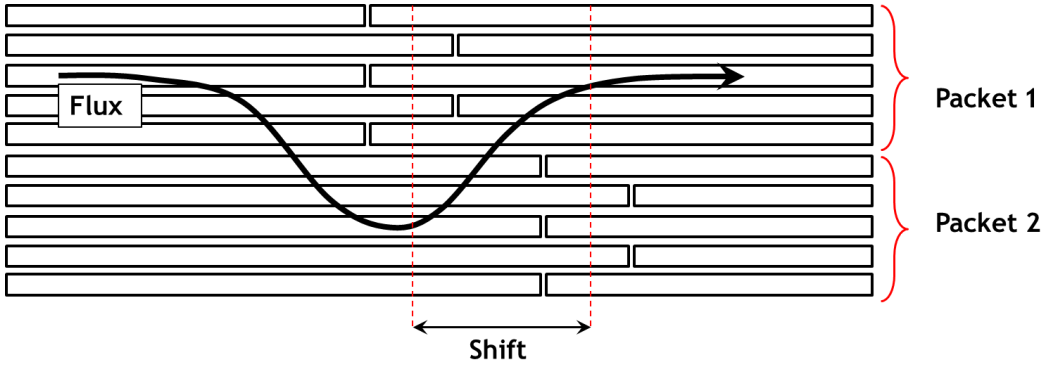

Fig 3-26 2D schematic diagram of two core packets with shifted joint region exhibiting a bulk interlaminar flux transfer

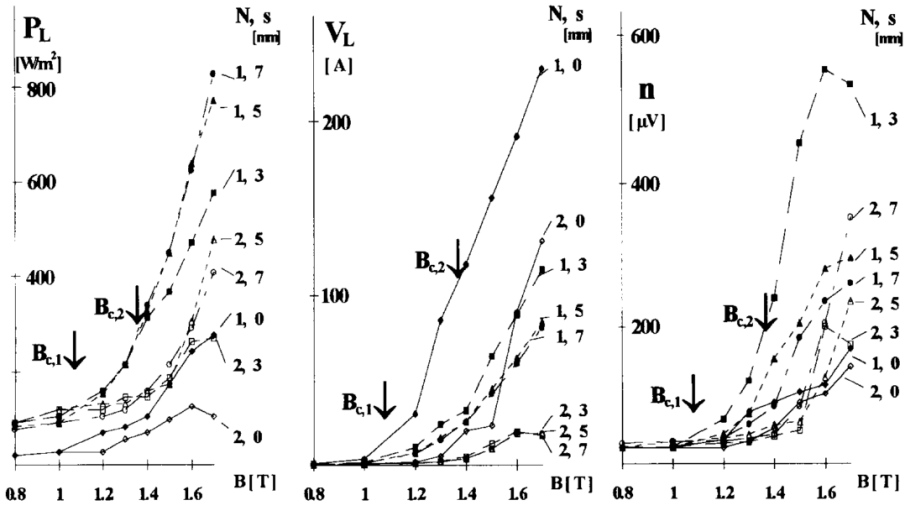

(a) (b) (c)

Fig 3-27 Typical experimental results for various package shifts s as a function of induction B when the airgap length is 1 mm and the overlap length is 10 mm. (a) Power loss P_L, (b) excitation current V_L, (c) noise n [68]

3.10 Effect of Adhesive and epoxy resins

Epoxy adhesive with high bonding and dielectric strength are usually used for bonding rigid structures like transformer cores where flexibility is not required [77]. In [78] Moses conducted an investigation on flexible bonding of laminations in a 20 kVA single phase single step lap transformer core and showed that the noise at an operating flux density of 1.5 T would reduce by 3 dB after bonding.

The effect of bonding on the emitted noise of a single phase core assembled form CGO material in MSL configuration is reported in [2]. The resin was only applied to the outer surface of the fully built core and it was observed that the emitted noise reduced by 4 to 10 dB as shown in Fig 3-28. At 1.50 T, when the core works below the critical induction [79], the bonding is more effective than at 1.70 T where the core working point is in a critical region. This is because operating the core below critical induction has higher interlaminar stress in the normal direction than above critical induction therefore the reduction in the noise at 1.5 T is higher than at 1.7 T.

Mainly, bonding the laminations reduces the emitted noise. The amount of this reduction depends on the flux distribution. No report has been found about the effect of applying the resin on the surface of each layer.

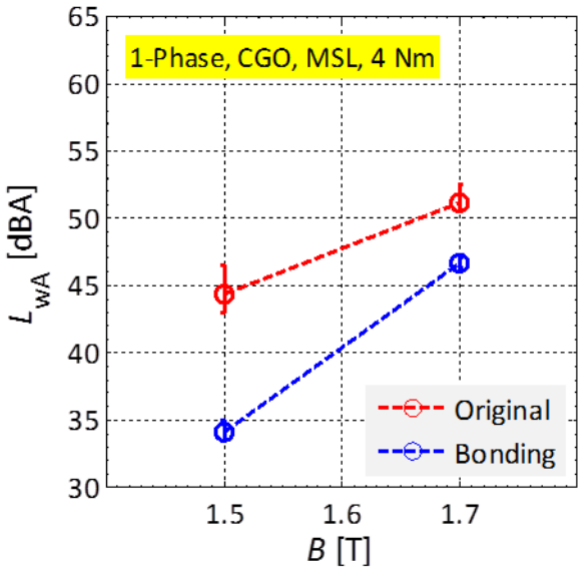

Fig 3-28 Comparison of A-weighted sound power level of core with and without bonding at clamping torque 4 Nm, 50 Hz [2]

3.11 Non-core-dependant sources of noise and power loss

In addition to the transformer core, the windings and the cooling equipment of the transformers are sources of noise. The interaction between the leakage flux and the load current causes the windings to vibrate. The main frequency of the produced sound is twice the current frequency. If the current has some harmonics, the emitted noise would contain higher frequencies. It is reported that the reducing the current by 50 percent provides a reduction of the load current noise by 12 dB [80].

3.12 The Mutual effects

The topics which were covered in this chapter were a general review of the parameters which affect the magnetic, mechanical and acoustic performance of transformer cores. There are many other metallurgical parameters relating to steel properties which ultimately can affect the core performance. Beyond this, some parameters can be affected by the dynamic behaviour of the core, e.g. elasticity as shown in Fig 3-12. Discussing the metallurgical parameters and the mutual effects are beyond the scope of this study. As shown in Fig 3-29, all these parameters impact the flux distribution in the core which ultimately causes the

core to vibrate and make noise. This flowchart clearly shows that studying the flux distribution in the core is the key point to make the mechanism of producing unwanted noise and vibration of the core more intelligible.

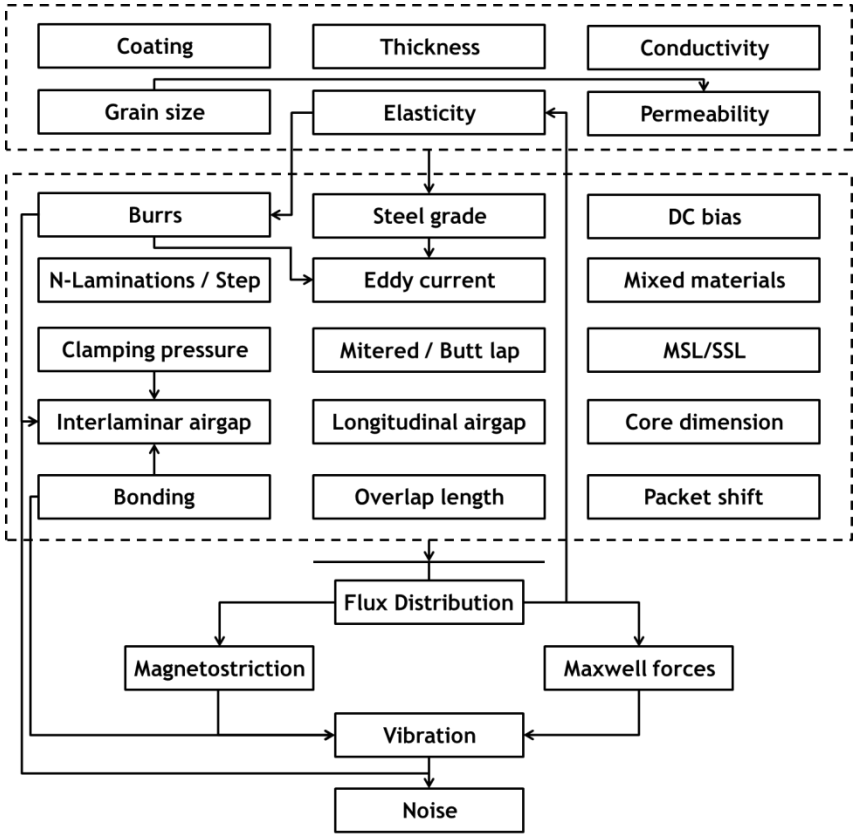

Fig 3-29 Parameters affecting the performance of a core and the interactive effects

3.13 Literature review of flux distribution in transformer cores

In this section some of the previous works on flux distribution will be discussed.

3.13.1 Flux distribution in transformer core corner joints

In 1962 Brailsford [81] studied the alternating magnetic flux density distribution in the right-angled corner of transformer laminations. Two types of materials were used in this research: hot rolled 4% silicon iron transformer sheet, 0.35 mm thick, with maximum core loss of 1.63 W/kg at 1.30 T 50 Hz and cold roll grain oriented 3% silicon-iron transformer sheet, with maximum core loss of 1.12 W/kg at 1.5 T 50 Hz. The materials were cut in L shaped 25 cm × 7 cm strips and assembled with butt-lapped corner joints in a core with the height of 13 mm (See Fig 3-30).

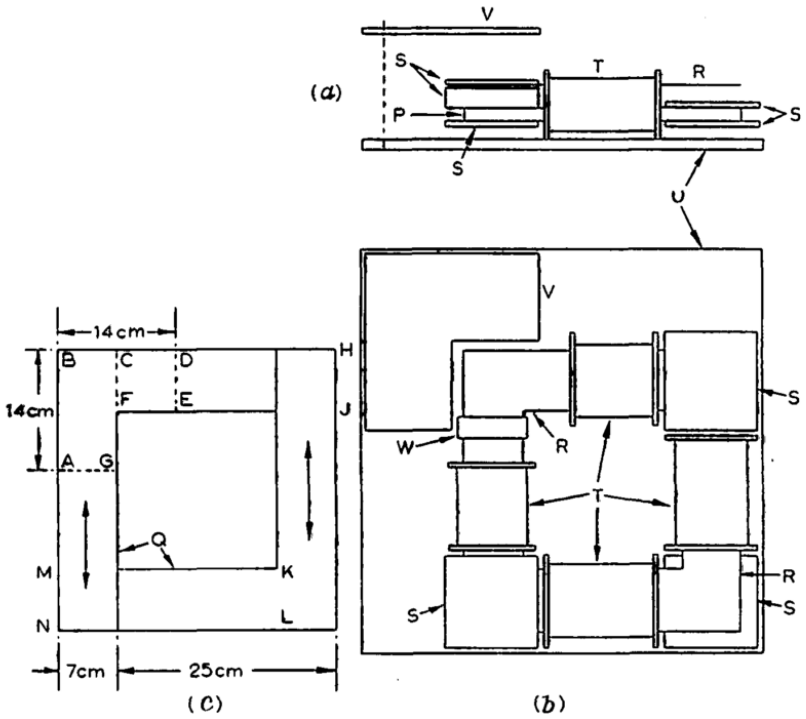

Fig 3-30 General arrangement of experimental core and specimens. (a) Side elevation (b) plan view (c) Plan view of specimens [81]

In order to observe the flux distribution in the specimen, a complete lattice of search coils was used as shown in Fig 3-31. The stack of material A and material B then were magnetised up to 1.3 T and 1.7 T respectively and the flux density distribution measured and recorded in each search coil. The reported estimated accuracy of the measurements was ±5% in the amplitude of the fundamental and ±10% for the third harmonic.

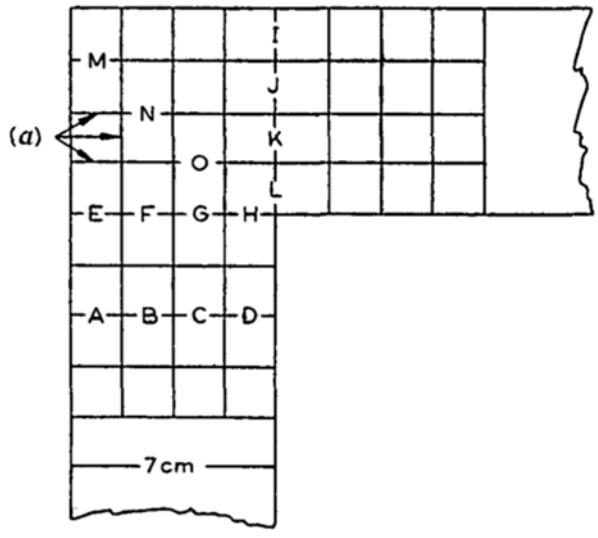

Fig 3-31 Each side of the square presents a search coil and all the intersections are the drilled holes [81]

The results for both materials shown in Fig 3-32, presented very high third harmonics for the grain oriented electrical steel in comparison to the non-oriented material. The researchers reported that the flux waveform was double humped in each half cycle which they believed was due to subsidiary hysteresis loops in each cycle of magnetisation for the material in each position. It is claimed that by comparing the flux density of neighbouring search coils some flux leakage amounting to 15% between the search coils occurred in grain oriented electrical steel. Using harmonic analysis, the authors showed that the third and fifth harmonic fluxes circulated in the corner region.

In this research, the flux was studied in a one piece lamination without any airgaps so the measured flux distribution cannot be compared directly to current jointed laminations which others have reported.

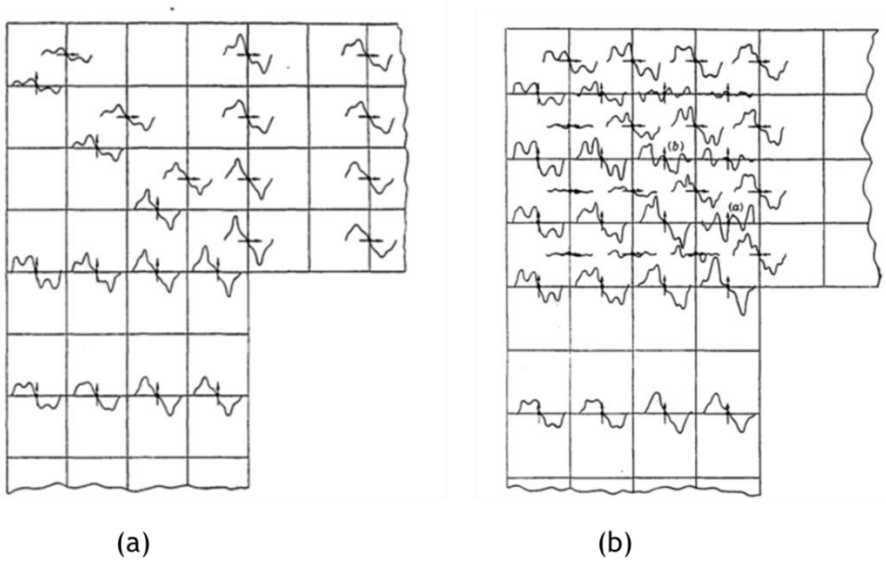

Fig 3-32 E.M.F waveforms for (a) Material A at 1.30 T (b) Material B at 1.70 T [81]

In 1973 Jones [19] investigated the flux distribution and power loss in the mitred overlap joint in a power transformer core. Two cores with mitred joints were built such that the length of overlap could be varied. The length of the limb in one core was one meter and the other was smaller. The material grade was not mentioned in the paper. In the study, the longitudinal, transverse and normal flux densities were measured separately in cores with mitred joints. The results for longitudinal flux density measurements are shown in Fig 3-33. As reported, in the regions where the electrical steel bridges the longitudinal airgap the flux density reached almost 2.0 T. The longitudinal airgap flux densities were reported to be around 200, 500 and 900 mT for 1.0, 1.5 and 1.8 T respectively. The normal flux density

at the jointed region was reported to be less than 60 mT as shown in Fig 3-34. The authors reported that by decreasing the overlap length from 2.0 to 0.0 cm, the peak value of the normal flux density increased from 30 mT to more than 70 mT. Furthermore, it was claimed that the peak flux density in the overlap region would increase if the overlap length increased, which seems contradictory to the previous statement. In an assembled core changing the overlap length without changing the longitudinal gap length is impossible. These contradictory statements might be the result of changing the gap length which would entirely change the magnetic circuit. Two optimum overlap length equal to 0.5 and 1.0 cm were introduced to have minimum loss for the big and small cores respectively.

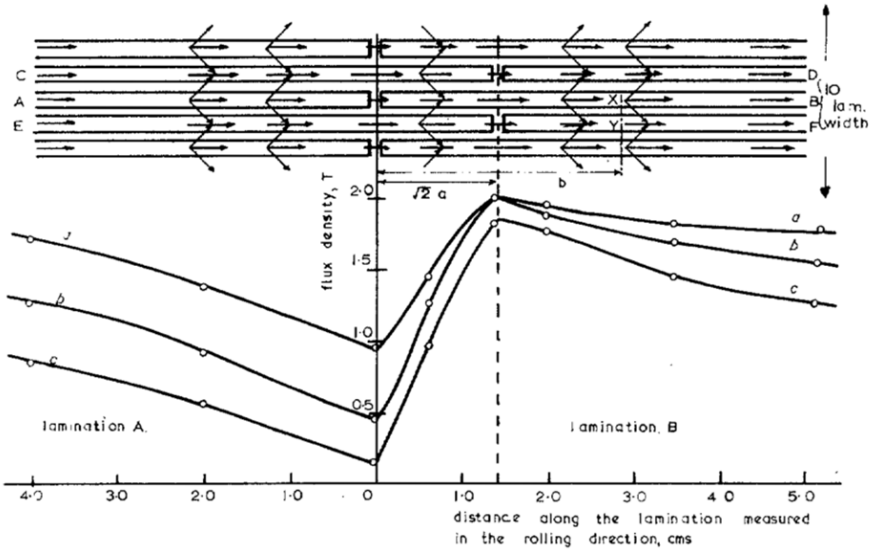

Fig 3-33 Longitudinal flux density in two adjacent laminations in 45° mitred overlap corner measured at core flux densities of (a) 1.8, (b) 1.5, and (c)1.0 T, for a 1.0 cm overlap (Each limb of the core considered of a 10-lamintation stack) [19]

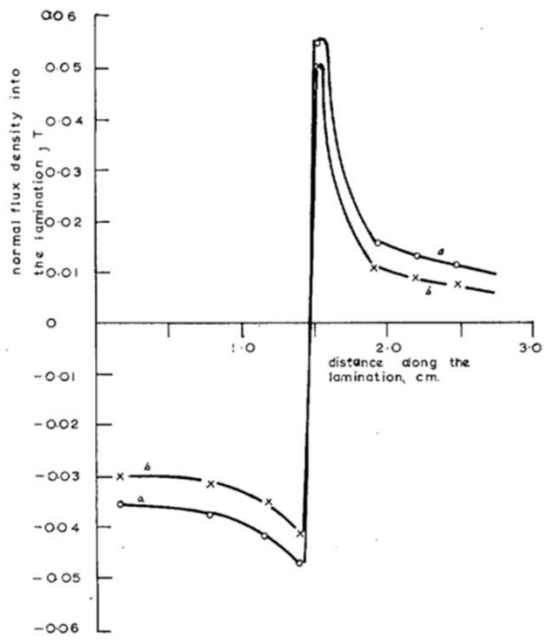

Fig 3-34 Normal flux density distribution in a 1.0 cm mitred overlap corner joint in lamination B. Overall core flux densities (a) 1.8 and (b) 1.5 T

In 1974, Jones [82] also studied the flux density distribution in the butt lap and mitred overlap corner joints and their localised power loss. Stacks of 10 layers were assembled with 0.33 mm thick and 920 mm long laminations. The material grade was not mentioned again but the nominal loss was 0.95 W/kg. The author observed that the longitudinal flux density in the layer which bridges the longitudinal airgap reached approximately 2.30 T at the overall induction level of 1.8 T as shown in Fig 3-35. In the limbs, the normal flux density was reported as 0.5 mT but at the butt gap it increased to 10 mT. In the mitred joint, the maximum measured normal flux density in the overlap region was reported as 1 mT. Considering the power loss and the dimensions of the core, it seems that the same grade of steel which was used in [19] was used here. Comparing the reported values in [19] with those presented in [82] reveals some deficiencies in [82]. The amount of airgap flux at 1.8 T was reported as approximately 900 mT in both papers but in [82] gap bridge flux densities were reported as 2.3 T which is 15% higher than [19]. Higher flux density in the gap bridge is a result of more normal flux travel to the lamination from adjacent layers. Contrary to this fact the normal flux density at the edge of the lamination was reported as 10 mT which is 3 to 7 times smaller than that of [19].

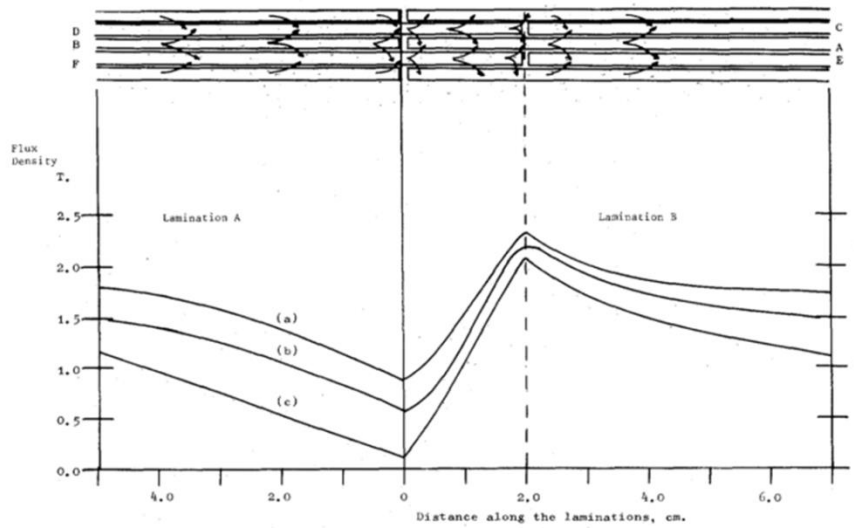

Fig 3-35 Longitudinal flux density distribution in two adjacent laminations in the 45° mitred joint measured at the core flux density of (a)1.8, (b)1.5, and (c) 1.1 T for a 1.0-cm overlap [82]

In 1982 Nakata [83] presented one of the early computer models to study the magnetic performance of step lap joints in transformer cores. He included the eddy current effect in his model. The author studied the effect of the number of laminations per book in the core and the airgap length on flux distribution and power loss in the core. He showed that by decreasing the number of laminations per book (SSL) in the core, the gap bridges saturated and some of the flux passed through the air gap. However, he asserted that when the number of layers per book was increased (MSL) in the core the percentage of the flux passing through the gap was decreased. The author showed that by increasing the airgap length the power loss of the core increased. Also it was proved that if the number of laminations per step lap is small the effect of gap length on magnetic characteristics is significant.

In 1995 [65] Löffler studied the relevance of step lap joints for the magnetic characteristics of transformer cores. He described that the benefit of multistep lap does not become clear until the assembled core incudes some imperfections like unequal airgap length g. The 'critical induction' at which the excitation of the overlap region significantly increases is strongly dependant on the number of step laps N_s. The sensitivity of the core to the unwanted imperfections (bad airgap distribution and size and the package shift effect) reduces as the number of step laps increases in its configuration which will lead to less variability between the cores of same type. In this research the effect of core joint configuration on global parameters like power loss and the apparent power of the core were discussed and the superiority of the MSL over SSL was proved.

In 1998 [76] Weiser conducted research on the relevance of magnetostriction and forces for the generation of audible noise of transformer cores. To study the contribution of forces, the flux distribution was investigated in the jointed region. The authors developed two numerical models of SSL and MSL configurations using an equivalent electric network as shown in Fig 3-36. The author reported that the flux distribution in the joints depends strongly on critical induction B_c which is characterised by saturation of gap bridges. He explained that for low induction levels the flux avoids the longitudinal airgap and takes the interlaminar air gap to close its path. At high Inductions, where $B>B_c$, the excess flux is distributed over both the gap bridges and the longitudinal airgap. The modelling results for the SSL configuration at 1.8 T showed that the flux density in the gap bridges increased up to 2.8 T while in the longitudinal airgap it was around 0.8 T. The corresponding normal to the plane induction level was reported to be 0.5 T. Although this model generally presented how the flux distributes in transformer joint it had some limitations. The first and the most important one is the lack of the modelling of the surrounding air which ignores the fringing flux. This caused the flux to be confined to the electrical steel and the flux density in the gap bridges reached 2.8 T which according to the experiments seems unattainable. The second unclear point in this model is the normal flux transfer area which had a very big influence on the normal and longitudinal airgap flux density.

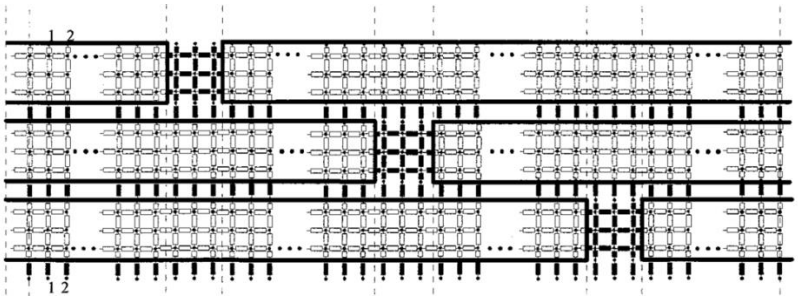

Fig 3-36 Example of an electric equivalent network (for N=2) as established for numerical modelling by means of SPICE [76]

In 2000 Mechler [64] investigated the flux distribution in transformer core joints through analytical studies. The author developed a single step lap (SSL) model with two layers per step and a multistep lap (MSL) model with 5 steps and one layer per step. All the studies were conducted with a 2D model. The influence of material grade and the joint parameters on flux distribution were studied. It is reported that in an SSL joint with a gap width of 3 mm at the overall flux density of 1.7 T, the flux density in the gap bridge region reaches 2.70 T. Also he showed that the normal to the plane interlaminar flux density at the vicinity of the joint

and the longitudinal airgap flux density reached 0.8 T and 0.7 T respectively. The results for a MSL joint showed that at 1.7 T, very little flux passed through the gap (0.04 T). The normal flux density was reported to be 0.25 T which was at least 3 times smaller than the SSL core. It was reported that the flux density in the gap bridging laminations reached 2.035 T which shows a better flux distribution in the MSL joint. In addition to 0.23 mm thick highly oriented electrical steel the authors tested 0.3 mm thick regular grain oriented electrical steel. The author claimed that using the conventional grain oriented electrical steel in SSL configuration caused the flux density to reach 2.9 T in the gap bridge region. He explained that the longitudinal gap length and the overlap length did not have a major influence on the gap flux density in the MSL configuration. Like [76] the fringing flux (the flux in the magnetic core which spreads out into the surrounding medium) was ignored in this study. Furthermore, It was not clear what interlaminar airgap was considered in the models.

In 2015 Penin [74] investigated the impact of mechanical deformation of transformer corners on core loss. A computer model was built with 0.30 mm thick laminations with 0.1 mm of airgap length. The material grade and the overlap length are not mentioned in the paper. The model was magnetised at 1.60 T and the gap bridge and the airgap flux density in the core was reported as 2.55 and 0.40 T respectively which means that the fringing flux effect was considered in this model. The interlaminar airgap was assumed to be 5 μm in this model which in practice is double this amount. Despite the lack of information on the model parameters and considering the computer aided approach limitations, the results presented in this research work are thought to be the closest reported values to the reality.

In 2015 Tang [84] investigated the magnetic flux distribution in power transformer core with mitred joints in 2D and 3D finite element SSL and MSL models. The models were built with 0.3 mm thick laminations. The airgap length of 2 mm and an interlaminar airgap of 10 μm were selected. The overlap of the multi-step lap configuration was 9 mm while for the single step lap model it was considered as 42 mm. The anisotropic B-H characteristic of grain oriented electrical steel grade M6, from the COMSOL materials library, was used to model the core as shown in Fig 3-37. The B-H curve which was provided for the transverse direction was used to model the material characteristic in the normal direction. The provided B-H characteristics were extended to less than 2.0 T and no comments were made on

higher induction values. The magnetising mechanism was clarified in the paper but it is thought that the flux in the model was established using the boundary conditions and the surrounding air was not included in the model.

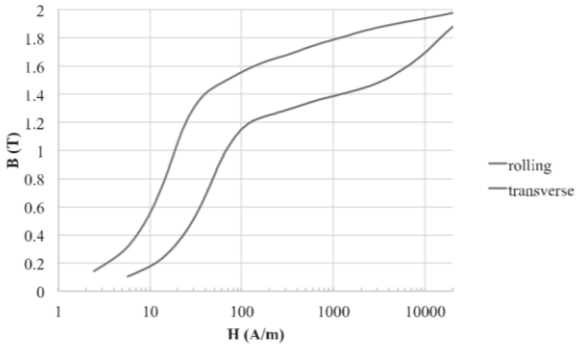

Fig 3-37 Anisotropic B-H characteristic of silicon steel GO M6 from COMSOL material library

In the SSL model the authors showed that the longitudinal flux density in the gap bridges reached 2.75 T and, the normal flux density at the edges of the lamination reached 1.25 T. This amount of flux density is very close to that which was reported in [64] for 1.7 T and was about 30% more than that was measured in experiments in [19]. So it seems that the presented model overestimated the amount of flux density in the gap bridges. The longitudinal airgap flux density in SSL configuration was reported as 250 mT. The normal to the plane flux in this configuration was calculated as 1.25 T which seems at least 30 % more than the highest reported value in [64]. For the MSL model, 2.20 T is reported for the longitudinal flux density in the gap bridges, which was again higher than previously reported values (e.g. 2.0 T [64]). The results of a sweep of inductions from 1.5 T to 1.9 T was presented in the paper which illustrated that the flux in the gap bridges in SSL configuration reached approximately 3.5 T when the overall flux density was 1.9 T. This level of flux density was not reported in any other literature. It is claimed that a good agreement between the 2D and 3D model results and the experiments were found but no comparison presented in the paper. Like [76] and [64] the fringing flux is not considered in the models, so the results are significantly different form the measured values presented in [19]. A possible reason for these overestimated results is the wrong definition of the B-H characteristics in saturation region. The B-H slope in saturation region (B>2.04 T) should be equal to μ_0 while it was linearly extrapolated by the characteristic below the saturation level.

3.13.2 Magnetostriction and magneto static Forces in transformer cores

Weiser [85], in 2000, investigated the relevance of magnetostriction and forces for the generation of audible noise of transformer cores. The author categorised the forces which act in the core in four groups. The first type is the in-plane forces due to the flux transfer in the longitudinal airgaps. These magnetostatic forces cause an attraction between the limbs and yokes when the core flux exceeds the critical induction level and yields a stress proportional to B^2 acting at the sheet ends. This type of force, which is because of B_{gap}, is illustrated in Fig 3-38-(a). The authors argued that this type of force is reduced as the number of step-laps increases in a core. It is calculated that for single step lap configuration with an airgap length of 2 mm the amount of tensile strain would not exceed 100 nm which is equal to the magnetostrictive strain of a 0.3 meter long sheet region [85]. This force reduces as the number of step laps increases, which means that the effect of the in-plane magnetostatic force in multi-step lap configurations is almost negligible.

The second type of force is the off-plane magnetostatic force which acts in the interlaminar airgap regions. Considering 0.6 T normal to the plane flux and a 0.3 mm transfer length in the SSL configuration, the exerted pressure would be 100 kPa. The author assumed the elasticity modulus of the stack of laminations in the Z direction was equal to 10^4 MPa which yields a local strain of 10 μm/m. As the strain increases the flux density goes beyond the critical induction level of the core, the authors concluded that the strain caused by this force exceeds the nominal magnetostriction caused strain in the rolling direction.

In-plane stress, which is caused by magnetostriction in the rolling direction, is introduced as the third type of stress which is exerted on the laminations. The authors claimed that the in-plane magnetostriction in the transformer core cannot be the source of excessive noise coming from the core in SSL. They argued that the length of the gap bridges in the core which go into saturation is far smaller than the core length, so the magnetostrictive strain of this area should be approximately 200 times bigger than other region in order to explain the large difference between the emitted noise of SSL and MSL, which is less likely.

Off-plane magnetostrictive stress is the fourth type of stress which appears in the core. It is claimed that the thickness of the lamination's edge at the vicinity of

the joint changes due to the interlaminar flux density. This mechanism is superimposed to that of the attractive forces, both yielding a tendency of decreased interlaminar airgap length [85]. This effect is smaller in the MSL configuration due to better flux distribution.

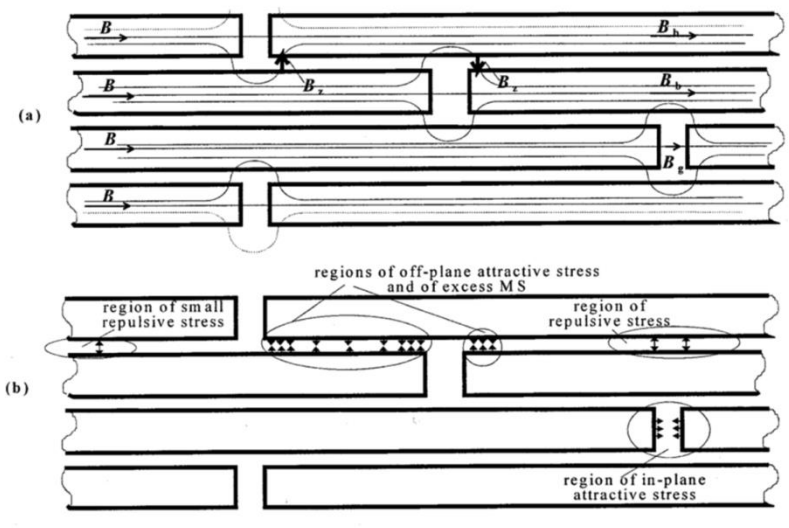

Fig 3-38 Schematic diagram of a multistep lap (N=2) joint configuration (a) Flux distribution (b) Consequences [85]

Shilyashki [86] studied the distribution of magnetostrictive strain in different regions of a three phase model transformer core, using strain-gauges, and reported that the strain in the jointed regions were at least 4 times bigger than the strain in the other part. In the V-type joint the measured strain was 25 percent higher. The author reported that the measured strain in the middle of the limbs agree with the magnetostriction catalogue data of the electrical steel. They professed that the higher measured strains are not explainable by the magnetostriction, so they claimed that this excess strain is due to the magnetostatic forces.

In [87] the magnetostriction force spectrum in a power transformer was studied using numerical approaches. A 2D linear SSL joint was assumed with an average flux density of 1.74 T near the overlapping area. The flux density in the overlap and airgap region was 2.61 T and 0.88 T respectively. This model did not take into account the fringing flux. The resulting force calculated from magnetostriction showed a maximum vertical attractive force of 2500 N in the side limb joints and 2000 N in the middle limb joint. The in-plane force has a repulsive and attractive nature with different peak values as shown in Fig 3-39. Also shown in Fig 3-39 is

the force in the side joints which are purely oscillating in opposition to the central joint.

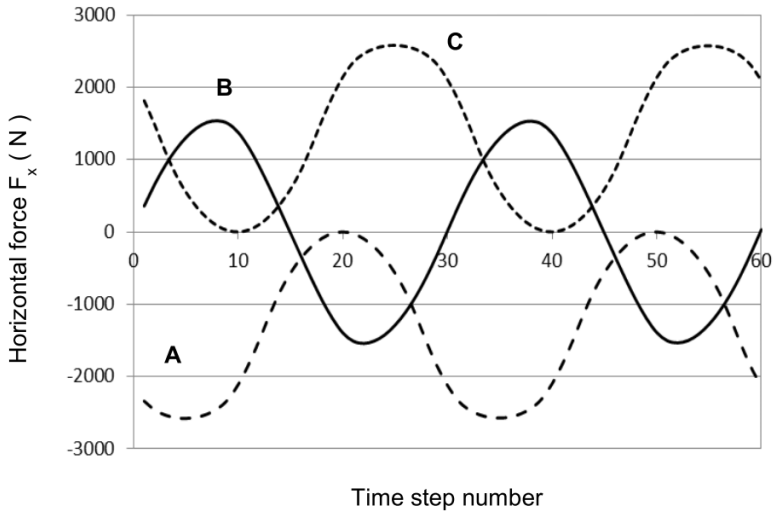

(a)

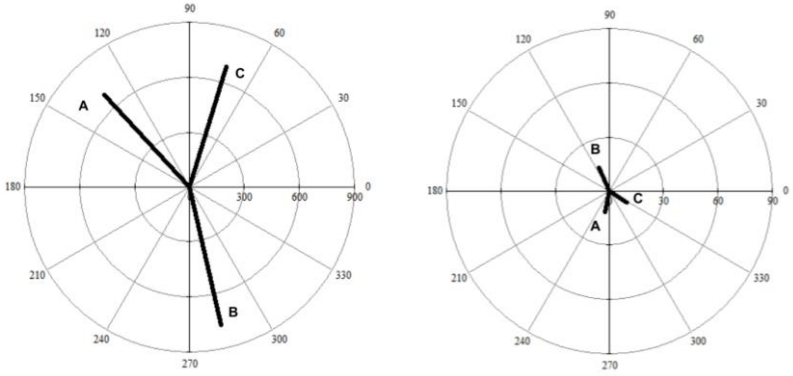

(b) (c)

Fig 3-39 Time distributions of horizontal magnetostriction forces acting in core joints, (A, C – side joints, B – middle joint) (a) time domain (b) components of 100 Hz (c) components of 200 Hz

3.13.3 Study of transformer core vibration

Mizokami [88] studied the vibration of a 3-phase model transformer core using a vibration meter utilising the laser Doppler effect. The 3 phase 3 limb model transformer was built of 0.23 mm thick Hi-B material. The core was assembled with an SSL configuration, 2 layers per step and the thickness of the core was 150 mm. The average clamping pressure on the yokes and limbs were 0.3 MPa. The core was scanned from five directions including the face, back, top and two sides. The average displacements on the face and back of the core was reported as 2 to

3 times larger than the other surfaces. The fundamental frequency of the vibration waveform was reported as twice the excitation frequency. The vibration in the limbs was bigger than in the yokes and the vibration of the central part of the limbs was higher compared to other areas. Comparing the vibration phase on the face and back of each limb showed that the vibration on the limb does not involve a change in the volume of the limb. The author argued that the limbs move backward and forward and the origin of this movement is the resonant vibration which occurs in the whole body of the core. Also it was reported that the vibration waveforms on the centre limb were out of phase with other limbs. The author mentioned that "The vibration waveforms on the side of the limbs contained various harmonic components which may represent the effect of the composition of various vibration sources".

Weiser [76] reported the vibration distribution of a single phase core stacked from 40 layers of 0.27 thick MOH material. The core was clamped to have a stacking factor of approximately 0.97. The clamping pressure was not mentioned directly. Vibration of the core was measured using a miniature triaxial accelerometer which attached to the core. The core was magnetised at 1.70 T and it was observed that the largest displacements were situated in the joint regions. The inner part of the joints showed larger accelerations than other regions.

Ishida [33] studied the normal to the plane vibration distribution in four three-phase transformer cores which were constructed from 0.3 mm thick electrical steels with different grades. The cores were assembled both in SSL and MSL (5 step in each book) configuration. The cores were magnetised at 1.70 T. It was observed that the vibration amplitude was higher in joints between yokes and limb. The vibration in the middle of the yoke and limb was significantly less than the joints. The cores with MSL configurations had lower vibration in all materials.

3.13.4 Summary

Based on the literature, all the researchers agree that the way the flux distributes in the core; especially core joints, is the main source of noise and vibration in the core.

Magnetic flux densities in longitudinal airgaps (B_{gap}), interlaminar airgaps (B_{normal}) and air gap bridging regions ($B_{gap\ bridge}$) are three important parameters which should be taken into account in the flux distribution and vibration studies.

Table 3-5 summarises previous works on flux distribution in transformer cores. A dash sign was used when no data were provided.

As can be seen in the table, the reported flux density for the longitudinal airgap is varying from 4 mT (#27) to 900 mT (#1). The gap bridge flux density has also a wide variability - 1.8 T (#11) to 3.4 T (#26). The normal to the plane flux density which has a direct influence on the core vibration was also reported very differently - 5 mT (#2) to 1250 mT (#24). The importance of having a good estimation of flux distribution becomes clearer during the interlaminar force calculation using equation (2-24). For example, a 250 times (=1250÷5) larger value in normal flux density will yield 62500 (250^2) times bigger value from the force calculations. Therefore, a better estimation of the flux distribution in the core joints helps to understand the force distribution in the core and hence the vibration and emitted noise.

Table 3-5 summary of the flux distribution studies in linear and mitred joints, in different inductions and different configurations

Reference	B_{gap} (mT)	$B_{gap\ bridge}$ (T)	B_{normal} (mT)	Experimental / Modeling	Longitudinal airgap(mm)	Mitered / Linear	Assembly type	Induction level (T)	Material grade	Interlaminar airgap (μm)	No. lamination	Lamination thickness (mm)	Laminations per step	Phase	Overlap length (mm)	#
[82]	900	2.10	6	E	-	M	SSL	1.8	CGO	-	10	0.33	1	1	14	1
	450	2.10	5					1.5								2
	160	1.85	-					1								3
[19]	910	2.34						1.8							20	4
	590	2.21						1.5								5
	210	2.08						1.1								6
[85]	530	2.42	600	M	0.4	L	2 SL	1.7	-	-	-	0.3			1.6	7
[64]	700	2.70	700		3		SSL	1.7	CGO	-	20	-	2	1	15	8
	40	2.04	250				6 SL				36	-			6	9
	200	2.15	300					1.8								10
	≈0	1.80	63					1.5								11
	700	2.90	-				SSL	1.7			20	0.3			15	12
	<50	2.11					6 SL				36				6	13
	500	2.70					SSL		HiB		20	0.23			15	14
	50	2.00					6 SL				36	-			6	15
	<60	2.11	260		3				-						9	16
	<60	2.17	-		1										3	17
	-	-	370								-		1			18
			1060		3										9	19
			700												20	20
[74]	413	2.58	-		<1		SSL	1.6	CGO	5	10	0.3			-	21
	414	2.56								10						22
	414	2.55								15						23
[84]	250	2.75	1250		2		SSL	1.5	M6	10	10	0.3			42	24
	-	3.07	-					1.7								25
		3.40						1.9								26
	4	1.88					5 SL	1.5							9	27
	-	2.09						1.7								28
		2.30						1.9								29
	200	2-2.5				M	SSL	1.5			-		-	1	42	30

4 Magnetising and measurement system development and procedures

4.1 Magnetic properties measurement

This chapter describes different assemblies of linear and mitred joints which were used in the study of the flux distribution in the joints. The layout of the installed search coils are introduced in each configuration. The magnetising and the measurement system and the procedure of the tests are described.

4.1.1 Epstein frame

The Epstein frame or square shown in Fig 4-1 is a measurement device for measuring the magnetic properties of electrical steels according to the standard IEC 60404-2 [89].

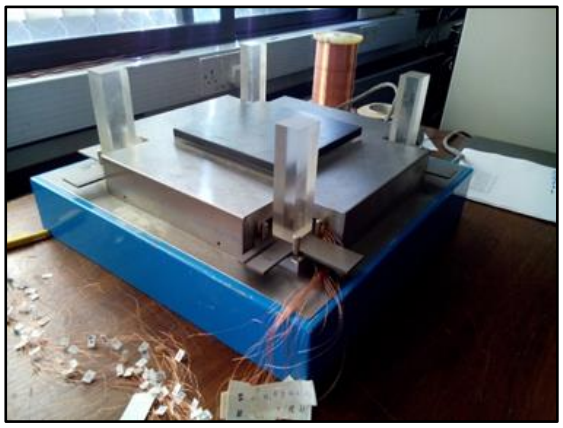

Fig 4-1 Standard Epstein frame with assembly of laminations inside the arms and four 100gr weights on four corners

It comprises four rectangular cross section arms within which the Epstein strips are situated. Each arm enwrapped by a 700 turn secondary coil on which is wound a 700 turn primary coil. The basic operation of the Epstein square is to inject current through the primary to magnetise the samples to the required flux density and then reading the secondary voltage to determine the magnetic flux density

and other specifications of the electrical steel such as power loss, permeability and the B-H curve.

Electrical steel sheet is cut in to 300mm by 30 mm strips for insertion into the Epstein square. In the standard assembly of the Epstein square each layer of strips is double-lapped in the corners as shown in Fig 4-2. The air gap between the strips in the overlapping portions should be as small as possible therefore after stacking; the laminations were pressed together at the four corners with 100 g weights which each produced a force of 1 N at each corner. This pressure is applied to keep the end of laminations tightly together to eliminate the air gap between the laminations in the joints (see Fig 4-1).

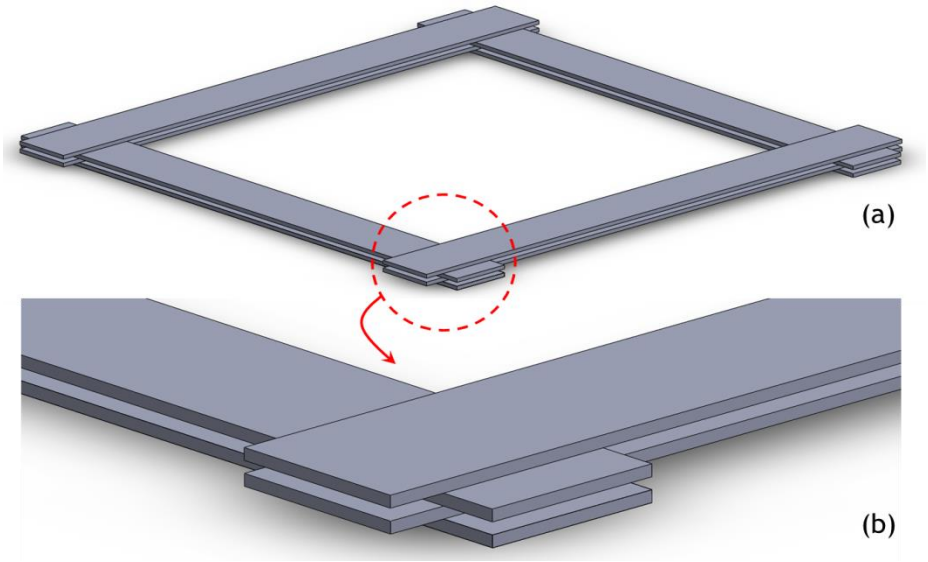

Fig 4-2 Schematic diagram showing stacking of four layers of laminations in standard Epstein frame (a) all the arms (b) a double-lapped corner

By definition and from Ampere's Law, the effective magnetic path length (l_m) is the ratio of ampere-turns to the average magnetizing force. According to the standard, this length is 0.94m for the standard Epstein frame as shown in Fig 4-3. Therefore, the active mass, m_a, of the magnetic circuit, that is the mass of the test specimen which is magnetically active is defined as follows:

$$m_a = \frac{l_m}{4l} m \quad \text{(kg)} \qquad (4\text{-}1)$$

where l is the length of the test specimen strips and m is the total mass and the $m_a$is the active mass of the test specimen.

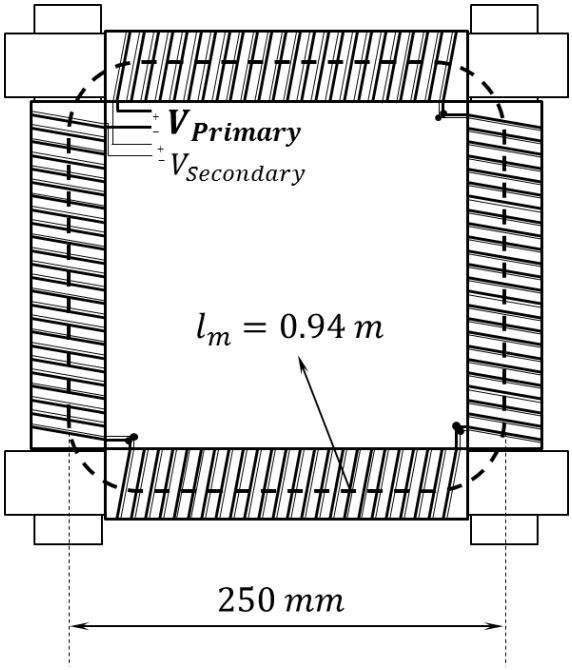

Fig 4-3 Schematic diagram of the magnetic path length of Epstein frame

Although the Epstein frame is used widely to determine the magnetic properties of electrical steels, it has some intrinsic deficiencies. The magnetic mean path length in this assembly varies with peak flux density and the permeability of the material [90]. Due to the narrow samples the influence of the cut edge is significant and therefore annealing should be conducted before each test which is costly and time consuming. Lastly, it is reported that for grain oriented electrical steels the results from Epstein frame are less reproducible because of the higher permeability of these materials [91]. To overcome these problems, single sheet testers were introduced.

4.1.2 Single Sheet tester

Several of the problems of the Epstein frame have been solved by the single sheet tester. Single sheet tester operates on a 500 mm × 500 mm sheet according to IEC 404-3 standard [92] so the adverse effect of edges can be neglected. A schematic diagram of a single sheet tester with two U-shape yokes and windings is illustrated in Fig 4-4. Due to the heavy weight of the top yoke, a pneumatic system is usually used to lift the yoke such that the applied force on the specimen is confined between 100 N to 200 N. The primary and secondary windings should be at least 440 mm in length [93]. The single sheet tester which was used in this research had 396 turns in primary and 400 turns in secondary. The conventional magnetic path length of single sheet tester is 0.45 m [93].

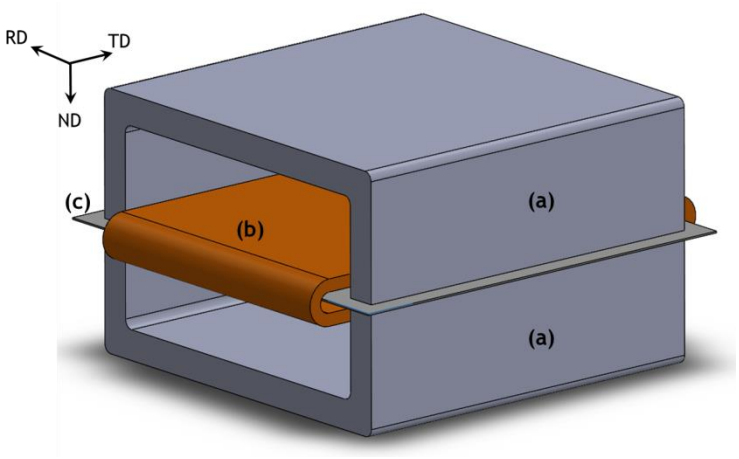

Fig 4-4 Schematic diagram of a single sheet tester including, (a) the yoke frame, (b) magnetising and measuring coils, (c) 500×500 mm electrical steel sheet under the test with the specified rolling direction

4.2 Localised magnetic flux density measurement

The needle probe technique [94] and search coil technique are two popular ways of measuring the localised magnetic flux density. In stacked structures, like transformer cores, search coils can be used to measure the flux density. The sensors are made up of a fine wire and operate according to Faraday's law. This wire is usually wound around the cross sectional area which is to be measured. Therefore the magnetic flux density can be calculated using the following equation:

$$B = \frac{1}{A.N}\int_0^T edt \qquad \text{(T)} \qquad (4\text{-}2)$$

Where, A is the cross sectional area of the search coil, N_t is the number of turns, e is the induced voltage in the search coil and T is the period of the magnetizing current. The uncertainty involving this type of measurement will be discussed in section 4.7.

4.3 Sample selection and preparation

Two types of materials including 0.35 mm thick non-oriented electrical steel of grade M250-35A and grain oriented electrical steel of grade M140-35S were used to study the flux distribution in linear joints. Similar thickness was chosen to remove thickness as a variable when comparing the flux distribution in cores assembled from the two materials. The magnetic properties of NO which were

provided in Epstein strips were measured using an Epstein frame according to IEC 60404-2. The GO material was provided in sheets of 500 mm × 500 mm, so the magnetic properties of GO were measured with a single sheet tester according to IEC 60404-3 as it is more reliable for GO materials. The measured relative permeability of GO and NO materials are illustrated in Fig 4-5. The sheet was cut into Epstein strips size and annealed. The stress which is introduced by cutting has adverse effects on magnetic properties of the electrical steel. Annealing treatments were undertaken to relieve internal stresses and to modify the grain structure. These operations were carried out by heating to 850ºC at 200ºC per hour and soaking at this temperature for two hours followed by slow cooling at the predetermined rate (100ºC per hour). To prevent the oxidation of the lamination, the air in the furnace chamber was evacuated.

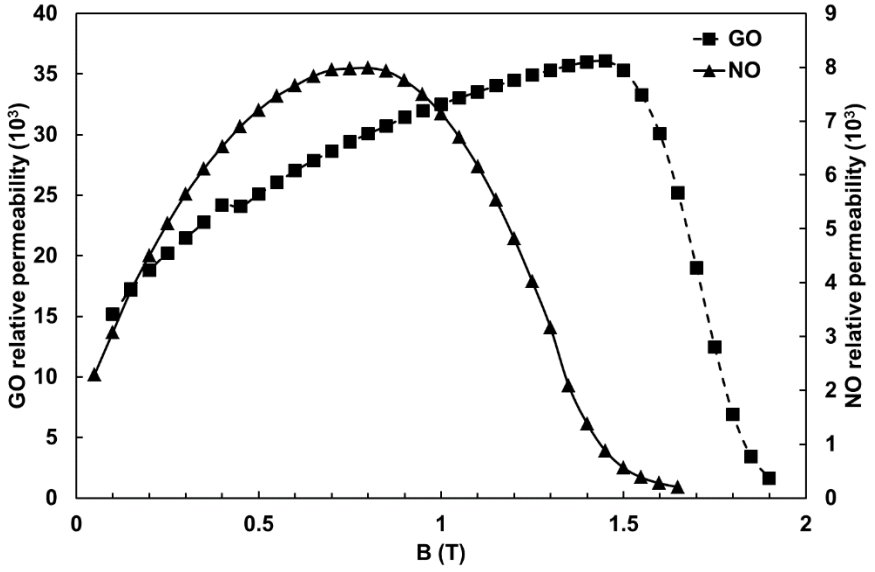

Fig 4-5 Measured relative permeability characteristics of the materials used in linear joint set ups

In mitred joint studies, 0.3 mm thick conventional grain oriented electrical steel were cut as a model single step lap core with dimensions shown in Fig 4-6. In order to measure the flux in the rolling direction some local search coils had to be installed perpendicular to the rolling direction of the lamination. The flux deviates from the rolling direction when it reaches the 45° mitred joint. Therefore in order to measure both components of the flux in each point two search coils installed perpendicular to each other in rolling and transverse directions. Two layers of yoke and two layers of limb were selected and the predetermined points were drilled with a 0.4 mm diameter drill bit, the width of each search coil was 10 mm. A schematic diagram of the drilled yoke is shown in

Fig 4-7 as an example. The drilled points were investigated with a domain viewer and no abnormal magnetic texture changes were found at the vicinity of the holes as shown in Fig 4-8. The burrs around the holes which emerged from drilling were removed by super extra fine 12000 grit sand papers to ensure the coating was not damaged.

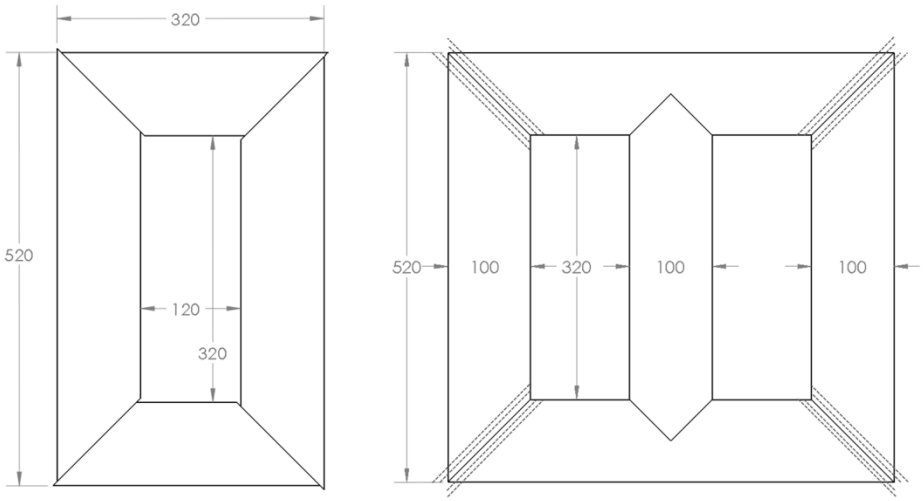

Fig 4-6 Dimensions of the model cores which were used in mitred joints studies (a) the single phase single step lap core (b) Three phase five step laps core (the middle layer of the book is highlighted. In a five step lap transformer core, a book is formed of five laminations)

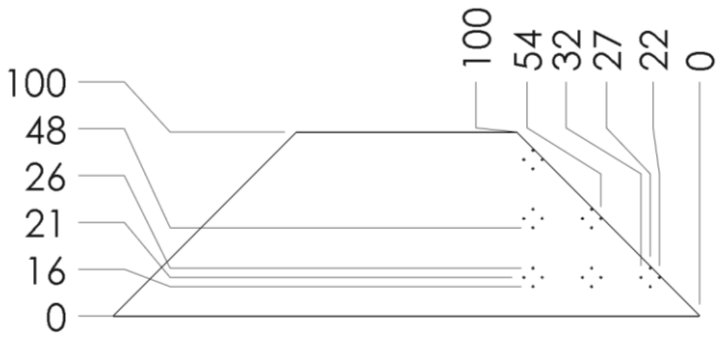

Fig 4-7 schematic diagram of the prepared yokes with 0.4 mm holes on them to install the search coils. The vertical and horizontal ordinates are in mm (Not to scale)

Fig 4-8 A lamination after drilling a group of holes with 0.4 mm diameter. The introduced stress on the lamination due to the drilled holes was negligible

4.4 Linear joint set up in Epstein frame

The standard Epstein frame is assembled as shown in Fig 4-2. As seen, a uniform interlaminar air gap exists between adjacent laminations. In practice the laminations bend slightly under their own weight making this gap non-uniform along the length of the limbs unless the gap is filled with a non-magnetic spacer (which is not done during routine testing since it would be very time consuming).

In a normal transformer core assembly there is no air gap between the laminations surfaces because the double overlap joint is not used. This fundamental difference between the assembly of laminations in the Epstein frame and that in a single phase transformer core gives rise to differences in the flux distribution in their corner joints and to a lesser extent probably even along the length of the limbs. Since in this study the flux distribution in the corner joints of the single phase core is of primary interest therefore another method of assembly is used. In the new configuration the laminations are not overlapped in the corner joints so the assembly is the same as a conventional single phase transformer core with butt and lap outer corner joints. In this configuration, the ends of the laminations in each layer protrude outside the main frame. This typical artificial joint is shown in Fig 4-9.

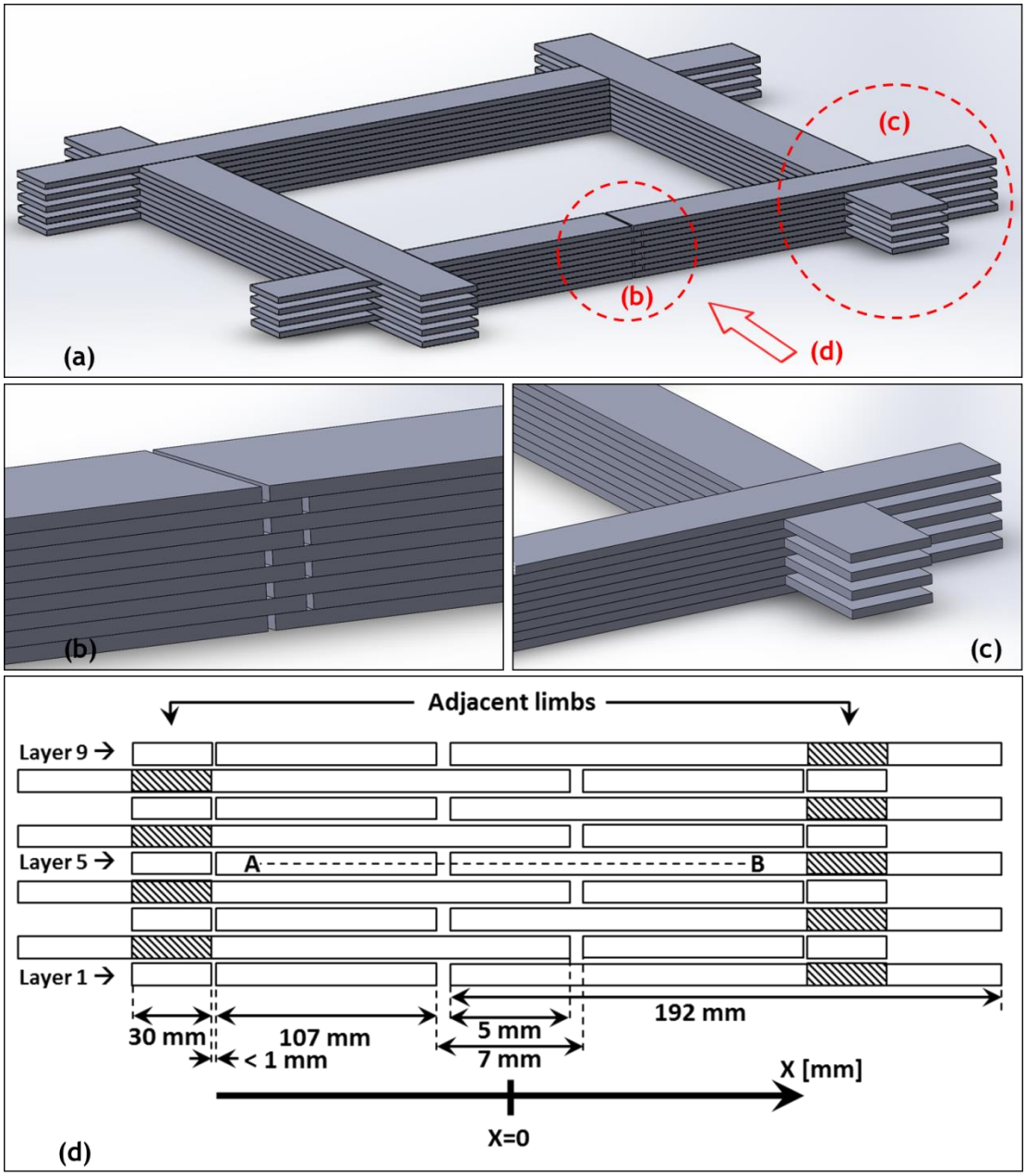

Fig 4-9 Schematic diagrams of the jointed assembly in the Epstein frame showing (a) Full view of nine layers of the jointed assembly (b) Jointed region at the middle of the limb. The air gap length was 1 mm and the overlap length was 5 mm. (c) Four corners of the assembly are in butt lap joint configuration, hence the laminations are not overlapped in the corner joints so the assembly is the same as a conventional single phase transformer core with butt and lap outer corner joints (d) cross section of laminations in the jointed limb (front view of the assembly). Ends of laminations in adjacent limbs shown hatched. The origin of the x axis is placed at the centre of the overlap for future addressing purposes (The figure is not to scale)

To assemble the joint stack nine Epstein strips were cut into two pieces of 107 mm and 192 mm. Search coils were installed in predetermined locations and the laminations were placed next to each other with a 1 mm air gap as shown in Fig 4-9. To fix the laminations in place, edges were glued to adjacent layers. Since the glue is non-magnetic and non-conductive it should have no impact on the flux distribution. The stress imposed on the electrical steel by the adhesive

after it had set is negligible. All the laminations of the test limb (shown in Fig 4-9-b) were assembled as a single rigid piece then the whole the limb was inserted into the Epstein frame. After inserting the test limb into the Epstein frame, other laminations in the remaining limbs were stacked layer by layer.

4.4.1 Search coils

Localised search coils were used to measure the flux density in various regions in the laminations. Both in-plane and normal-to-the-plane search coils were installed in order to measure the magnetic flux density at positions in individual laminations and at selected positions between pairs of laminations.

Since the jointed stack including the search coils had to slide into the Epstein frame simultaneously, the in-plane search coils had to be robust but introduce as small as possible air gap to cause minimum change in the flux distribution by increasing only a very small additional interlaminar air gap. Search coil wire, 25 μm [95] and 20 μm [96] diameter has been used previously but those were positioned in more accessible regions of cores. In this assembly the search coils were not easily accessible and were more liable to damage so 60 μm diameter enamelled copper wire was used to produce the search coils as a compromise between search coil integrity and the introduction of larger interlaminar air gaps.

The number of turns of the search coils was determined by considering the anticipated localized flux densities and corresponding voltages to be measured and the sensitivity of the voltage measuring system. In the worst case for in-plane search coils, the output voltage of a 30 mm wide single turn in-plane coil at 50 Hz magnetisation wound around a 0.35 mm thick lamination when the peak flux density at 0.1 T was 330 mv. For a single turn normal-to-the-plane search coil with an area of 30 mm^2 and peak flux density of 1.0 mT the output voltage would be $9.4\,\mu V$ which is within the range which the system could measure. These calculations confirm that single turn in-plane and normal-to-the-plane search coils would be suitable to measure the flux density.

Single turn search coils formed from enamelled copper wire positioned at points along laminations in layer 5 were installed to measure the distribution of the longitudinal component of localised flux density along the path AB (see Fig 4-9-d). The search coils were glued on the lamination in order to fix them in place and to ensure that they were tightly wrapped around the strips. The glue was gently

spread to ensure that the search coils were not damaged and that the thickness of the glue layer was negligible. In the same way the normal-to-the-plane search coils were installed at the predetermined positions – mainly at the vicinity of the linear joint.

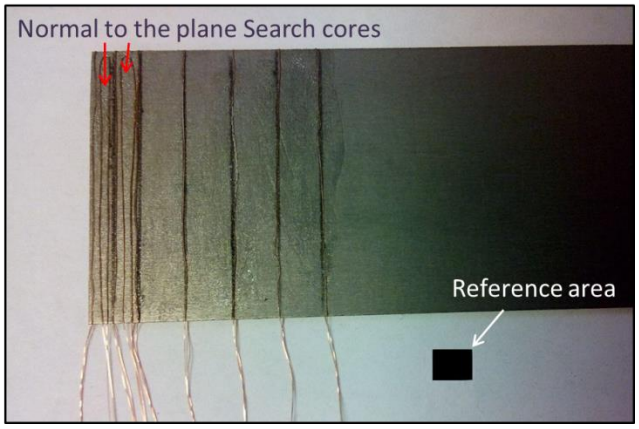

Fig 4-10 some search coils installed on the Epstein strip. The normal-to-the-plane search coils are pointed by red arrows; the rest-unmarked search coils are the in-plane ones. The reference area was put next to the search coils to enable normal search coils area colocation

The enclosed area of the in-plane search coils is easy to calculate however measuring or calculating the area of the normal-to-the-plane search coils was difficult due to the non-regular shape of these search coils (see Fig 4-10). The interlaminar flux is typically less than 20 mT; therefore the induced voltage across the normal-to-the-plane search coils is less than 0.2 mV. Hence, to measure the magnetic flux density sufficiently accurately, it is essential to measure the area of the normal to plane search coils precisely.

In order to calculate the area of the normal-to-the-plane search coils one 5 mm × 5 mm square was cut from electrical steel and put together with target search coils. A photograph was taken perpendicular to the surface of the square steel and the search coils and then loaded into Matlab software. The numbers of pixels both in the square sample and inside of each search coil were counted. Knowing the area of the square steel (which was 25 mm^2) yields the area of the search coil. In Matlab software, the boundary of each search coil and the square sample was defined manually by hovering the mouse pointer over the boundaries. Since this might cause some small errors, this process was carried out five times and the average value was considered as the numbers of the pixels. The uncertainty of the measurements was less than 1% percent of the measured area. After positioning the search coils the glued laminations were slid into the Epstein frame magnetizing coil.

4.4.2 Linear model set ups

In order to study the flux distribution in linear joint, nine linear model joint (LM) setups with different configurations and number of search coils were built and measured to find the suitable arrangement of search coils for each material. In Table 4-1, the most suitable set ups are mentioned and will be discussed.

Table 4-1 Number and specification of the linear joints developed in the Epstein frame arm

Linear Model #	Material	Layers	Air gap (mm)	Overlap (mm)	search coils
LM1-NO	NO	9	Without joint		21
LM1-GO	GO	9	Without joint		21
LM2-NO	NO	9	1	5	46
LM2-GO	GO	9	1	5	49

4.5 Mitred joint set up

A translation table as shown in Fig 4-11 was used to assemble the single phase mitred joint assemblies. The table was designed to be used for both single phase and three phase cores. The top yoke of the assembled core is mounted on a moveable part of the table. The moveable part of the table is driven manually with two linear gearboxes with output maximum torque of 32 Nm in two directions. The linear movements were measured by Hepco linear measuring systems with a resolution of 0.01 mm. The top surface of the moveable part and the fixed part of the translation table was levelled with a precision of 10μm. A groove with cross section of 140 mm × 20 mm was machined under the centre of the limbs to thread the windings.

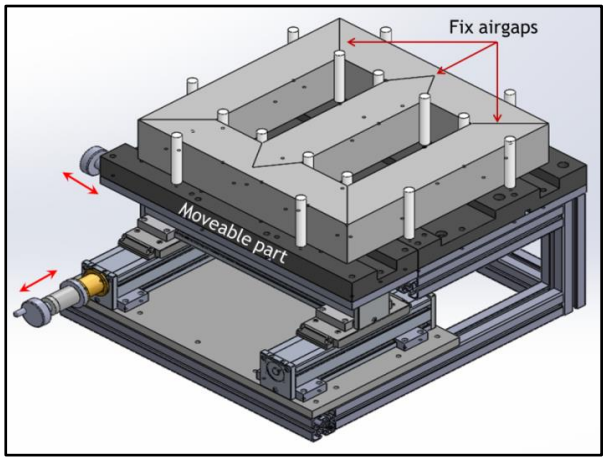

Fig 4-11 Schematic diagram of the translation table with three phase model transformer core assembly

A wire with a thickness of 60 µm was used to thread the search coils and then twisted to prevent excess flux pick up. Search coils were installed on two layers of the core – 24 search coils on each layer. The search coils were not glued to the laminations but twisted as that they fixed well in place. Prior to placing the laminations in the stack a continuity test was conducted to make sure that the search coils were intact. Also the continuity test conducted between the search coils and the laminations to make sure that they search coils are insulated from each other and the laminations. The layouts and the relative positions of the search coils are shown in Fig 4-12.

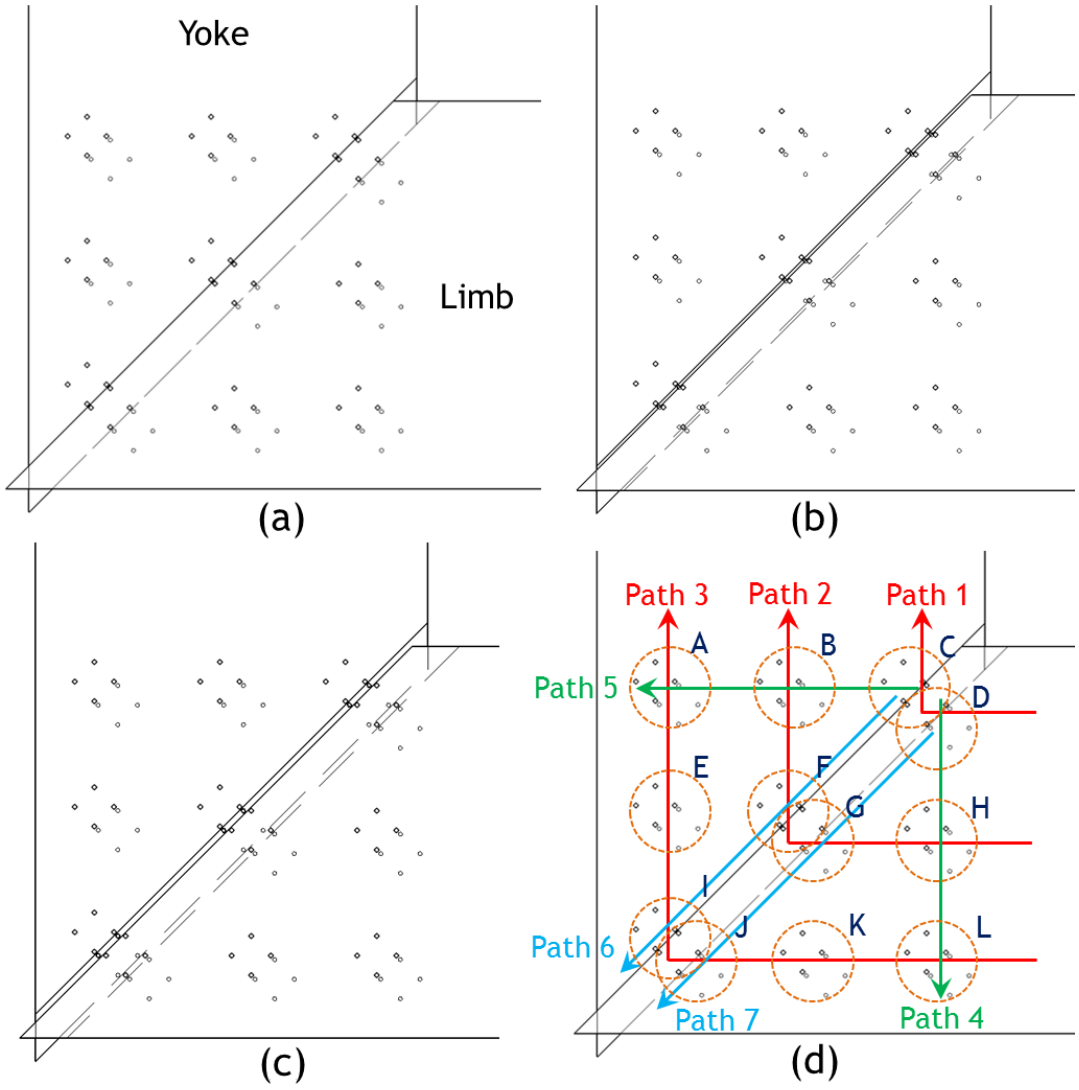

Fig 4-12 Schematic diagram of the mitred joints and the positions of the search coils in limb and yoke laminations. Two layers which were used to install the search coils are overlapped in these figures in order to highlight their relative positions. The holes in bottom layer are marked with thin circles while the holes in top layer are marked with thick squares at (a) air gap=0 mm (b) air gap=1 mm (c) air gap=2 mm. (d) Highlighted seven path lines to study the flux distribution along them. (The figures are not to scale)

Groups of search coils are marked with letters from A to L in Fig 4-12-d. Each group contains two search coils in each layer which are not on top of each other. This is to prevent introducing further interlaminar air gaps between the laminations. More than four different cores were assembled in order to study the effect of longitudinal air gap length and the stack height on flux distribution in a laminated mitred core. The tests were conducted for SSL configuration in single phase model transformer cores (MC). A Net-like search coil arrangement was used as in [81] and the data were analysed. Two selected core assemblies with their specifications which are selected to present in this thesis are listed in Table 4-2. The overlap length in these cores where 6 mm.

Table 4-2 Number and specification of the linear joints developed in the Epstein frame arm

Model Tr. core #	Material grade	Number of Phases	Config.	Layers	Tested Air gaps (mm)	Tested Layers
MC1	GO	Single	SSL	9	0/0.5/1.0/1.5/2.0	5/6
MC2	GO	Single	SSL	31	0/0.5/1.0/1.5/2.0	5/16

The core limbs were wound with secondary and then primary windings. A 0.5 mm diameter thick solid enamelled copper wire was used for the secondary winding. The edge of the laminations in the surface and bottom layers of the core was covered by 3 layers of electrical insulation tape to prevent the sharp edge of top side laminations cutting the wire's insulation and making a short circuit. A 2.5 mm diameter thick stranded insulated wire used to wind half of the primary winding on top of the secondary one and half on the other limb. The primary winding was divided into two series windings in order to have a more uniform flux distribution in the core. The number of turns in the primary winding were different for each setup and were calculated using equations (2-1) and (2-13) constrained by the maximum output voltage (70 V_{rms}) and current (15 A_{rms}) of the amplifier.

4.6 Magnetising system and the process of localised flux density measurement

The hardware of the magnetising system comprised a PC equipped with LabVIEW and a NI PCI 6120 data acquisition card, an amplifier in series with an insulation transformer and a 0.47 Ohm shunt resistor in order to read the input current of the primary winding. A schematic diagram of this system is illustrated in Fig 4-13.

The primary current is driven by the PC through the amplifier and the shunt resistor. The voltage drop across the shunt resistor was used to calculate the magnetizing current and consequently the power loss of the electrical steel. The secondary winding open circuit voltage was also read and passed to the software for power loss and magnetic induction calculations.

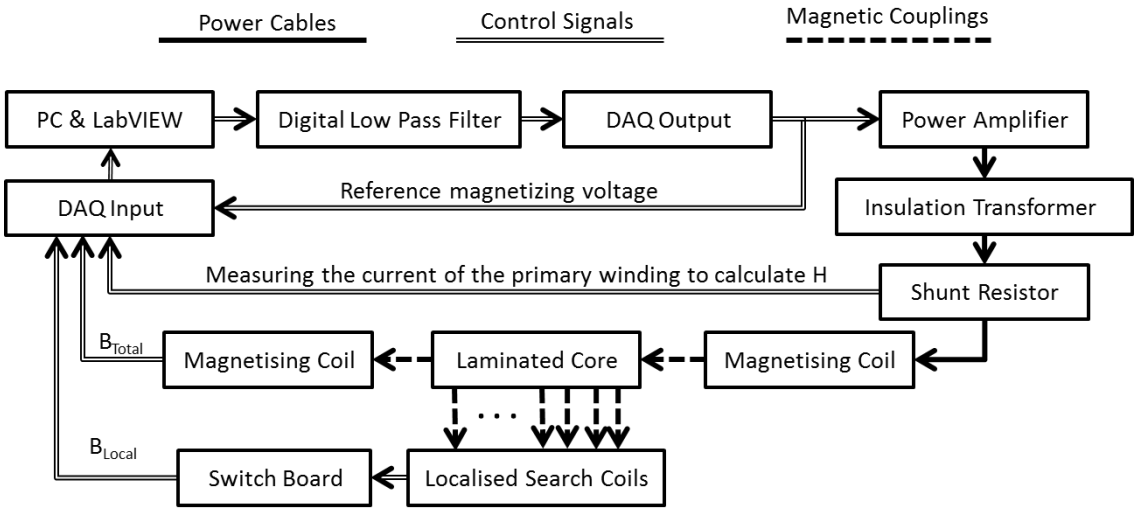

Fig 4-13 Schematic diagram of the system used to magnetize the Epstein frame and the model transformer cores

The measurement system was connected to one of the search coils and then the steel was magnetised at 50 Hz over a flux density range from 0.10 T to 1.70 T in 0.10 T steps. Using a feedback control system, the overall limb flux density waveform was kept sinusoidal and the error of the magnetising system was within the 0.05% of the nominal Bpk at each data point. The readings were the average of five cycles and the measurements were conducted three times on the same assembly. The instantaneous emf induced in each of the single turn coils was measured and the localised instantaneous flux density B was calculated using the equation (4-2).

4.7 Uncertainty of the measurements

The uncertainty of the measurement system was calculated according to the guidelines given in UKAS M3003 [97].

The uncertainty of the measurement is the probability of the value existing in a given range. There are two ways to estimate uncertainties: Type A and Type B.

Type A evaluations calculated from statistics and usually shows the repeatability of the measurements. Type B evaluations usually extracted from the calibration certificates, manufacturers specifications and calculations.

All contributing uncertainties should be expressed at the same confident level by converting them into standard uncertainty u(y). For type A evaluations this value is calculated from:

$$u(y) = \frac{S}{\sqrt{n}} \qquad (4\text{-}3)$$

Where S is the estimated standard deviation which is calculated form the data set and the n is the number of the measurements in the set. For Type B evaluations after determining the distribution of the information the appropriate divisor assumed. The divisor of the normal distribution is equal to 2 while the divisor of rectangular distribution $\sqrt{3}$.

Individual standard uncertainties can be combined by root mean square which is called the combined standard uncertainty ($u_c(y)$):

$$u_c(y) = \sqrt{{c_1}^2 u^2(x_1) + {c_2}^2 u^2(x_2) + \cdots + {c_N}^2 u^2(x_N)} \qquad (4\text{-}4)$$

Where c_i are the sensitivity coefficients which can be determined experimentally from $\frac{\Delta y}{\Delta x}$ by varying the value of x_i.

Scaling the combined standard uncertainty by multiplying it by a coverage factor gives a result which shows the uncertainty at another level of confidence. Using the coverage factor K_{95}=2 gives a level of confidence of approximately 95 percent:

$$U(y) = K_{95} u(y) \qquad (4\text{-}5)$$

Uncertainty budgets for in-plane and normal-to-the-plane search coils in different setups are presented in Table 4-3 to Table 4-5 .These values have been estimated in the following way:

- The accuracy of the NI 6120 data acquisition card has been extracted from the manual and highest uncertainty among the possible ranges was selected [98].

- Frequency setting uncertainty value was taken from the base clock accuracy of the NI 6120 DAQ card.
- The mass of the samples was measured using an Avery Berker FB312 scale with a resolution of 0.01 grams. The samples were measured 5 times and the expanded uncertainty of all samples was within ±0.01%.
- The length of the samples was measured using a ruler with a resolution of 0.5mm. Therefore the uncertainty of the measurement was assumed as a half of the resolution. The nominal length of the laminations was 305 mm.
- The length of the air gap was measured using a micrometre. The resolution of the Vernier was 0.02mm. The uncertainty of the measurement was assumed to be half of the resolution and the air gap size was 1mm. The sensitivity of the air gap was calculated using COMSOL software by changing the air gap by 0.1 mm and measuring the B_x and B_Y and calculating the $\Delta x/\Delta Y$.
- The repeatability of the setup was tested by assembling –measuring-dismantling of the Epstein frame laminations for five times and then measuring the B value in each time.
- The repeatability of the measurement was calculated by measuring the B value for five times while the setup remained the same.
- Lamination thickness uncertainty was calculated by measuring the thickness of 100 points on 8 laminations. The average was 35.05 mm with the standard deviation of 0.43.
- The area of the normal-to-the-plane search coils were calculated five times by means of the image processing toolbox of Matlab. The area of all the normal-to-the-plane search coils were measured 5 times and the maximum repeatability of 0.3 % was selected to cover all the measurements for all normal-to-the-plane search coils.
- The uncertainty of the area of the in-plane search coils in rolling and transverse directions used in model transformer cores is composed of the uncertainty of the place of the wire in the 0.4 mm hole and the added overlapping region in crossing point.

Table 4-3 Determination of uncertainties in magnetic flux distribution measured by in-plane search coils in Linear models

Source of Uncertainty	Value ± %	Probability distribution	Divisor	c_i	U_i ± %
Data Acquisition card calibration	0.100	Normal	2.00	1.0	0.05000
Frequency setting	0.010	Normal	2.00	1.0	0.00500
Mass (Scale calibration)	0.010	Rectangular	1.73	1.0	0.00578
Length of the Samples (Ruler Calibration)	0.100	Rectangular	1.73	1.0	0.05780
Length of the air gap (Vernier Calibrations)	1.000	Rectangular	1.73	0.05	0.57803
Repeatability of setup, drift	0.100	Normal	2.00	1.0	0.05000
Repeatability of measurement, drift	0.375	Normal	2.00	1.0	0.18750
Area of the in-plane search coil	2.800	Normal	2.00	1.0	1.61850
Sum of squares					2.99561
combined uncertainty					1.73078
Expanded uncertainty		K_{95}=2		2.0	4.20580
Declared uncertainty at a confidence level of 95%					**4.5**

Table 4-4 Determination of uncertainties in magnetic flux distribution measured by normal-to-the-plane search coils in Linear models

Source of Uncertainty	Value ± %	Probability distribution	Divisor	c_i	U_i ± %
Data Acquisition card calibration	0.1000	Normal	2.00	1.0	0.05000
Frequency setting	0.0100	Normal	2.00	1.0	0.00500
Mass (Scale calibration)	0.0100	Rectangular	1.73	1.0	0.00578
Length of the Samples (Ruler Calibration)	0.1000	Rectangular	1.73	1.0	0.05780
Length of the air gap (Vernier Calibrations)	1.0000	Rectangular	1.73	0.05	0.57803
Repeatability of setup, drift	0.0600	Normal	2.00	1.0	0.03000
Repeatability of measurement, drift	0.3750	Normal	2.00	1.0	0.18750
Area of the normal-to-the-plane search coils	0.3000	Rectangular	1.73	1.0	0.17300
Sum of squares					0.40615
combined uncertainty					0.63730
Expanded uncertainty		K_{95}=2		2.0	1.27459
Declared uncertainty at a confidence level of 95%					**1.5**

Table 4-5 Determination of uncertainties in magnetic flux distribution measured by rolling and transverse search coils in model transformer cores

Source of Uncertainty	Value ± %	Probability distribution	Divisor	c_i	U_i ± %
Data Acquisition card calibration	0.1000	Normal	2.00	1.0	0.05000
Frequency setting	0.0100	Normal	2.00	1.0	0.00500
Mass (Scale calibration)	0.0100	Rectangular	1.73	1.0	0.00578
Length of the Samples (Ruler Calibration)	0.1000	Rectangular	1.73	1.0	0.05780
Length of the air gap (Vernier Calibrations)	0.5000	Rectangular	1.73	0.05	0.28900
Repeatability of setup, drift	0.0600	Normal	2.00	1.0	0.03000
Area of the in-plane search coil	9.4285	Normal	2.00	1.0	4.71428
Sum of squares					22.3147
combined uncertainty					4.72385
Expanded uncertainty					9.44769
Declared uncertainty at a confidence level of 95%					**10**

5 Sound and vibration measurements

This chapter describes the noise measurement system and the 3D laser scanning vibrometer which were used to study the transformer core noise and vibration respectively. A brief introduction of related sound and vibration terms will be highlighted at the beginning of each section. More details on sound measurement setup and the devices specification is available in [2].

5.1 Noise measurement

5.1.1 Basic terms and measurement principals

Sound is a form of energy which travels by changing the pressure of the medium through which it travels. Sound waves are produced by a source which is vibrating and sending its vibration in the air. The sound pressure, SP, (measured in Pa) is the local pressure change from the medium average pressure, caused by a sound wave. The human ear is capable of hearing sounds with frequencies between 20 Hz to 20 kHz and sound pressure from 20 μPa to 100 Pa. Sound pressure is usually expressed in the decibel scale related to the threshold of normal human hearing at 1000 Hz and called sound pressure level SPL. The sound pressure level can be calculated using the following equation:

$$L_{pi} = 20 \log\left(\frac{p}{p_0}\right) \qquad (5\text{-}1)$$

Where p is the measured root mean square of sound pressure and p_0 is the reference sound pressure. As the human ear is only sensitive to certain above-mentioned frequencies, the A-weighting filter (Fig 5-1) is used to demonstrate how the human ear perceives the noise. Measurements made using A weighting are shown with dB(A) to show that the information is A-weighted decibels. The A weighting filter which is described in equation (5-2) can be used in any frequency to calculate the A-weighted sound pressure level $L_{pA.}$

$$A_w(f) = 2 + 20log\left(\frac{12194^2 f^4}{(f^2+20.6^2)(f^2+107.7^2)^{\frac{1}{2}}(f^2+737.9^2)^{\frac{1}{2}}(f^2+12194^2)}\right) \quad (5\text{-}2)$$

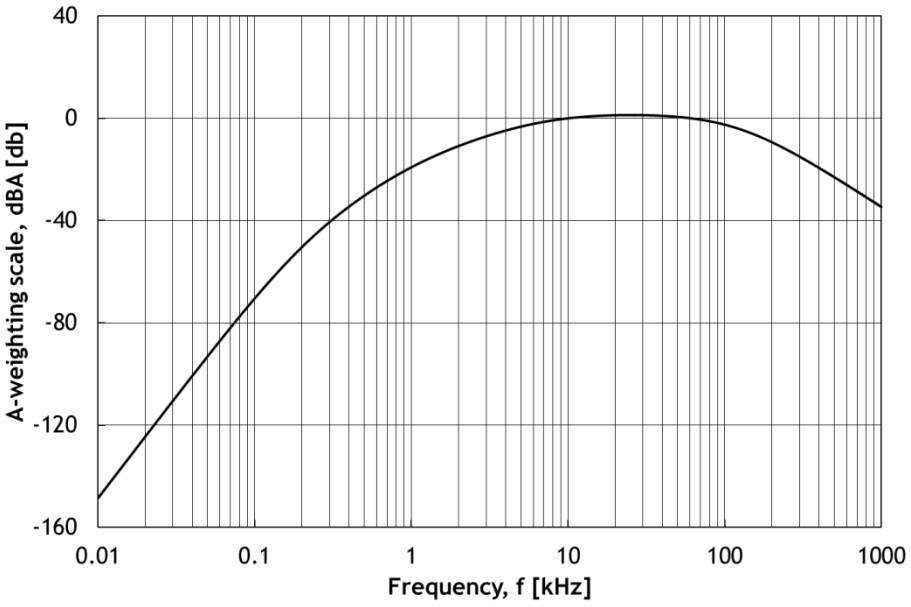

Fig 5-1 A- weighting filter curve

When noise is measured using several microphones the average A-weighted sound pressure level can be calculated form the A-weighted sound pressure level using equation (5-3):

$$L_{pA} = 10log_{10}\left(\frac{1}{N_{mic}}\sum_{i=1}^{N_{mic}} 10^{\frac{L_{pAi}}{10}}\right) \quad (5\text{-}3)$$

5.1.2 Noise measurement technique

The test procedure of measuring the emitted noise of a transformer is described in IEC 60076-10 standard [99]. Firstly, the background noise level should be measured. Then; in the no load condition, the transformer is magnetised at the nominal voltage. The acoustic noise should be measured around the transformer at the distance of 0.3 m from the principal radiating surface and the mid-point of the half of the height of the transformer. The number of the measurement points should not be less than 6 and their distance from each other not more than 1.0 m. The acoustic noise level of a transformer can be calculated using three methods: sound power level method, sound intensity method and sound pressure method.

The SPL is related to the source itself and is independent of distance. The sound intensity is the sound energy per unit area per unit time perpendicular to the direction of sound waves and is a vector quantity. These two methods have not been used to study the acoustic noise in this research; instead, the sound pressure was used by taking into account the corrections for the background noise and reflections [2, 99].

5.1.3 Noise measurement setup

The acoustic measurement system was developed with reference to [99] and comprises eight B&K 4188-A-021 microphones with preamplifiers with a frequency range 20 Hz-12.5 kHz, a B&K 2694 conditioning amplifier, an NI 9215 analogue input module and a computer, with National Instruments LabVIEW installed. The schematic diagram of the noise measurement setup and the flowchart of calculating the overall averaged A-weighted sound pressure level of the transformer core are shown in Fig 5-2. The microphones were mounted on clamp-stands and arranged on the prescribed contour at a distance of 30 cm from the core as shown in Fig 5-3. The microphones were connected to the conditioning amplifier using single high quality BNC cables. The conditioning amplifier then fed the analogue input module. The microphone setup is shown in Fig 5-3. The transformer was magnetised at a predefined induction level and then the program recorded the acoustic samples for 10 seconds before calculating the average A-weighted sound pressure level. All the tests were conducted in an anechoic 2 m× 3.5 m× 2.2 m (W×L×H) room with the background average A-weighted sound pressure level of 30 dB(A).

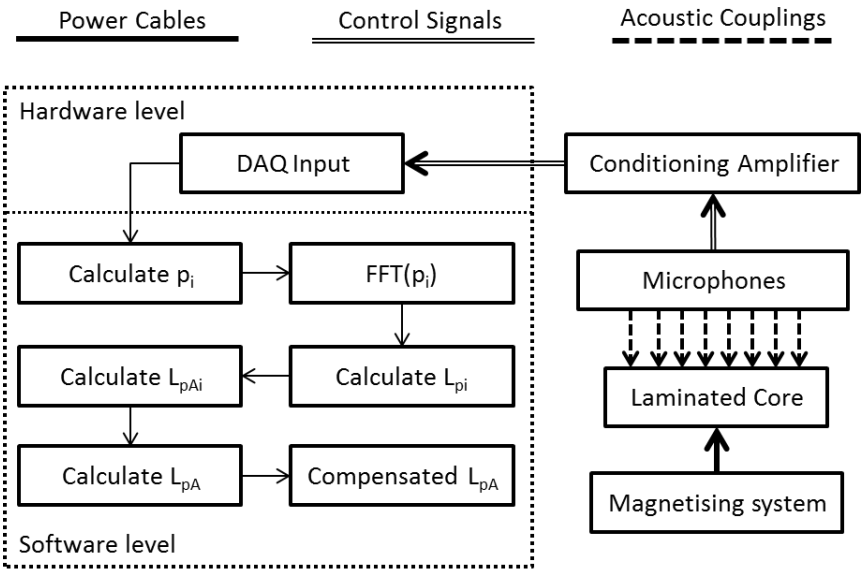

Fig 5-2 Schematic diagram of the noise measurement setup and the flowchart of calculating the overall averaged A-weighted sound pressure level of the transformer core

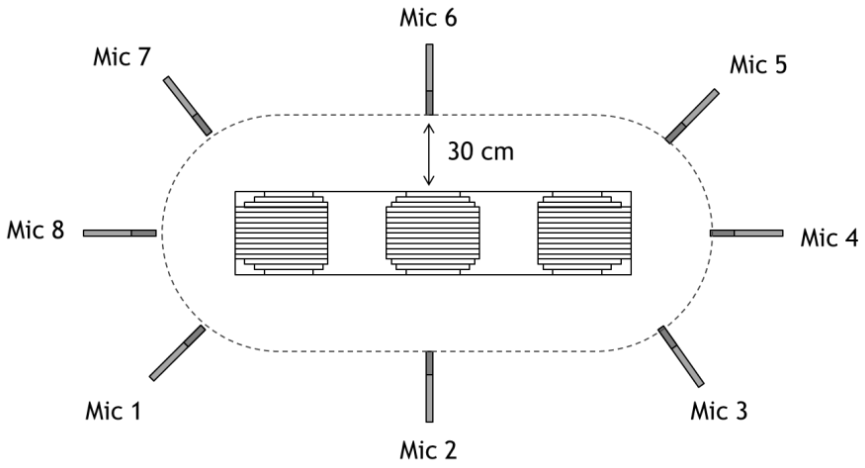

Fig 5-3 Microphones' positions around the transformer core (top view)

5.2 Vibration measurement

5.2.1 Vibration measurement techniques

Vibration measuring equipment can measure different quantities and may be called an accelerometer, velocity meter or vibrometer [100]. Accelerometers are capable of measuring the acceleration signal over a wide range of frequency; usually from 1 Hz to 10 kHz [101]. Many researches (e.g. [61, 74, 76, 88, 102]) have been conducted to study the vibration of transformer cores using piezoelectric accelerometers. These accelerometers are attached with adhesives

to the surface of the transformers. For best accuracy, it is important that the accelerometer is tightly coupled to the core surface. Even with best practice, the accelerometer will affect the measurements because of being attached to the measurand. The low cost and minimal time for setting up the measurements together with the relatively high resolution is the advantage of these accelerometers. Fig 5-4 shows a three phase transformer core with two accelerometers attached on the top yoke.

Scanning the whole surface of a transformer core using an accelerometer is a very time and labour demanding procedure. To avoid the above problems, vibration meter utilising the laser Doppler Effect were used recently to study the transformer core vibration [88, 103]. The working principal of these types of vibrometer are explained in section 5.2.2.

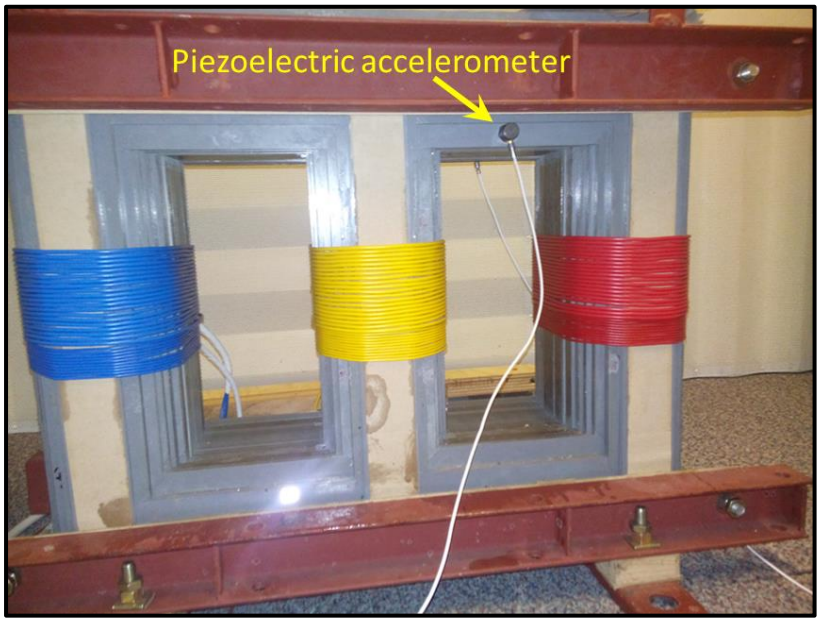

Fig 5-4 Two piezoelectric accelerometers are attached on the front and the back of the top yoke of a three phase model transformer core in order to measure the core vibration. The signals from the accelerometers should be double integrated in order to calculate the displacement

5.2.2 Principal of vibration measurement based on laser beam

Laser vibrometry uses the Doppler Effect for non-contact optical vibration measurement. The effect describes how the frequency of light is changed slightly when the light is scattered from a moving object, e.g. in this research a transformer core surface. Within a Polytech vibrometer a high precision interferometer detects the minor shift of the frequency in the backscattered laser light. To achieve this, the interferometer splits the beam into two parts. The so

called reference beam propagates directly to a photo detector, while the measurement beam is incident on the test object, where the light is scattered by the moving surface. Depending on the velocity and the displacement the backscattered light is changed in frequency and phase. The characteristics of the motion are completely contained in the backscattered light. The superposition of this light with the reference beam creates the modulated detected output signal revealing the Doppler shift in frequency. Signal processing and analysis provides the vibrational velocity and displacement of the transformer core surface. Vibratory motion is properly characterised as a true 3D phenomena if three laser heads are utilised of the same measurement part. A completed measurement using a 3D scanning vibrometer includes the spatial nature of the motion. The 3D scanning vibrometer uses the light as the sensor, eliminating the influence of the traditional contact transducers on the test object motion. By using scanning mirrors the light is sequentially placed on the grid of points measuring the motion of the scanning surface. Three measurement head sample each grid point in three separate directions uniquely determining the vector point of that point. Fig 5-5 shows the flowchart of working principal of a 3D scanning laser vibrometer.

The equipment used in this investigation was manufactured by Polytec and is a PSV-500-3D-M consisting of one PSV-I-500 scanning laser head with high definition video camera and the PSV-G-500 geometry scan unit. The other two laser heads are PSV-I-520 units which do not have video camera and geometry scan units. The vibrometer consists of a controller (PSV-F-500) with three digital decoders, signal generator and reference channel data acquisition. This is connected to the laser head and the data management system (PSV-W-500) via the junction box (PSV-E-500), the complete system can be seen in Fig 5-6. The system has a bandwidth from dc to 1MHz and can detect vibration velocities up to 10m/s.

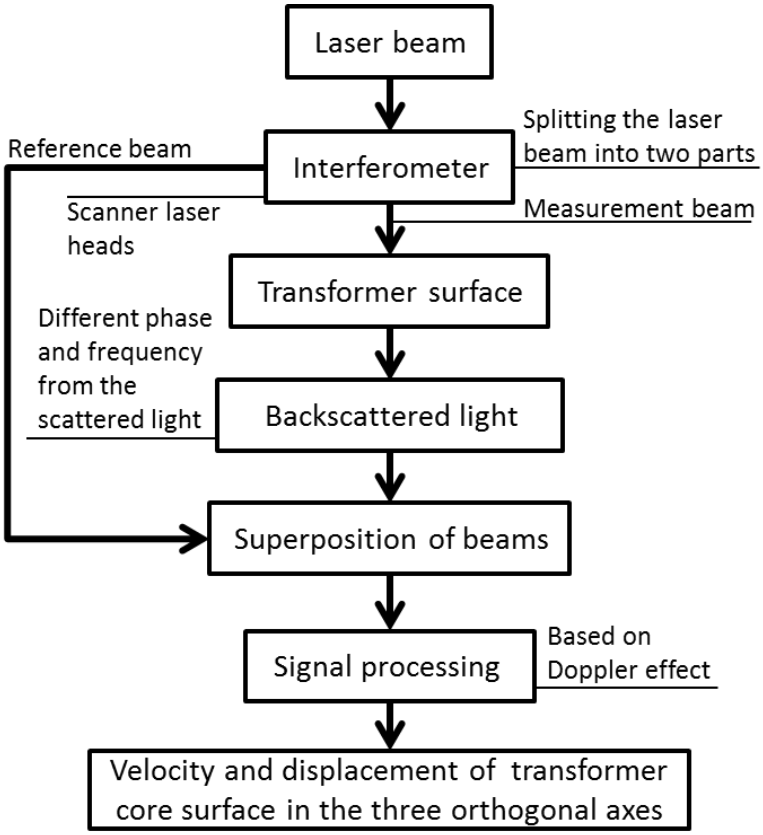

Fig 5-5 Flowchart showing the principal of a 3D scanning laser vibrometer

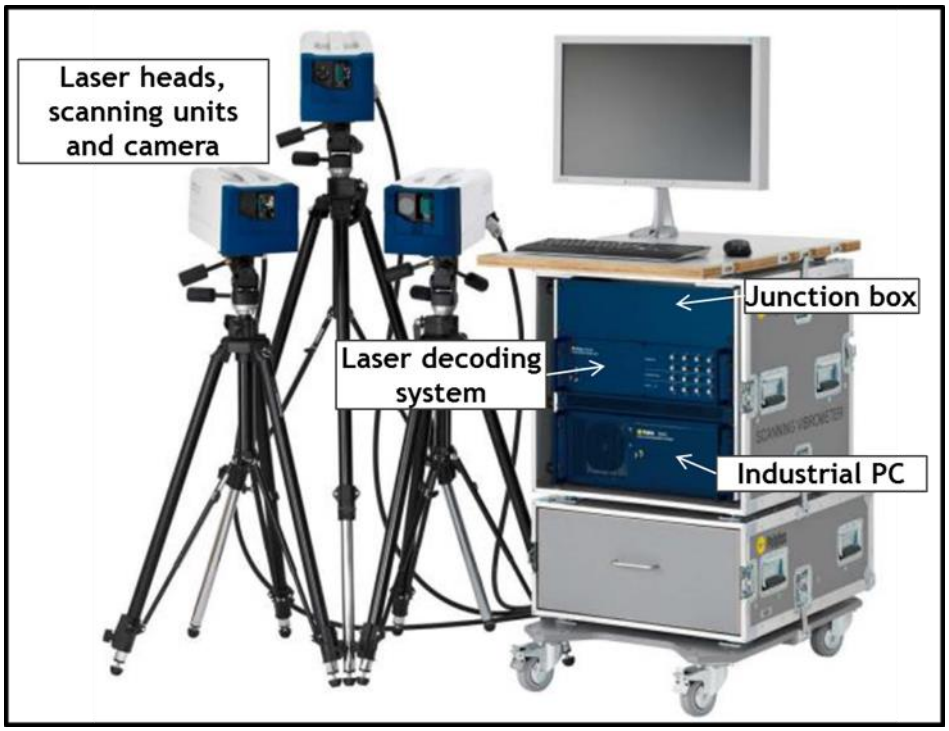

Fig 5-6 PSV-500-3DM laser vibrometer

The system has a working distance of 125mm to up to 5m with scan angles of 50 x 40° which results in area scans of a few mm^2 to several m^2. The only requirement

is to have a sufficient amount of back scattered light as this defines the signal to noise ratio.

5.2.3 Laser vibrometer setup

The 3D scanning laser vibrometer was used to monitor the surface vibration velocities of the transformer core. The scanner laser heads were installed on the Polytec's table tripod. For the vertical production core the distance between the transformer and laser heads was approximately 1.7m. This allowed the whole transformer structure to be in the field of view of the HD camera. It also allowed the laser beams to reach all possible areas of the transformer core. The transformer was magnetised at 1.7 T, 50 Hz and allowed to run for 4 hours prior to running a complete scan of the structure in order to allow the temperature to stabilise. An attenuator on the secondary voltage output was used to trigger data acquisition. The same arrangement was used to measure the vibration velocity of the horizontal cores on the translation table.

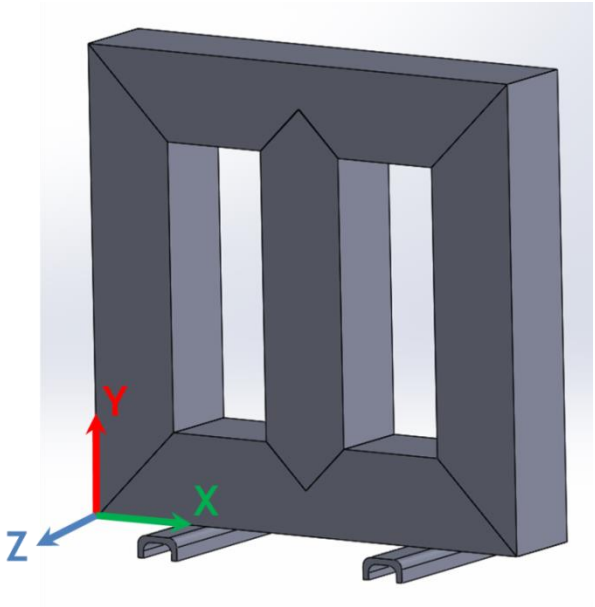

Fig 5-7 Orientation of the axis with respect to the transformer

5.2.4 Post processing of the scanned data on mitred joints

After the transformer core was assembled on the translation table and was ready to be magnetised, more than 1700 points on the joint were selected to be scanned as shown in Fig 5-8. In order to understand the correlation between the flux distribution and the surface vibration of the jointed region specific scan points were selected based on the situation of the search coils on layer 5 as described in Fig 4-12. The path lines presented in figure 4-12-d were regenerated on this layer as shown in Fig 5-9. Analysing the vibration of the marked data points would enable us to compare the vibrational behaviour of the core on these lines with the flux distribution on the associated path lines on layer 5.

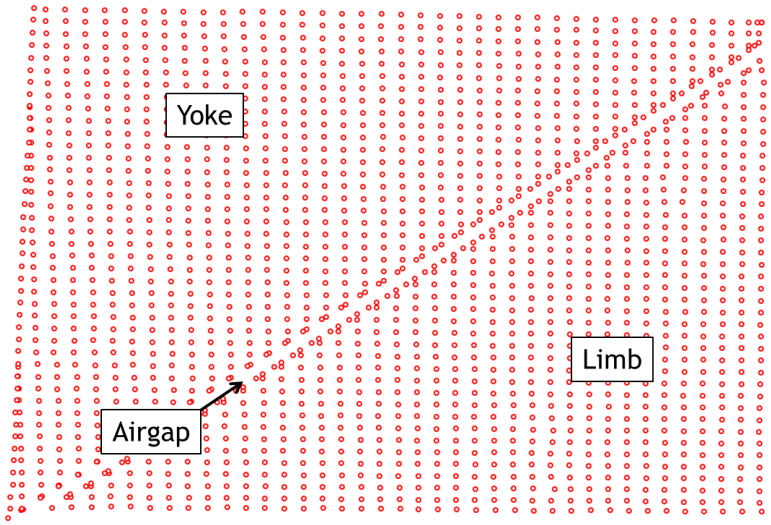

Fig 5-8 Scan points on the mitred corner joint

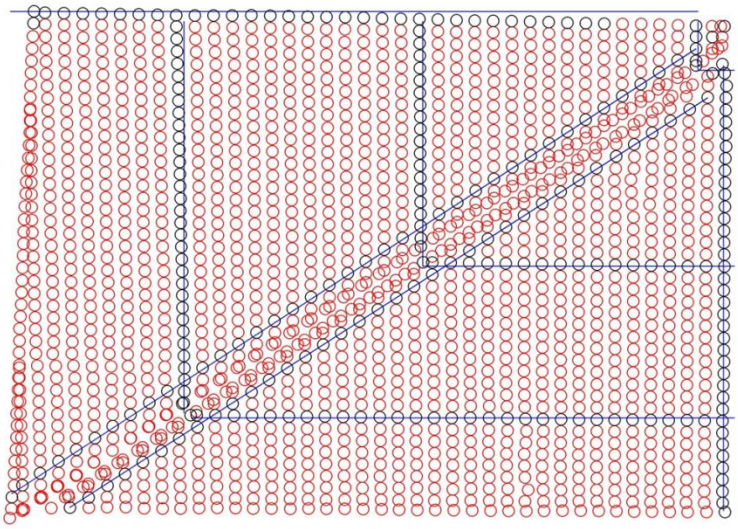

Fig 5-9 The scan points marked in black (along the blue lines) are selected to be analysed

Each scan point contains the waveform of the velocity at that point which was sampled at 25kHz. Each velocity waveform was integrated and differentiated numerically to calculate the vibration displacement and the acceleration of that point. The integral of the waveforms were calculated using the cumulative trapezoidal numerical integration algorithm in MATLAB after taking the DC component off the waveforms using a high-pass filter. The passband frequency was considered to be 30 Hz. The differentiation process was not straightforward because of the noise in the waveforms. Curve fitting toolbox of MATLAB was used in order to fit an analytical function on the velocity waveforms. Differentiating the analytical functions instead of the numerical waveforms would help to get rid of the notoriously unreliable spikes in the differentiated waveforms. As the velocity waveforms were sinusoidal, the Sum of Sine model with 8 sums as shown in equation (5-4) was used to make a sufficiently fit equation.

$$y=a_1\sin(b_1x+c_1)+ \ldots + a_8\sin(b_8x+c_8) \quad \textbf{(5-4)}$$

The maximum root mean square error (Standard Error) of the fit of all points was just 0.002 which shows a very good fit on all waveforms. The differentiation of the fitted functions was then calculated as the acceleration waveform. A fast Fourier transformer of the acceleration, velocity and displacement waveforms was then calculated for frequency studies.

5.3 The relationship between the vibration and acoustic noise

Sound waves are generated when a vibrating structure causes the surrounding medium to vibrate. Transformer cores are built up of laminations which are vibrated due to several exerted forces. The vibration of these laminations is translated in sound by vibrating the air. The laminated structure of the transformer cores is a very complicated system to be analysed analytically. Instead, to understand the behaviour of this system, the vibration of a plate is introduced and discussed here.

Equation (5-5) describes z-deflections of a plane which is bounded by the planes $z = \pm\frac{h}{2}$ where the h is the thickness:

$$D\nabla^4 W + \rho h W_{tt} = q \tag{5-5}$$

where ρ is the density of the plate, q is the exciting source and expressed in Pascal, $W = W(x, y, t)$ is the z deflection of the plate and D is defined as follows:

$$D = \frac{Yh^3}{12(1 - v^2)} \tag{5-6}$$

In which Y and v are the Young's modulus and the Poisson ratio of the plate respectively. Using the separation of variables technique the analytical homogenous solution for $W(x, y, t)$ is presented in [104] that $W(x, y, t)$ is consider as follows:

$$W(x, y, t) = \phi(x)\psi(y)T(t) \tag{5-7}$$

Knowing that equation (5-7) satisfies equation (5-5) and assuming that q and $T(t)$ are series of sine waves we would have:

$$\nabla^4[\phi(x)\psi(y)]T(t) - \rho h\omega^2\phi(x)\psi(y)T(t) = q \tag{5-8}$$

which, states that the vibration frequencies would be equal to the frequency of exciting source. It should be noted that q in equation (5-5) is expressed in Pascals, therefore it is a type of force. The exciting source frequency in a transformer core is double of the magnetising source frequency because the exerted pressure on the laminations emerges twice in a magnetising cycle.

Vibrating the plate generates acceleration forces acting on the air. Therefore the surface acceleration of the plate acts as a source for acoustic radiation. Equation (5-9) [105] describes the sound pressure wave in lossless medium as follow:

$$\frac{1}{\rho c^2}\frac{\partial^2 P}{\partial t^2} + \nabla.\left(\frac{-1}{\rho}(\nabla P - \rho W_{tt})\right) = 0 \tag{5-9}$$

Where, c is the sound speed, $P(x, y, t)$ is the sound pressure and $W_{tt}$is the vibration acceleration of the plate which is substituted as the sound source. Like (5-5), this equation is a wave equation which can be solved by the separation of variables technique. Like vibration, it is expected that the acoustic noise frequency content matches with the vibration acceleration frequencies.

In this research the surface vibration velocity of the transformer cores will be measured with a laser scan vibrometer and the expected emitted noise would be a function of vibration acceleration.

6 Computer model of flux distribution in core joint

In this research, Finite Element Modelling (FEM) was used in order to understand the flux distribution in the joints of transformer cores and the related Maxwell forces on the laminations. These models are not exact simulations of a mitred joint due to the lack of information about the electrical steel permeability in heavily saturated regions but they greatly aid understanding of the flux distribution around the joints and the forces generated. In this chapter the specifications and the geometry of the developed COMSOL model will be discussed in detail.

6.1 FEM theory

The concept of FEM firstly was proposed in the field of structural mechanics in 1956 by the emergence of computers [106]. Nowadays, FEM has become the most popular method for analysing different structures in engineering. Any engineering phenomena can be described by governing equations (which are usually differential equations) and boundary conditions. FEM approximates the governing equations and boundary conditions with a set of simultaneous algebraic equations:

(Behaviour)= (Properties) (Action source) (6-1)

For an electromagnetic study, the (Behaviour), (Properties) and (Action source) matrices can be filled by magnetic induction, permeability and the magnetic field respectively. Making the algebraic equations for the entire domain of a structure is extremely difficult, so the structure is divided into a number of small elements. These elements are connected at nodes. By putting all the element equations together and solving them, the unknown variables at nodes can be obtained explicitly. The field quantity is then interpolated by a polynomial over an element at non-nodal points.

6.2 Electromagnetics modelling

COMSOL, like all magnetic FE packages, uses the equations which are listed in Table 6-1.

Table 6-1 Sets of equations which COMSOL uses to solve the electromagnetic problems

	Maxwell Equations		
1	Gauss's law	$\nabla.\vec{D} = \rho_f$	Any free charge (ρ_f) is accompanied by a divergence of electric field displacement (D).
2	Gauss's law for magnetism	$\nabla.\vec{B} = 0$	The magnetic field (B) has divergence equal to zero.
3	Maxwell-Ampere law	$\nabla \times \vec{H} = \vec{J} + \frac{\partial \vec{D}}{\partial t}$	Currents, either current density (J) or some displacement current is going to be accompanied by rotation of magnetic field(H).
4	Faraday's law	$\nabla \times \vec{E} = \frac{-\partial \vec{B}}{\partial t}$	Time varying magnetic field (B) is always accompanied by a spatially-varying electric field (E).
5	continuity equation	$\nabla.\vec{J} = \frac{-\partial \rho_f}{\partial t}$	Any divergence of the current density (J) must be accompanied by increasing the free charge (ρ_f) in that point in space.
	Constitutive Relations		
6	Electric field	$\vec{E} = \frac{\vec{D}}{\epsilon_0 \epsilon_r}$	Relationship between electric field (E) and electric displacement (D) where $\epsilon_0 = 8.854 \times 10^{-12}\ \mathrm{F}.m^{-1}$.
7	Magnetic field	$\vec{H} = \frac{\vec{B}}{\mu_0 \mu_r}$	Relationship between magnetic field (H) and the magnetic flux density (B) where $\mu_0 = 4\pi \times 10^{-7}$.
8	Ohm's law	$\vec{J} = \sigma \vec{E}$	Describes the current reaction in the presence of an electric field where σ is electric conductivity.
	Auxiliary Equations		
9	Electric potential	$\vec{E} = -\nabla \vec{V} - \frac{\partial \vec{A}}{\partial t}$	A is known as magnetic vector potential
10	Magnetic potential (Vector)	$\vec{B} = \nabla \times \vec{A}$	A is known as magnetic vector potential

If the Maxwell-Ampere law in tier 3 is taken and rewritten as the following:

$$\nabla \times \vec{H} = \vec{J_i} + \vec{J_e} + \frac{\partial \vec{D}}{\partial t} \quad (6\text{-}2)$$

In which J in tier 3 of the Table 6-1 is divided into two components. J_i is the current density which is induced by changing magnetic fields and J_e is the externally generated current.

If constitutive relations from tier 6 to tier 8 are substituted in the above equation, the following equation would be obtained:

$$\nabla \times (\mu^{-1}\vec{B}) = \sigma\vec{E} + \vec{J_e} + \partial(\frac{\epsilon\vec{E}}{\partial t}) \quad (6\text{-}3)$$

If tier 9 and tier 10 equations were substituted in the above equation, the following expression would be obtained:

$$\nabla \times \left(\mu^{-1}\nabla \times \vec{A}\right) = -\sigma(\frac{\partial \vec{A}}{\partial t}) + \vec{J_e} + \epsilon(\frac{\partial^2 \vec{A}}{\partial t^2}) \quad (6\text{-}4)$$

Recursively, all the other parameters can be calculated once the A value is calculated. For stationary studies – which were used in this research – if time variation of A was assumed to be zero then the above expression would be simplified as the following:

$$\nabla \times \left(\mu^{-1}\nabla \times \vec{A}\right) = \vec{J_e} \quad (6\text{-}5)$$

6.3 Model Creation

6.3.1 Geometry

The geometry of the core was drawn in COMSOL in 2D as shown in Fig 6-1. A uniform flux distribution and closed flux path was required in the test zone. In order to minimize the number of finite elements a solid yoke was attached to the test zone to close the magnetic path. The model was designed parametrically to allow any changes in length of study region and the solid yoke length. This was essential to establish a uniform flux distribution in the core. Also the airgap length, interlaminar gap and the overlap length was variable. Magnetizing coils were placed on both sides of the studied region to help the uniformity of the flux in this region. The coils were driven by the current density which was input manually by the user. All the parameters which were defined in the model and their values are listed in table 1.

Table 6-2 The COMSOL model parameters

Parameter name	Value	Description
Sheet_thickness	0.35 mm	The thickness of the lamination in the model
Number_layers	9	The number of layers in the model
Gap	1 mm	The longitudinal gap in the linear joint region
InsualtionGap	16 μm	The interlaminar gap between the lamination across the height of core.
LimbLength	150 mm	The length of the left and the right arm of the core in the model.
YokeLength	200 mm	The length of the top and the bottom arm of the core in the model.
TestZone	130 mm	The length of the laminated part of the magnetic circuit
Coil_width	190 mm	This was assumed to be 95% of the length of the Yoke. The height of the coil was considered to be 1 mm in all the coils.
CurrentDensity	2.65e6 Am^{-2}	For GO at 1.6 T. The value of the current density changes for each material in various induction levels.
Overlap	5 mm	The overlap length in the jointed region which is measured from the edges of two adjacent laminations in the jointed region.

In order to avoid sharp edges and subsequently less triangular elements a circular boundary was used to model the environment. The centre of the circle was set to be on the centre of the solid yoke and the radius was set to be 160 mm.

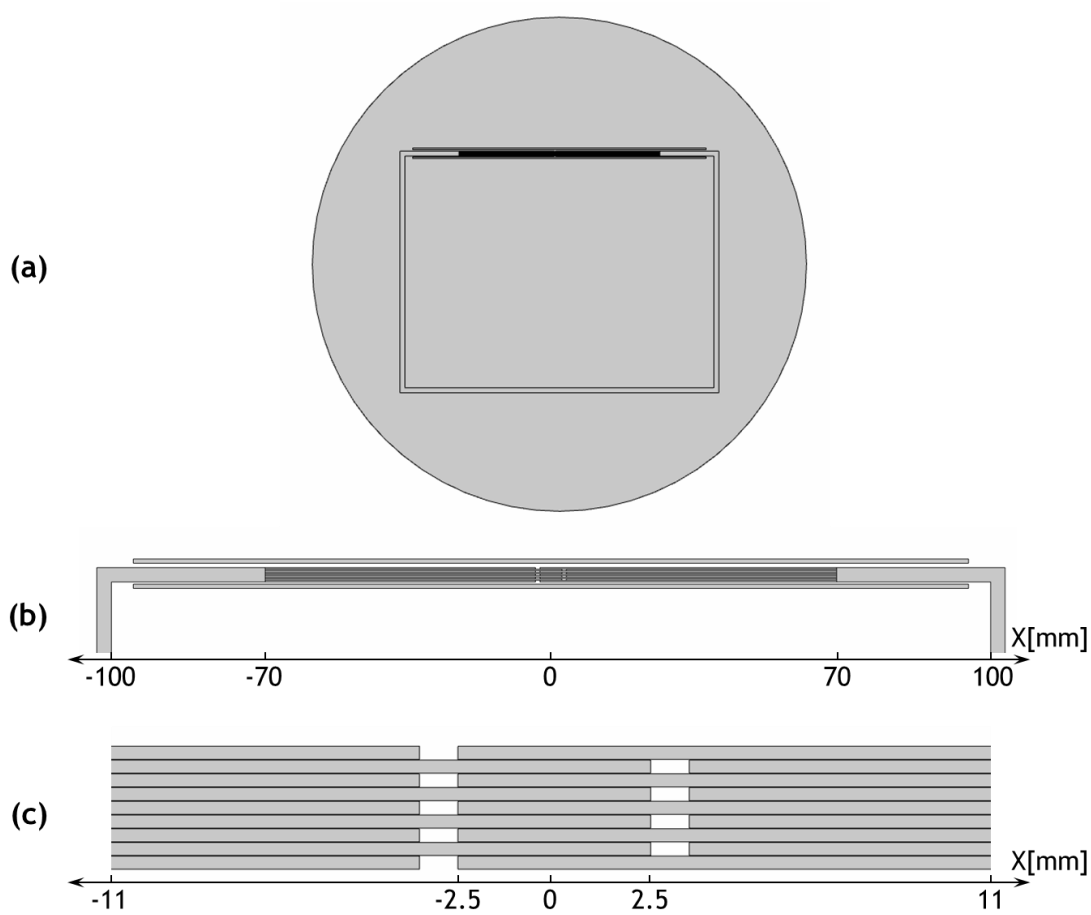

Fig 6-1. Schematic diagram of the linear joint modelled in COMSOL. (a) The modelled geometry including the circular environment and the square shape magnetic circuit. (b) The top arm including the laminated part. (c) The test zone including the linear joint with the airgap length of 1 mm

6.3.2 Material properties

Three materials were involved in this model; air, copper and electrical steel. Built-in materials for the air and the copper were used. For electrical steel the properties of the material were defined. In COMSOL, the non-linear magnetic material can be implemented either with an analytic expression for the relationship between the B and the H fields, or with the help of a lookup table. If a look-up table is used, there is an option to choose the interpolation method. If linear interpolation and extrapolation method are chosen, then out-of-range values are calculated using the entered data. The properties of non-oriented and grain oriented electrical steels; which were measured and presented in chapter 4.3, were entered into the model. The four last points which were beyond the saturation point were calculated manually considering that the slope of the curve should be equal to $\mu_0 = 4\pi \times 10^{-7}$ H.m^{-1} in this region.

6.3.3 Boundary conditions

Since the whole core is modelled, the magnetic insulation boundary condition is used on the outer boundaries of the air box. This boundary condition specifies the magnetic field to be contained within the model, thus the normal component of the flux on the boundary is zero. An initial value which applied to the outer boundary of the model and contained the magnetic vector potential was set to zero.

6.3.4 Meshing and solving

The mesh of the test zone was problematic because of the long thin spaces between the laminations. The interlaminar gap between the laminations was around 16 μm. In this narrow region and in the vicinity of the airgaps at the edge of the laminations the flux density variation was very high. Therefore to minimize the error, the resolution of the mesh in these narrow regions should be at least three elements. Considering that the elements maximum growth rate (the maximum rate at which the element size can grow from a region with small elements to a region with larger elements) is 1.3, this is a compromise between the number of elements and the run time. In the other parts of the model (including the yoke, copper and the air box), where the flux density variations are less, a coarser mesh with the minimum and average element quality of 0.46 and 0.93 respectively. The mesh element quality is a dimensionless quality between 0 and 1, where 1 represent a perfectly regular element in the chosen quality measure, and 0 represents a degenerated element [107]. Total numbers of elements are more than 600 thousand. Typical solving time of the problem is less than 24 hours with a quad core Xeon processor and 64 GB of DDR2 ram.

6.3.5 Post processing

The visualization of flux distribution facilitates a simple visual verification of the solution. In order to compare the results with the empirical measurements three cutlines were defined as described in Fig 6-2 to export the variables' values.

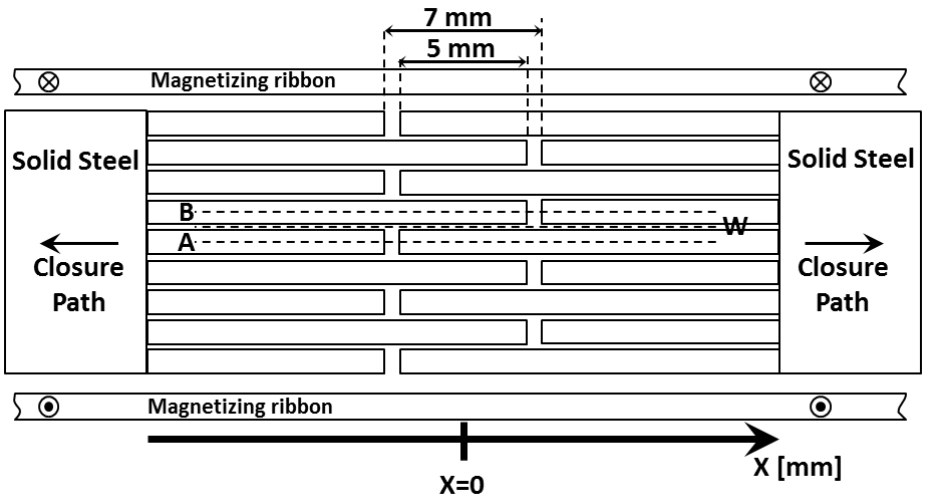

Fig 6-2 Schematic diagram of the computational model in COMSOL including three cutline A, B and W which are used to read the flux density of lamination 5, 6 and the interlaminar airgap respectively

It is feasible to apply a modifying function to flux values at each point. In order to study the effect of core height on flux distribution the logarithmic function was used to highlight some specific flux levels in the core. In Fig 6-3, as an example, the logarithmic function is applied to the linear function y=x twice. As can be seen, the point x=1 is marked as the least point. Any point can be marked by this function with a shift in the function's arguments. The logarithmic function was applied twice on the flux density norm distribution to study the effect of the height of the stack on flux distribution.

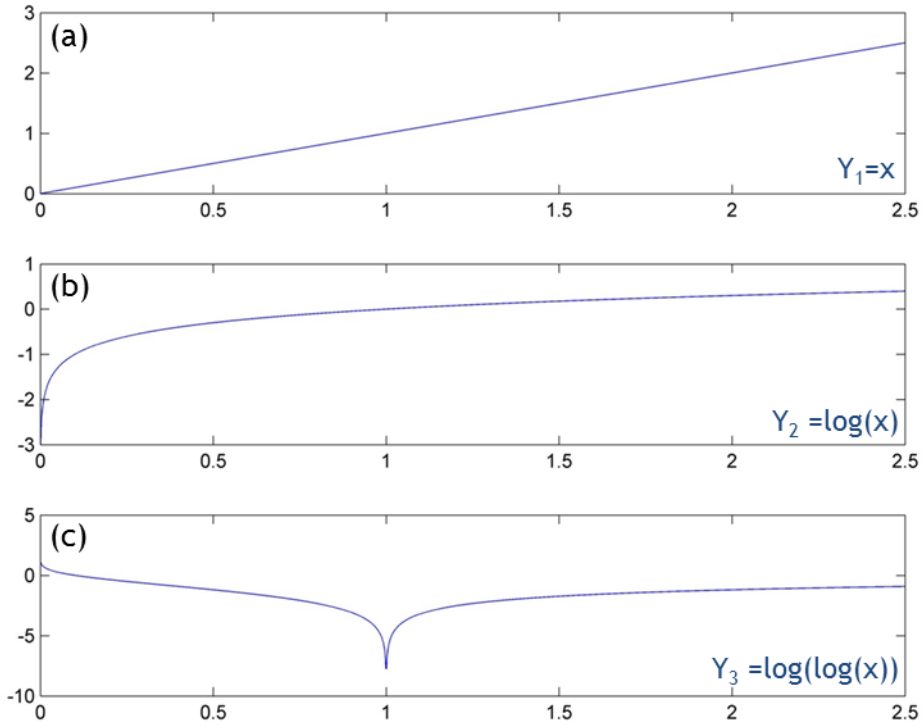

Fig 6-3 The effect of using logarithmic function recursively on the linear function y=x

The built-in force calculation feature in COMSOL will not deliver correct values in this model because the target object (in this case lamination) must be completely surrounded by air. Therefore, the pressure on the boundaries was calculated manually using the Maxwell stress tensor. COMSOL defines a value for the stress on either side of each boundary in two different materials. Each boundary has a normal vector associated with it. The *down()* operator gives the value of the variables on the side of the boundary opposite to the normal vector and the *up()* operator gives values of the variables on the side of the boundary in the direction of the normal vector. The signed net force would be the difference between the two. Subtracting the variables extracted by the *up()* operator from those extracted by the *down()* operator will give the value of the force in the direction of the COMSOL normal vector. The directions of the normal vectors on the laminations in the model are shown in Fig 6-4. In this research, the Maxwell upward magnetic surface stress tensor y-component is subtracted from the Maxwell downward magnetic surface stress y-component in order to calculate the pressure in the y-direction in the direction of the normal vectors.

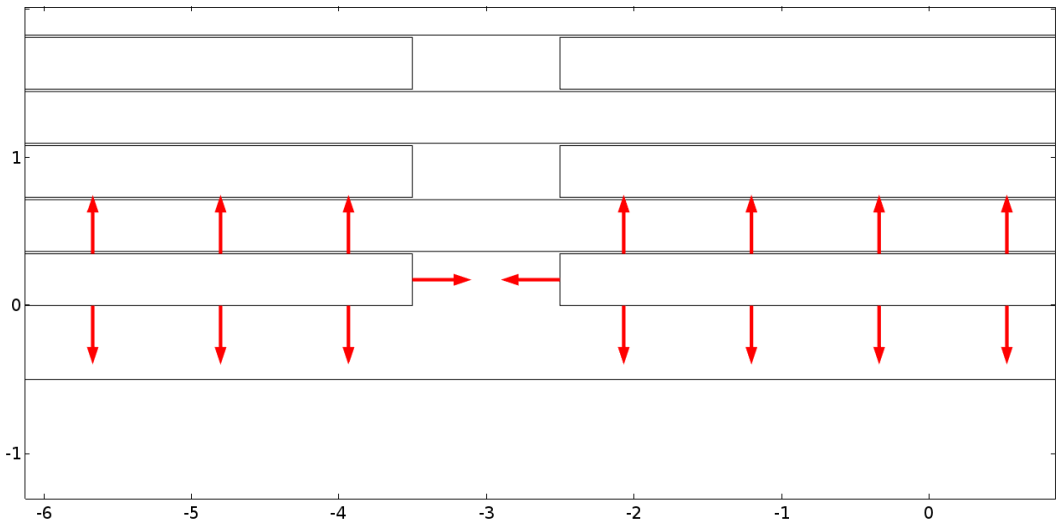

Fig 6-4 Normal to the surface vectors for the first layer. All the dimensions are in mm

6.4 Studying the minimum limb length necessary for studying true flux distribution in the assembly with central limb joint

In order to carry out accurate measurements of the effect of the air gap, overlap length and joint geometry (such as stepped or double layer assemblies) the flux entering the region affected by the joint must be uniform. The length of the non-uniform flux region (measured from the outer edge of a corner joint) depends on the material permeability, the type of joint, the induction level and how close the overall induction in the core is to saturation point.

The minimum length of limb to test the effect, ensuring that the flux distribution approaching the central joint region is not affected by the outer corners, was evaluated with the aid of the COMSOL software. The basic geometry shown in Fig. 6.1 and discussed in chapter 6.3.1 was used with various nominal flux densities from 0.4 T to 1.7 T for the two materials. The flux distribution along the limb in each case was calculated. The model shown in Fig 6-1 was used with a laminated part length of 150 mm (measured from the centre of the overlap) on each side of the gap.

The flux distribution in all nine layers along the core at 5 mm intervals was obtained at inductions from 0.4 T to 1.7 T (DC simulation) and the flux distribution in all nine layers along the core at the intervals of 5 mm was

recorded. An algorithm was developed in MATLAB to scan the recorded data in order to find a specific uniformity pattern as follows.

1- Run the model for 0.4 T.

2- Record the |B| profile value along each lamination (from 0 mm to 140 mm)

3- Extract the |B| values from the above |B| curves from x=0 to x=140 mm in the intervals of 5 mm so at each interval there would be 9 values of B associated to 9 layers:

$$\{B_{ij} \,|\, i = 1{:}9\ layers,\ j = 0{:}5{:}140\, mm\} \qquad (6\text{-}6)$$

4- Calculate the standard deviation S_d and the mean of the above B_{ij} s in each interval. To calculate the uniformity percentage of the flux in each interval, use equation (6-6):

$$\%\, Uniformity_j = \left(1 - \frac{Sd_j}{\overline{B}_j}\right) \times 100, \quad j = 0{:}5{:}140 \qquad (6\text{-}7)$$

5- Start to scan the $\overline{B}_j$ s from x=0 mm to find a slice with a length of 10 mm (3 consecutive) such that the first and last $\overline{B}_j$ s differ by less than 0.5% of the nominal B value of the core and the corresponding uniformity index is more than 99%. The first $\overline{B}_j$ position indicates the minimum required length of jointed limb to have a uniform length of 10 mm with a variation of 0.5% and uniformity of 99% at the induction level of 0.4 T.

6- Redo from row 5 for the length of 20, 30, 40, and 50 mm.

7- Redo the evaluations from row 2 by adding 0.1 T to the previous induction level (Step two should be 0.5 T).

The above algorithm was run for both NO and GO materials.

6.5 Structural mechanics modelling

In order to calculate the deformation of the laminations due to the Maxwell stress tensor, a Solid Mechanics study node was added to the current magnetic model. The Solid Mechanics model was solved for the laminated part of the model. The ends of the laminations which are attached to the solid part of the model were fixed by applying the Fixed Constraint boundary condition. The Boundary Load condition, in which the source was set to the Maxwell surface stress tensor, was applied to all the laminated parts. The Young's modulus and the Poission's ratio of the electrical steel were considered as 207.5 MPa and 0.21 [108] respectively. The model then computed the force and deformation due to the flux distribution.

6.6 Modelling Assumptions

This section provides the list of assumptions which were made in modelling the transformer joints. There is always a compromise between taking everything into account and the computational cost of the process. In the model which is developed here, the model is kept as simple and representative as possible while the computational cost is optimum. Some of the assumptions and simplifications in the model are listed here:

1- The model was built in 2D instead of 3D. So the effect of the triangular airgap regions on the flux distribution in the inner corner of the joints has been neglected. In comparison to the limb and yoke dimensions, these regions are relatively big in model transformer cores but in real cores their effect is less important. Although modelling the joints in 2D will ignore the transverse flux in the mitred joint but this flux is not involved in generating vibration and would not influence the results of the modelling.

2- The anisotropy of the magnetic and elastic properties of electrical steel has not been considered in the model. The magnetic properties in the transverse direction are available but in the normal direction are not measured, thus the magnetic properties of the material were considered as isotropic. The relative permeability of the electrical steel at the working point of the core is usually around 5000 to 6000 depending on the induction level. Due to the cubic crystalline structure of the electrical steel, it is believed that the permeability in the normal direction is similar to the permeability in the transverse direction. The permeability in the transverse (and normal) direction is 20 times smaller than the permeably in rolling

direction at 1.5 T and becomes closer as the induction increases. Comparing the reluctance of the electrical steel with the normal to the plane permeability and the reluctance of the interlaminar airgap reveals that the interlaminar airgap is much more dominant than the anisotropy in dictating the flux path.

3- A uniform texture was assumed for the GO material. No domains or grains were assumed and therefore the effect of misoriented grains was neglected. Despite of this assumption, it is believed that any change in the flux distribution due to any grain disorientation would be local and would not affect the overall flux distribution in the core.

4- The effect of magnetostriction of the electrical steel on flux distribution and vibration is neglected in the model. In small model transformer cores, the change of the length of the laminations is negligible in compare to the longitudinal airgap length. The effect of magnetostriction on flux distribution when the core limbs are long and the airgaps are small becomes important.

5- The magnetic characteristics of the electrical steel in heavily saturated regions is still unknown. The measured permeability and B-H curve values for NO and GO are available up to 1.7 T and 1.95 T respectively. Therefore, in general, the B-H characteristics of the electrical steels in saturated regions were extrapolated / estimated. Since the rate of change is unknown, there are some uncertainties involved with the results.

7 Analysis and discussion of flux distribution and vibration results

The results in this chapter will be presented from the simplest tested geometry to the most complicated ones. Since all the linear joints were implemented in an Epstein frame arm, it was crucial to understand the flux distribution in the intact Epstein frame before introducing the joints. Therefore, the initial step was to study the flux density distribution in the butt-lap Epstein limb. Knowing the flux distribution in an intact limb would help to distinguish the joint effects from the intrinsic geometry effects. Secondly, the linear joints were introduced to the arm of the Epstein frame and the resultant flux distribution was investigated. In section 7.1 , the results of the simulations with COMSOL are also presented and compared with the ones which were measured practically. Thirdly, an algorithm was introduced to calculate the minimum limb length necessary to keep the geometry intrinsic effects separate from the joints effects on flux distribution in a linear joint. Till this point, the flux density distribution in linear joints has been characterised by empirical and analytical approaches.

In section 7.4, the flux distribution in a mitred joint with the same thickness as the linear joint is investigated to understand the effect of the 45^{o} cut on the flux distribution in the joint; especially across the laminations. The configurations to this point are composed of just nine layers. To be representative of real cores, in the section 7.5, configurations with a higher number of laminations were investigated both empirically and analytically. Due to the geometrical limitations of Epstein frame, these tests were not conducted on linear joints. Knowing the flux distribution across the lamination in each layer and across the stack of the core, in addition to detailed knowledge of the flux distribution in the vicinity of the joints, gives a good understanding of the flux distribution in mitred joints.

The linear model was used in sections 7.7 and 7.8 to estimate the Maxwell force distribution across the core and to quantify the laminations' deformation in the

vicinity of the joints. In section eight, the vibration results from the core which was used to study the flux density distribution are presented.

Knowing the detailed flux density distribution in a mitred joint and having a good estimation of the exerted force on the laminations in the jointed region along with the real measurements in a mitred joint provide sufficient information to explain the core vibration in the mitred joint. In section 7.9, a whole scan of a production core is provided to compare the results and discuss other factors that affect the core vibration.

7.1 Flux density distribution in butt-lap Epstein limb

The first step of understanding the flux distribution in the mitred joint is to study the flux distribution in a linear joint. In this research, linear joints are implemented in a limb of an Epstein frame; therefore, it is essential to measure the flux distribution in the limb before introducing the joints so the effect of the corner joints of the Epstein frame would be distinguishable from the effect of linear joints at the centre of the limb. The flux distribution in a limb of an Epstein frame assembled from NO and GO materials will be studied in a range of overall flux densities varying from 0.5 T to 1.6 T using search coils. The geometry of the core and the arrangement of the search coils are fully described in chapter 4.4.

Flux distributions in the vicinity of butt-lap corner joints are shown schematically in Fig 7-1. For clarity, only three layers of laminations (L4, L5 and L6) are shown and it is assumed that no fringing flux is present.

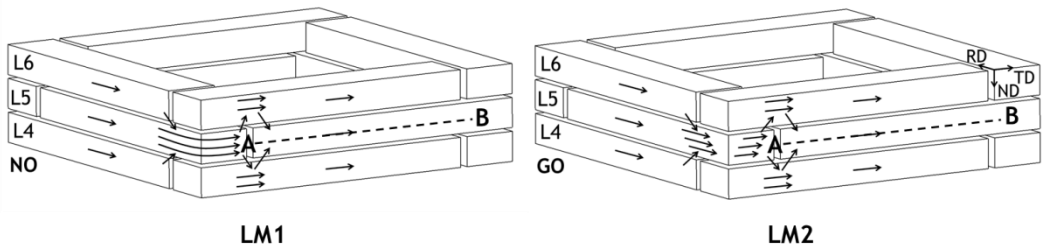

Fig 7-1 Flux paths in layers of a butt-lap corner joint assembled from isotropic NO electrical steel in LM1 and GO steel laminations cut parallel to the RD in LM1-GO. (Arrowed lines represent approximate magnitude and direction of local flux). Just layers 4 to 6 are shown out of 9 layers in the assembly

In the isotropic joint assembled from NO steel, the flux rotates in the plane of the laminations in the corner region, following the path of least reluctance partially

passing through the short in-plane air gaps between pairs of adjacent in-plane laminations, and partially passing through the top and bottom laminations which are shunting the airgaps.

However, the large anisotropy of GO steel, forces the flux to remain along the RD (rolling direction) in the plane of the laminations. In strip L6 the flux density decreases linearly toward the joint, rotates by 90° in the longitudinal gaps and increases linearly along the line AB in layer L5.

The flux density distribution along line AB of the LM1 and LM1-GO linear models in different flux densities are shown in Fig 7-2 and Fig 7-3 respectively.

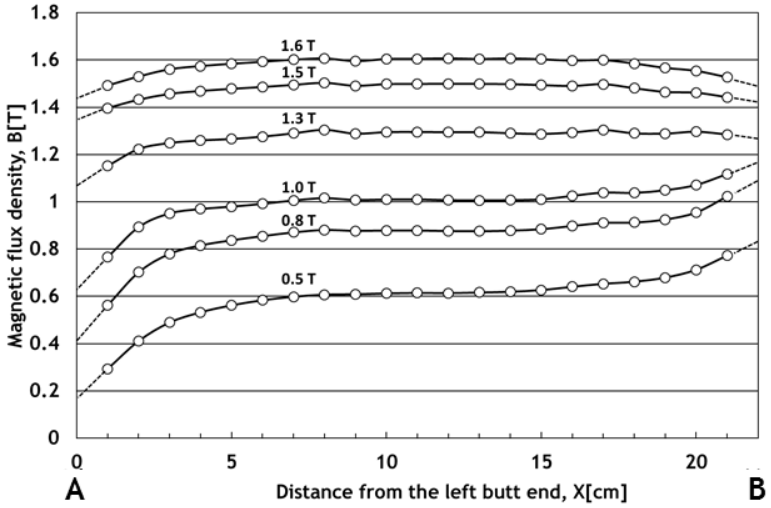

Fig 7-2 Longitudinal flux density distribution along line AB in NO electrical steel. The nominal flux density in the core is written above each curve

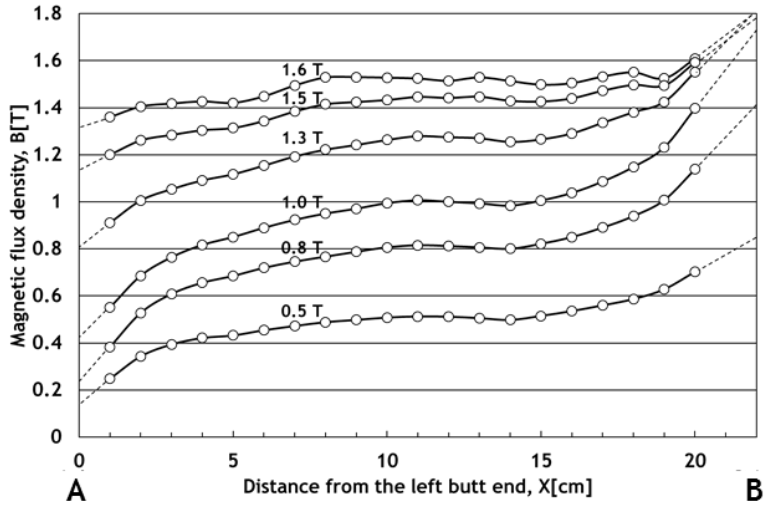

Fig 7-3 Longitudinal flux density distribution along line AB in GO electrical steel. The nominal flux density in the core is written above each curve

The results from LM1-NO, assembled from NO electrical steel, shows that the flux density at point A is less than the nominal flux density in the core. This is the effect of the airgap between two strips of steel in the layer. The magnitude of the flux at the edges of the strips are extrapolated using the next two search coils' data and are shown with dotted lines. It is observed that the flux becomes uniform 6-7 cm away from the butt joint independent of the core induction level.

At point B of the lamination the flux density increases at lower inductions because strip 5 is the shunting strip of the airgaps in layer 4 and layer 6 in point B. So it is expected that it should carry the adjacent laminations flux in gap regions. In contrary, at higher induction levels (more than 1.3 T), the flux around the gap bridging region is slightly less than the overall flux density in the core. This is due to the excess fringing flux at higher inductions in NO assembly. The permeability of the NO at higher induction level drops significantly, therefore the flux closes itself through the shortest path in the air as shown in Fig 7-4.

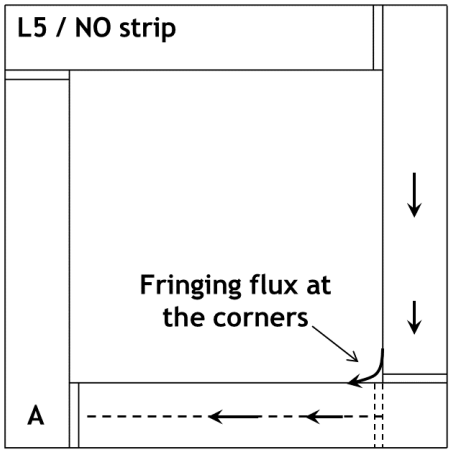

Fig 7-4 Top view of the layer 5 of the Epstein frame (shown in Fig 7-1) showing the schematic diagrams of the fringing flux path when the frame is assembled from NO steel and magnetised at B≥1.3 T

As seen in the results of the GO assembly, the amount of the flux at point A (X=0) is less than that which was measured in the NO assembly in the same point. In the GO assembly, the length of the non-uniform region varies from 7-9 cm around point A at the left end butt joint. The length of 8-9 cm was already reported in [82] which was measured in a larger model with 920 mm × 150 mm × 0.33 mm laminations.

The length in which the flux is uniform in the lamination reduces as the induction level in the core increases. In contrast to the NO assembly, the flux density at

point B of the GO assembly increases independently of the induction level in the core which means there is less fringing flux around the butt-joint due to the high permeability of the GO steel. The flux density level in the lamination increases monotonically from point A to point B in lower induction levels, but at higher inductions ($B \geq 1.5\,T$) the flux density along the lamination varies unpredictably.

The large variations at 1.60 T in GO are likely to be due to textural variations in the very large grains (approximately 20 mm diameter) of the GO material. Those grains which are larger than the others are more aligned in the rolling direction of the electrical steel and provide a high permeability medium. The flux takes a path with the highest permeability, so the flux tends to avoid smaller misaligned grains passing through the interlaminar airgap and continuing through adjacent laminations. Even if the permeability of the adjacent layers at some points becomes equal to the current layer the anisotropy of the material does not allow the flux to return back to its original layer unless the flux faces another misaligned grain which forces it to return.

The non-uniformity of the flux density with no central limb gap can be attributed to the effect of the flux transfer through the butt-lap joints at the corners of the square. It is well known that within the corners the flux is highly non-uniform [82] but the non-uniformity will tend to be continued outside the joint. Although not directly referred to in [82], it is shown that the flux does not become uniform, to within 2% of the nominal value at 1.5 T, in GO until 80 mm from the edge of the joint. No corresponding data could be found for NO steel.

This infers that when a centre gap is introduced the outer corners affect the flux distribution in the gap region unless the limb is sufficiently long to enable flux transfer to be completed before the uniform flux region.

7.2 Flux density distribution in linear joint

In this section the flux distribution of linear joints with length 1 mm and overlap 5 mm, which were implemented at the centre of the NO and GO Epstein assemblies, are investigated using arrays of search coils. The results are further investigated by analytical solutions in COMSOL software.

7.2.1 Empirical results of the flux density distribution in the rolling direction at the vicinity of the linear joint measured in the limb of an Epstein frame

Fig 7-5 shows the flux density variations along layer 5 and layer 6 in the rolling direction in linear model LM2-NO magnetised at 1.60 T.

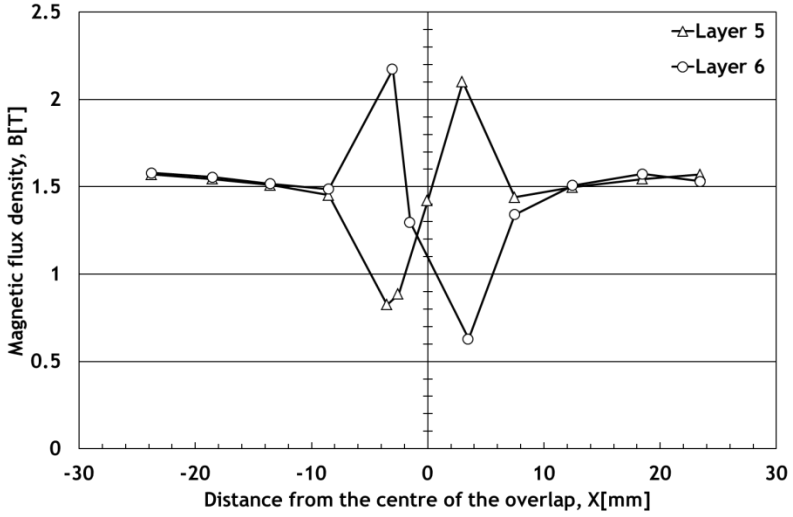

Fig 7-5 Longitudinal flux density in linear joint LM2-NO assembled from NO electrical steel at overall flux density 1.60 T 50 Hz. The airgap and the overlap length were 1 mm and 5 mm respectively (Model LM2-NO)

The flux in the rolling direction is equally distributed between the two vertically adjacent layers at 1.6 T. As the flux approaches the airgap region, the reluctance of the magnetic circuit increases on line B, due to the low permeability of the air. The flux deviates from the rolling direction on line B and crosses the interlaminar airgap between the laminations and enters the adjacent lamination. The magnitude and the location of the flux transfer greatly depend on the relative permeability of the steel on each path. In NO steel, by transferring the flux from layer 6 to layer 5, the relative permeability of the steel on layer 5 will drop. The relative permeability of the NO steel when it is heavily loaded with the flux (the permeability above 1.6 T is less than 273) is 30 times less than its maximum permeability. Therefore, the flux tends to stay in layer 6 until close to the airgap. Beyond this point, the reluctance of the shunting lamination reduces relative to the path containing the airgap so the majority of the flux takes this path and the flux density of this region of steel reaches 2.17 T. The flux density could not be measured in the airgap due to technical limitations but the flux at the edge of the laminations next to the airgap is 0.82 T. It is clear that the airgap flux is lower than this value.

Fig 7-6 shows the flux density distribution in LM2-GO which was assembled from GO electrical steel and magnetised at 1.60 T. Unlike the NO steel assembly, the flux is not equally distributed between the strips in vertically adjacent layers which is the effect of the corner joints of the Epstein frame as discussed in section 7.1. The interlaminar flux transfer is both gradual and continual over a large region. According to the curves shown in Fig 4-5, the relative permeability of the GO steel is 30050 at 1.6 T. In contrast with NO, even if the adjacent layer is driven to 1.8 T, the relative permeability of the layer would be about 7000 so the flux in the GO material does not tend to return to the current layer leading to the non-uniformity.

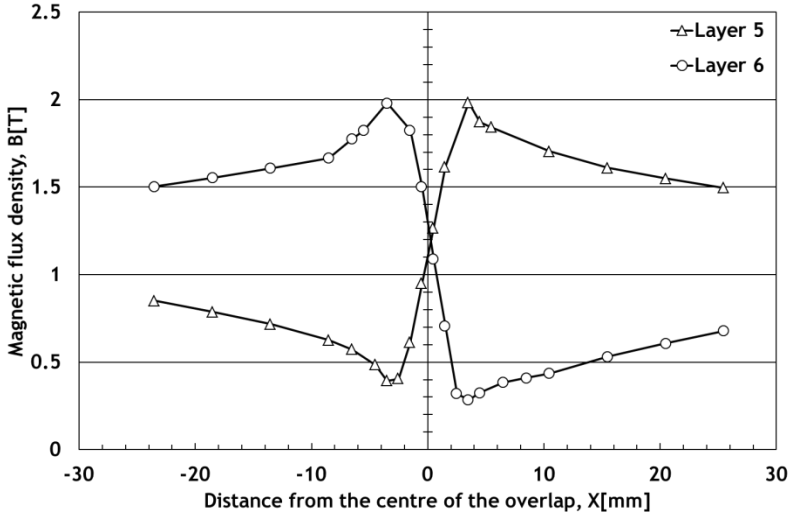

Fig 7-6 Longitudinal flux density in linear joint assembled from GO electrical steel at overall flux density 1.60 T 50 Hz. The airgap and the overlap length were 1 mm and 5 mm respectively (Model LM2-GO)

In Fig 7-6 the flux densities in the vicinity of the airgaps on layer 5 and 6 were measured to be 0.39 T and 0.28 T respectively while the gap bridge flux densities were 1.98 T on both lines. No search coils were installed on X=0 mm but the flux density curves of each layer cross each other at 1.40 T, which means that there is a fringing flux equal to 0.2 T that closes its path through the air at the vicinity of the joint.

The most critical regions of the joints are the gap bridges due to their tendency to saturate. Fig 7-7 shows the longitudinal flux density in the gap bridges in each layer of LM2-NO at 1.6 T. As illustrated, the maximum measured flux density in this region in any layer does not exceed 2.24 T. The measured flux in layer 1 is much less than expected which might be due to the defect in the associated search coil or a very small movement of the bottom layer during the arm insertion

in the Epstein frame. The excess flux density of the gap bridge in layer 2 is due to the defect in layer 1. The average gap bridge flux density in the nine layers is 2.07 T which is slightly higher than the associated saturation induction of the electrical steel. The flux fluctuations in GO material were observed to be higher than in NO therefore more search coils were installed in the GO assembly.

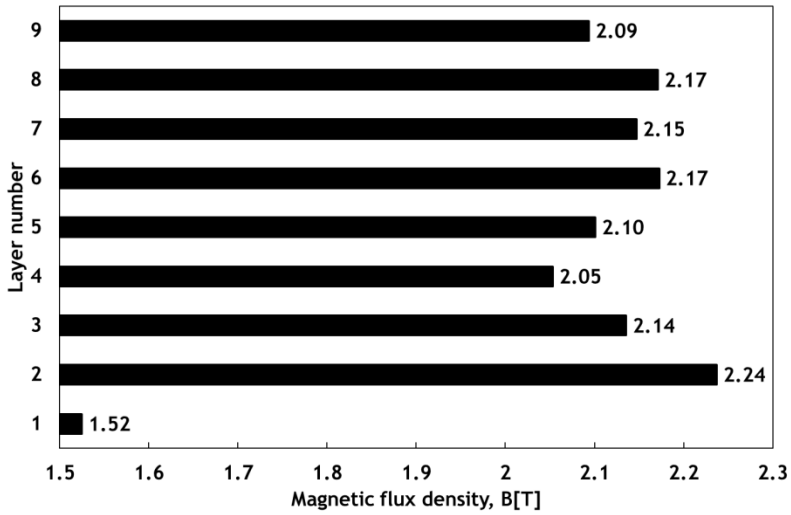

Fig 7-7 Longitudinal magnetic flux density at the gap bridges in each layer of linear joint assembled from NO electrical steel (Model LM2-NO) at overall flux density 1.6 T, 50 Hz

7.2.2 Theoretical results of the flux density distribution in the rolling direction at the vicinity of the linear joint calculated in COMSOL

The flux density distribution in the vicinity of the linear joint is theoretically calculated using the model described in chapter 6. The calculated flux density distribution at an overall flux density of 1.0 T and 1.6 T for NO and GO materials are shown in Fig 7-8. Comparing the experimental results with simulated results on layer 5 along line AB reveals that the measured flux density values for $x<0$ in both materials are significantly lower than the simulations. In the GO this difference is as large as almost 50% of the simulated value. Furthermore, at $x>0$ it is observed that the measured results are considerably higher than the calculated values.

As depicted in Fig 7-9 the butt joints marked with “L” and “R” at either side of the jointed strip in layer 5 are dissimilar. The “L” is perpendicular to the rolling direction of the jointed specimen but the “R” is in parallel.

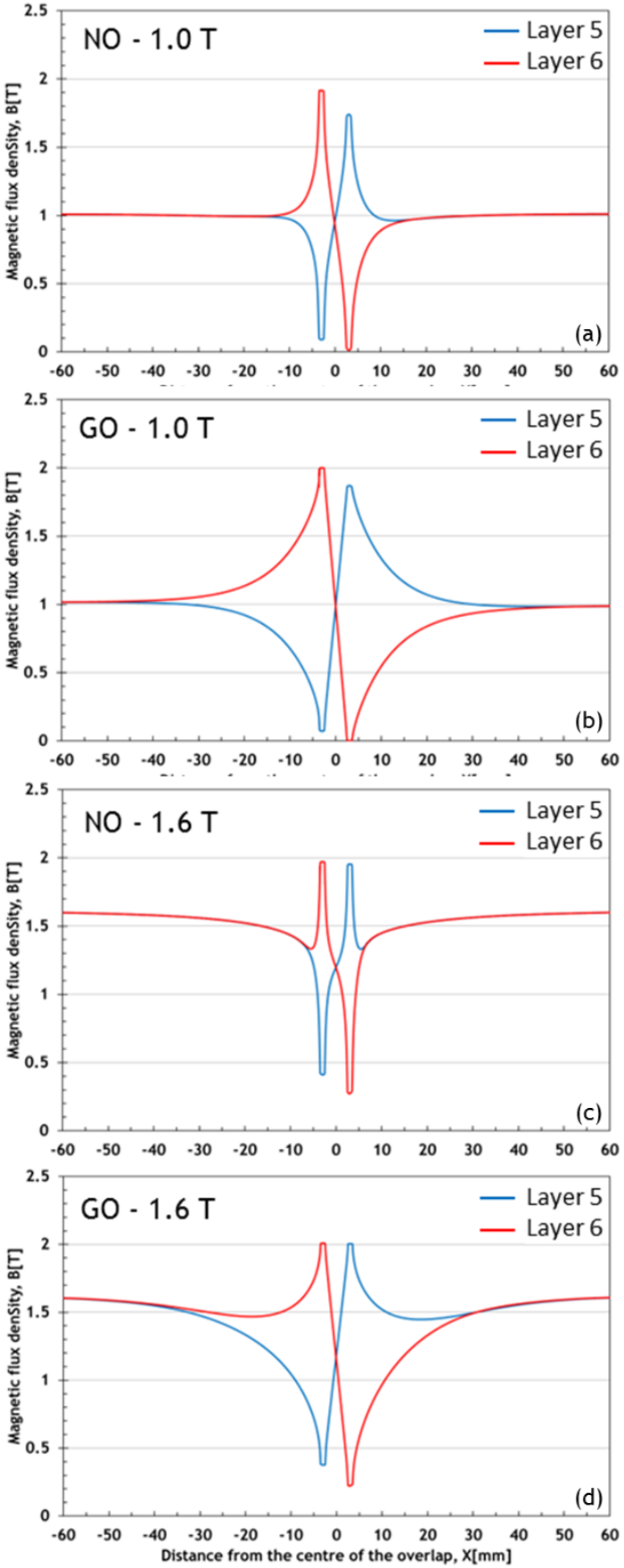

Fig 7-8 Longitudinal magnetic flux density distribution in linear joint modelled in COMSOL. (a) NO at 1.0, (b) GO at 1.0 T, (c) NO at 1.6 T, (d) GO at 1.6 T

The flux from the side limb in layer 5 takes the lowest reluctance path and in this case, the magnetic reluctance of the path including the butt joint L in layer 5 is higher than the path which includes the interlaminar air gap and either layer 4 or 6. It is estimated that if the longitudinal and interlaminar airgap sizes are 0.1 mm and 16 μm, and the cross sectional areas assumed to be equal, then the longitudinal airgap reluctance is at least 6 times larger than the interlaminar gap.

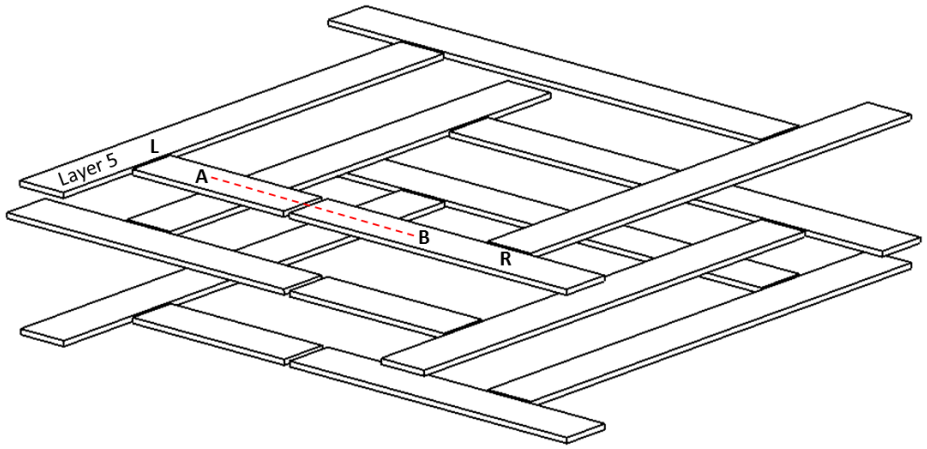

Fig 7-9 Schematic diagrams of the jointed assembly in the Epstein frame showing cross section of laminations in the jointed limb

The cross section experiencing interlaminar flux varies from 6 mm to 25 mm, therefore the interlaminar reluctance can be even lower than estimated. In this configuration, the flux from the butt joint would not uniformly distribute along the laminations especially in GO. In experiments, this effect causes the longitudinal flux distribution at $x<0$ to be lower than the calculated values. At $x>0$ the lowest reluctance path for the flux appears in layer 5 rather than layer 4 and layer 6. Therefore in this region the measured flux density is higher than the calculated one. This shows the importance of butt and lap joint longitudinal airgap on flux redistribution in the limb and the test zone. The effect of this type of airgap on flux distribution is dominant when the flux level in the core is not close to the saturation point. In NO at 1.60 T these airgaps are not affecting the flux as much as in GO at the same flux density. Thus, the effect of anisotropy, asymmetry of the geometry in the jointed region and a very small air gap on flux non-uniformity in a lamination are more than a linear 1mm airgap.

7.2.3 Interlaminar flux density distribution at the vicinity of the linear joint: empirical and theoretical results

Interlaminar flux density is significant, whether in or outside of the overlap region, close to the joint (usually less than a few millimetres). Interlaminar flux density measurement is always accompanied with a large uncertainty due to introducing an extra interlaminar airgap. Thus it is expected that the experimental results just mark a minimum value for the interlaminar flux density. On the other hand, due to the model inaccuracy in defining the material specifications, the analytical results overestimate the interlaminar flux density. In this section the results of the measured and calculated interlaminar flux density in a linear joint are introduced and compared in NO and GO steels.

Fig 7-10 and Fig 7-11 show the normal flux density waveforms in the overlap region between layer 5 and layer 6 measured in the NO and GO materials. In NO, the maximum measured values of the interlaminar flux densities are 77 mT and 68 mT and in GO are 57 mT and 46 mT respectively. The difference in the peak value of the normal flux density is due to the asymmetry in the model. The number of gap bridges at $x<0$ is 4 while it is 5 at $x>0$, so the normal flux has a smaller amplitude at $x>0$. If the model was symmetric, the interlaminar peak flux density would be the average of the above values, 70 mT for NO and 50 mT for GO. The amount of the normal flux density which has been measured experimentally is less than 10 mT in [82] and [19] in mitred joints. In [109], using 50 μm thick printed foil, the interlaminar magnetic flux density was measured in different regions of a real small transformer core at different induction levels and the maximum value of 90 μT was reported at 1.8 T. Since the measurements have been conducted between all layers of the transformer core and 4 induction levels (more than 700 measurements), the length of the airgap in each layer was not controlled or mentioned.

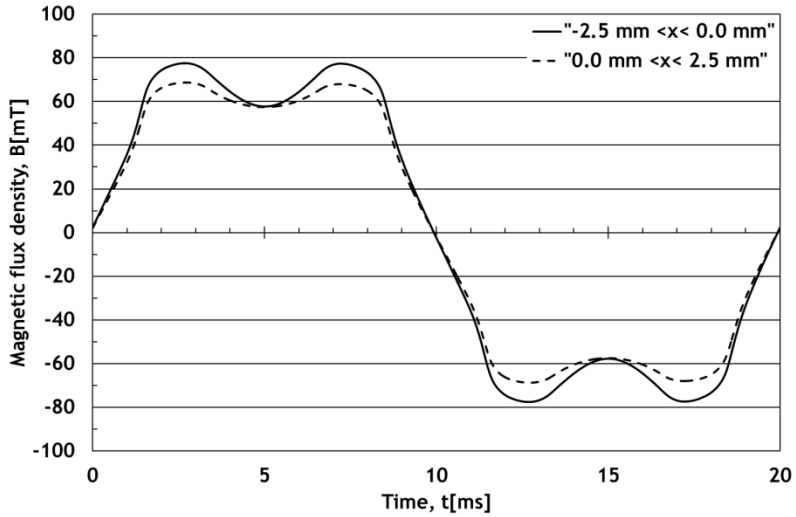

Fig 7-10 Normal to the plane magnetic flux density waveforms measured at the overlap region between layer 5 and layer 6 of the linear joint assembled form NO electrical steel at overall flux density 1.6 T, 50 Hz

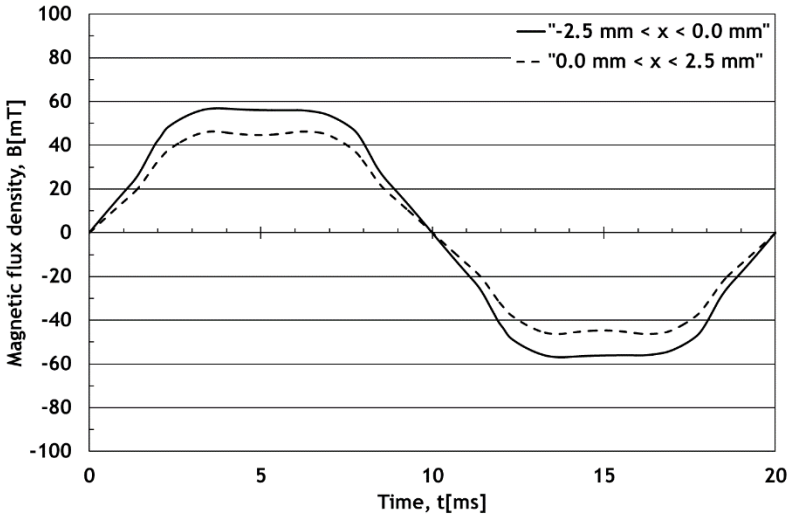

Fig 7-11 Normal to the plane magnetic flux density waveforms measured at the overlap region between layer 5 and layer 6 of the linear joint assembled form GO electrical steel at overall flux density 1.6 T, 50 Hz

The asymmetry in the graphs is due to the asymmetry of the model as mentioned above. The average interlaminar flux density in NO at both induction levels is higher than the GO which correlates with the flux density distribution in the rolling direction. The average peak interlaminar flux density at 1.6 T for NO is calculated as approximately 350 mT for NO and 200 mT for GO. The interlaminar flux density is strongly dependant on induction level, material grade and the geometry of the core. The values which are reported at 1.5 T in the

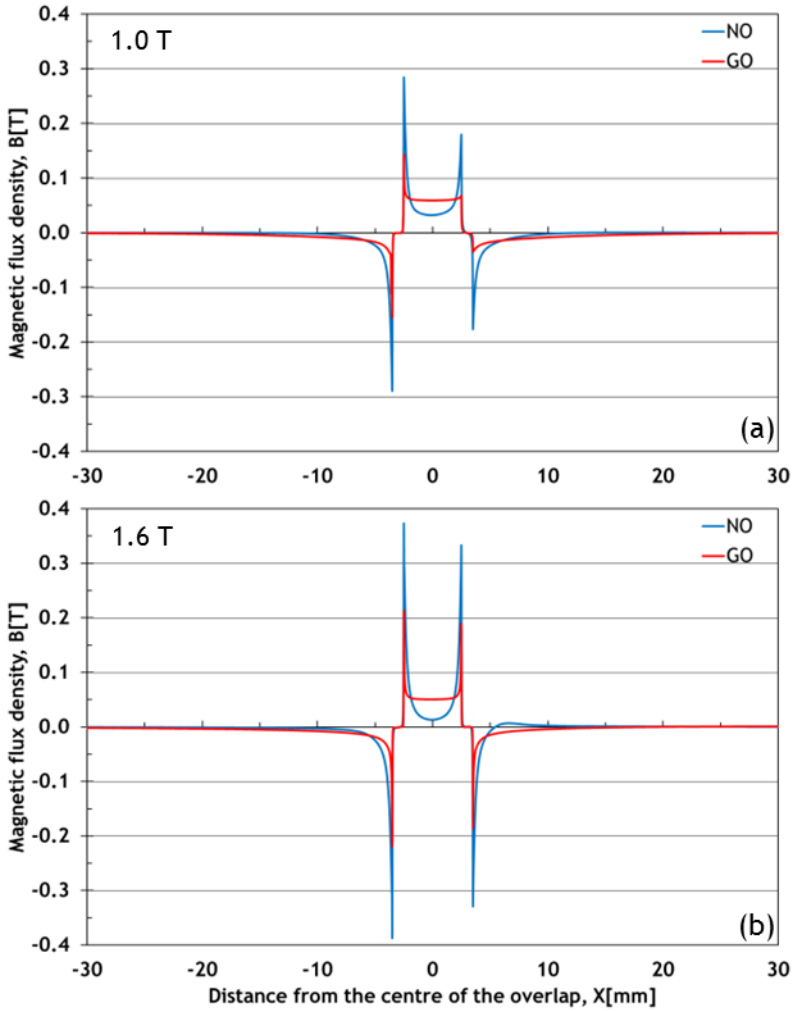

Fig 7-12 Interlaminar flux density distribution in NO and GO at (a) 1.0 T, (b) 1.6 T

literature vary from 63 mT for multistep lap geometry to 1250 mT in a single step lap geometry which was presented in Table 3-5.

The empirical and analytical results from the linear joints propose that the interlaminar flux density in the NO assembly is between 70 mT and 350 mT and in GO is between 50 mT and 200 mT.

7.3 Estimation of minimum limb length necessary for studying true flux distribution in the assembly with central limb joint

Interference of the effect of corner butt-lap joints in Epstein frame with the effect of linear joints on flux density distribution in some flux densities is due to insufficient limb length in the test rig. In this section, the results of the developed

algorithm to calculate the required minimum limb length for having a uniform flux density in the limb will be presented.

The algorithm which was presented in chapter 6.4 was used for both NO and GO materials and the results are presented in Fig 7-13. As shown, to obtain a uniform flux density (0.5% variation along the limb and 99% uniformity of the flux between the layers) over a length of 10 mm in NO at 1.6 T and 1.0 T, a limb length of 130 mm (60 mm × 2 + 10 mm) and 90 mm (40 mm × 2 + 10 mm) is required respectively. 20 mm of uniformity at these inductions needs 180 mm (80 mm × 2 + 20 mm) and 160 mm (70 mm × 2 + 20 mm) for 1.6 T and 1.0 T respectively.

In GO, having 10 mm of uniform flux at 1.6 T and 1.0 T requires 60 mm and 50 mm respectively. According to Fig 7-13 more than 10 mm uniform flux in the core is not possible at 1.6 T in the GO material. Although the flux distribution depends on several parameters in the magnetic circuit, Fig 7-13 implies that when the material is at its higher relative permeability, the flux becomes uniform closer to the airgap. As illustrated, to obtain just 10 mm of uniform flux in the limb at 1.6 T, at least 70 mm continuous flux path (60 mm +10 mm) is needed. Therefore, to have another similar joint at the other end of the limb there would be at least 140 mm distance between them.

In these experiments the jointed region was between two butt-lap joints. As illustrated, the effect of butt-lap joint on flux distribution is present for 40 mm to 90 mm in the best and worst cases respectively. Furthermore, noting the effect of the jointed region on flux disturbance along the core shows that the required minimum length to have uniform flux surrounding the joints is 40 mm to 60 mm. Superimposing these two facts implies that to have a uniform flux at either side of a linear joint, at least 80 mm to 140 mm free continuous distance should be considered. For longer limbs, it is expected that the flux becomes uniform closer to the airgap and all the values which are presented here become slightly smaller because the ratio of the reluctance of any kind of discontinuity to the reluctance of the magnetic circuit would be smaller.

Different interlaminar and longitudinal gap lengths will also change the uniformity pattern in the cores. These curves can be used as a gauge for developing models in software whilst the uniformity of the flux in actual laboratory cores depends on several other parameters, such as the primary winding distribution and stacking accuracy.

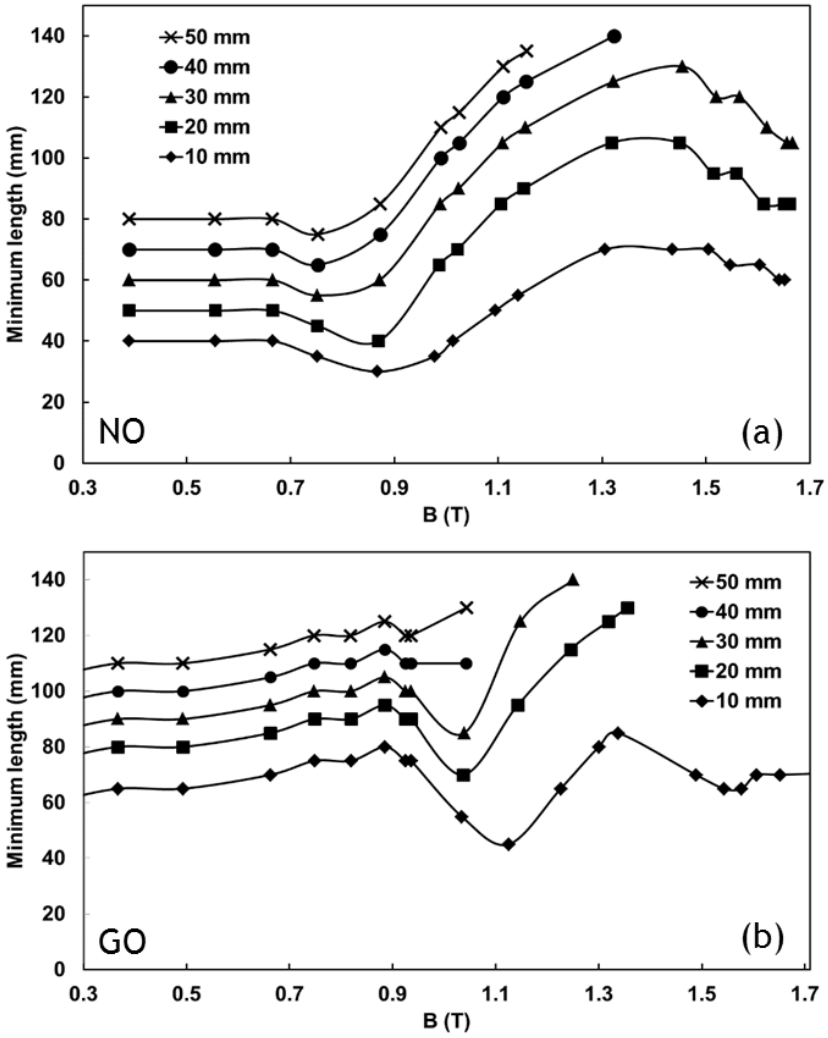

Fig 7-13 Required minimum length before joints to have x_i mm of uniform B at the core with 0.5% variation along the limb and 99% uniformity of the flux in that region: (a) NO (b) GO

7.4 Flux density distribution in mitred joint of a single phase SSL core

In the previous sections, simplified linear joints were studied empirically and analytically. In this section, the flux density distribution in a proper mitred joint - as shown in Fig 4-12- will be studied. Furthermore, the effect of the airgap length on flux density distribution will be investigated, using a translation table.

Fig 7-14 shows the rolling direction flux density distribution in the mitred joint of a single phase transformer core assembled from nine layers of 0.3 mm thick grain

oriented electrical steel. The overall flux density in the core was 1.6 T. The flux density distribution is shown in seven path lines and three different airgap lengths in layers five and six as described in Fig 7-14-a. The amount of measured flux density at points A and L in both layers show that the average flux density in the vicinity of the joint dropped to about 1.3 T at 7 cm away from the joint. Looking at the flux density variations along path 4 and path 5 reveals that by moving toward points L and A the amount of the flux in the laminations increases slightly due to increasing the distance from the airgap. Furthermore, it is observed that the magnetic flux density magnitude at these points does not change significantly by changing the airgap length which means that the effect of the airgap on flux density distribution is not going beyond this point in the limb.

The effect of the triangular free space at the inner corner of the joint on the flux distribution in the rolling direction is shown in Fig 7-14-b. As seen in layer 5, the flux density at point D is less than at point C while point D is closer to the centre of the lamination. This means that the triangular areas introduce some regions which are not utilised efficiently. This triangular region is relatively large in comparison to the dimensions of the model core but in real power transformer cores in which the width of the laminations are at least a few times wider than the model cores, the effect of these regions is much less.

The flux density in the rolling direction in the vicinity of the joint reduces as the airgap length increases. The only exception is in layer 6 along path 7 where the flux in the rolling direction increases as the airgap length increases which is due to the shift of path 7 search coils from the overlap region to the gap bridging region.

Fig 7-15 illustrates the transverse flux density in the same assembly. Fig 7-15-e and Fig 7-15-f show that the transverse flux density in paths 4 and 5 are only significant at the points near the joint, where the flux deviates from the rolling direction in order to enter the yoke lamination. By changing the airgap length, the transverse flux in points A and L remain almost unchanged which again confirms that any change in the airgap length would just affect the flux density distribution in the vicinity of the joint. As the distance from the airgap decreases, the amount of flux in transverse direction increases as shown in Fig 7-15-c and Fig 7-15-d. Increasing the airgap length also increases the amount of the transverse flux in the joint. The transverse flux on path 6 and path 7 in Fig 7-15-g and Fig 7-15-h show the flux concentrating in the centre of the laminations. This excess flux

leaking from the regions either side of the laminations causes the flux in the rolling direction at the centre of the lamination to increase. It should be noted that this effect might be less significant in large transformer cores because the effect of the triangular region is exaggerated in the model core. In bigger cores the excess transverse flux in points I and J might be reduced.

The modulus and phase of the third harmonic component of the localised flux densities in the rolling direction are shown in Fig 7-16 and Fig 7-17 respectively. The third harmonic is higher on path 5 than path 4 which has a good correlation with the transverse flux distribution. So as the transverse flux increases, the undesired harmonic components will increase. This is due to the alignment of the domains in the rolling direction and the difficulty of being magnetised in any other directions. The discontinuity of the flux generates harmonics. The average of the modulus and the phase of the third harmonic in two layers on the paths 6 and 7 do not change significantly by changing the airgap length but the share of each harmonic in each layer changes. E.g. on path 6, as the airgap length increases, the amount of the third harmonic flux which passes through layer 6 decreases while on layer 5 it increases. This trend is observed on the other path lines as well which shows that by changing the flux density the amount of the third harmonic in the core would remain the same. This means that the overall power loss of the core due to 3^{rd} harmonic would not change but the imbalanced flux distribution will lead to mechanical issues. Fig 7-18 shows the trend of change of third harmonic modulus by changing the airgap length.

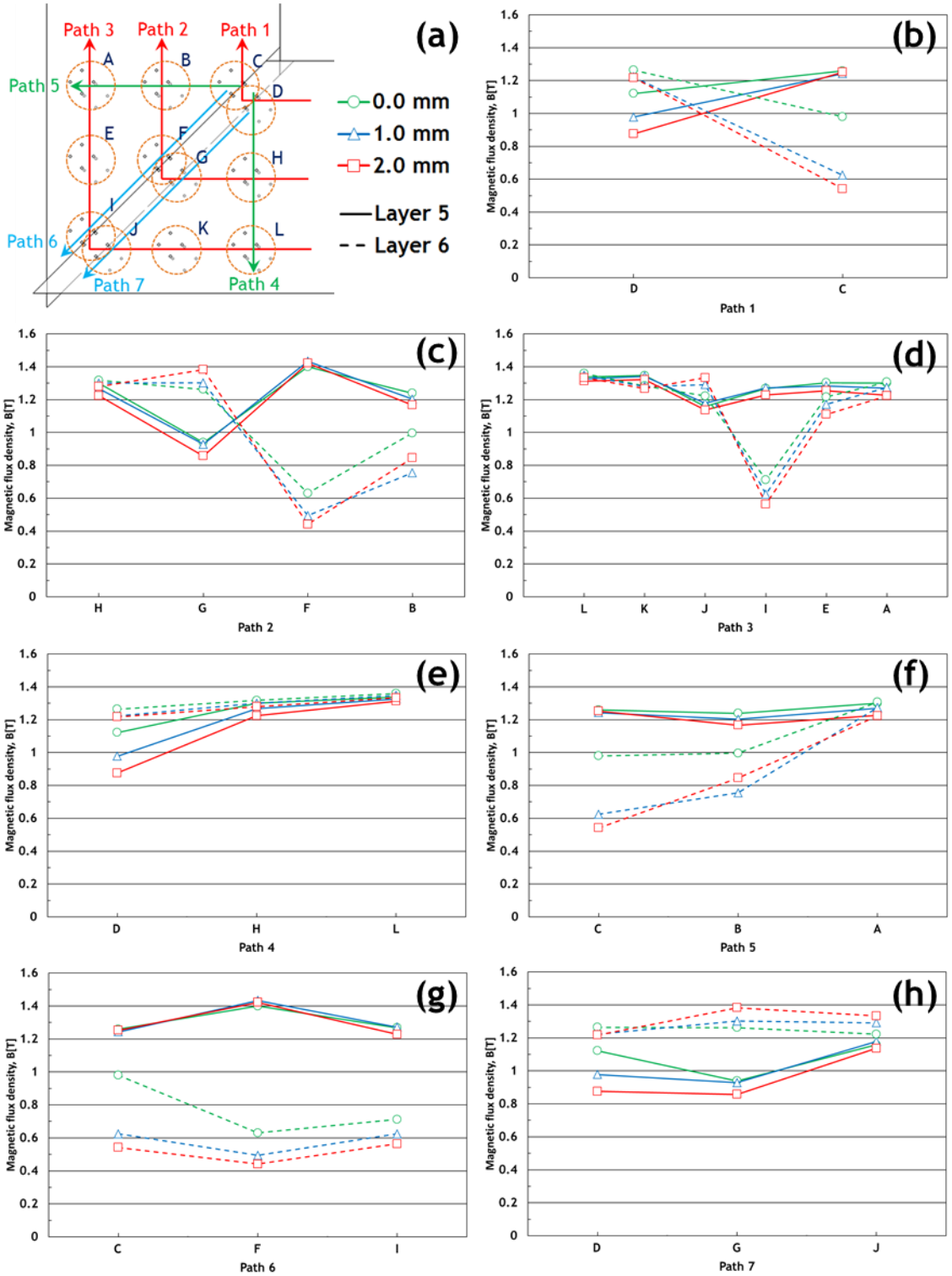

Fig 7-14 Magnetic flux density distribution in rolling direction measured in a mitred joint of a transformer core assembled with nine layers of grain oriented electrical steel. The flux density in each point was measured in 3 different airgap lengths. (a) The guide for the paths and the legend (b) to (h) show the flux density in path 1 to path 7 respectively

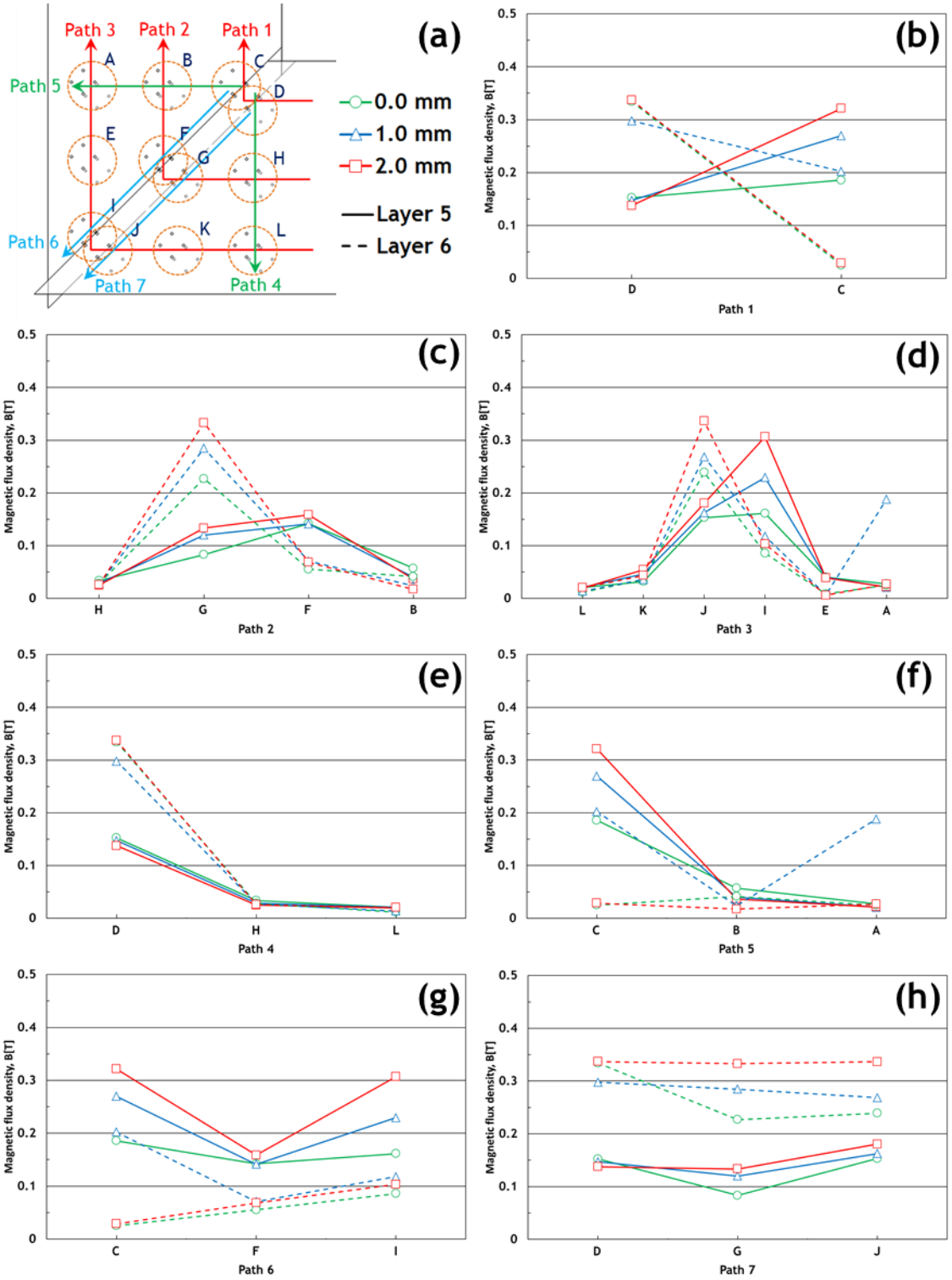

Fig 7-15 Magnetic flux density distribution in Transverse direction measured in a mitred joint of a transformer core assembled with nine layers of grain oriented electrical steel. The flux density in each point was measured in 3 different airgap lengths. (a) The guide for the paths and the legend (b) to (h) show the flux density in path 1 to path 7 respectively

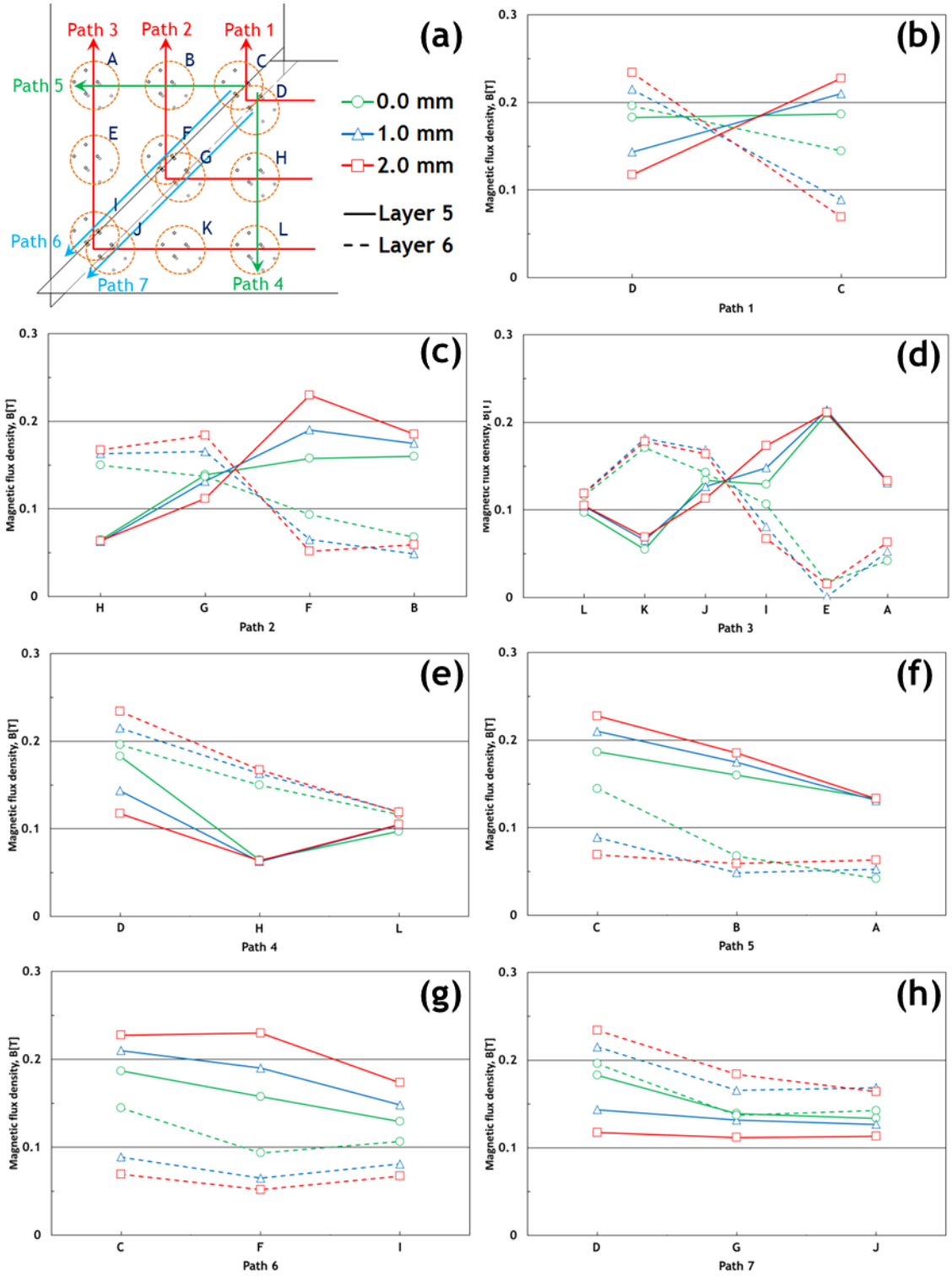

Fig 7-16 The modulus of the third harmonic of the flux density in the rolling direction calculated from the measured waveforms shown in Fig 7-14. The flux density in each point was measured in 3 different airgap lengths. (a) The guide for the paths and the legend (b) to (h) show the flux density in path 1 to path 7 respectively

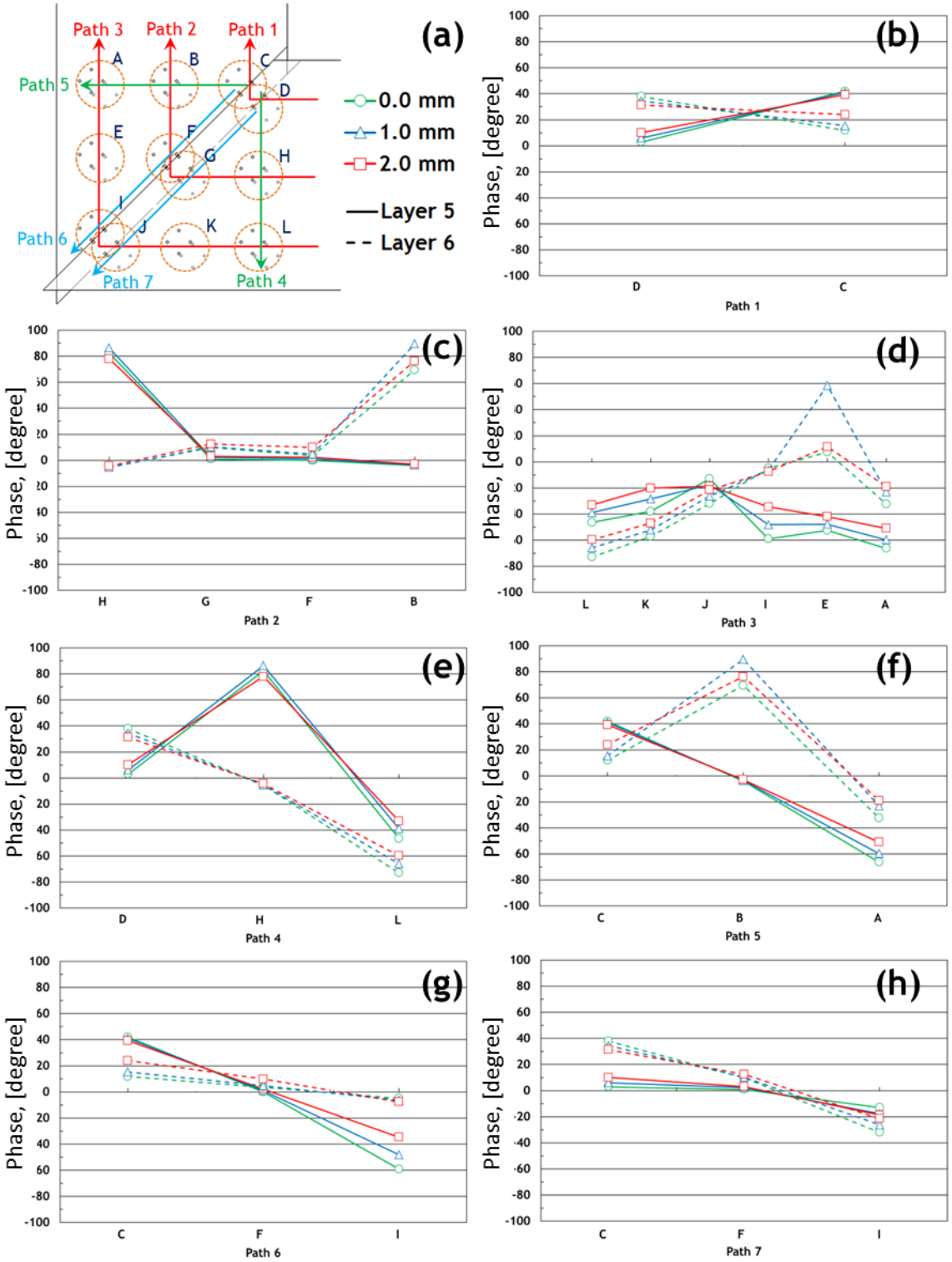

Fig 7-17 The phase of the third harmonic of the flux density in the rolling direction calculated from the measured waveforms shown in Fig 7-8. The flux density in each point was measured in 3 different airgap lengths. (a) The guide for the paths and the legend (b) to (h) show the flux density in path 1 to path 7 respectively

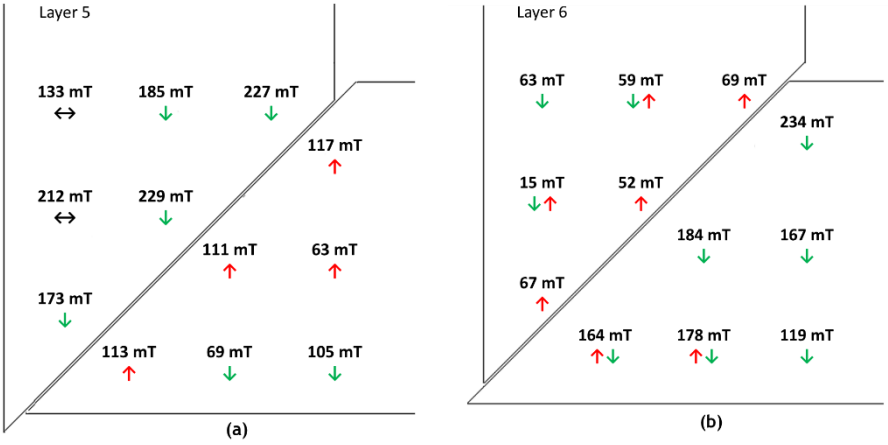

Fig 7-18 Modulus of the third harmonic component of the flux density in rolling direction at 1.6 T when the air gap length is 2.0 mm. The arrows show the trend of the changes of the third harmonic, when the airgap length reduces down to 1.0 mm and 0.0 mm. (a) Layer 5 (b) Layer 6

7.5 Influence of stack height on flux density distribution

Flux distribution in transformer core joints is usually investigated in plane and normal to the plane of the laminations and assumed that its distribution is similar in other layers. In order to investigate the flux distribution across the core, 4 models with linear joints were designed and studied in COMSOL with NO and GO at 1.60 T. The models were validated in an experimental linear joint setup and the mitred joint.

7.5.1 Flux density distribution across the height of the stack in linear joint: analytical approach

The 2D linear joint model was used to study the flux distribution across the core. The simulation was conducted for NO and GO materials at 1.6 T. The logarithmic function was applied twice on the B norm distribution in order to highlight the regions with 1.0 T flux density in the model as described in chapter 6.3.5. This is used to have a gauge to compare the results in different assemblies. The results are shown in Fig 7-19 to Fig 7-22.

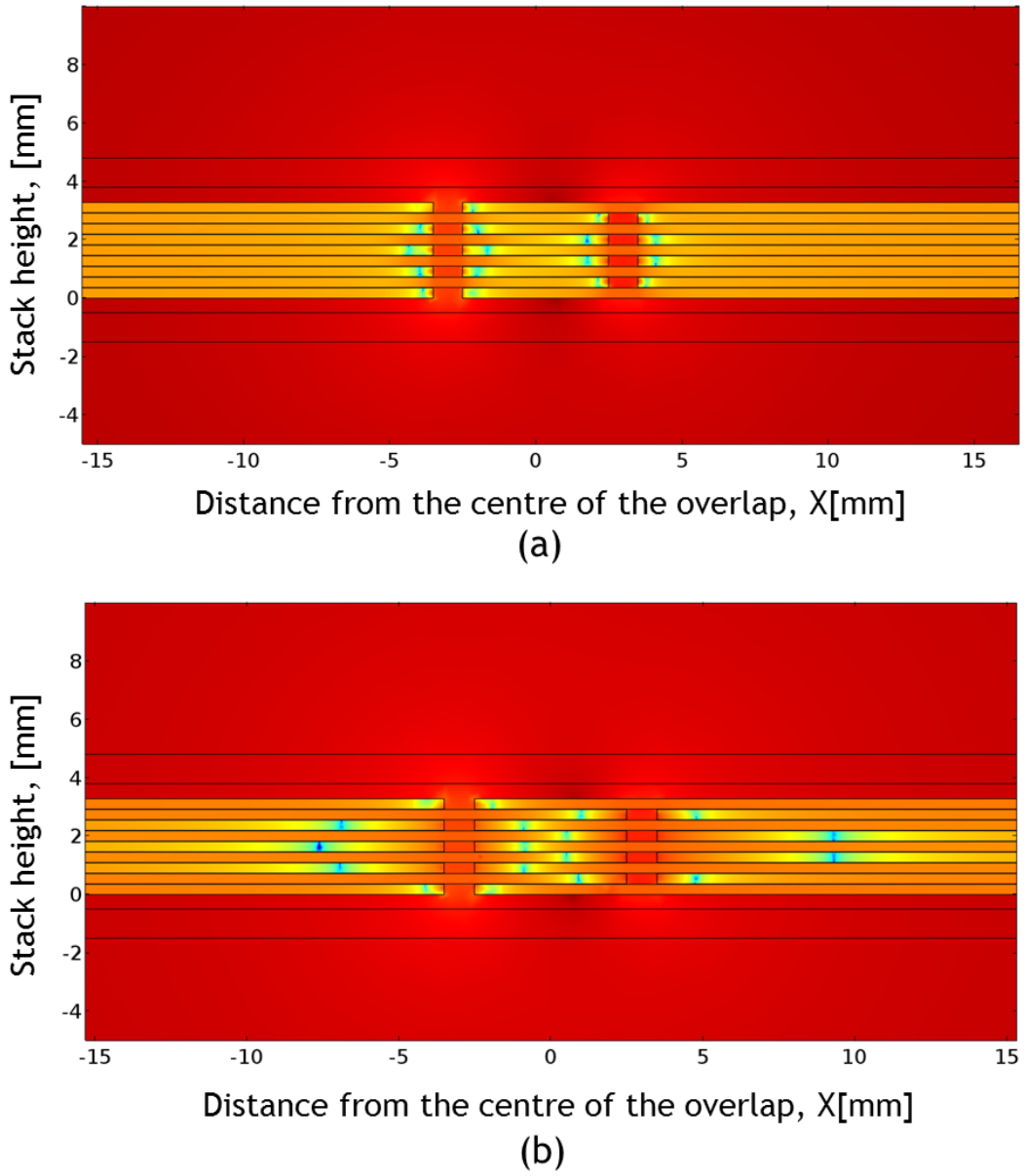

Fig 7-19 The blue regions are the locus of the magnetic flux density equal to 1.0 T when the linear joint is assembled from 9 layers with 1 mm airgap and 5 mm overlap, magnetised at 1.6 T in (a) NO and (b) GO

In the assembly of nine laminations, the flux tends to deviate from the centre of the assembly and pass through the outer laminations. As shown in Fig 7-19, in the NO assembly the 1.0 T regions are very close to the edge of the laminations and the maximum distance of the 1.0 T region from the edge of the lamination in the central layer is less than 1 mm while in GO it is at least 4 mm. In the outer laminations the 1.0 T highlights are closer to the jointed regions which means that the magnetic flux density in those laminations is higher than the inner laminations.

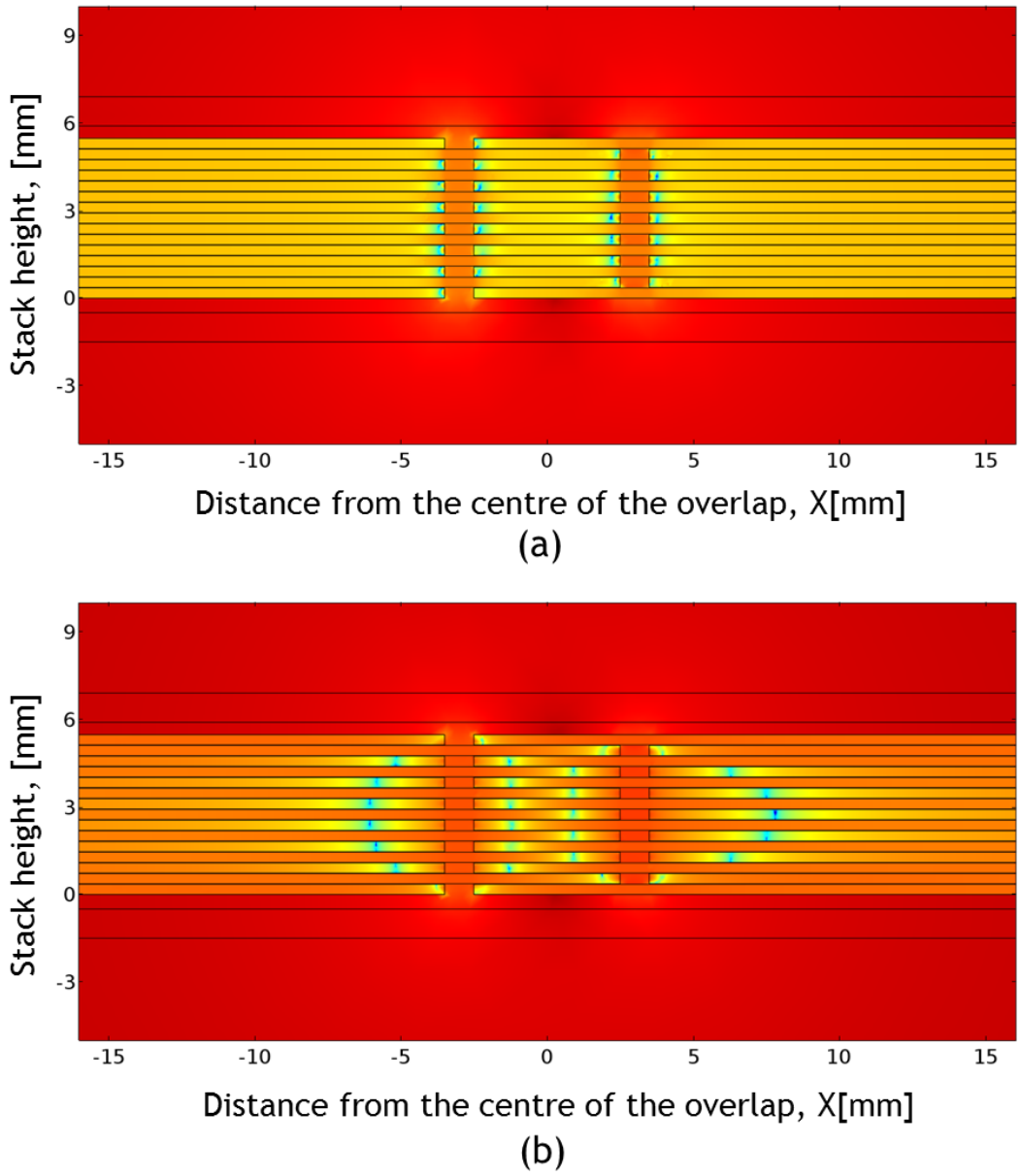

Fig 7-20 The blue regions are the locus of the magnetic flux density equal to 1.0 T when the linear joint is assembled from 15 layers with 1 mm airgap and 5 mm overlap, magnetised at 1.6 T in (a) NO and (b) GO

Comparing the overlap regions in the two assemblies reveals that the tendency of the flux to become uniform in NO is greater than GO. By increasing the number of laminations in the assembly to 15 layers the locus of the 1.0 T regions get closer to the joints, as the furthest 1.0 T region is less than 3 mm away from the joints in the central layers of the GO assembly as shown in Fig 7-20. In the case of the NO assembly, the 1.0 T regions are not further than 0.2 mm away from the joint which means that the flux is more confined in NO laminations than in GO therefore the locus is very close to the joint in NO.

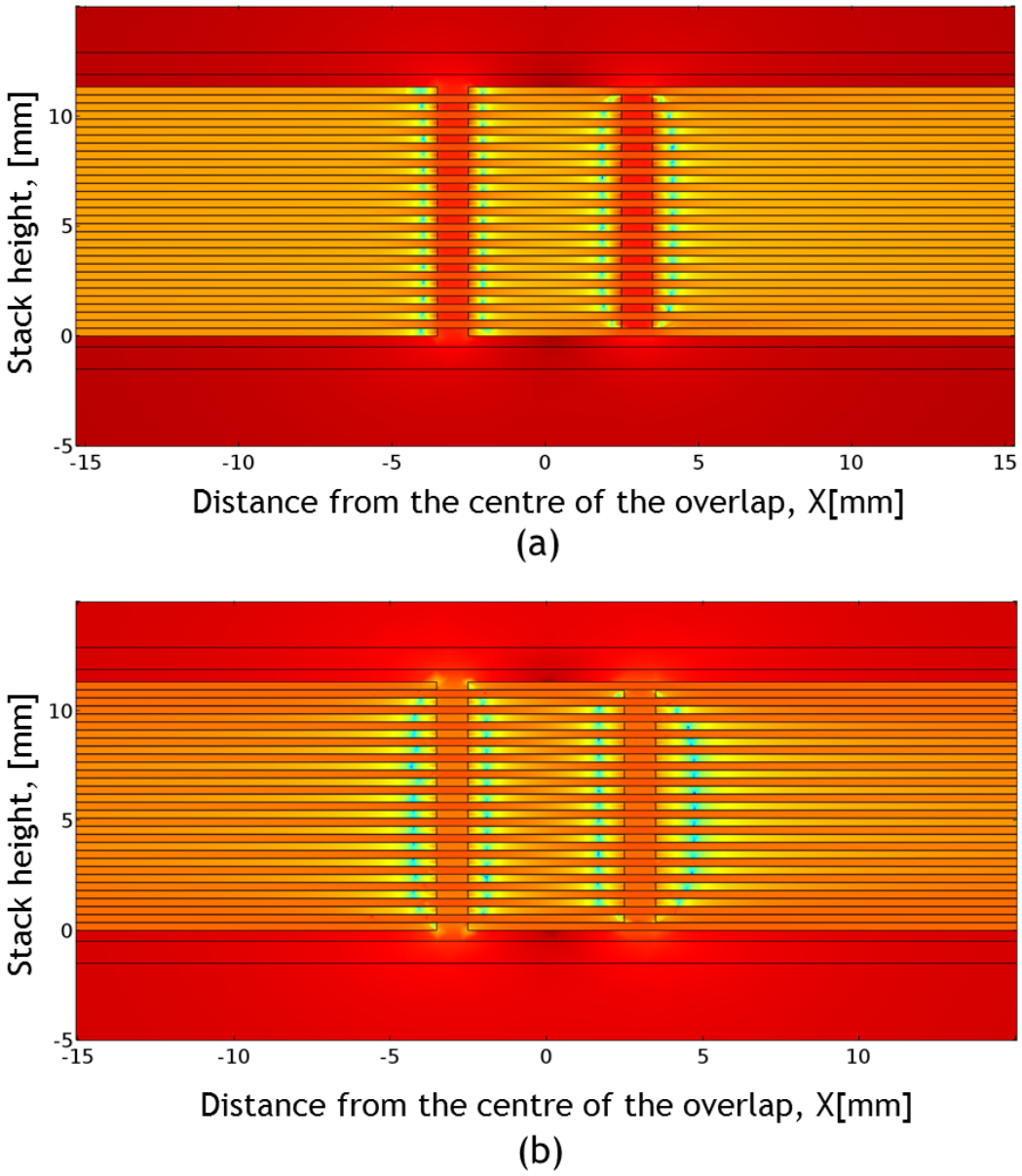

Fig 7-21 The blue regions are the locus of the magnetic flux density equal to 1.0 T when the linear joint is assembled from 31 layers with 1 mm airgap and 5 mm overlap, magnetised at 1.6 T in (a) NO and (b) GO

Increasing the number of laminations to 31 layers, as shown in Fig 7-21, makes the 1.0 T regions linear in the vicinity of the joint in the NO assembly. In the GO assembly, all the 1.0 T regions are confined to the range within 1.5 mm from the edge of the laminations. The outer laminations show higher magnetic flux density. Fig 7-22 shows the 1.0 T flux density distribution in the core assembled from GO material for 64 layers. Except for the first few laminations, the flux distribution in all the other central laminations are identically uniform.

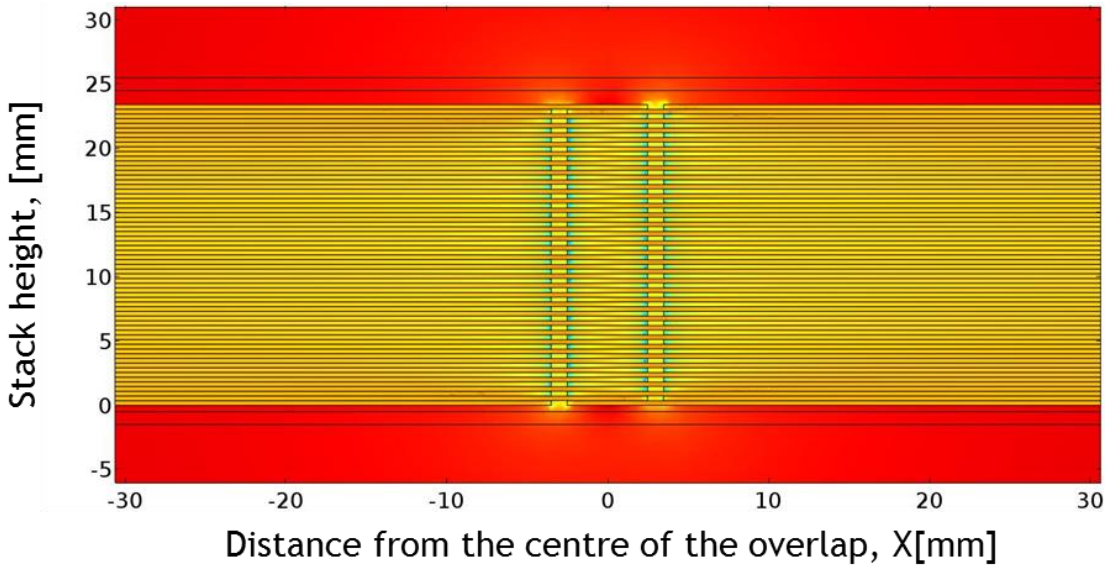

Fig 7-22 The blue regions are the locus of the magnetic flux density equal to 1.0 T when the linear joint is assembled from 64 layers with 1 mm airgap and 5 mm overlap, magnetised at 1.6 T in GO

7.5.2 Flux density distribution across the height of the stack in linear joint: experimental approach

The magnetic flux density distribution across the laminations around the linear joint assembled from GO and NO materials were measured experimentally at an overall flux density of 1.6 T in the core. The measured flux densities in each lamination at a distance of 20 mm away from the edge of the laminations in NO and GO assemblies are shown in Fig 7-23 and Fig 7-24. The flux densities measured by the search coils which are closest to the airgap in each layer are marked by black bars and those which are closer to the gap bridges are shown with white bars.

No significant difference was found in the flux density distribution between the laminations in the NO assembly as shown in Fig 7-23. The measured flux distribution pattern in the GO (Fig 7-24) is very similar to that which was shown in Fig 7-19-b. The outer layer's flux density is at least 45% higher than the central layer. Due to the effect of the Epstein frame joints, it is not expected that the absolute value of the flux in the experimental setup and the simulations become identical, thus these values are not compared.

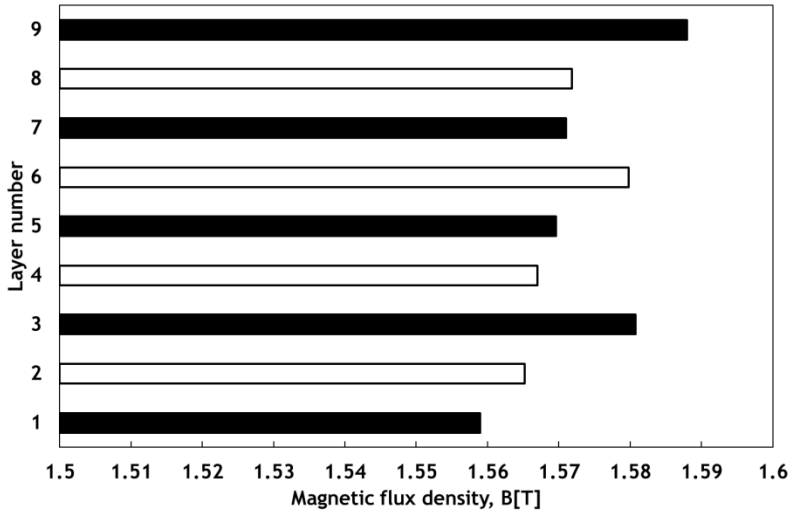

Fig 7-23 Magnetic flux density distribution along line Z in linear joint assembled from NO electrical steel when the core is magnetised at 1.6 T, 50 Hz

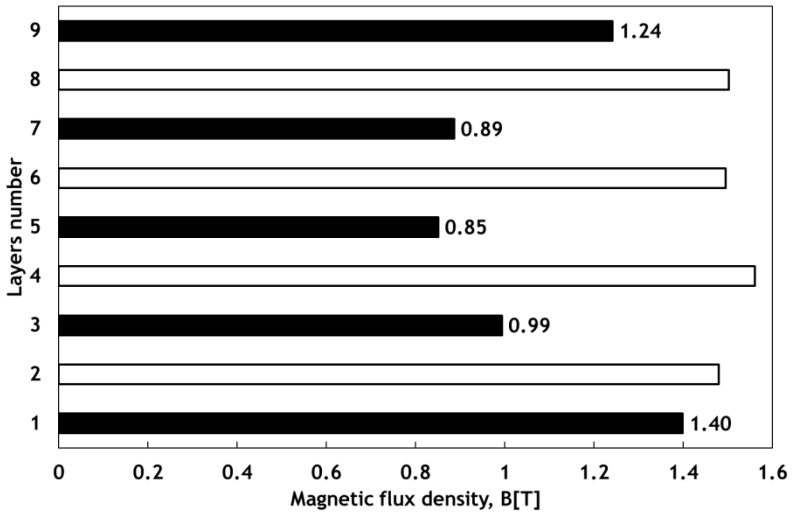

Fig 7-24 Magnetic flux density distribution along line Z in linear joint assembled from GO electrical steel when the core is magnetised at 1.6 T, 50 Hz

7.5.3 Flux density distribution across the height of the stack in mitred joint: experimental approach

The effect of increasing the number of laminations on the flux distribution at the vicinity of the mitred joint was studied with 0, 1.0 and 2.0 mm airgap lengths. The flux density in layer 5 was measured for the assembly composed of 9 and 31 layers of GO at 1.6 T 50 Hz and the results are shown in Fig 7-25. On Path 1, as shown in Fig 7-25-b, the flux density in layer 5 increases as it was situated at the outer part of the core. The only exception is at point C, when the core is

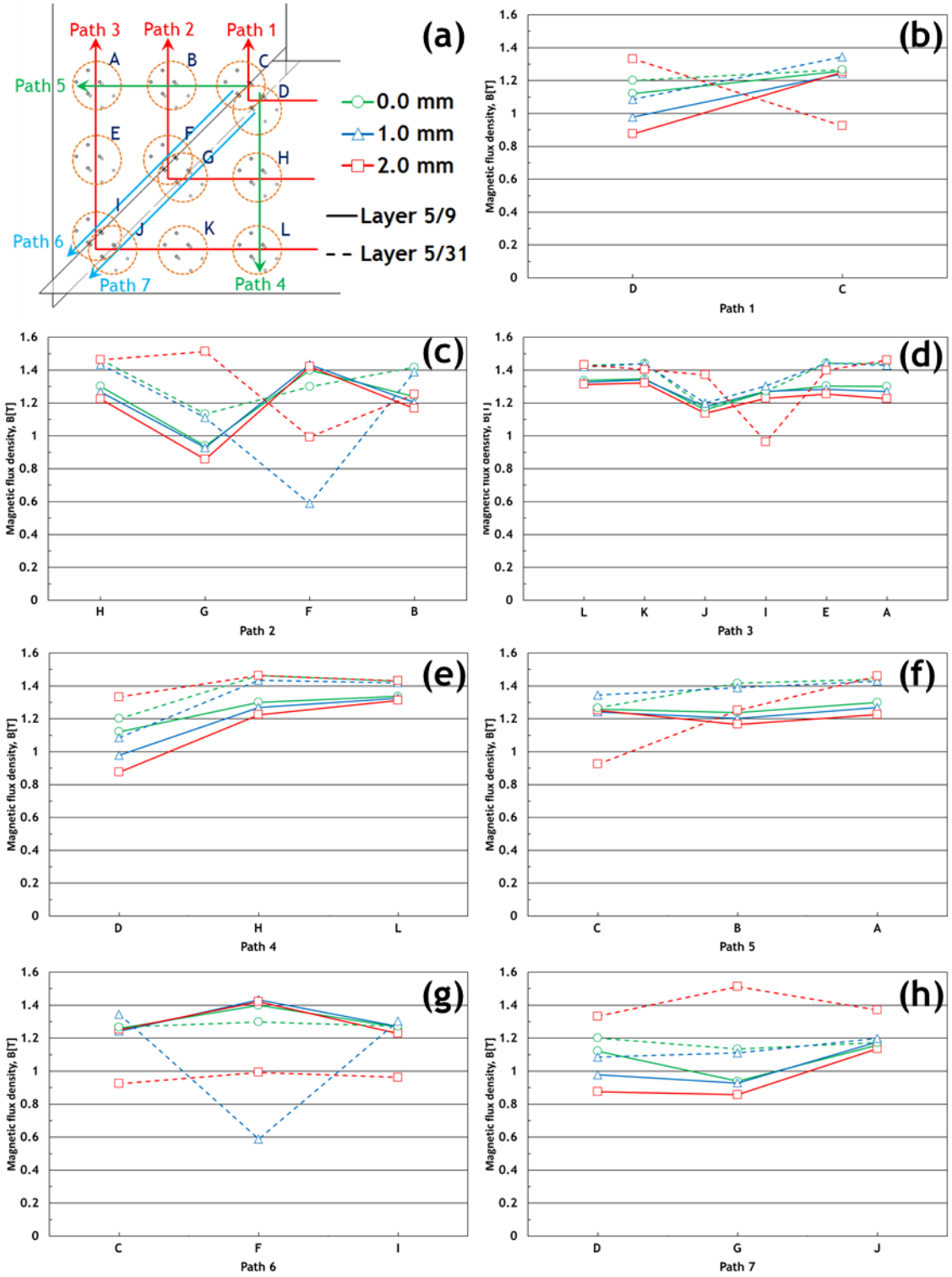

Fig 7-25 Comparison of the magnetic flux density distribution in the corner joint of a single phase SSL core in layer 5 when the core was assembled from 5 and 31 layers. The experiments were conducted in three airgap length (a) The guide for the paths and the legend (b) to (h) show the flux density in path 1 to path 7 respectively

assembled with 31 layers and 2.0 mm airgap length, the expected trend is not observed. At 0 mm and 1.0 mm airgap lengths in the thicker stack the flux density at Point C increases but it drops significantly when increasing the airgap length to

2.0 mm whilst the flux density at point D increases about 40%. It is assumed that these results are due to the search coils being damaged from the yoke shift and the weight of the laminations with the search coils near the airgap region being very vulnerable. The flux density distribution on path 2, which is shown in Fig 7-25-c, shows almost the same trend as path 1. In path 2 the only exception is point F which, like point C and point D, is on the overlap region and is in close contact with the laminations' edges and burrs. In the outer route, which includes path 3, the flux density of the fifth layer in the thick core is again higher than the thin core. Point I, which is again on the overlap line, shows irregularity at the 2.0 mm airgap. The flux density on path 4, 5 – with exception - and 7 clearly show that layer number 5 carries more flux when it is part of a thicker core. It is believed that the search coils on path 6 are damaged. Putting the damaged coils – C, I and F – aside it is generally observed that the amount of the flux density in the outer layer of the core is notably higher than the central part.

The results from the mitred joint agree with the analytical findings in section 7.5.1 and experimental measurements in section 7.5.2. In the next section, the reason of flux divergence in the joint will be analytically explained.

7.5.4 Flux divergence theorem

The duality principle is usually used to describe the magnetic flux distribution like current distribution in an electric circuit. All the describing equations of an electric circuit have a magnetic equivalent. However, the current in electrical circuits is confined in the copper wires whilst the magnetic flux will follow the lowest permeability path.

In the linear joints discussed earlier, the longitudinal airgaps provide a very high reluctance path for the flux and their reluctance ($\Re$) is calculated as follows:

$$\Re = \frac{l}{\mu_0 A} \tag{7-1}$$

where l and A are the length and the cross sectional area of the airgap and μ_0 is the permeability of the air. Practically, the length of the airgap is fixed and in our experiments is equal to 1.0 mm. The cross sectional area of the airgap is usually assumed to be equal to the cross sectional area of the electrical steel but in reality the flux follows the path with minimum reluctance. Therefore, by diverging from the anticipated path at the airgap the flux increases the effective

cross sectional area of the magnetic path. Hence, according to equation (7-1), the magnetic reluctance of the airgap is reduced. In a stack of jointed laminations the excess flux coming from the central layer propagates across the stack due to this effect and hence a hyperbolic pattern of the flux density distribution is created in the stack of laminations.

As shown, the divergence of the flux in the core assembled from GO begin further form the joint than the one with low permeability material. The relative permeability of the core in GO at 1.6 T is 7000, while for NO is less than 300. In the jointed region, the gap bridges are heavily saturated and therefore their relative permeability is very close or equal to 1.0 – like airgaps. Therefore, the permeability of the airgaps and their shunting gap bridges is equal to 1.0 in both cores independent of the material. The ratio of the relative permeability of the core working point to the relative permeability of the saturated region determines the degree of the flux diversion. As this ratio gets bigger (as in the GO assembly) the flux diversion happens earlier. In addition to the material type the geometry of the core joint, like the ratio of the core thickness to the airgap length, plays a very important role on the flux diversion. The results shown in Fig 7-26 plot the distance of the 1.4 T loci from the centre of the overlap in different layers at an overall induction of 1.7 T. The solid lines are the curves fitted to the measured data points using MATLAB. From the figure, it is clear that even by increasing the number of laminations to 300 layers the outer laminations would still carry extra flux in comparison to the central layer but building laboratory scale transformer cores with 300 laminations would make the test results more representative.

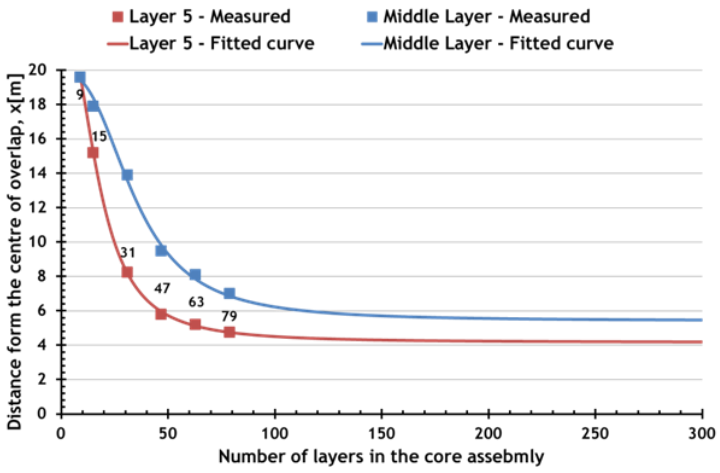

Fig 7-26 Distance of the 1.4 T loci from the centre of the overlap in different layers at the overall induction in the core 1.7 T in GO material

Based on the author's knowledge, this effect in a transformer core joint has not been reported in any previous research. In a recent paper [109] on developing very thin printed search coils to assess the interlaminar magnetic flux a series of layer to layer measurements have been performed in the vicinity of the joint. The experimental results on the real transformer core with 3 packets also show the same trend as presented here. The interlaminar flux density in the central part of the core was less than 10 μT and the interlaminar flux between the peripheral packets rose by 90 μT when the core was working at 1.8 T.

7.6 Modelling of Force distribution in linear joints due to magnetic forces

The Maxwell surface stress X and Y components of the outer and centre laminations of an assembly of GO material are shown in Fig 7-27 and Fig 7-28. The majority of the stress in the rolling direction is at the edge of the laminations in the joints and is of the order of 0.3 MPa. The normal stress is observed at the edge of the laminations in the joints. This stress is exerted on the gap bridges which are heavily saturated and are of the order of 0.25 MPa. The regions where the stress is applied on limited to the very edges of the lamination and the gap bridges. Knowing that the other end of each lamination is fixed, the lamination in the left side of each layer (X<=-3.5 mm) is compressed while tensile stress is applied on the adjacent lamination in the same layer. The direction of these stresses will change by changing the direction of the magnetisation of the core. The net stress exerted in the normal direction on the gap bridges is upwards and presents a repulsive force between the laminations.

To distinguish the difference between the stresses exerted on the outer and central laminations of the stack, the colour legend of the plots are separated in Fig 7-29 and Fig 7-30. The maximum amount of the stress in the rolling direction in the top lamination's edges is at least 50% more than the central lamination while the normal to the plane stress is 25% more. The difference in the amount of the stress in the central and outer laminations fully complies with the flux distribution in the core which discussed in section 7.5. These analyses show that the majority of the measured surface vibration is due to the surface lamination, not the whole core.

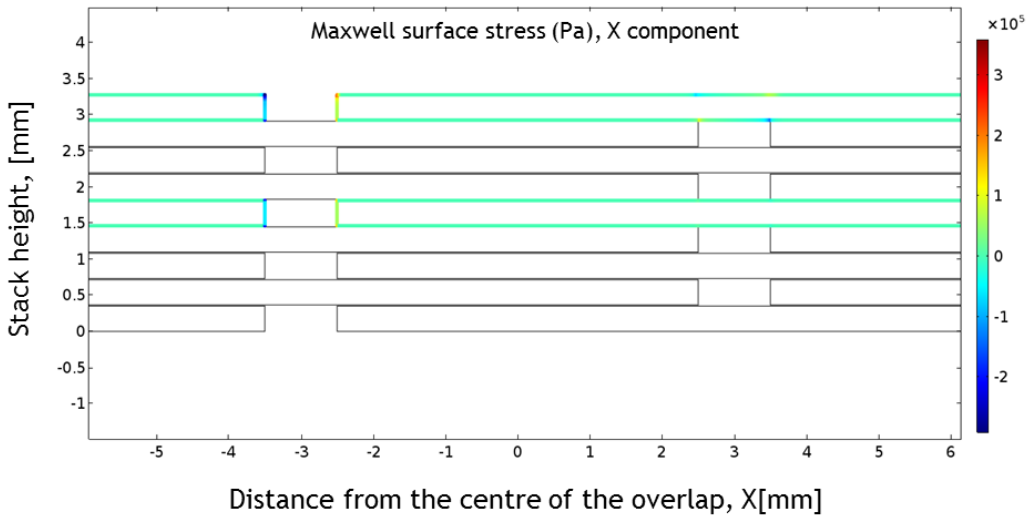

Fig 7-27 Maxwell surface stress on layer five and layer nine in the rolling direction in the assembly of GO at the flux denisty level of 1.6 T. The stress is in the direction of normal to the surface vector

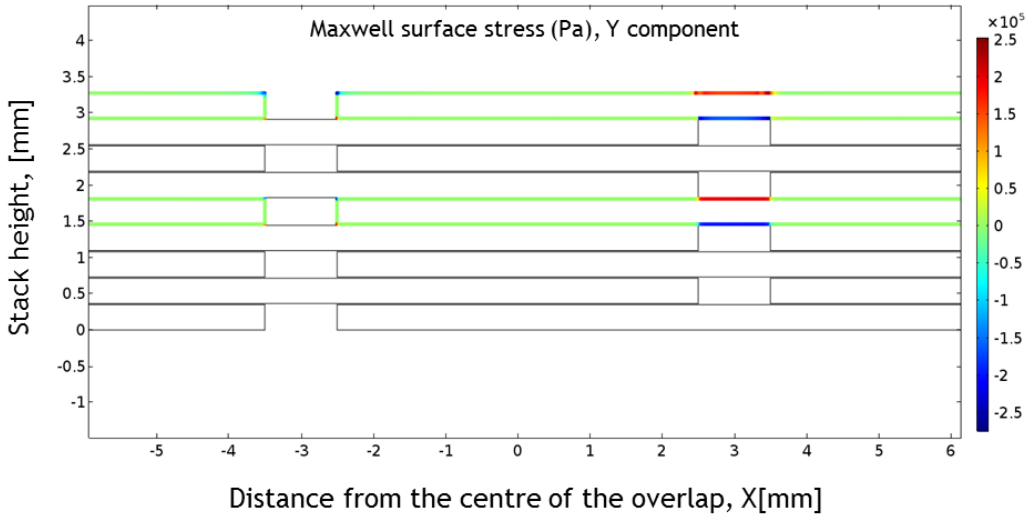

Fig 7-28 Maxwell surface stress on layer five and layer nine in normal to the plane direction in the assembly of GO at the flux denisty level of 1.6 T. The stress is in the direction of normal to the surface vector

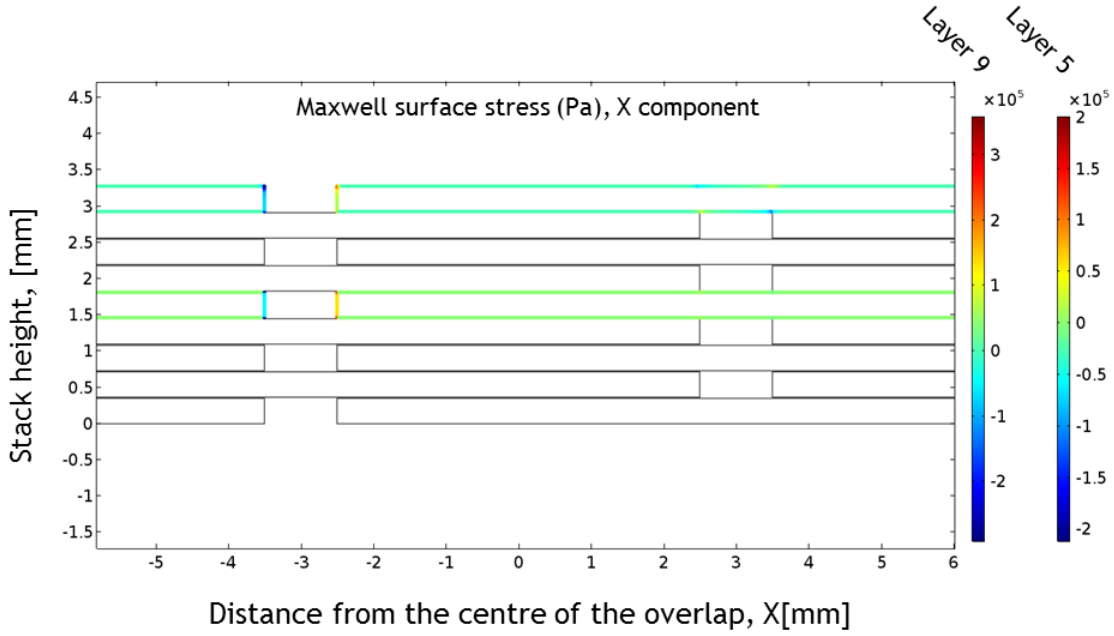

Fig 7-29 Maxwell surface stress on layer five and layer nine in the rolling direction in the assembly of GO at the flux denisty level of 1.6 T. The stress is in the direction of normal to the surface vector. The legends are seperated in this diagram: top layer is layer 9 and the middle layer is layer 5

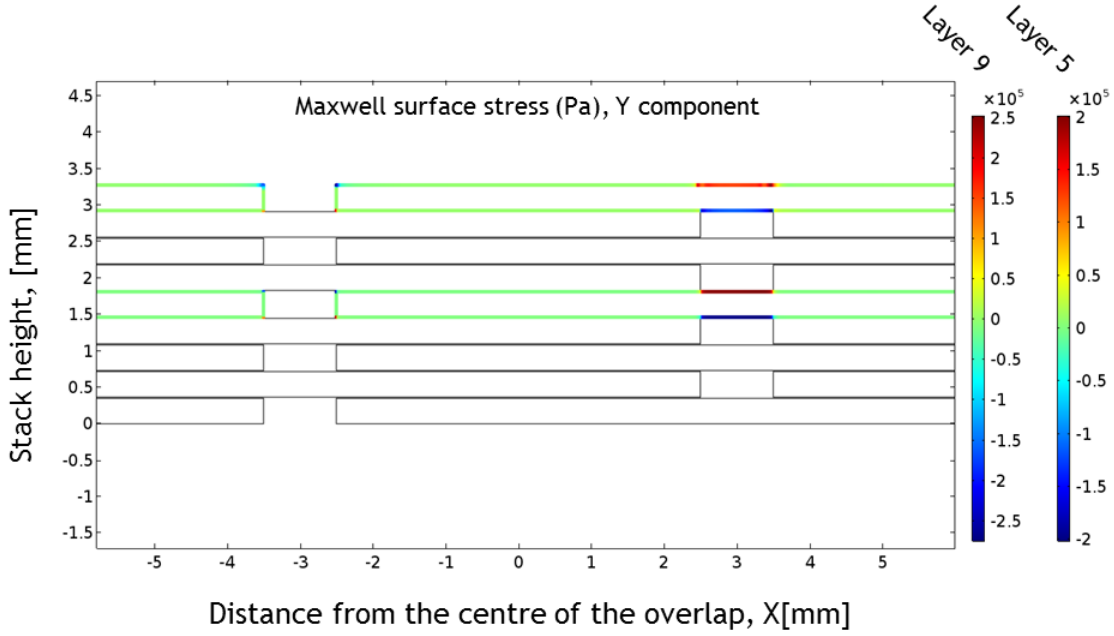

Fig 7-30 Maxwell surface stress on layer five and layer nine in normal to the plane direction in the assembly of GO at the flux denisty level of 1.6 T. The stress is in the direction of normal to the surface vector. The legends are seperated in this diagram: top layer is layer 9 and the middle layer is layer 5

7.7 Modelling of linear joint deformation due to Maxwell forces

Deformation of the laminations in the jointed region of the linear model LM1-NO at 1.6 T due to the Maxwell forces are presented in Fig 7-31. The net forces in the vicinity of the joint act in a way that the core in the jointed region tends to explode. As expected, the deformation of the outer layers is bigger than the inner layers of the core which is due to the flux divergence in the vicinity of the joint in the core. The maximum deformation in the model is 2.5 mm which is much bigger than the maximum vibration amplitude in a real transformer core which is excited by an AC source. The model is excited with a DC current source while the excitation of a real core is 50 Hz. If the vibration displacement $X(t)$ of the laminations is considered sinusoidal:

$$X(t) = X_{pk} \sin(2\pi f t) \tag{7-2}$$

where f is the vibration frequency. The velocity of the vibration $V(t)$ then can be described by the following equation:

$$V(t) = 2\pi f X_{pk} \cos(2\pi f t) \tag{7-3}$$

The associated instantaneous kinetic energy $E_k(t)$ of the vibrating laminations is equal to:

$$E_k(t) = \frac{1}{2} m V^2 = 2\pi^2 f^2 {X_{pk}}^2 \, m \, cos^2(2\pi f t) \tag{7-4}$$

The rate of using the kinetic energy is equal to:

$$P = \frac{dE_k(t)}{dt} = 4\pi^3 f^3 {X_{pk}}^2 m \sin(4\pi f t) \tag{7-5}$$

Where the peak power P_{pk} is:

$$P_{pk} = 4\pi^3 f^3 {X_{pk}}^2 m \tag{7-6}$$

Equation 7.6 describes the effect of frequency change on peak vibration displacement when the drawn peak power is considered to be constant:

$$\left(\frac{f_1}{f_2}\right)^3 = \left(\frac{X_{2_{pk}}}{X_{1_{pk}}}\right)^2 \tag{7-7}$$

Although this equation cannot be used to evaluate the DC condition, it can be used to understand that by increasing the frequency, the amplitude of the vibration reduces at the rate of $\left(\frac{f_{Initial}}{f_x}\right)^{1.5}$. For example, if the DC condition is approximated with 1 Hz and 2.5 mm deformation is assumed for this frequency then deformation in 50 Hz will be about 7 µm.

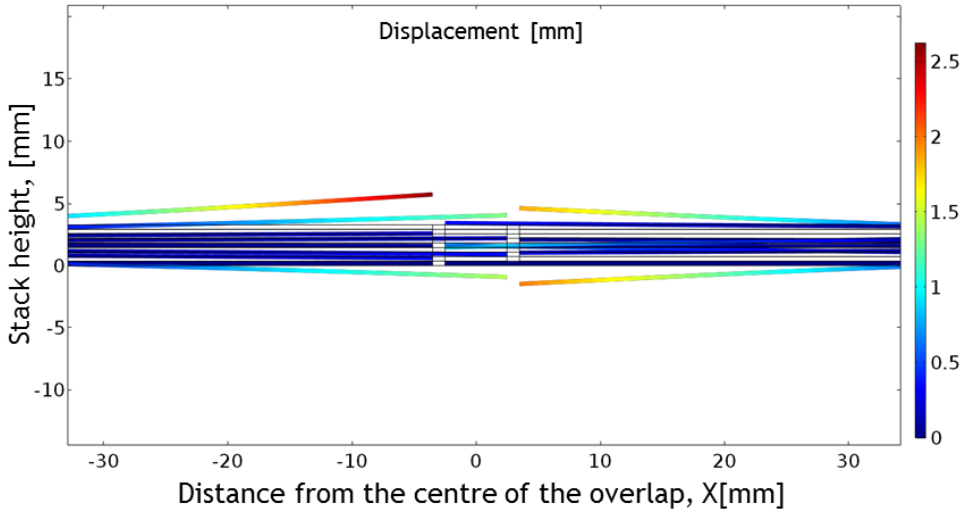

Fig 7-31 Deformation of the laminations due to the Maxwell forces in a static linear joint model magnetised at 1.6 T

As seen in Fig 7-31, the deformation of the top lamination at 15 mm away from the joint is half of that at the edge of the lamination and it is almost insignificant. Thus, it can be concluded that in a linear joint the Maxwell forces are mainly confined within 15 mm to 20 mm around the joints but the amount of the displacement strongly depends on flux distribution and the joint configuration.

7.8 Vibration measurement of the mitred joint

The Vibration of the corner joint of the model core 1 was measured using the 3D laser scanning vibrometer at 0, 1.0 and 2.0 mm air gap lengths and an induction level of 1.0 and 1.7 T, 50 Hz. The velocity of the vibration in a magnetising cycle at 0, 1.0 and 2.0 mm airgap length and 1.7 T are shown in figures Fig 7-32,

Fig 7-33 and Fig 7-34 respectively. The velocity of the vibration at 1.0 T and 0 mm airgap is also presented in Fig 7-35.

In one magnetising cycle the vibration pattern is repeated twice. The amplitude of the vibration velocity on the outer edge of the mitred joint is higher than the inner part. The maximum surface vibration velocity of the core increases from 20 mm/s to 40 mm/s as the length of airgap increases from 0 mm to 2.0 mm. By increasing the longitudinal airgap length, the amount of normal to the plane flux increases. Therefore, the associated Maxwell forces would increase. Furthermore, from the mechanical point of view, the rigidity of the joint reduces as the longitudinal airgap length increases due to the greater freedom of the laminations. By increasing the airgap length, the vibration velocity pattern also changes. For example, when the airgap is 0, the highest value of the velocity at 60^{o} is at the outer corner edge of the yoke but by increasing the airgap length to 1.0 and 2.0 mm the limb (which includes the winding) presents higher values which is due to the change of flux distribution in the vicinity of the joint. Increasing the airgap length, increases the transverse flux density around point J on layer 6 as shown in Fig 7-15-h while at point I on layer 6 it will reduce. The transverse flux in the bottom layer ultimately deviates from its plane and jumps into the adjacent top layer and the exerted force will change the vibration pattern. A similar pattern is observed at 240^{o}. The change of the velocity from positive to negative becomes steeper when the longitudinal airgap increases. By increasing the airgap length the area of the regions of the corner joint which are flapping with higher velocity becomes smaller but the vibration velocity of these regions increases significantly.

Fig 7-35 shows the vibration velocity distribution at 1.0 T, 0 mm airgap length. The vibration distribution pattern at 1.0 T is similar to that at 1.7 T. Comparing Fig 7-32 and Fig 7-35 reveals that a 40% drop in overall induction level leads to 75% drop in the absolute maximum vibration velocity which shows a non-linear trend. In order to find a correlation between the flux distribution and the surface vibration, the displacement of the laminations at the joint and on the 7 pre-defined paths are calculated and shown in Fig 7-36. The displacement on path 1 is always less than 10 μm. Close to the joint on path 2, the vibration displacement has a local maxima and increases again by moving away from the joint which shows that the laminations bend in the vicinity of the joint.

This effect is more significant in the outer part of the joint, e.g. on path 3 where the joint and the limb displacement is about 50 μm at 2.0 mm airgap. The effect of increasing the airgap length on vibration displacement is more significant in the inner and outer regions of the joint rather than the central part which might be due the freedom of movement of the lamination in the outer regions.

Looking at the vibration displacement on path 4 and path 5 reveals that the displacement at the outer part of the laminations is more than the inner part and the central part is almost motionless. Comparing the vibration displacement on paths 4 and 5 at different airgap lengths highlights that the surface displacement of core on the limbs and yokes away from the joint is independent of the airgap length. This was predictable by looking at the trend of the flux in Fig 7-14-e Fig 7-14-f. As discussed, by moving further away from the joints, the effect of the airgap length on flux distribution vanishes. The vibration displacement on path 6 and path 7 reveal that the maximum displacement on the surface happens at the protruding edge of the lamination and is more than 30 μm when no airgap has been introduced to the joint. Based on equation (5-9) the vibration born acoustic emission depends on the vibration acceleration and frequency. Thus 100, 200 and 300 Hz vibration accelerations were calculated and shown in Fig 7-37, Fig 7-38 and Fig 7-39 respectively. Neglecting the nonlinear magnetostriction effect and presuming that everything else is linear it can be stated that if the core was excited with a sine waveform, the acceleration, vibration and displacement waveforms would be sine or cosine, therefore, the trend of change of vibration peak acceleration is very similar to the vibration peak displacement as expected. The side regions of the laminations, especially the protruding region present larger vibration acceleration. Hence it can be concluded that these regions generate more noise in comparison to other areas of the laminations.

As proved, the influence of the airgap length extends into the limb and yoke for a few centimetres, so it is beneficial to just focus on the jointed region on path 6 and path 7. Fig 7-37 to Fig 7-39 show that when there is no airgap in the joint (airgap= 0 mm), 100 Hz is the dominant component of the vibration velocity. The second and third dominant frequencies are 200 Hz and 300 Hz respectively. By increasing the airgap length to 2.0 mm, on path 6 (which is the overlap region) the above mentioned trend is reversed and 300 Hz component becomes dominant while the 100 Hz component is even less than 200 Hz. At 1.00 mm airgap length, which is the middle of the two extremes and is very close to the airgap lengths in

real transformer cores, the 200 Hz component is dominant and then 300 Hz. The 100 Hz component is slightly less than 200 Hz component. This irregular pattern for 1.00 mm airgap is repeated on path 7 as well but the 100 Hz component is more than 300 Hz, while 200 Hz component is the least. As the longitudinal airgap increases, the higher harmonic components of the flux emerge and develop in the airgap. Furthermore, the mechanical constraints in the joint decrease by increasing the airgap length. More mechanical freedom along with bigger amplitudes of higher harmonics magnifies the harmonic content of the vibration displacement.

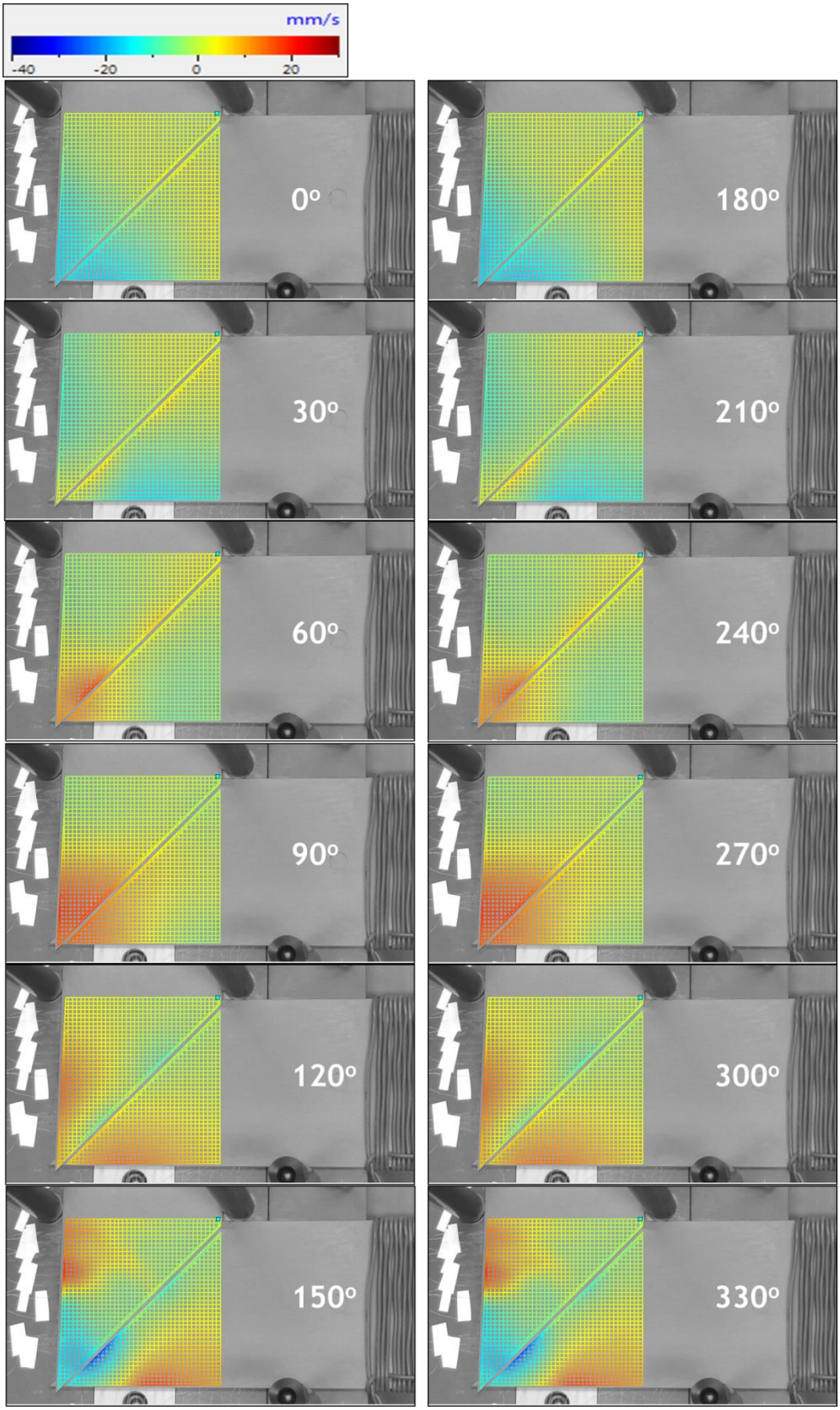

Fig 7-32 One cycle of the vibration distribution in normal to the surface direction on 0 mm airgap corner joint of MC1, single phase, single step lap CGO, without clamping at magnetic flux density 1.7 T, 50 Hz

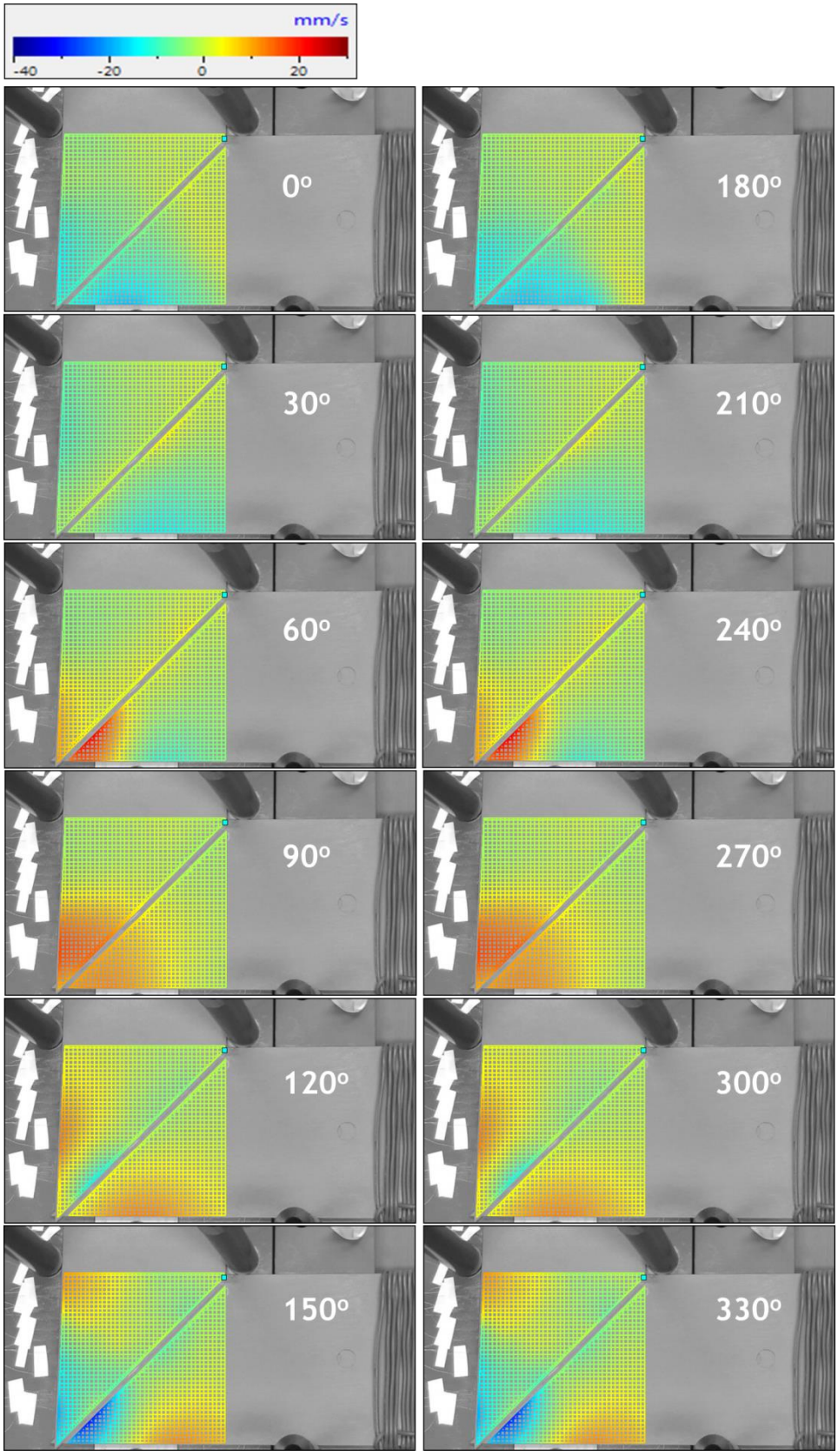

Fig 7-33 One cycle of the vibration distribution in normal to the surface direction on 1.0 mm airgap corner joint of MC1, single phase, single step lap CGO, without clamping at magnetic flux density 1.7 T, 50 Hz

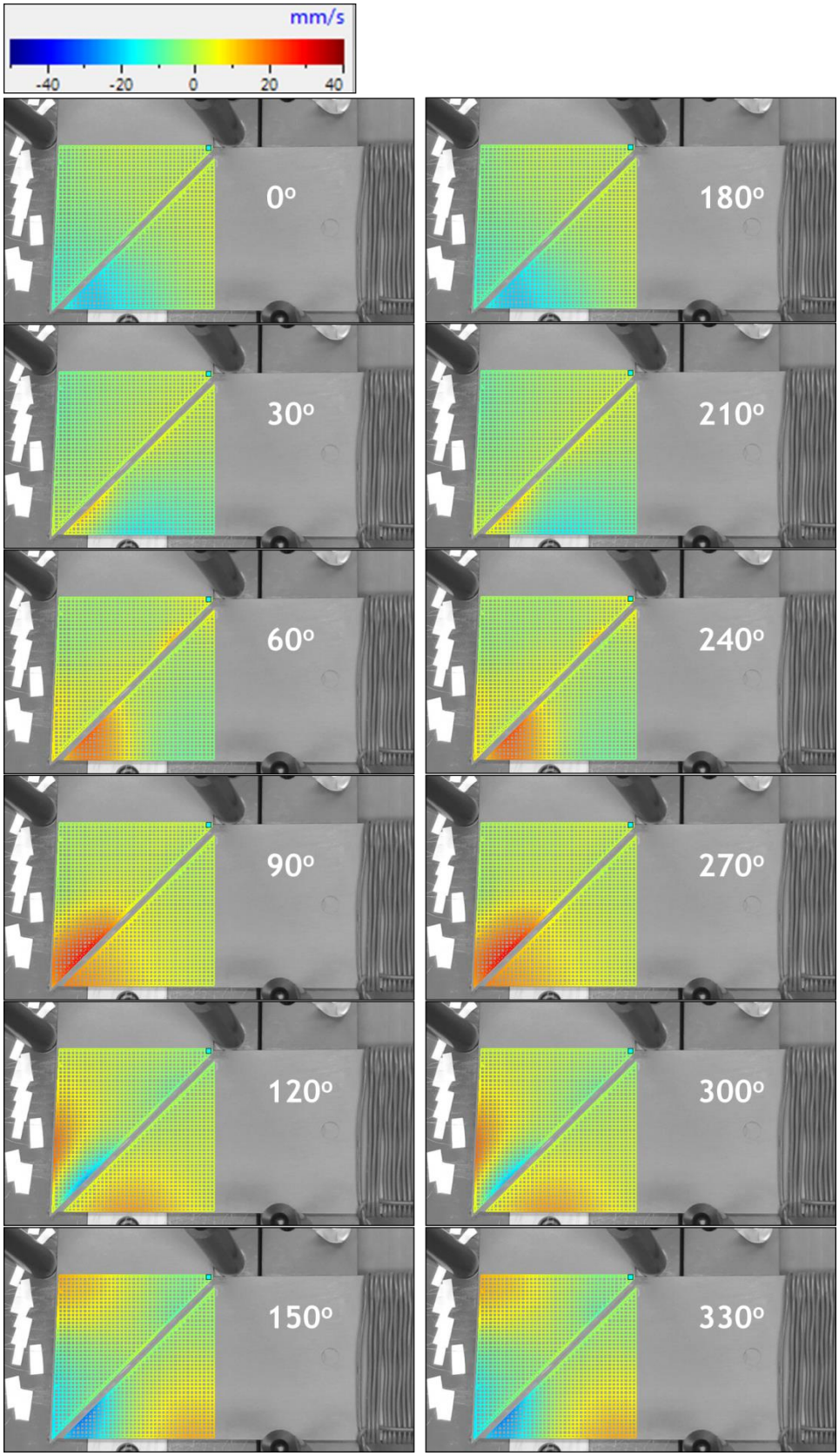

Fig 7-34 One cycle of the vibration distribution in normal to the surface direction on 2.0 mm airgap corner joint of MC1, single phase, single step lap CGO, without clamping at magnetic flux density 1.7 T, 50 Hz

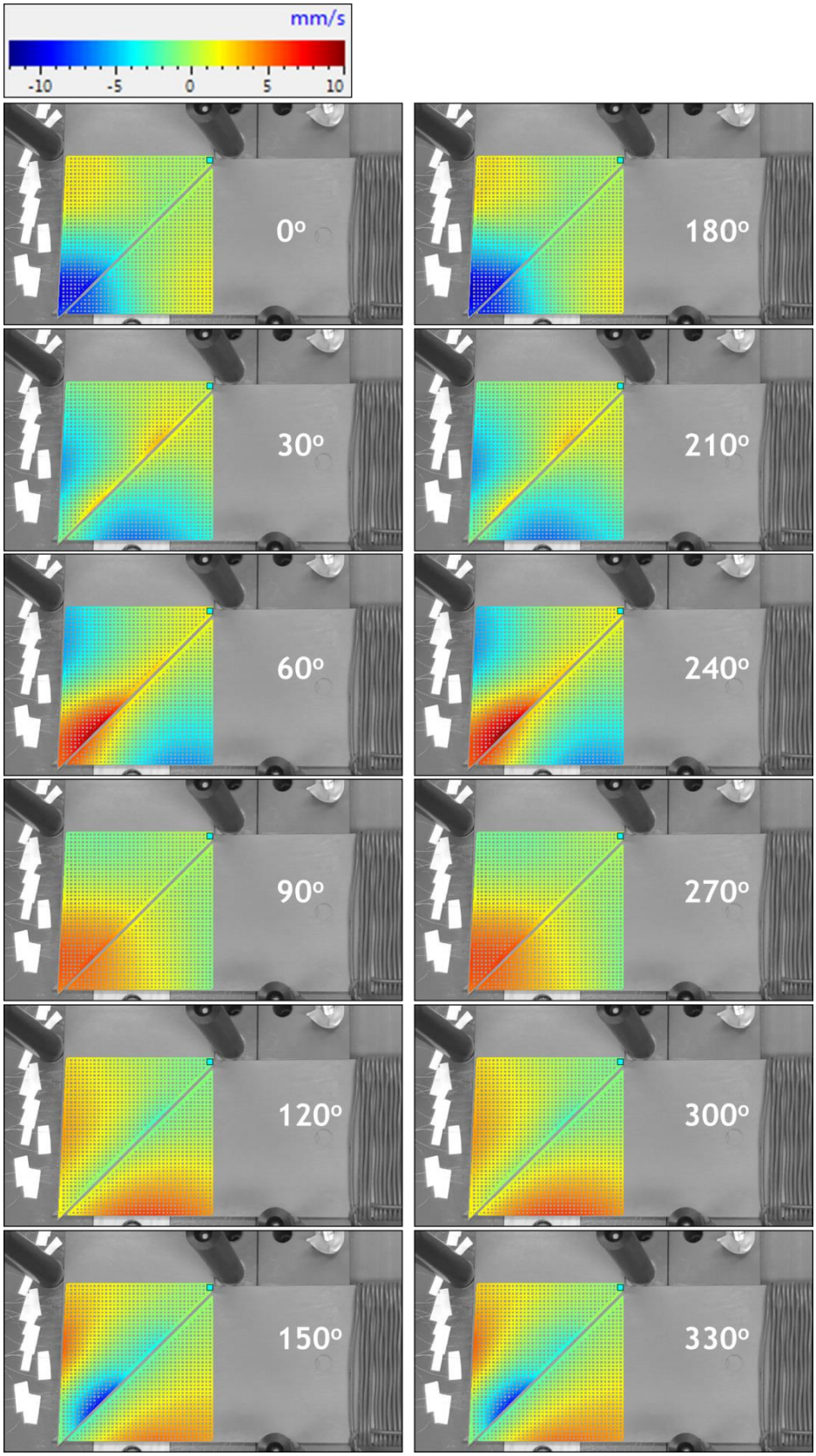

Fig 7-35 One cycle of the vibration distribution in normal to the surface direction on 0 mm airgap corner joint of MC1, single phase, single step lap CGO, without clamping at magnetic flux density 1.0 T, 50 Hz

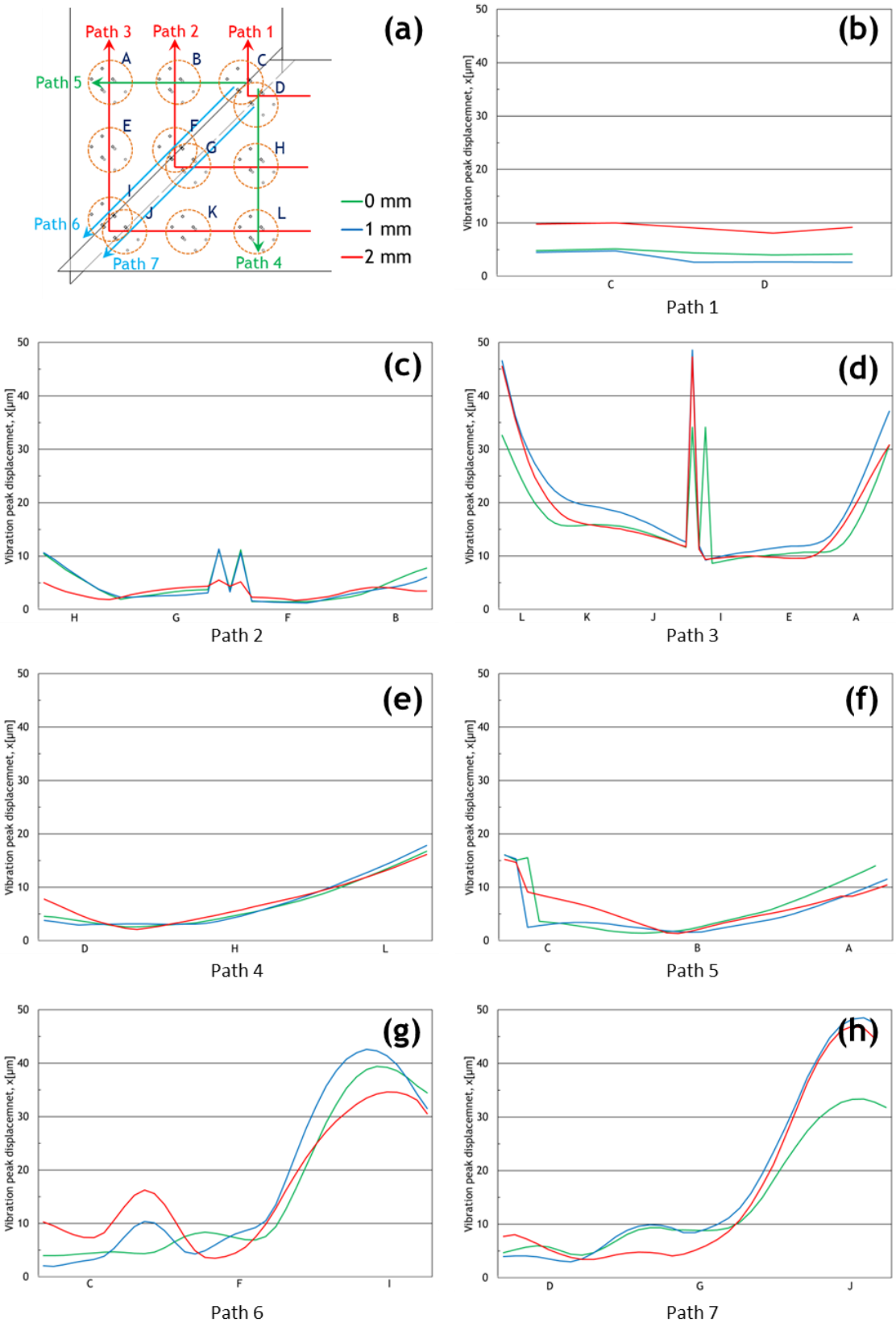

Fig 7-36 Vibration peak displacement measured in a mitred joint of a transformer core assembled with nine layers of GO electrical steel at 1.7 T in 0, 1.0 and 2.0 mm airgap lengths. (a) The guide for the paths and the legend (b) to (h) show the peak displacement in path 1 to path 7 respectively

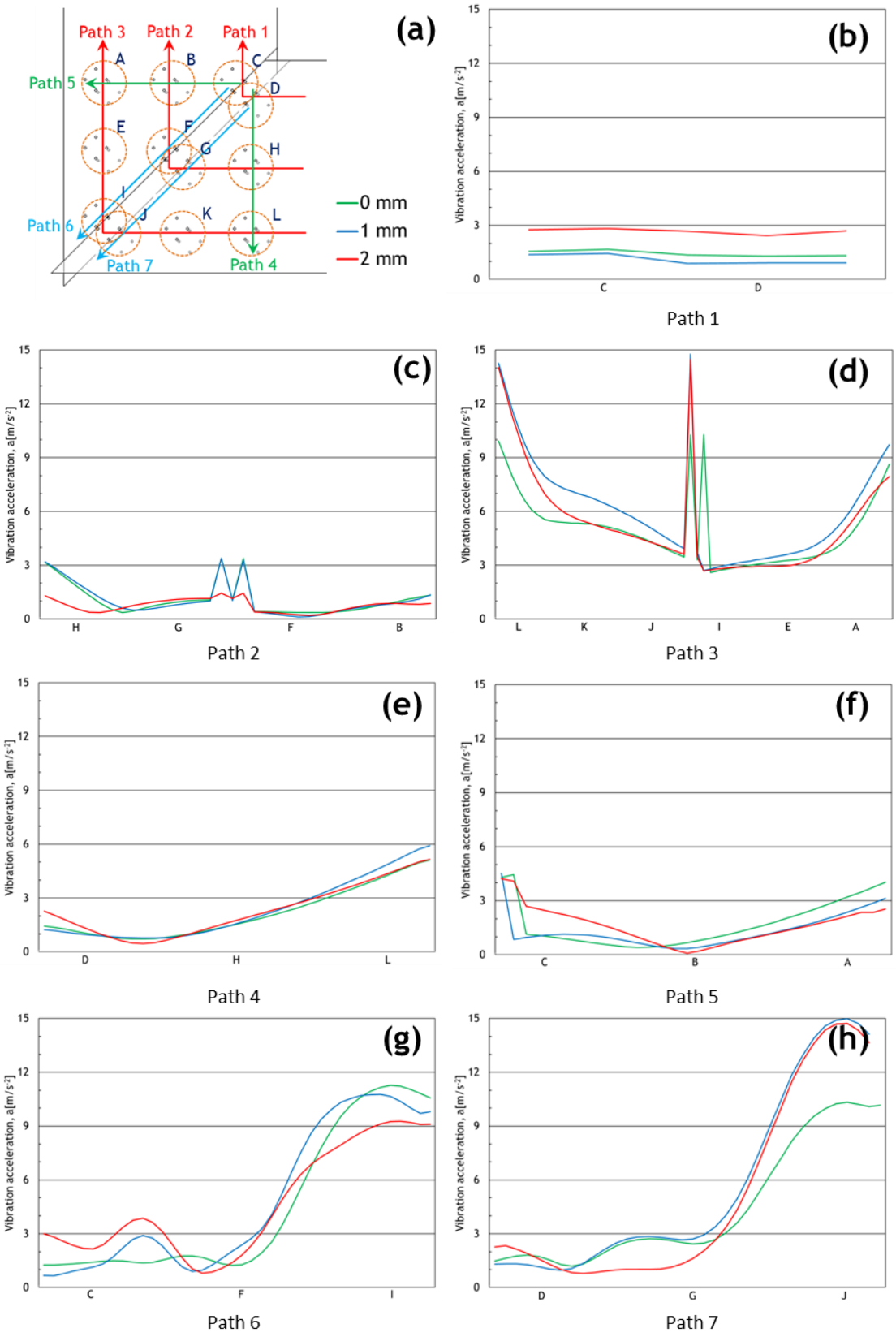

Fig 7-37 100 Hz component of vibration acceleration calculated in a mitred joint of a transformer core assembled with nine layers of grain oriented electrical steel at 1.7 T in 0, 1.0 and 2.0 mm airgap lengths. (a) The guide for the paths and the legend (b) to (h) show the peak acceleration in path 1 to path 7 respectively

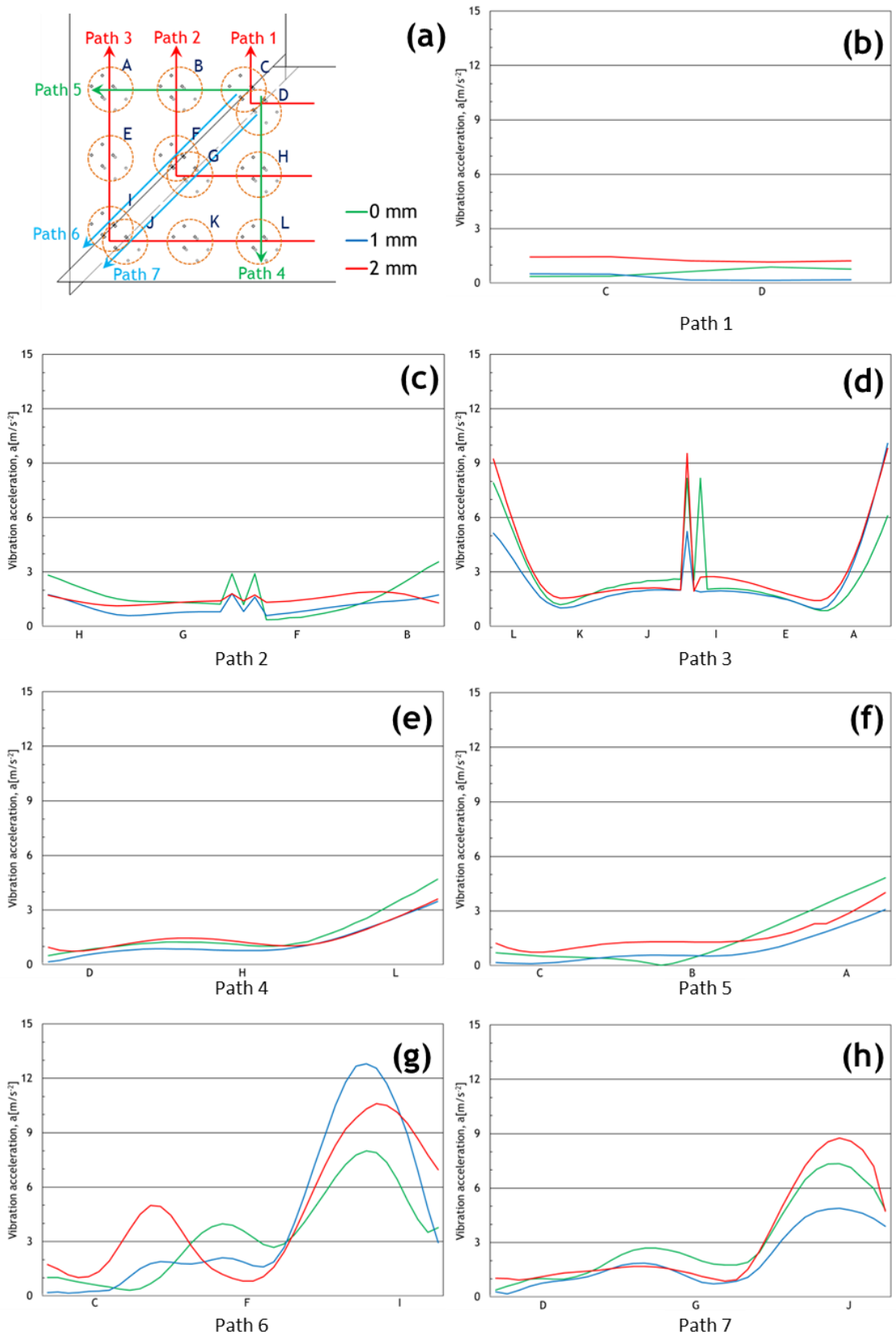

Fig 7-38 200 Hz component of vibration acceleration calculated in a mitred joint of a transformer core assembled with nine layers of GO electrical steel at 1.7 T in 0, 1.0 and 2.0 mm airgap lengths. (a) The guide for the paths and the legend (b) to (h) show the peak acceleration in path 1 to path 7 respectively

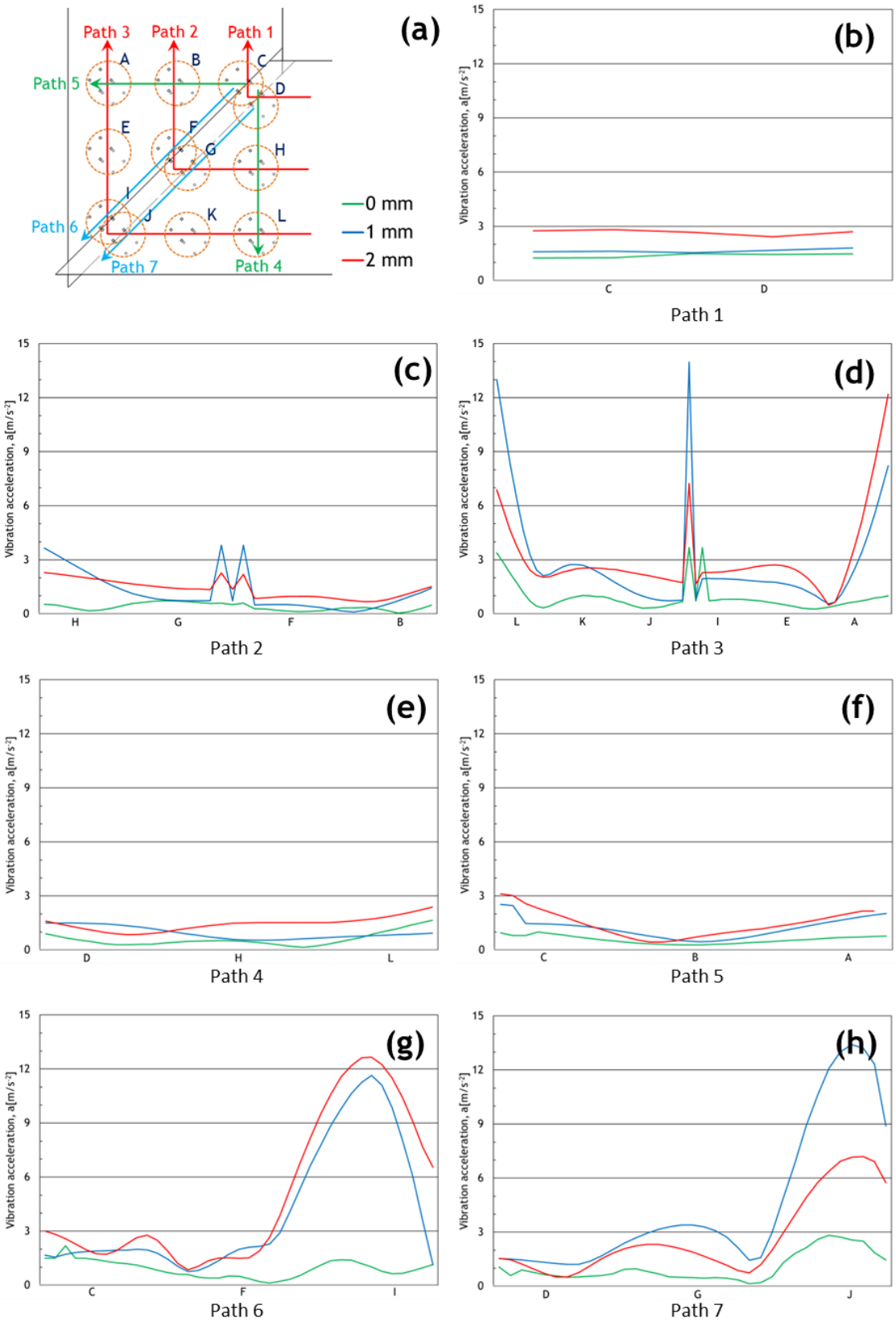

Fig 7-39 300 Hz component of vibration acceleration calculated in a mitred joint of a transformer core assembled with nine layers of GO electrical steel at 1.7 T in 0, 1.0 and 2.0 mm airgap lengths. (a) The guide for the paths and the legend (b) to (h) show the peak acceleration in path 1 to path 7 respectively

7.9 Noise and surface vibration measurements of a three phase transformer core

In order to understand the relationship between the joint's vibration and the whole core vibration it is good to look at the whole production core surface vibration scan and compare the values with those taken from the model core. The correlation between the generated noise and the surface vibration of the transformer core is investigated in this section. The core production core was clamped with a clamping torque of 10 N/m in this investigation.

In order to assess the frequency domain vibration velocities and displacements in more detail, the transformer was divided into specific regions. This was achieved by selecting data points on the central limb, outer limbs and outer corner joints and calculating the corresponding average FFT for those specific regions for 100-500 Hz. Fig 7-40 and Fig 7-41 present the frequency spectrum of the average surface vibration velocity of a 3 phase transformer core at 1.7 T 50 Hz in three directions on limbs and corner joints of a production transformer core.

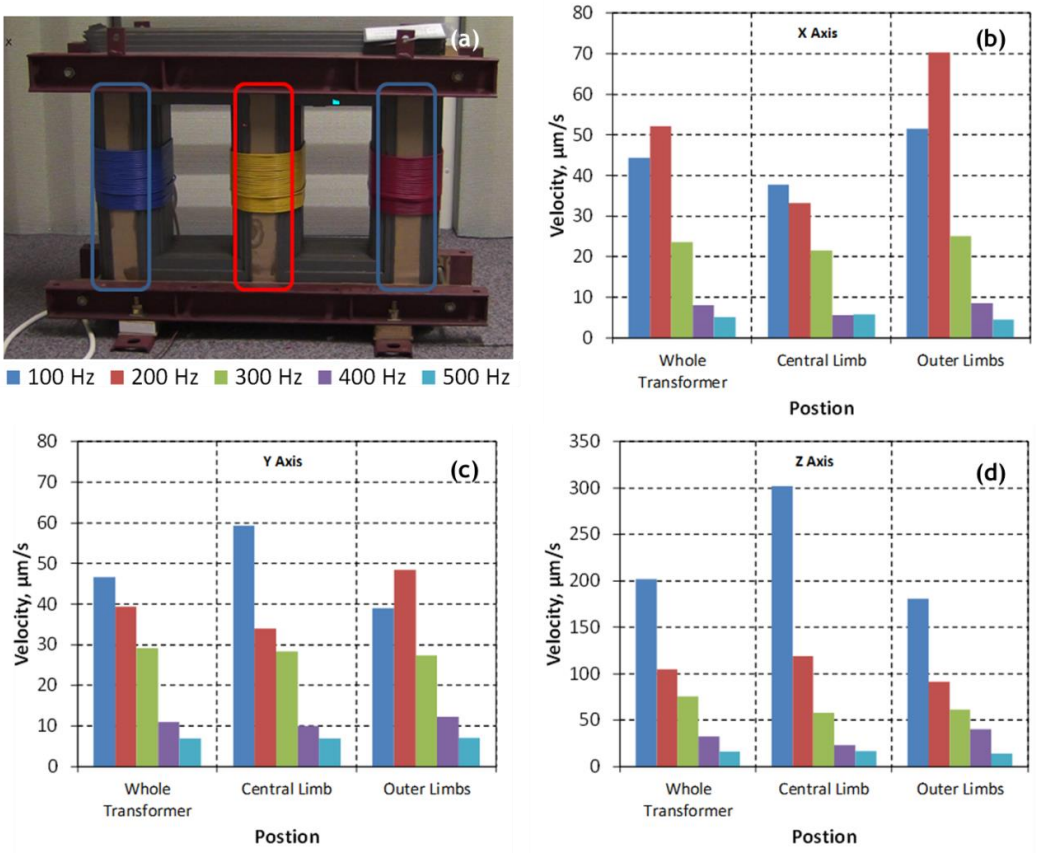

Fig 7-40 Frequency spectrum of average surface vibration velocity of a 3 phase transformer core in (b) x axis (c) Y axis (d) Z axis. In (a) the central limb is marked with a red rectangle and the side limbs are marked with blue ones

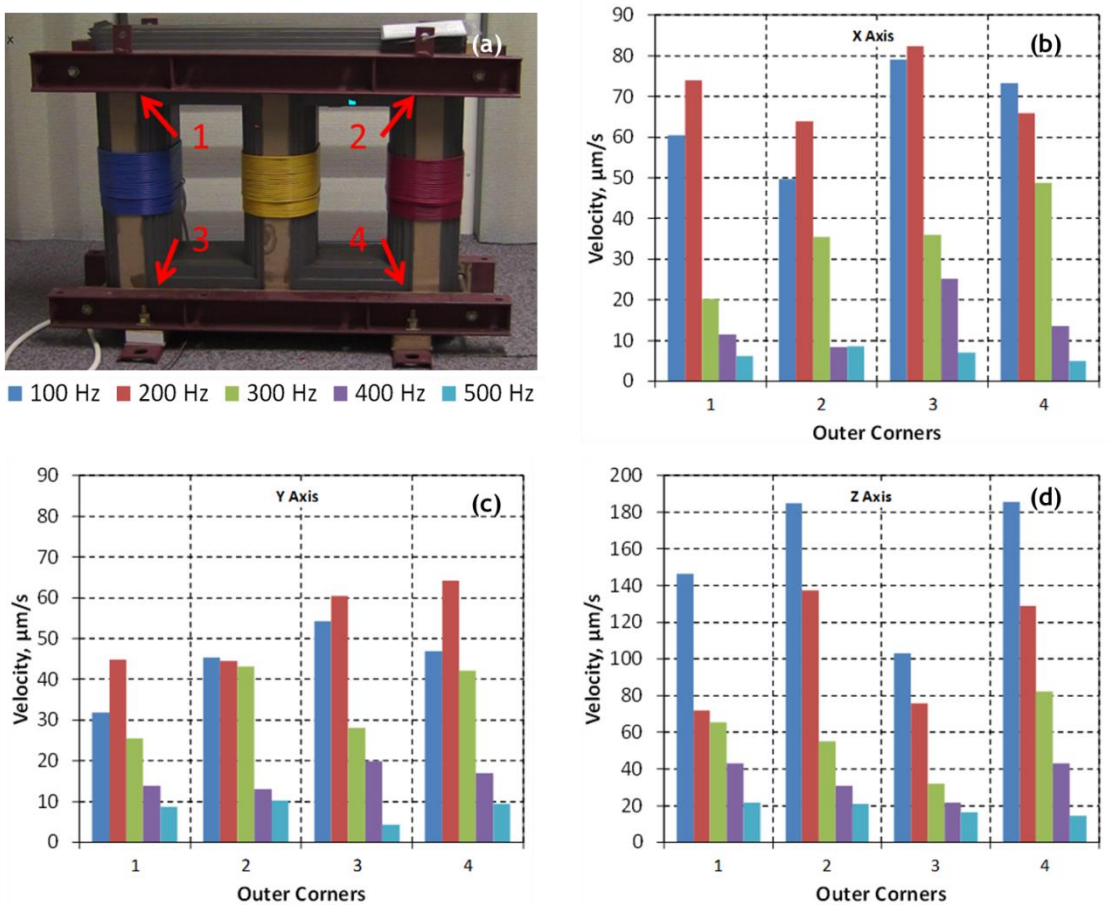

Fig 7-41 Frequency spectrum of average surface vibration velocity of a 3 phase transformer core corner joints in (b) x axis (c) Y axis (d) Z axis

The vibration velocity in the out of plane direction (z) and 100 Hz are dominant in both cases. The average out of plane vibration velocity on four corner edges at 100 Hz is 150 $\mu m.s^{-1}$ while the average out of plane vibration velocity of the outer limbs at 100 Hz is 175 $\mu m.s^{-1}$.Although the absolute value of the vibration velocity of the corner joints is 15% smaller than the rest of the core it should be noted that the corner joints were clamped. It is very well known that part of the vibration of the limbs is due to stimulating the core resonant frequencies.

Fig 7-42 shows the average FFT of the vibration displacement for all the scan points. As shown, vibration displacement at 100 Hz is dominant. The amplitude of the vibration displacement decreases exponentially by increasing the frequency. The low frequency signals in X and Y Axes are due to the environmental noise.

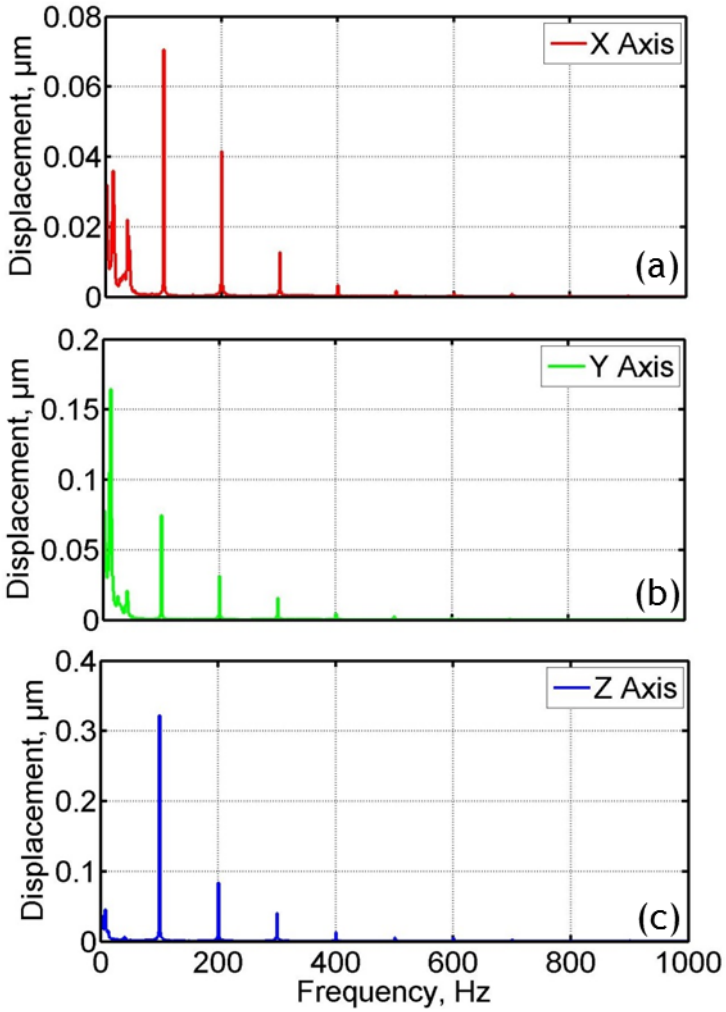

Fig 7-42 Average FFT of the vibration displacement for all the scan points at 1.7 T 50 Hz along the (a) X axis (b) Y axis and (c) Z axis

The average sound pressure level of the transformer core was measured using eight microphones and the results are shown in Fig 7-43. The sound pressure level at 200 Hz is found dominant with 100 Hz component at approximately one third of its value and 300 Hz component being slightly less than 200 Hz. Regarding the equation (5-9) the noise frequency spectrum seems contradictory in comparison to the vibration displacement. In order to make this clear, a set of scanned data from the centre of each limb was extracted and averaged. As the results are shown in Fig 7-44 the outer limbs vibrate in phase with each other at 100 Hz but the central limb has an 180^0 phase shift. The amplitude of the vibration displacement of the central limb is almost twice the amplitude of the individual side limbs. At 200 Hz, the side limbs show 30^0 phase difference but still are closer to each other in comparison to the outer limb. Furthermore, the amplitude of the vibrations in each limb at this frequency are close to each other. At 300 Hz, the amplitudes of the vibration displacement in each limb are almost equal

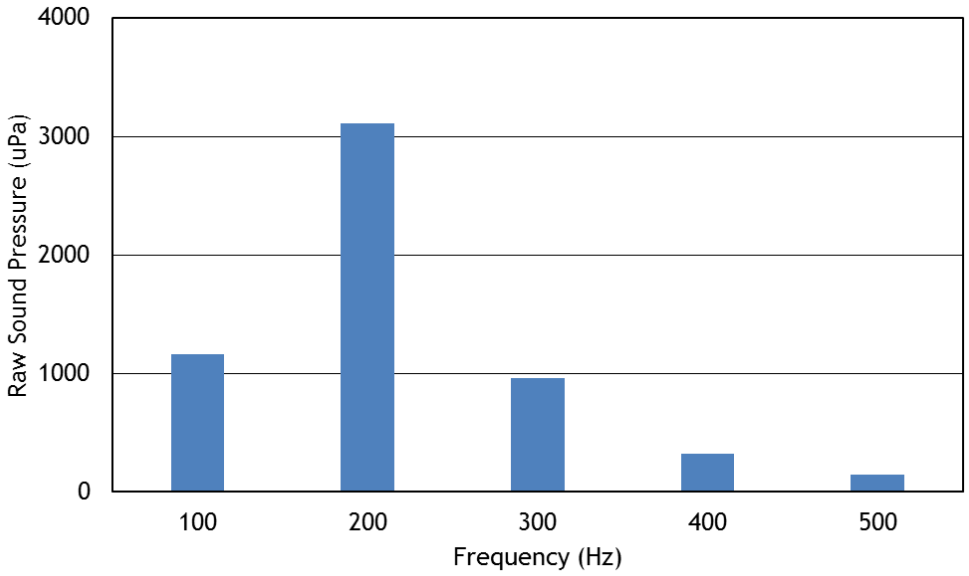

Fig 7-43 Average A weighted sound pressure level of the production core

and the phase difference between each phase in this frequency is 120°. The relationship between the vibration and the measured noise can be explained in two ways. First, based on the above information it can be concluded that the vibration-born noise of the side limbs at 100 Hz is cancelled out with the noise generating from the vibration of the central limb, and so the noise interference is destructive while at 200 Hz the noise interference is constructive. The second theory can be explained based on equation (5-9) and this fact that the noise in each frequency is related to the vibration acceleration in this formula. Therefore the measured displacement values should be converted to the vibration acceleration and then compared with the generated noise. If the vibration displacement, **x**(t), is assumed as follows:

$$\boldsymbol{x}(t) = x_1 \sin(\omega t) + x_2 \sin(2\omega t) + x_3 \sin(3\omega t) \qquad (7\text{-}8)$$

where x_1, x_2 and x_3 are the amplitudes of 100, 200 and 300 Hz in the FFT of the displacement signal and ω is equal to 200π. Then, the vibration acceleration, **v**(t), can be calculated by double differentiation of the displacement signal as follows:

$$\boldsymbol{v}(t) = \frac{d^2X(t)}{dt^2} = \omega^2(x_1 \sin(\omega t) + 4x_2 \sin(2\omega t) + 9x_3 \sin(3\omega t)) \qquad (7\text{-}9)$$

As seen in (**7-9**),the amplitude of the vibration displacement at 200 Hz is scaled up 4 times in comparison to the vibration displacement at 100 Hz which remains the same. Therefore, depending on the amplitude of x_2 the 200 Hz frequency can be dominant. There is still chance for 300 Hz to present higher amplitude in

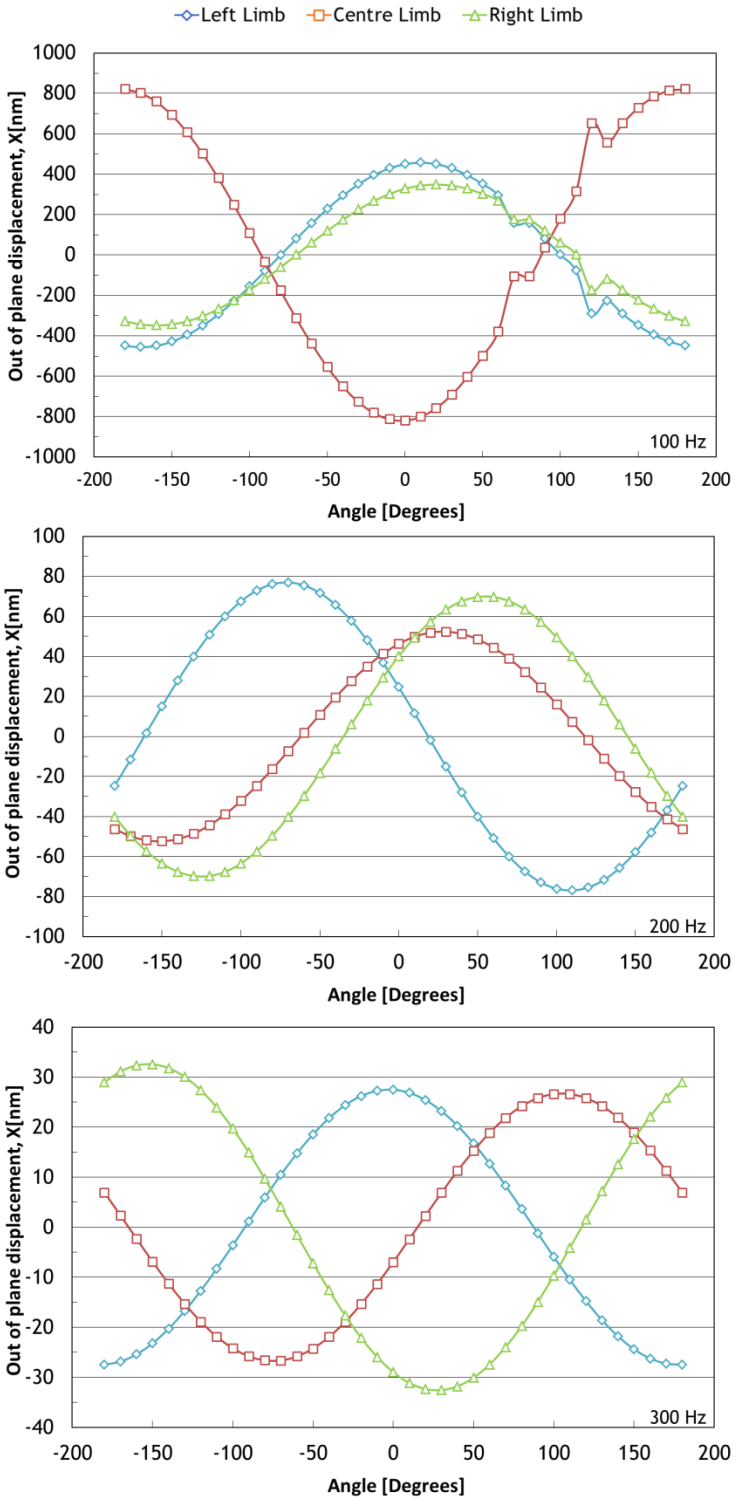

Fig 7-44 Average time displacement vibration measured at the centre of each limb at 1.7 T in 100, 200 and 300 Hz

comparison to 100 and 200 Hz but due to the very small value of x_3 regarding to x_1 and x_2 it is less likely. The level of contribution of the above-mentioned explanations to the vibration-born noise is not clear but it is obvious that the

noise is a function of vibration acceleration and the phase relation of the limbs play an important role to shape the acoustic characteristic of a transformer.

7.10 Summary of main points

The flux density distribution in the un-jointed butt-lap Epstein frame model (LM1-NO and LM1-GO) showed that the flux is not uniform along the limb of the Epstein frame as desired. This non-uniformity extends into the limb to some extent and the amount of the non-uniformity greatly depends on the material grade and the working point of the core. The non-uniformity increases when the magnetic working point of the core is not close to the saturation point of the material.

Introducing joints in a limb of this assembly introduces additional non-uniformity in the core limb. The length of this non-uniformity varies based on the geometry and the grade of the electrical steel. The minimum length occurs when the core operates at it's material highest permeability. As the core induction gets closer to saturation the flux becomes more uniform again.

The experimental and analytical flux density distribution studies in the linear joints showed that the maximum flux density in the gap bridges of the joints can reach 2.2 T. In materials with lower permeability the normal flux density in the vicinity of the joint increases significantly. As the permeability of the materials increases, the normal flux at the edge of the laminations in the joints decreases. The experimental and analytical investigations on the effect of stack height on flux distribution in the linear and mitred joint show that the flux diverges from the central part of the core toward the outer layers. Flux divergence worsens when the core is thin. In the thicker cores (more than 100 layers) flux divergence reduces significantly but it never becomes zero. Using high permeability materials at lower induction levels (not close to their saturation level) increases the flux divergence. This effect is one of the factors which causes noise and vibration in transformer core joints.

Vibration velocity measurement of the mitred joint and its FFT analysis show that the regions in the laminations which have more freedom of movement have more displacement and they move with higher acceleration compared to the rest of the core at all frequencies. Higher acceleration at each frequency means higher noise produced in that frequency. The displacement of the core is due to a mix of the Maxwell forces at the joints and the bending of the limbs due to the

magnetostriction and natural frequencies of the core structure. The effect of the joints is local and is confined in the region limited to a few millimetres away from them. The measurements show that the outer part of the corner joint has a higher value of vibration displacement and acceleration which will lead to higher noise level. The inner region of the corner joint experiences higher Maxwell force but it has less displacement as it is more constrained and rigid.

7.11 Industrial significance of the findings

Designs of real power transformer cores are much more complicated than the models which were used in this research. As shown in section 3.11 there are lots of parameters which affect the flux density distribution in the core, hence vibration and noise. In this section, the relevance of the findings of this research to the real large transformer cores is discussed.

Depending on the rating of a transformer, the lengths of the limbs are often more than 2 metres. The airgap length of the cores are kept as small as possible but based on the assembly quality the airgap length usually vary from less than a millimetre to more than 5 mm. As shown, the flux non-uniformity due to the joints extends into the limb to some extent. Mitered joints assembled from GO conduct the flux better than a butt-lap joint but the non-uniformity of the flux in the limb is unavoidable. As mentioned in section 7.3, by increasing the limb length it is expected that the non-uniformity length reduces in comparison to the models used here. The ratio of the limb length to the butt-joint airgap length (if airgap length is 0.5 mm) in the Epstein frame is about 440 (220÷0.5). This length in a real transformer can vary from 400 (2000÷5) in worst case to at least 6000 (3000÷0.5) in a properly assembled transformer. This means that even in big transformers the flux non-uniformity in the vicinity of the joint can be significant if the core assembly is poor. The MSL joint configuration which is dominantly used in almost all power transformers, redistributes the flux in the joint much better than the SSL configuration and does not introduce concentrated interlaminar flux as in SSL. The length of the flux non-uniformity in MSL is longer than in SSL in each layer but it is distributed between the step laps. As this effect is not concentrated in a small region the effect of non-uniformity in MSL is felt less than in SSL. The packet shift may overwrite the benefit of MSL in power transformers due to the imbalanced flux density in the joint and therefore increase the flux non-uniformity. Power transformers are usually assembled with 2 or 3 laminations

per step which will increase the flux non-uniformity in the vicinity of the joint and increase the interlaminar flux density at the border of each step. The flux non-uniformity ultimately depends on the relative permeability of the electrical steel at the core's magnetic working point. The ratio of the reluctance of the steel at the magnetic working point of the transformer core to the equivalent reluctance of the jointed region determines the amount of non-uniformity in the core, e.g. for a fixed reluctance for the jointed region, if the reluctance of the limb decreases (using electrical steel with higher relative permeability) the flux non-uniformity will increase in the limb. This means that the airgaps should be kept as small as possible in cores assembled with high permeability electrical steels otherwise the consequences of the large airgaps would be more significant than in the cores assembled with lower permeability materials. The flux non-uniformity is ultimately translated to more vibration and noise in the jointed region, beside this, flux harmonics emerges in the jointed regions which cause excess power loss in the core.

Divergence of the flux in the vicinity of the joint increases by increasing the difference between the equivalent reluctance of the longitudinal airgaps in the joint and the reluctance of the limb. This effect causes the outer layers of the transformers to vibrate more than the inner ones. This means that if a core is going to be assembled from high permeability materials more care should be taken to keep the airgaps as small as possible, otherwise, surface vibration of the core will increase in comparison to a core assembled from low permeability material. Increasing the clamping of the core to reduce the vibration will also degrade the magnetic properties of the laminations and introduce other side-effects.

In addition to the flux divergence toward the outer laminations, the flux tends to close its path through the air in 90^{o} joints from the side of the laminations (as shown in Fig 7-4). Although this is unavoidable in real transformer cores it can increase in the presence of large longitudinal airgaps.

The vibration pattern of corner joints in power transformers due to Maxwell forces is not expected to be the same as in the model transformer because, unlike model cores the real core is assembled from few thousand laminations, therefore the flux divergence is expected to be less. However, the outer corner of the joint which has more freedom to vibrate is thought to have a significant contribution in generating noise over the central or inner regions of the corner.

In real large transformer cores other factors like magnetostriction and vibration due to natural frequencies also significantly contribute to generate noise. It is believed that the impact of magnetostriction and resonant frequency of the core is magnified in real transformer cores in comparison to model cores because of their larger dimensions.

8 Conclusion and Future works

8.1 Conclusion

This work investigated the flux density distribution in transformer core joints and its contribution to the vibration and emitted noise of the core. The investigations conducted experimentally on linear and mitred joints and the results were verified analytically with finite element modelling.

A novel translation table with the precision of 10μm was developed, to study the effect of airgap length on flux distribution and vibration in a mitred joint, together with a digital magnetisation system to establish a sinusoidal B in the transformer core. A 3D scanning laser vibrometer was used on joints and core sections to illustrate the complex vibration mechanisms which were correlated with acoustic measurements and the flux density distributions although it should be noted that the vibration is not solely dependent on flux distribution but also on the core build and mechanical characteristics of the core.

It was shown that by increasing the airgap length the vibration of the transformer core increases at the joints with the outer corner region being especially sensitive. Attention to the structure of the outer free ends of the laminations in transformer cores could make significant improvements to core noise.

The three dimensional flux density distribution patterns in transformer cores were shown to be dependent on the magnetic properties of the electrical steel laminations. Lower permability electrical steels tend to increase the flux uniformity in the rolling direction leading to higher normal to the plane flux density and Maxwell forces at the edge of the laminations. The flux density in the transverse direction reduces as the permeability of the electrical steel increases and therefore the flux density is higher at the outer corners of the joint. Higher flux density in a region which is mechanically less constrained would make more vibration and hence more noise.

For cores assembled from high permeability materials the flux tends to divert from the central laminations toward the outer laminations due to the fringing effect. This flux transfer introduces additional normal Maxwell forces across the core and contributes to an increase in the noise generated. The Maxwell force on the outer laminations in cores assembled with high permeability materials is much higher than those with low permeability. When it comes to designing a low noise and low loss transformer, this non-uniformity could become a significant problem, as the material with less power loss will be likely to introduce higher non uniformity and hence noise.

Finite element modelling of a simplified joint showed a good correlation with the experimental results giving confidence in the findings and allowing calculation of Maxwell forces in the normal and in-plane directions. The net force in the normal direction is exerted on the outer layer and its maximum value is at the outer laminations' edge which is 25% greater than the force exerted on the central lamination. The maximum repulsive force in the in-plane direction was greater than the normal force but due to the larger Young's modulus in the rolling direction, the deformation is smaller in this direction. The result of this is that the in-plane deformation appears to be primarily due to magnetostriction whilst Maxwell forces mainly act in the normal to the plane direction.

8.2 Future work

Based on the findings of this research and the experiences of the researcher the following future work is recommended:

- The investigations on linear joints have enabled a great deal of theoretical investigation without the influence of material anisotropy. The next stage will be to introduce a mitred joint. However, it will be essential to precisely-cut the laminations in order to minimise corner gap variation.

- The dimensions of the core were found to be one of the crucial parameters in flux density distribution study. To quantify this effect investigations on larger transformers in which the corner to limb ratio is more representative of real cores could be conducted.

- Manufacturing the search coils could be achieved with metallic laser jet printers decreasing the additional interlaminar airgaps hence the uncertainty of the measurements.

- Ultimately a complete simulation of the laminated core in 3D FEM software would enable a complete study the flux density distribution. Mechanical coupling could then be included in order to model the magnetostriction and natural frequency studies.

References

[1] National Electrical Manufacturers Associations (NEMA), "Transformers, step voltage regulators and reactors" in *TR1*, 2013.

[2] T. Phophongviwat, "Investigation of the influence of magnetostriction and magnetic forces on transformer core noise and vibration," School of Engineering, Cardiff University, Cardiff, 2013.

[3] R. J. D. Tilley, *Crystals and Crystal Structures*: Wiley, 2006.

[4] R. K. Rajput, *A Textbook of Electrical Engineering Materials (U.P. Technical University, Lucknow)*: Laxmi Publications Pvt Limited, 2004.

[5] R. Boll and S. Aktiengesellschaft, *Soft Magnetic Materials: Ed*: Heyden, 1979.

[6] F. Brailsford, *Physical Principles of Magnetism*: London, 1966.

[7] D. Gubbins and E. Herrero-Bervera, *Encyclopedia of Geomagnetism and Paleomagnetism*: Springer Netherlands, 2007.

[8] M. R. Srinivasan, *Physics for Engineers*: New Age International Publishers, 1996.

[9] H. Kronmüller and S. Parkin, *Handbook of Magnetism and Advanced Magnetic Materials*: Wiley, 2007.

[10] J. Shilling and G. Houze, "Magnetic properties and domain structure in grain-oriented 3% Si-Fe," *IEEE Transactions on Magnetics,* vol. 10, pp. 195-223, 1974.

[11] S. Thuanboon and T. U. o. Utah, *Magnetic, Magnetostrictive and Elastic Behaviors of Iron-binary Alloys*: University of Utah, 2008.

[12] D. Jiles, *Introduction to Magnetism and Magnetic Materials* Second ed. vol. 1: Chapman and Hall, 1997.

[13] P. Beckley and I. o. E. Engineers, *Electrical Steels for Rotating Machines*: Institution of Engineering and Technology, 2002.

[14] Y. H. Kim, M. Ohkawa, K. Ishiyama, and K. I. Arai, "Iron loss of grain size controlled very thin grain-oriented silicon steels," *IEEE Transactions on Magnetics*, vol. 29, pp. 3535-3537, 1993.

[15] J. M. D. Coey, *Magnetism and Magnetic Materials*: Cambridge University Press, 2010.

[16] J. Winders, *Power Transformers: Principles and Applications*: CRC Press, 2002.

[17] R. M. D. Vecchio, B. Poulin, P. T. Feghali, D. M. Shah, and R. Ahuja, *Transformer Design Principles: With Applications to Core-Form Power Transformers, Second Edition*: CRC Press, 2010.

[18] X. M. López-Fernández, H. B. Ertan, and J. Turowski, *Transformers: Analysis, Design, and Measurement*: CRC Press, 2016.

[19] M. A. Jones, A. J. Moses, and J. E. Thompson, "Flux distribution and power loss in mitred overlap joint in power transformer cores," *IEEE Transactions on Magnetics,* vol. MAG-9, pp. 114-122, 1973.

[20] D. J. Griffiths, *Introduction to Electrodynamics*: Pearson, 2013.

[21] J. C. Aurich, D. Dornfeld, P. J. Arrazola, V. Franke, L. Leitz, and S. Min, "Burrs—Analysis, control and removal," *CIRP Annals - Manufacturing Technology,* vol. 58, pp. 519-542, // 2009.
[22] O. D. Lascoe and A. International, *Handbook of Fabrication Processes*: ASM International, 1988.
[23] J. Powell, *CO2 Laser Cutting*: Springer London, 2012.
[24] M. Lindenmo, A. Coombs, and D. Snell, "Advantages, properties and types of coatings on non-oriented electrical steels," *Journal of Magnetism and Magnetic Materials,* vol. 215–216, pp. 79-82, 6/2/ 2000.
[25] A. J. Moses and M. Aimoniotis, "Effects of artificial edge burrs on the properties of a model transformer core," *Physica Scripta,* vol. 39, pp. 391-393, 1989.
[26] R. Mazurek, P. Marketos, A. Moses, and J. N. Vincent, "Effect of artificial burrs on the total power loss of a three-phase transformer core," *IEEE Transactions on Magnetics,* vol. 46, pp. 638-641, 2010.
[27] R. Mazurek, H. Hamzehbahmani, A. J. Moses, P. I. Anderson, F. J. Anayi, and T. Belgrand, "Effect of artificial burrs on local power loss in a three-phase transformer core," *IEEE Transactions on Magnetics,* vol. 48, pp. 1653-1656, 2012.
[28] H. Hamzehbahmani, P. Anderson, J. Hall, and D. Fox, "Eddy current loss estimation of edge burr-affected magnetic laminations based on equivalent electrical network - Part I: Fundamental concepts and FEM modeling," *IEEE Transactions on Power Delivery,* vol. 29, pp. 642-650, 2014.
[29] H. Hamzehbahmani, P. Anderson, J. Hall, and D. Fox, "Eddy current loss estimation of edge burr-affected magnetic laminations based on equivalent electrical network - Part II: Analytical modeling and experimental results," *IEEE Transactions on Power Delivery,* vol. 29, pp. 651-659, 2014.
[30] Z. Valkovic, "Effect of electrical steel grade on transformer core audible noise," *Journal of Magnetism and Magnetic Materials,* vol. 133, pp. 607-609, 1994.
[31] L. Lahn, C. Wang, A. Allwardt, T. Belgrand, and J. Blaszkowski, "Improved Transformer Noise Behavior by Optimized Laser Domain Refinement at ThyssenKrupp Electrical Steel," *IEEE Transactions on Magnetics,* vol. 48, pp. 1453-1456, 2012.
[32] D. Snell, "Measurement of noise associated with model transformer cores," *Journal of Magnetism and Magnetic Materials,* vol. 320, pp. e535-e538, 2008.
[33] M. Ishida, S. Okabe, and K. Sato, "Analysis of noise emitted from three-phase stacked transformer model core," *Kawasaki Steel Technical Report,* pp. 29-35, 1998.
[34] S. V. Kulkarni and S. A. Khaparde, *Transformer Engineering: Design and Practice*: CRC Press, 2004.
[35] *Transformers*: Tata McGraw-Hill, 2003.
[36] M. A. Laughton and D. F. Warne, *Electrical Engineer's Reference Book*: Elsevier Science, 2002.
[37] R. M. Bozorth, *Ferromagnetism*: Books on Demand, 1959.
[38] P. Anderson, "A novel method of measurement and characterisation of magnetostriction in electrical steel," Wolfson centre for magnetics, Cardiff University, Cardiff, 2000.
[39] H. Chun-Kan, "The effects of grain size on the magnetic properties of fully processed, continuous-annealed low-carbon electrical steels," *IEEE Transactions on Magnetics,* vol. 32, pp. 471-477, 1996.

[40] S. Somkun, "Magnetostriction and magnetic anisotropy in non-oriented electrical steels and stator core laminations," PhD thesis, Wolfson Centre for Magnetics, Cardiff University, Cardiff, 2010.
[41] H. Berns, G. Scheibelein, and W. Theisen, *Ferrous Materials: Steel and Cast Iron*: Springer Berlin Heidelberg, 2008.
[42] G. C. Stone, E. A. Boulter, I. Culbert, and H. Dhirani, *Electrical Insulation for Rotating Machines: Design, Evaluation, Aging, Testing, and Repair*: Wiley, 2004.
[43] F. J. G. Landgraf, M. Emura, J. C. Teixeira, M. F. de Campos, and C. S. Muranaka, "Anisotropy of the magnetic losses components in semi-processed electrical steels," *Journal of Magnetism and Magnetic Materials,* vol. 196–197, pp. 380-381, 5/1/ 1999.
[44] A. J. Moses and S. Hamadeh, "Effects of mixing materials on losses and cost of operation of three-phase transformer cores," *Journal of Applied Physics,* vol. 64, pp. 5379-5381, 1988.
[45] A. J. Moses, "Some effects of core geometry on building factors of transformer cores assembled from Powercore® strip," *Journal of Materials Engineering,* vol. 12, pp. 195-202, 1990.
[46] D. Snell and A. Coombs, "The influence of core materials and mix on the performance of a 100kVA three phase transformer core," *Journal of Magnetism and Magnetic Materials,* vol. 254, pp. 349-351, 2003.
[47] M. Balehosur, "Predphiction of no-load losses of stacked 3-phase, 3-limb transformer cores," PhD thesis, Wolfson Centre for Magnetics, Cardiff University, Cardiff, 2012.
[48] M. Enokizono, "A measurement system for two-dimensional DC-biased properties of magnetic materials," *Journal of Magnetism and Magnetic Materials,* pp. 39-42, 2003 2003.
[49] T. Yoshida, M. Nakano, D. Miyagi, K. Fujiwara, and N. Takahashi, "Development of measuring equipment of DC-biased magnetic properties using of open type single sheet tester," in *INTERMAG 2006 - IEEE International Magnetics Conference*, San Diego, CA, 2006, p. 355.
[50] L. Cao, J. Zhao, and J. He, "Improved power transformer model for DC biasing analysis considering transient leakage reluctances," in *2006 International Conference on Power System Technology, POWERCON2006*, Chongqing, 2007.
[51] E. Mulasalihović, H. Pfützner, S. Traxler, and H. Yamaguchi, "Effects of geomagnetically induced currents on the magnetic performance of transformer cores," *Journal of Magnetism and Magnetic Materials,* vol. 320, pp. e920-e924, 2008.
[52] Y. Chen, T. Lu, L. Li, and Z. Zhao, "Study on the electromagnetic influence of DC bias on the power transformer," in *2009 IEEE International Symposium on Electromagnetic Compatibility, EMC 2009*, Austin, TX, 2009, pp. 301-304.
[53] M. A. S. Masoum and P. S. Moses, "Impact of balanced and unbalanced direct current bias on harmonic distortion generated by asymmetric three-phase three-leg transformers," *IET Electric Power Applications,* vol. 4, pp. 507-515, 2010.
[54] S. YANASE, M. UCHIYAMA, S. ISHIKAWA, and Y. OKAZAKI, "AC Magnetic Properties of Electrical Steel Sheet under DC-biased Magnetisation," *PRZEGLĄD ELEKTROTECHNICZNY (Electrical Review),* vol. 87, pp. 52-56, 2011.
[55] S. Ishikawa, S. Yanase, and Y. Okazaki, "AC magnetic properties of electrical steel sheet under two-dimensional DC-biased magnetisation," *IEEE Transactions on Magnetics,* vol. 48, pp. 1413-1416, 2012.

[56] Z. Zhao, Y. Li, F. Liu, Z. Cheng, L. Liu, J. Zhang, *et al.*, "Magnetic property modelling of laminated silicon steel sheets under DC-biasing magnetisation," in *2012 6th International Conference on Electromagnetic Field Problems and Applications, ICEF'2012*, Dalian, 2012.

[57] F. Bachinger, A. Hackl, P. Hamberger, A. Leikermoser, G. Leber, H. Passath, *et al.*, "Direct current in transformers: effects and compensation," *e & i Elektrotechnik und Informationstechnik,* pp. 1-5, 2013.

[58] W. Jiayin, B. Baodong, L. Hongliang, and M. Chuang, "Research on Vibration and Noise of Transformer under DC Bias based on magnetostriction," in *International Conference on Electrical Machines and Systems*, Busan, Korea, 2013, pp. 2225-2228.

[59] H. Pfützner, G. Shilyashki, F. Hofbauer, D. Sabic, E. Mulasalihovic, and V. Galabov, "Effects of DC-bias on loss distribution of model transformer core," *Journal of Electrical Engineering,* vol. 61, pp. 126-129, 2013.

[60] H. Inouea and S. Okabe, "Magnetic properties of grain oriented electrical steel in model transformer under direct current-biased magnetisation," *Journal of Applied Physics,* vol. 115, 2014.

[61] M. Mizokami and Y. Kurosaki, "Variation of noise and magnetostriction associated with joint types of transformer core," *IEEJ Transactions on Fundamentals and Materials,* vol. 134, pp. 334-339, 2014.

[62] Z. Valkovic, "Effects of transformer core design on noise level," *Journal De Physique. IV : JP,* vol. 8, pp. Pr2-603-Pr2-606, 1998.

[63] R. S. Girgis, E. G. t. Nijenhuis, K. Gramm, and J. E. Wrethag, "Experimental investigations on effect of core production attributes on transformer core loss performance," *IEEE Transactions on Power Delivery,* vol. 13, pp. 526-531, 1998.

[64] G. F. Mechler and R. S. Girgis, "Magnetic flux distributions in transformer core joints," *IEEE Transactions on Power Delivery,* vol. 15, pp. 198-203, 2000.

[65] F. Loffler, T. Booth, H. Pfutzner, C. Bengtsson, and K. Gramm, "Relevance of step-lap joints for magnetic characteristics of transformer cores," *IEE Proceedings: Electric Power Applications,* vol. 142, pp. 371-378, 1995.

[66] A. Ilo, "Behavior of transformer cores with multistep-lap joints," in *2003 Industrial and Commercial Power Systems Technical Conference*, USA, 2002, pp. 42-47.

[67] Z. Valkovic, "Investigations of core noise levels using a dry-type transformer model," *Journal of Magnetism and Magnetic Materials,* vol. 160, pp. 205-206, 1996.

[68] A. Ilo, B. Weiser, T. Booth, and H. Pfützner, "Influence of geometric parameters on the magnetic properties of model transformer cores," *Journal of Magnetism and Magnetic Materials,* vol. 160, pp. 38-40, 1996.

[69] A. Basak, A. J. Moses, and R. AlBir, "Effect of Clamping Stress on Power Loss in Powercore Strip and SIFE Transformer Cores," *IEEE Transactions on Magnetics,* vol. 26, pp. 1999-2001, 1990.

[70] A. Basak, A. J. Moses, and M. R. Yasin, "Effect of stacking method and clamping on distribution transformers built with amorphous magnetic material," *5th Joint MMM-Intermag Conference,* vol. 27, pp. 5196-5198, 1991.

[71] I. Daut and A. J. Moses, "Some Effects Of Clamping Pressure On Localised Losses And Flux Distribution In A Transformer Core Assembled From Powercore Strip," *IEEE Transactions on Magnetics,* vol. 27, pp. 5262-5264, 1991.

[72] I. Daut, D. Maizana, S. Uthman, and S. Taib, "Different clamp stress impact on losses and flux distribution between two of 3 phase distribution

transformer 1000 kVA assembled with stagger yoke of transformer core lamination," in *2007 International Conference on Intelligent and Advanced Systems, ICIAS 2007*, 2007, pp. 851-853.
[73] C. H. Hsu, S. L. Lee, C. C. Lin, C. S. Liu, S. Y. Chang, M. F. Hsieh, *et al.*, "Reduction of Vibration and Sound-Level for a Single-Phase Power Transformer With Large Capacity," *IEEE Transactions on Magnetics,* vol. 51, pp. 1-4, 2015.
[74] R. Penin, G. Parent, J. P. Lecointe, J. F. Brudny, and T. Belgrand, "Impact of mechanical deformations of transformer corners on core losses," *IEEE Transactions on Magnetics,* vol. 51, pp. 1-5, 2015.
[75] M. Mizokami and Y. Kurosaki, "Noise increase by abnormal joints in transformer cores," *IEEJ Transactions on Fundamentals and Materials,* vol. 132, pp. 192-197, 2012.
[76] B. Weiser and H. Pfützner, "Relevance of magnetostatic forces for transformer core vibrations," in *Journal De Physique. IV : JP* vol. 8, ed, 1998, pp. Pr2-591-Pr2-594.
[77] E. W. Flick, *Epoxy Resins, Curing Agents, Compounds, and Modifiers, Second Edition: An Industrial Guide*: Elsevier Science, 2012.
[78] A. J. Moses and S. M. Pegler, "The effects of flexible bonding of laminations in a transformer core," *Journal of Sound and Vibration,* vol. 29, pp. 103-112, 1973.
[79] A. Ilo, H. Pfützner, and T. Nakata, "Critical induction - a key quantity for the optimisation of transformer core operation," *Journal of Magnetism and Magnetic Materials,* vol. 215, pp. 637-640, 2000.
[80] R. Girgis, J. Anger, and D. Chu. (2008) The sound of silence. *ABB review*.
[81] F. Brailsford and V. R. Mazza, "The alternating magnetic flux distribution in right-angled corners of transformer laminations. An experimental investigation," *Proceedings of the IEE - Part A: Power Engineering,* vol. 109, pp. 173-180, 1962.
[82] M. A. Jones and A. J. Moses, "Comparison of the localized power loss and flux distribution in the butt and lap and mitred overlap corner configuration," *IEEE Transactions on Magnetics,* vol. MAG-10, pp. 321-326, 1974.
[83] T. Nakata, N. Takahashi, and Y. Kawase, "Magnetic performance of step-lap joints in distribution transformer cores," *IEEE Transactions on Magnetics,* vol. 18, pp. 1055-1057, 1982.
[84] Q. Tang, S. Guo, and Z. Wang, "Magnetic flux distribution in power transformer core with mitred joints," *Journal of Applied Physics,* vol. 117, 2015.
[85] B. Weiser, H. Pfützner, and J. Anger, "Relevance of magnetostriction and forces for the generation of audible noise of transformer cores," *IEEE Transactions on Magnetics,* vol. 36, pp. 3759-3777, 2000.
[86] G. Shilyashki, H. Pfützner, F. Hofbauer, D. Sabic, and V. Galabov, "Magnetostriction distribution in a model transformer core," *Journal of Electrical Engineering,* vol. 61, pp. 130-132, 2013.
[87] P. Witczak, "Magnetostriction force spectrum in power transformer," in *Electrical Machines (ICEM), 2014 International Conference on*, 2014, pp. 2246-2251.
[88] M. Mizokami, M. Yabumoto, and Y. Okazaki, "Vibration analysis of a 3-phase model transformer core," *Electrical Engineering in Japan (English translation of Denki Gakkai Ronbunshi),* vol. 119, pp. 1-7, 1997.
[89] I. E. Standard, "Part 2: Methods of measurements of the magnetic properties of electrical steel sheets and strip by means of an Epstein frame," in *IEC 60404-2*, ed, 2008.

[90] P. Marketos, S. Zurek, and A. J. Moses, "A Method for Defining the Mean Path Length of the Epstein Frame," *IEEE Transactions on Magnetics,* vol. 43, pp. 2755-2757, 2007.
[91] P. Di Barba and A. Savini, *Non-linear Electromagnetic Systems: ISEM '99*: IOS Press, 2000.
[92] IEC, "Magnetic materials - Part 3: Methods of measurement of the magnetic properties of magnetic sheet and strip by means of a single sheet tester," ed, 1992, p. 20.
[93] I. E. Standard, "Part 3: Magnetic materials. Methods of measurement of the magnetic properties of magnetic sheet and strip by means of a single sheet tester," ed: IEC, 1992.
[94] M. D. Wulf, L. Dupré, D. Makaveev, and J. Melkebeek, "Needle-probe techniques for local magnetic flux measurements," *Journal of Applied Physics,* vol. 93, pp. 8271-8273, 2003.
[95] P. Schönhuber and H. Pfützner, "Flux distribution analysis in a mitred transformer core corner," *Journal of Magnetism and Magnetic Materials,* vol. 101, pp. 86-88, 1991.
[96] F. Loffler, H. Pfutzner, T. Booth, C. Bengtsson, and K. Gramm, "Influence of air gaps in stacked transformer cores consisting of several packages," *IEEE Transactions on Magnetics,* vol. 30, pp. 913-915, 1994.
[97] UKAS, "The expression of uncertainity and confidence in measurements," in *M3003*, ed. UK: UKAS, 2012.
[98] National Instruments, "NI 6120 DAQ manual," NI, Ed., ed. US: NI.
[99] I. E. Standard, "Power Transformers - Part 10 - Determination of sound levels," ed: IEC, 2001, p. 38.
[100] G. Buzdugan, E. Mihâilescu, and M. Rades, *Vibration measurement*: Springer Netherlands, 2013.
[101] F. Levinzon, *Piezoelectric Accelerometers with Integral Electronics*: Springer International Publishing, 2014.
[102] G. Shilyashki, H. Pfützner, P. Hamberger, M. Aigner, A. Kenov, and I. Matkovic, "Spatial distributions of magnetostriction, displacements and noise generation of model transformer cores," *International Journal of Mechanical Sciences,* vol. 118, pp. 188-194, 2016.
[103] S. G. Ghalamestani, "Identification of transformer core vibrations and the effect of third harmonic in the electricity grid,"International Journal of Electrical, Computer, Electronics and Communication Engineering, vol. 8, pp. 871-874, 2014.
[104] Y. F. Xing and B. Liu, "New exact solutions for free vibrations of thin orthotropic rectangular plates," *Composite Structures,* vol. 89, pp. 567-574, 8// 2009.
[105] "Acoustic Module User's Guide," ed: COMSOL Multiphysics November 2013.
[106] G. Dhatt, E. Lefrançois, and G. Touzot, *Finite Element Method*: Wiley, 2012.
[107] C. M. v. 5.2, "COMSOL Multiphysics Reference Manual ", ed. Stockholm, Sweden, 2015.
[108] M. v. d. Giet, K. Kasper, R. W. D. Doncker, and K. Hameyer, "Material parameters for the structural dynamic simulation of electrical machines," in *2012 XXth International Conference on Electrical Machines*, 2012, pp. 2994-3000.
[109] G. Shilyashki, H. Pfutzner, and C. Huber, "Interlaminar Magnetic Flux Assessment of a Transformer Core Measured by an Extra-thin Printed Foil Detector," *IEEE Transactions on Magnetics,* vol. PP, pp. 1-1, 2017.

Publications

- H. Shahrouzi, A. J. Moses, P. I. Anderson, “Comparison between computed and measured magnetic flux density distribution of simulated transformer core joints assembled from grain-oriented and non-oriented electrical steel”, in 23rd Soft Magnetic Materials Conference, Seville, Spain, 2017.

- P. I. Anderson, J. Homewood, M. Pearson, H. Shahrouzi, “Vibration analysis of a three-phase production transformer core”, in 1&2-dimensional magnetic measurement conference, Tianjin, China, Sep. 2016.

- A. J. Moses, H. Shahrouzi, P. I. Anderson, “Effect of butt-lap joint on flux harmonics and localised building factors in the limbs of transformer cores”, submitted to IEEE Transactions on Magnetics and is under review.

Index